Quantum Chemical Modelling of Organo–Transition Metal Structure, Bonding, and Reaction Mechanism

Abigail Rose Elizabeth Mountain

A thesis submitted for the degree of Doctor of Philosophy

Department of Chemistry, University College London

June 2017

I, Abigail R. E. Mountain, confirm that the work presented in this thesis is my own. Where information has been derived from other sources, I confirm that this has been indicated in the thesis.

Signed

Abstract

In this thesis, density functional theory is used to investigate the structure, bonding, and reaction mechanisms of two families of organometallic compounds discussed below. The first chapter briefly introduces the research projects undertaken for this PhD, while the second introduces the theoretical background of electronic structure calculations.

Chapter 3 begins with an introduction to homogenous Ziegler-Natta catalysis of olefin polymerisation, with a focus on chain propagation and termination reaction mechanisms for propylene homopolymerisation. These mechanisms are then explored in benchmarking studies of the naked cationic post-metallocene catalyst $[\mathrm{MeTiCp^*\{CN(Ph)N(iPr)_2\}}]^+$, comparing reaction profiles calculated using different approaches to describe dispersion and solvent effects, as well as those found using *ab initio* methods. It is concluded that dispersion interactions play an important role in predicting the expected trends in reaction barrier height for propagation *vs.* termination, and the methodology which best describes this is chosen and implemented in the subsequent chapter.

The effects of the anionic co-catalyst $[\mathrm{B(C_6F_5)_4}]^-$ on homopolymerisation studies of ethylene and propylene with $[\mathrm{MeTiCp^*\{CN(Ph)N(iPr)_2\}}]^+$, are explored in Chapter 4. Differences between olefin complexation, chain propagation and termination reactions calculated with and without the anion are discussed, as well as predictions of macroscopic properties of polymers produced using this catalytic system.

Chapter 5 introduces a different research project; the investigation of the structure, bonding, and reactivity of metal boryl and gallyl compounds, $\mathrm{Ln\{E(NArCH)_2\}\{Me_3SiCH_2C(NCy)_2\}_2(THF)}_n$ (Ln = Sc, Y, Lu; E = B, Ga; n = 0, 1). The changes in structure and Ln–E bonding interaction are compared between five- and six-coordinate analogues of the systems, accounting for the difference in coordination number of the boryls *vs.* the gallyls, and their reactivity with carbodiimide iPrNCNiPr. Finally, the mechanism for carbodiimide insertion into the Mg–Ga bond of $\mathrm{Mg\{^{Dipp}NacNac\}Ga(NDippCH)_2\}}$ systems is explored.

Acknowledgements

First and foremost, I'd like to give great thanks to Nik, from whom my enthusiasm for computational chemistry was spawned five or so years ago during our discussions of Richard Bader. He has passed on a great deal to me over the years, not least the correct way in which to write the Schrödinger equation. I would like to express my sincerest gratitude to him for all his help over the years.

I am very lucky to have had the opportunity to collaborate with such a talented group of chemists. Professor Philip Mountford has been a wealth of knowledge and expertise in areas unfamiliar to me. Other thanks, of course, go to Dr Liban Saleh, Dr Matthew Blake, and Mr Adàn Reyes-Sanchez, who carried out the experimental work related to Chapter 5 of this thesis. I would also like to acknowledge my sponsors at both ARLANXEO Netherlands B.V. and DSM: Dr Alexandra Berthoud, Dr Betty Coussens, Dr Richard Scott, Dr Rafaela Bernado, John van de Moosdijk, and Dr Gerard van Doremaele. It has been a pleasure to work with such experts in the field.

The nature of a PhD is such that some very special friendships are built over its course. It is the occupants, and regular visitors, of G19 whom I will sorely miss on leaving UCL. Special thanks go to Eamonn, Eszter, Joe, Poppy, and Reece, who have been the greatest distraction and encouragement throughout my time as a PhD student, and to Belle, with whom I've shared my whole UCL experience.

External distractions and motivation have also been essential in maintaining my sanity, particularly during the last nine months. My friends outside of UCL have excelled in this respect and have always managed to make me laugh and smile. Kudos to Abi, Alex, Craig, Dana, Dave, Isobel, Sham, and Sal for their collective wit and meme-sharing. I, of course, owe a great deal to my emotional support group, Emily and Toria, who have always been on hand to send photos of motivational hedgehogs and a baby Bear. Thank you. Also, huge appreciation goes to Alex and Geoff - great friends, without whom I wouldn't have landed on my feet in the non-academic world in such a fantastic job.

My thanks also go out to the vast collection of Wilkinsons, Gills, Ramsays, and Kenchingtons. A special mention must be given to Sandy and Gray, who provided me with a home for nine months, and to Bridie, the best sister I never had. My own family, of

course, cannot be thanked enough. My mum, Greta, from whom I certainly inherited my passion for chemistry; my dad, Peter, who I know is terribly proud of me; and my brother, Daewoo - Science!

The person whom I find hardest of all to thank is Toby. Amongst everything else I have to be grateful to him for, I'd like to thank him for always believing in me, especially when I've struggled to do so myself.

Contents

1 Introduction **19**
1.1 Research Projects . . . 19
1.1.1 Post-Metallocene Catalysed Propylene Homo-polymerisation - A Benchmarking Study . . . 20
1.1.2 Ion-Pair Calculations of Ethylene and Propylene Homopolymerisation 20
1.1.3 Structure and Reactivity of Rare Earth Metal Boryl and Gallyl Compounds . . . 21

2 Theoretical Background **22**
2.1 The Born-Oppenheimer Approximation . . . 23
2.2 Hartree-Fock Self-Consistent Field Method . . . 24
2.3 Post-Hartree-Fock Methods . . . 26
2.3.1 Configuration Interaction . . . 27
2.3.2 Coupled Cluster . . . 28
2.3.3 Møller-Plesset Perturbation Theory . . . 28
2.4 Density Functional Theory . . . 29
2.4.1 Hohenberg-Kohn Theorems . . . 30
2.4.2 The Kohn-Sham Equations . . . 30
2.4.3 Exchange-Correlation Functionals . . . 31
2.5 Basis Sets . . . 33
2.6 Relativistic Effects . . . 35
2.7 The Quantum Theory of Atoms in Molecules (QTAIM) . . . 36
2.7.1 The Topology of the Electron Density . . . 36
2.7.2 Characterising the Chemical Bond Using QTAIM . . . 37
2.8 Dispersion Force and Non-Bonding Interactions in DFT . . . 38
2.8.1 The Performance of Standard DFT . . . 39
2.8.2 DFT-D Dispersion Correction . . . 40
2.8.3 The Minnesota M06-class of XC Density Functionals . . . 41
2.9 Inclusion of Solvents in DFT - Polarisable Continuum Model . . . 43
2.10 Codes . . . 43
2.10.1 Gaussian09 . . . 44
2.10.2 Amsterdam Density Functional . . . 44
2.10.3 AIMAll . . . 46
2.11 Modelling Chemical Reactions with DFT . . . 46
2.11.1 Geometry Optimisation . . . 47

2.11.2 Vibrational Frequencies 48
2.11.3 Locating Stationary Points Along a Reaction Path 49

3 Post-Metallocene Catalysed Propylene Homo-polymerisation - A Benchmarking Study 53
3.1 Introduction 53
3.1.1 Ziegler-Natta Catalysis 53
3.1.2 *Ansa*-metallocenes and Constrained Geometry Catalysts 55
3.1.3 Post-metallocenes 55
3.1.4 Mechanisms for Monomer Coordination and Insertion 57
3.1.5 Mechanisms for Chain Termination 58
3.1.6 Stereo- and Regiochemistry of α-Olefin Polymerisation 59
3.1.7 Theoretical Studies of Propylene Homo-polymerisation 61
3.2 Computational Details 63
3.3 Results and Discussion 64
3.3.1 The Effect of Changing the XC Functional 64
3.3.2 Testing Different DFT Methods 66
3.3.3 Temperature Corrections 72
3.3.4 *Ab initio* Benchmarking 74
3.3.5 Basis Set Benchmarking 76
3.3.6 Dissociation of BHTTi products to BHE products 78
3.4 Summary 80

4 Ion-Pair Calculations of Ethylene and Propylene Homopolymerisation 83
4.1 Introduction 83
4.1.1 The Role of Ion-Pairs in Homogeneous Olefin Polymerisation . . . 83
4.1.2 Olefin Complexation 87
4.1.3 Agostic Interactions in Olefin Polymerisation 88
4.1.4 Ethylene Homopolymerisation 90
4.1.5 Propylene Homopolymerisation 92
4.2 Computational Details 95
4.3 Results and Discussion 96
4.3.1 The Ion-Pair 96
4.3.2 Ethylene Homopolymerisation 100
4.3.3 Propylene Homopolymerisation 110
4.4 Concluding Remarks 124

5 Structure and Reactivity of Rare Earth Metal Boryl and Gallyl Compounds 125
5.1 Introduction 125
5.1.1 Rare Earth Metals 125
5.1.2 Group 13 127
5.1.3 Rare Earth Metal Boron and Gallium Bonded Compounds 130
5.1.4 Metal-Boryl Reactivity 131
5.1.5 Metal-Gallyl Reactivity 134
5.2 Computational Details 135
5.3 Results and Discussion 137

5.3.1 Rare-Earth Metal Boryl and Gallyl Compounds 137
5.3.2 Five- *vs.* Six-Coordinate Rare Earth Metal Boryl and Gallyl Compounds 141
5.3.3 The Electronic Structure of Ln–E in Five- and Six-Coordinate Rare Earth Metal Boryl and Gallyl Compounds 143
5.3.4 Relationship Between Ln–E Ionicity and the Structure of the E Heterocycles 149
5.3.5 Carbodiimide Insertion into the Ln–E Bond 152
5.3.6 Carbodiimide Insertion into the Magnesium Gallyl Bond - A Mechanistic Study 155
5.4 Conclusions 162

Appendices **164**

List of Figures

2.1 Potential energy curves for the interaction between two Kr atoms, and two benzene molecules. . . . 40
2.2 Performance of traditional XC functionals and the M06 suite at reproducing the binding curve of benzene and methane calculated with post-Hartree-Fock methods. . . . 42
2.3 A multi-dimensional potential energy surface showing the different types of stationary points. . . . 47
2.4 A linear transit of the C–C–C–C dihedral angle of n-butane. . . . 51

3.1 A schematic of the $TiCl_3$ coordination site for heterogenous Ziegler-Natta catalysis. . . . 54
3.2 Metallocene and post-metallocene catalysts capable of olefin polymerisation. 54
3.3 Tacticity variation found in polypropylene. . . . 55
3.4 Frontier orbitals of cyclopentadienide and imido NR^{2-} ligands. . . . 56
3.5 Keltan ACE^{TM} class of catalyst, containing CpR_5 and amidinate supporting ligands. . . . 56
3.6 An illustration of the different ways in which a propylene monomer may coordinate to the metal centre. . . . 60
3.7 Left: schematic showing the structure of the $[MeTiCp^*\{CN(Ph)N(iPr)_2\}]^+$ active catalyst. Right: ball and stick diagram of the active catalyst showing the sides of monomer approach. Ti, C, N, and H atoms are represented by yellow, grey, blue, and white balls, respectively. . . . 64
3.8 Relative Gibbs free energy profiles ($kJmol^{-1}$) for the insertion of propylene into the Ti-Me bond calculated with PBE and M06-2X in the gas-phase. . 65
3.9 Structures of the stationary points along the reaction pathways of CP, BHTTi and BHTM. . . . 67
3.10 Gibbs free energy profiles for the 1,2 insertion of propylene into the Ti-iBu bond from the iPr side (CP), β-hydride transfer to Ti (BHTTi), and β-hydride transfer to monomer (BHTM) calculated with different DFT methods in the gas-phase and at 298 K. . . . 69
3.11 A comparison of the Gibbs free energy profiles for CP, BHTTi and BHTM calculated in the gas-phase, with a PCM SP after gas-phase optimisation, and optimisation with a PCM, for both PBE and M06-2X XC functionals. . 71
3.12 Gibbs free energy profiles for CP, BHTTi and BHTM calculated with M06-2X in the gas-phase followed by a PCM SP at 298, 363, 373 and 393 K (25, 90, 100 and 120°C, respectively). . . . 73

3.13 Ball and stick diagram showing the real isobutyl catalyst and stripped down model. . . . 74
3.14 Electronic barrier heights for CP, BHTTi and BHTM reactions, calculated with DFT, HF, MP2 and CCSD(T) levels of theory. . . . 75
3.15 Ball and stick diagrams showing the ancillary H atoms in orange of the model and real isobutyl active catalyst. . . . 76
3.16 Gibbs free energy profile (298 K) showing the BHE reaction pathway ending in dissociation of the BHTTi products. . . . 78

4.1 Catalytic ion-pairs used in olefin polymerisation. . . . 85
4.2 Ion-pair geometries of $[Me_2Si(Cp)_2ZrMe]^+[BF_{20}]^-$. . . . 86
4.3 The cationic components of the ion-pairs studied by Laine *et al.*. . . . 87
4.4 Dewar-Chatt-Duncanson model of bonding in metal-olefin complexes. . . . 87
4.5 Representation of the front and back olefin monomer approaches, and the corresponding anion displacement transition state. . . . 89
4.6 Gibbs free energy profiles for the polymerisation of ethylene by $[Cp_2ZrEt]^+$ in the presence of $[MeBF_{15}]^-$ (c), $[BF_{20}]^-$ (b) and no anion (a). . . . 91
4.7 The orienatation of the ethylene monomer in their "normal" and "perpendicular" coordinations. . . . 92
4.8 Stereo- and regiochemistry of the growing polypropylene chain after two chain propagation steps *via* different insertion mechanisms. . . . 93
4.9 Transition states for insertion of propylene *via* the *back* and *front* directions of monomer approach, as reported by Sandhya *et al.* for the the $[SiH_2(Ind)_2ZrMe]^+$-$[MeBF_{15}]^-$ system . . . 94
4.10 Ball and stick model of the cationic active catalyst $[Cp^*\{NC(Ph)N(iPr)_2\}TiMe]^+$. . . . 96
4.11 Electrostatic potential (ESP) surfaces of $[BF_{20}]^-$ and $[Cp^*\{CN(Ph)N(iPr)_2\}TiMe]^+$ shown at an isovalue of 0.004 atomic units. . . . 97
4.12 The structures of inner- and outer-sphere ion-pairs $[Cp^*\{CN(Ph)N(iPr)_2\}TiMe]^+[BF_{20}]^-$. The cation is rendered as a ball-and-stick model, whereas the anion is displayed as a wire-frame. H atoms are omitted for clarity. . . . 98
4.13 Gibbs free energy profiles (298 K) for two chain propagation steps of ethylene homopolymerisation calculated with (**a**) and without (**b**) the $[BF_{20}]^-$ anion. 100
4.14 The ion-pair structures of the first ethylene π-adducts from the *front* and *back* directions of monomer approach. . . . 104
4.15 Geometries of n-propyl ion-pairs. . . . 106
4.16 Four orientations of "perpendicular" propylene coordination to the Ti-methyl centre, and the rotations yielding "normal" π-complexes required for insertion reaction to take place. . . . 111
4.17 Relative Gibbs free energies of coordination of propylene in "perpendicular" and "normal" orientations. . . . 112
4.18 Structures of the perpendicular adducts from the *front* and *back* directions of monomer approach. . . . 115

4.19 Gibbs free energy profiles (298 K) for two chain propagation steps of ion-pair propylene homopolymerisation from the *front* and *back* directions of monomer approach. 116
4.20 Representations of the second propylene insertion products *via* the 1,2 *re/si* mechanisms. 119
4.21 Gibbs free energy profiles (298 K) for two chain propagation steps of propylene homopolymerisation calculated with without the $[BF_{20}]^-$ anion. . 120
4.22 Gibbs free energy profiles for CP, BHTTi and BHTM calculated at 298, 363, 373 and 393 K (25, 90, 100 and 120°C, respectively). 121

5.1 Radial distribution functions of the 4*f*, 5*d*, 6*s*, and 6*p* orbitals of Sm^{3+}. . . 126
5.2 Ln^{3+} ionic radii of the lanthanides in pm. 127
5.3 Canonical structures of $[E(NRCH)_2]^-$. E denotes a group 13 atom. 128
5.4 Lone pair on sp^2-hybridised boryl ligand. 128
5.5 HOMO of phenyl anion, boryl anion, and boryllithium reported by Yamashita *et al.* 129
5.6 HOMO-1 and HOMO of $[(NHC)Ag\{Ga(NPhCH)_2\}]$ (NHC = :C(NPhCH)$_2$). 129
5.7 **a**) Nd–Ga NBO. **b**) La–Ga bonding orbitals. **c**) HOMO-2 Y–Ga bonding orbital 130
5.8 **a**) X-ray crystal structure of $Sc\{B(NArCH)_2\}(CH_2SiMe_3)_2(THF)$. **b**) X-ray crystal structure of $Lu\{B(NArCH)_2\}(CH_2SiMe_3)_2(THF)_2$. **c**) HOMO of $Y\{B(NArCH)_2\}(CH_2SiMe_3)_2(THF)_2$ showing Y–B interaction. 132
5.9 **a**) Scandium boryl oxycarbene. **b**) iPrNCNiPr inserted across Sc–B bond. . 133
5.10 The experimentally isolable **LnGa** and **LnB** ($Ln\{E(NArCH)_2\}\{Me_3SiCH_2C(NCy)_2\}_2(THF)_n$ (Ln = Sc, Y, Lu; E = B, Ga; n = 0, 1)). 137
5.11 Relaxed potential energy scans of the Ln–E bonds of $Sc(MeC(NMe)_2)_2\{Ga(NArCH)_2\}THF$ and $Ln(MeC(NMe)_2)_2\{B(NArCH)_2\}$. 140
5.12 The structure of five-coordinate $Ln(MeC(NMe)_2)_2\{B(NArCH)_2\}$ (**ScB**). . 140
5.13 Breakdown of the contributions of the total interaction energies between the $[Ln]^+$ and $[boryl/gallyl]^-$ fragments of the six-coordinate $\mathbf{LnB_{THF}}$ and **LnGa** (top), and of the five-coordinate **LnB** and $\mathbf{LnGa_{-THF}}$ systems. 144
5.14 A breakdown of the contributions of the total interaction energies between the neutral [Ln]· and [boryl/gallyl]· fragments of the six-coordinate $\mathbf{LnB_{THF}}$ and **LnGa**, and of the five-coordinate **LnB** systems. 145
5.15 Kohn-Sham HOMO and HOLO of **ScGa**. 148
5.16 The structure of $Ge\{Ga(NArCH)_2\}Me_3$ (**GeGa**). 149
5.17 N-Ga-N bond angle *vs.* Ga–N bond distance for compounds containing $M–Ga(NArCH)_2$ bonds. 150
5.18 Representation of four gallyl-based LOs of **ScGa**. 151
5.19 Carbodiimide insertion into the Ln–E bond. 152
5.20 Insertion of a carbodiimide into the Mg-Ga bond of $Mg(^{Dipp}NacNac)\{Ga(NArCH)_2\}$ (**MgGa**). 155
5.21 Carbodiimide adduct of **MgGa**. 156

5.22 Relative Gibbs free energy profile, calculated without dispersion corrections, for the insertion of MeNCNMe into the Mg–Ga bond of Mg(^{H}NacNac){Ga(NHCH)$_2$}. 156
5.23 Relative Gibbs free energy profiles, calculated without dispersion corrections, for the insertion of R"NCNR" into the Mg–Ga bond of Mg($^{R'}$NacNac){Ga(NR"'CH)$_2$}. The apostrophes around the TS labels indicate that they were located after building up the analogous TS with smaller R groups. 157
5.24 Relative Gibbs free energy profiles, optimised with Grimme D3 dispersion corrections, for the insertion of iPrNCNiPr into the Mg–Ga bond of Mg(^{iPr}NacNac){Ga(NiPrCH)$_2$}. 158
5.25 Relative Gibbs free energy profile, optimised with Grimme D3 dispersion corrections, for the insertion of TolPrNCNTol into the Mg–Ga bond of Mg(^{Dipp}NacNac){Ga(NDippCH)$_2$}. Structures corresponding to the stationary points are shown in Figure 5.26. 159
5.26 Structures of the stationary points along the reaction profile of insertion of TolPrNCNTol into the Mg–Ga bond of Mg(^{Dipp}NacNac){Ga(NDippCH)$_2$} shown in Figure 5.25. 161

List of Tables

3.1 $\Delta G^{\ddagger}$ (kJmol^{-1}) for the insertion of a propylene monomer into the growing methyl chain calculated using PBE and M06-2X in the gas-phase. Barriers are calculated relative to the monomer adduct preceding each TS. 66

3.2 The different DFT methods tested. Methods in rows 2-10 used the optimised structures from row 1 (PBE, no DFT-D3 correction, gas-phase) as input coordinates. 68

3.3 $\Delta G^{\ddagger}$ (kJmol^{-1}) for CP, BHTTi and BHTM reactions calculated with different DFT methods at 298 K. 70

3.4 $\Delta G^{\ddagger}$ for CP, BHTTi and BHTM calculated with M06-2X in the gas-phase followed by a PCM SP at 298, 363, 373 and 393 K (25, 90, 100 and 120°C, respectively). 73

3.5 $\Delta G^{\ddagger}$ for CP, BHTTi and BHTM calculated using SP of different basis sets and a PCM of 2,2,4-trimethylpentane in conjunction with thermodynamic corrections at 298, 363 and 393 K, from gas-phase optimisations. 77

3.6 $\Delta G^{\ddagger}$ (kJmol^{-1}) for CP, BHTTi, and the Gibbs energy of the dissociated BHE products relative to the isobutyl catalyst starting structure. 79

4.1 Relative Gibbs free energies (kJmol^{-1}) of the stationary points along the first two chain propagation steps of ethylene homopolymerisation calculated with and without an anion. 101

4.2 Key geometric parameters (in Å and °) of the stationary points along the ion-pair Gibbs free energy surfaces of ethylene homopolymerisation *via* the *front* and *back* directions of monomer approach. 103

4.3 Key geometric parameters (in Å and deg) of the stationary points along the naked cationic Gibbs free energy surfaces of ethylene homopolymerisation. Labels refer to those shown in Figure 4.13. 105

4.4 Gibbs free energy internal barriers (in kJmol^{-1}) for ethylene insertion from the monomer π-adducts. 105

4.5 Geometric data (in Å) for the perpendicular and "normal" propylene adducts from both *front* and *back* directions of monomer approach. 113

4.6 Relative Gibbs free energies (kJmol^{-1}) of the stationary points along the first two chain propagation steps of ion-pair propylene homopolymerisation calculated for the *front* and *back* directions of monomer approach.(a) and (s) refer to the propylene methyl anti and syn to the growing polymer chain, respectively. 117

4.7 Relative Gibbs free energies (kJmol^{-1}) of the stationary points along the first two chain propagation steps of propylene homopolymerisation calculated without the $[BF_{20}]^-$ anion. 120
4.8 Relative Gibbs free energies (kJmol^{-1}) of the ion-pair transition states (G_{TS}(rel.)) and differences between the relative energies of the CT TSs, and those of the CP TS ($\Delta G_{rel.}$) calculated at 298, 363, 373 and 393 K (25, 90, 100 and 120°C, respectively). All values are in kJmol^{-1}. 122

5.1 3+ ionic radii (pm) of Ln elements. 127
5.2 Key geometric parameters of the compounds **LnB** and **LnGa**. 138
5.3 Key computed geometric parameters of the compounds **LnGa**. 138
5.4 Thermodynamic data for the addition of THF to **LnB** and **LnGa$_{\text{-THF}}$**. . . . 141
5.5 Key geometric parameters for the hypothetical six-coordinate boryls (**LnB$_{\text{THF}}$**). Bond distances and angles in Å and °, respectively. 142
5.6 Key geometric parameters for the hypothetical five-coordinate gallyls (**LnGa$_{\text{-THF}}$**). Bond distances and angles in Å and °, respectively. 143
5.7 Data relating to the electronic structure of the Ln–E bonds of six-coordinate **LnGa** and **LnB$_{\text{THF}}$**. 147
5.8 Data relating to the electronic structure of the Ln–E bonds of five-coordinate **LnGa$_{\text{-THF}}$** and **LnB**. 148
5.9 Selected geometric and electronic structural parameters of the five- and six-coordinate gallyls, **LnGa$_{\text{-THF}}$** and **LnGa**, respectively. 150
5.10 Selected geometric and electronic structural parameters of the five- and six-coordinate gallyls, **LnB** and **LnB$_{\text{THF}}$**, respectively. 152
5.11 Homolytic bond dissociation energies (in kJmol^{-1}) of the Ln–E bonds of **LnB** and **LnGa**. 153
5.12 The thermodynamics of insertion of iPrNCNiPr into the Ln–E bonds of **LnGa**, **LnB** and **LnB$_{\text{THF}}$**. 154

Chapter 1

Introduction

Advances in modern computing have allowed the field of computational chemistry to make a significant impact in academic research. Not only does it enable us to confirm experimental results, but it can be used as a powerful tool to probe experimentally challenging situations, and in deepening our chemical understanding. One area in which the synergy between computation and experiment has proven invaluable is that of organo-transition metal chemistry, which is concerned with the transition metal–carbon bond, and all the various forms in which it exists. These types of bonds come under the broader umbrella of organometallic bonds, which may be considered to be those which contain a metal atom that has a Pauling electronegativity that is lower or comparable than that of carbon (2.5). The rich chemistry of the transition metals is centred around the involvement of partially filled *d*-orbitals in the bonds to ligands, as well as the coordination number and total number of valence electrons at the metal centre. Ligands are not limited to those in which a carbon atoms is bound to the metal centre, indeed those containing a heteroatom (usually O or N) are commonplace in the coordination chemistry of transition metals. This thesis explores the bonding, structure and reactivity of two very different organometallic systems, and as such a more detailed introduction to their background chemistry is given in their respective results chapters.

1.1 Research Projects

The following sections briefly introduce the research projects presented in this thesis. The studies carried out for Chapters 3 and 4 were sponsored by ARLANXEO Netherlands B.V.,

and all three research projects were second-supervised by Professor Philip Mountford at the Department of Chemistry, University of Oxford. The research contained in Chapter 5 was carried out in collaboration with Drs Liban Saleh and Matthew Blake, previously of the Mountford group.

1.1.1 Post-Metallocene Catalysed Propylene Homo-polymerisation - A Benchmarking Study

The active species in transition metal-catalysed olefin polymerization and the mechanisms by which they assist such reactions have been the topic of a vast area of research for both experimentalists and theoreticians for many decades. In particular, early transition metals have been extensively studied and a plethora of evidence has established the cationic group 4 component of certain catalytically active species. However, their interaction with the counter-anion co-catalyst during the polymerisation process has yet to be fully understood.

Initial work studied the anion-free post-metallocene catalytic system, $[\mathrm{MeTiCp^*\{CN(Ph)N(iPr)_2\}}]^+$, and focused on testing different approaches of DFT that allow dispersion and solvent effects to be included in the model. The resulting changes in reaction profiles of chain propagation and termination mechanisms were examined, with the aim of determining the most suitable computational method. *Ab initio* calculations on stripped-down model analogues of our systems, as well as a basis set benchmarking study, are also presented.

1.1.2 Ion-Pair Calculations of Ethylene and Propylene Homopolymerisation

The work described above was extended to include the tetrakis(pentafluorophenyl)borate ($[\mathrm{BF_{20}}]^-$) counter-anion. Such ion-pair studies have not yet been reported for a post-metallocene catalyst. The position of the anion in relation to the cationic active site was predicted using electrostatic potential surfaces in order to determine regions of electro- and nucleophilicity of the cationic and anionic counterparts, respectively. The resultant inner-sphere ion-pair was used as the starting point for ethylene and propylene

homopolymerisation reactions.

Structures from ethylene homopolymerisation studies were used as a basis upon which to build those for an analogous study of propylene, owing to the absence of regio- and stereo-chemistry of the insertion reactions. The orientation of the incoming monomers and their adducts were examined and, in the case of propylene, the relative energies of such adducts were used as a predictive measure for stereo-selectivity of the catalytic ion-pair. The reaction profiles for two monomer enchainment steps are presented, and compared to those calculated for the naked-cationic model.

1.1.3 Structure and Reactivity of Rare Earth Metal Boryl and Gallyl Compounds

The exploitation of unique properties of rare earth (RE) metals, alternatively classed as lanthanides, has allowed huge technological advances to be made in recent decades. Technologies include electrical vehicles, medical imaging, and wind turbines, to name but a few. Heavy use has led the US Department of Energy to develop a "Critical Materials Strategy" to safeguard the supply of RE metals, and we must therefore further our understanding of the physical and chemical properties of rare earth metal compounds in order to maximise the efficiency of their use. The chemistry of the RE metals has been dominated by ligands based on nitrogen and oxygen donors, whereas research presented in this thesis demonstrates the extension beyond this to boryl and gallyl ligands.

The Mountford group synthesised the lanthanide (Ln) boryl and gallyl compounds, Ln{E(NArCH)$_2$}{Me$_3$SiCH$_2$C(NCy)$_2$}$_2$(THF)$_n$ (Ln = Sc, Y, Lu; E = B, Ga; n = 0, 1), which are computationally assessed in this thesis. Differences in the coordination number of the boryl and gally compounds were examined, and a detailed analysis of the character of the Ln–E bonds is presented. Furthermore, the reactivity of the bonds to insertion of a carbodiimide is discussed, along with a mechanistic study of such an insertion into the related Mg–gallyl system, Mg{$^{\text{Dipp}}$NacNac}Ga(NDippCH)$_2$}.

Chapter 2

Theoretical Background

The calculation of many molecular properties of interest to the computational chemist relies on the ability to first solve the time-independent Schrödinger equation (SE),

$$\hat{H}\Psi = E\Psi \tag{2.1}$$

which describes the energy E a system that has a wavefunction Ψ. $\hat{H}$ is the Hamiltonian energy operator,

$$\hat{H} = \hat{T} + \hat{V} \tag{2.2}$$

consisting of $\hat{T}$ and $\hat{V}$ kinetic and potential operators, respectively.

Methods that solve the Schrödinger equation in such a way are loosely termed "electronic structure calculations", which include *ab initio* (from the beginning) and semi-empirical methods. *Ab initio* methods calculate the Hamiltonian integrals, which must be known to solve the Schrödinger equation, using the explicit mathematical form of the Hamiltonian, and use only atomic numbers and fundamental constants as inputs. Conversely, semi-empirical methods make approximations to the electronic Hamiltonian and utilise experimental data in the fitting of parameters. In general, *ab initio* calculations are more accurate, but more computationally expensive, than semi-empirical, and an important objective for the user is to find an acceptable balance between the accuracy and speed with which results are obtained.

2.1 The Born-Oppenheimer Approximation

The SE may be solved exactly only for hydrogenic, one-electron systems and approximations must be made for many-body, polyelectronic systems. For such complex systems the Born-Oppenheimer (BO) approximation[1] decouples the motion of electrons and nuclei, allowing them to be treated separately:

$$\Psi_{\mathrm{total}} = \Psi_{\mathrm{e}}\Psi_{\mathrm{n}} \tag{2.3}$$

This assumption is generally valid due to the fact that the nuclei, having much larger masses, move more slowly than the electrons, and therefore the electrons adjust almost instantaneously upon a change in nuclei position. Within this approximation, Ψ_{e} depends on only the nuclear positions and not on their momenta. If we consider the nuclei to be fixed in space, then the kinetic energy of the nuclei, $\hat{T}_{\mathrm{n}}$, can be neglected and only the Coulomb potential "felt" by the electrons, and the nucleus-nucleus interactions are considered. The Hamiltonian for a system of N electrons i or j, and M nuclei a or b of charge $Z_{a/b}$ is therefore given (in atomic units) by:

$$\begin{aligned}\hat{H} &= \hat{T}_{\mathrm{e}} + \hat{V}_{\mathrm{ne}} + \hat{V}_{\mathrm{ee}} + \hat{V}_{\mathrm{nn}} \\ &= -\sum_{i=1}^{N}\frac{1}{2}\nabla_i^2 - \sum_{i=1}^{N}\sum_{a=1}^{M}\frac{Z_a}{r_{ia}} + \sum_{i=1}^{N}\sum_{j>i}^{N}\frac{1}{r_{ij}} + \sum_{a=1}^{M}\sum_{b>a}\frac{Z_a Z_b}{r_{ab}}\end{aligned} \tag{2.4}$$

The first term in Equation 2.4 corresponds to the kinetic energy of the electrons, the second to the nucleus-electron attraction, and the third to the electron-electron repulsion. Often the final term describing the nucleus-nucleus repulsion is not included in $\hat{H}$, and instead is added as a classical term at the end of molecular calculations - this is owing to the fact that the nuclei positions are fixed. The Hamiltonian in Equation 2.4 then becomes the *electronic Hamiltonian*.

2.2 Hartree-Fock Self-Consistent Field Method

The Hartree-Fock (HF) Self-Consistent Field (SCF) method solves the electronic SE by assigning a trial electronic wavefunction, Ψ_{trial}, and iteratively evaluating the total energy until self-consistency is reached. This method neglects relativistic effects and utilises the variation theorem that states the Raleigh ratio ε approaches the real, or ground-state, energy of the system:

$$\varepsilon \geq E_0 \tag{2.5}$$

$$\varepsilon = \frac{\langle \Psi_{\text{trial}} | \hat{H} | \Psi_{\text{trial}} \rangle}{\langle \Psi_{\text{trial}} | \Psi_{\text{trial}} \rangle} \tag{2.6}$$

Ψ_{trial} is defined as the antisymmetrised product of the one-electron spin-orbitals ϕ, each of which is the product of a spin function (α or β) and a spatial orbital. Arranging the spin-orbitals in a Slater determinant Φ_{SD}, the form of which is shown in Equation 2.7, allows the wavefunction to obey the Pauli exclusion principle, which states that no two electrons (fermions) may occupy the same quantum state. The Slater determinant below is for an N electron system, and contains N spin-orbitals ϕ along the columns, with N electronic coordinates along the rows.

$$\Psi_{\text{trial}} = \Phi_{\text{SD}} = \frac{1}{\sqrt{N!}} \begin{vmatrix} \phi_1(\mathbf{x}_1) & \phi_2(\mathbf{x}_1) & \dots & \phi_N(\mathbf{x}_1) \\ \phi_1(\mathbf{x}_2) & \phi_2(\mathbf{x}_2) & \dots & \phi_N(\mathbf{x}_2) \\ \vdots & \vdots & \ddots & \vdots \\ \phi_1(\mathbf{x}_N) & \phi_2(\mathbf{x}_N) & \dots & \phi_N(\mathbf{x}_N) \end{vmatrix} \tag{2.7}$$

The energies of the one-electron spin-orbitals ϵ_i are found using the Hartree-Fock equations,

$$\hat{F}_i \phi_i = \epsilon_i \phi_i \qquad i = 1, ..., N \tag{2.8}$$

where $\hat{F}_i$ is the Fock operator, and replaces the electron-electron repulsion term found in the Hamiltonian of Equation 2.4 with the Coulomb $\hat{J}_j$ and exchange $\hat{K}_j$ operators.

$$\hat{F}_i = \sum_{i=1}^{N} \hat{h}_i + \sum_{j=1}^{N} (\hat{J}_j - \hat{K}_j) \tag{2.9}$$

$$\hat{h}_i = -\frac{1}{2}\nabla_i^2 - \sum_{a=1}^{M} \frac{Z_a}{r_{ia}} \tag{2.10}$$

The expectation values of the Coulomb and Exchange operators are as follows:

$$\langle \phi_i(\mathbf{x}_1)|\hat{J}_j|\phi_i(\mathbf{x}_1)\rangle = \langle \phi_i(\mathbf{x}_1)|\,\langle \phi_j(\mathbf{x}_2)|\frac{1}{r_{ij}}|\phi_j(\mathbf{x}_2)\rangle\,|\phi_i(\mathbf{x}_1)\rangle = J_{ij} \tag{2.11}$$

$$\langle \phi_i(\mathbf{x}_1)|\hat{K}_j|\phi_i(\mathbf{x}_1)\rangle = \langle \phi_i(\mathbf{x}_1)|\,\langle \phi_j(\mathbf{x}_2)|\frac{1}{r_{ij}}|\phi_i(\mathbf{x}_2)\rangle\,|\phi_j(\mathbf{x}_1)\rangle = K_{ij} \tag{2.12}$$

J_{ij} represents the repulsive Coulomb potential that electron in ϕ_i experiences due to the charge distribution of an electron in ϕ_j, and K_{ij} represents the potential associated with exchanging two electrons of like spin between ϕ_i and ϕ_j and has no classical interpretation. $\hat{J}_j$ is a local operator, whereas $\hat{K}_j$ is non-local and requires knowledge of ϕ_i throughout all space. The expressions in Equations 2.11 and 2.12 require knowledge of both electrons interacting with each other and are therefore known as two-electron operators. As they both contain ϕ the HF SCF equation must be solved iteratively.

The total Hartree-Fock energy of the system may then be calculated using Equation 2.13,

$$E_{\mathrm{HF}} = \sum_{i=1}^{N} h_i + \frac{1}{2}\sum_{i=1}^{N}\sum_{j=1}^{N}(J_{ij} - K_{ij}) + V_{\mathrm{nn}} \tag{2.13}$$

where h_i is the expectation value of the one-electron core Hamiltonian $\hat{h}_i$ (Equation 2.10). Note that the total energy is not simply a sum of the spin-orbital energies ϵ_i calculated using Equation 2.8, as this would account for each electron-electron repulsion interaction twice. While this method of solving the SE reduces the problem of solving many-electron wavefunction to solving a set of one-electron equations, each of these equations depend on the other $N-1$; in order to solve the i^{th} HF energy the $N-1$ spin-orbitals must be known. The energy is therefore reduced to a minimum by systematically varying the spin-orbitals while maintaining orthogonality to give a set of SCF orbitals.

The spin-orbitals $\phi_i(\mathbf{x})$ may be considered as spatial spin-restricted molecular orbitals (MOs) $\phi_i(\mathbf{r})$, each of which is defined as a linear combination of P atomic orbitals, or basis

functions, $\chi_\alpha(\mathbf{r})$ with variable coefficients $c_{i\alpha}$:

$$\phi_i(\mathbf{r}) = \sum_{i=1}^{P} c_{i\alpha}\chi_\alpha(\mathbf{r}) \tag{2.14}$$

The mathematical form of $\chi_\alpha(\mathbf{r})$ is described in Section 2.5, however it is the values of coefficients $c_{i\alpha}$ that are varied during the SCF method to find the best solution to the HF equations. The lowest energy solution to the SE within HF theory is found for an infinite set of basis functions, i.e. $P \longrightarrow \infty$, and is termed the HF limit. This, however, is not computationally possible, and as such an exact description of the system cannot be computed.

There are two main problems with the HF SCF method, the first being that it does not consider relativistic effects. These are particularly important for the inner core electrons of heavy atoms, and will be briefly discussed in Section 2.6. The second limitation is that HF theory accounts for the electron-electron repulsion in only an average fashion: each electron experiences the effects of the $N-1$ electrons as a distribution rather than as an instantaneous interaction. This is not physically reasonable as electron motion is correlated.

Electron correlation energy, E_{corr}, within the domain of HF theory is the difference in energy between the true energy of the system, E_0, and E_{HF} at the HF limit. As HF theory does not account for electron correlation, the electrostatic repulsion energy is an overestimation and $E_{\text{HF}} > E_0$. Although E_{corr} is only a small contribution to the total energy, failure to account for it can result in large errors, for example when predicting bond breaking and formation. E_{corr} can be broken down into two parts: dynamic, and static electron correlation energies. The static contribution corresponds to the correlation of electrons occupying different spatial orbitals and is a long-range effect, whereas dynamic correlation is a consequence of electrons within the same spatial orbital avoiding each other.

2.3 Post-Hartree-Fock Methods

Methods that build upon HF theory and address how electron correlation may be included in *ab initio* calculations are termed Post-Hartree-Fock methods. Approaches to incorporate correlation mostly fall into two categories, the first of which is by approximating the

wavefunction as a combination of Slater determinants, such as the Configuration Interaction (CI) and Coupled Cluster (CC) methods. The second technique considers the correlation energy as a perturbation to the HF wavefunction, namely Møller Plesset perturbation theory. Results from these types of calculations are reported only briefly in Chapter 3, therefore the methods are not discussed in mathematical detail. In order to correct for static correlation multi-configuration SCF (MCSCF) methods may be used, which optimise virtual orbitals in addition to those which are occupied. However, this technique is not studied in the present work and will not be discussed further.

2.3.1 Configuration Interaction

The Configuration Interaction (CI) method introduces more Slater determinants to the expression of the total wavefunction, incorporating excited electronic configurations *via* a linear combination:

$$\Psi_{\mathrm{CI}} = a_0\Phi_{\mathrm{HF}} + \sum_{\mathrm{S}} a_{\mathrm{S}}\Phi_{\mathrm{S}} + \sum_{\mathrm{D}} a_{\mathrm{D}}\Phi_{\mathrm{D}} + \sum_{\mathrm{T}} a_{\mathrm{T}}\Phi_{\mathrm{T}} + ... \tag{2.15}$$

where the ground state and singly, double, triply excited determinants are given by Φ_{HF}, Φ_{S}, Φ_{D}, andΦ_{T}, respectively. The computed energy is the exact solution to the non-relativistic time-independent SE for a given set of basis functions if all possible configurations are included, known as full CI. This is possible only for small systems as the calculation is highly computationally expensive. CISD simplifies the method by just considering the singles and doubles terms, as the largest contributions to the overall CI wavefunction are from the double excitation terms. Truncating the CI wavefunction in this way results in this method not being *size extensive*, as the sum of two fragment energies at large separation will not equal the sum of the fragment energies calculated separately. Such truncated CI methods recover less electron correlation as system size increases for this reason. Quadratic CISD (QCISD) is an example of methods which include higher order terms to increase its size extensivity.

2.3.2 Coupled Cluster

Coupled Cluster (CC) theory is based on the assumption that a full CI may be calculated for a given system,[2] i.e. it also defines the wavefunction as an expansion of excited determinants, given by:

$$\Psi_{\mathrm{CC}} = e^{\hat{T}}\Psi_{\mathrm{HF}} \tag{2.16}$$

where $\hat{T}$ is the cluster operator and $e^{\hat{T}}$ are expanded as a Taylor series of $\hat{T}_i$ which generates a series of i^{th} excited determinants, with reference wavefunction Ψ_{HF}. If the series is truncated after two terms the method is referred to as CCSD, Coupled Cluster Singles and Doubles. Energies resulting from calculations using other methods are often compared to the "gold standard" CCSDT energy which includes electron correlation contributions from triple excitations. The latter is extremely computationally expensive, therefore CCSD(T) may be preferable, where the (T) refers to the triple excitations being considered as a Møller-Plesset perturbation (see Section 2.3.3). The CC method is not variational, however, and therefore can result in a total energy that is artificially low. While this method is size extensive is it is generally only feasible for small systems.

2.3.3 Møller-Plesset Perturbation Theory

By assuming that the perturbation to the HF wavefunction due to electron correlation effects is small, many-body perturbation theory may be employed to account for electron correlation. The correlation corrected Hamiltonian is given by the sum of the known reference Hamiltonian $\hat{H}_0$ and a small perturbation Hamiltonian $\hat{H}'$ with coefficient λ:

$$\hat{H} = \hat{H}_0 + \lambda\hat{H}' \tag{2.17}$$

Møller-Plesset perturbation theory defines the HF system as the unperturbed reference system, and $\hat{H}_0$ is therefore the sum of the Fock operators. As electron-electron repulsion is double counted in this manner, the perturbation Hamiltonian is thus the exact repulsion

minus twice the average repulsion:

$$\hat{H}' = \hat{H} - \hat{H}_0 = \hat{V}_{\mathrm{ee}} - 2\langle\hat{V}_{\mathrm{ee}}\rangle \tag{2.18}$$

The perturbed wavefunction may be written as a Taylor series in power of λ,

$$\Psi = \Psi_0 + \lambda^1\Psi_1 + \lambda^2\Psi_2 + ... \tag{2.19}$$

Electron correlation arises only from the second order term, as the first order correction term plus the zeroth energy recovers the HF energy. The inclusion of higher terms up to the n^{th} order is denoted by MPn, however improvement in terms of correlation energies are found to be significant in steps of $2n + 2$. MP2 is a relatively cheap method which can account for electron correlation, being advantageous over truncated CI methods in that it is size extensive. It is limited, however, to systems where electron correlation is not expected to be a large contribution to the overall energy.

2.4 Density Functional Theory

An alternative approach to methods based on HF theory is density functional theory (DFT); the method employed in the present work. DFT differs from the aforementioned *ab initio* and semi-empirical methods in that it does not calculate the electronic wavefunction of a molecular system, but instead derives the electron probability density, ρ. The underpinning principle of the theory is that of the Thomas-Fermi method, in which the electronic energy of a molecular system is treated as a functional of ρ. As discussed below, for a given function $\rho(\mathbf{r})$, there is only one solution to the total electronic energy, depending on only three variables - the coordinates of the electron density. This is a major advantage of DFT over the wavefunction approaches as, for a system of N electrons, these depend on $3N$ variables, whereas the *ab initio* methods described above can scale up to n^8 or higher, where n in the number of basis functions.

2.4.1 Hohenberg-Kohn Theorems

Application of the Thomas-Fermi method is subject to the conditions described by two theorems of Hohenberg and Kohn, the first of which is their existence theorem: *The ground state energy, and all other ground state electronic properties, are uniquely determined by the electron density.*[3] We can therefore write,

$$E[\rho] = T[\rho] + V_{\mathrm{ee}}[\rho] + V_{\mathrm{ne}}[\rho] \tag{2.20}$$

where E, T, V_{ee}, and V_{ne} are the total, kinetic, electron-electron repulsion, and electron-nucleus attraction energies, respectively.

Formal proof of the validity of the Thomas-Fermi model was not given until 1964[3] when an analogous theorem to the variation principle for wavefunctions was proposed. The Hohenberg-Kohn variational theorem states: *For a trial charge density* $\rho_{\mathrm{trial}}, E_0 \leq E[\rho_{\mathrm{trial}}]$. The significance of this theorem is that it established that the energy of a system, as a functional of the electron density, is a minimum for the ground state density. The objective of a DFT calculation is therefore to minimise the energy for a given functional.

2.4.2 The Kohn-Sham Equations

The theorems of Hohenberg and Kohn prove only that the density functional exists, but do not give us information about the form of the functional dependence. The contribution from Kohn and Sham[4] allowed the exact ground state energy of an N electron system to be written in terms of one-electron spatial orbitals, $\phi_i (i = 1, 2, ..., N)$, referred to as Kohn-Sham orbitals:

$$E[\rho] = -\frac{1}{2}\sum_{i=1}^{n}\int \phi_i^*(\mathbf{r}_1)\nabla_1^2\phi_i(\mathbf{r}_1)d\mathbf{r}_1 - \sum_{a=1}^{M}\frac{Z_a}{r_{a1}}\rho(\mathbf{r}_1)d\mathbf{r}_1 + \frac{1}{2}\int\frac{\rho(\mathbf{r}_1)\rho(\mathbf{r}_2)}{r_{12}}d\mathbf{r}_1 d\mathbf{r}_2 + E_{\mathrm{XC}}[\rho] \tag{2.21}$$

The terms on the right-hand side correspond to the kinetic energy of the electrons; the electron-nucleus attraction summing over all M nuclei of index a and atomic number Z_a; the Coulomb interaction between the total electron distribution, summed over all Kohn-Sham orbitals, at $\mathbf{r}_1$ and $\mathbf{r}_2$; and the exchange-correlation energy of the system. This last term,

E_{XC}, cannot be obtained exactly, and approximations to its form must therefore be made. We do know, however, that it must be a functional of the electron density. The ground state electron density of a system for which we know ϕ_i is given by

$$\rho(\mathbf{r}) = \sum_{i=1}^{N} |\phi_i(\mathbf{r})|^2 \tag{2.22}$$

In order to solve Equation 2.22 we must be able to determine the Kohn-Sham orbitals. This is achieved by solving the Kohn-Sham equation, given below.

$$\left\{ -\frac{1}{2}\nabla_1^2 - \sum_{I=a}^{M} \frac{Z_a}{r_{a1}} + \int \frac{\rho(\mathbf{r}_2)}{r_{12}} d\mathbf{r}_2 + V_{\mathrm{XC}}(\mathbf{r}_1) \right\} \phi_i(\mathbf{r}_1) = \varepsilon_i \phi_i(\mathbf{r}_1) \tag{2.23}$$

The Kohn-Sham orbital energies are denoted ε_i, and V_{XC} is the exchange-correlation potential, the functional derivative of E_{XC}:

$$V_{\mathrm{XC}}[\rho] = \frac{\delta E_{\mathrm{XC}}}{\delta \rho} \tag{2.24}$$

Therefore, if we can obtain an expression for E_{XC} we can solve for the Kohn-Sham orbitals and thus find the ground state charge density from Equation 2.22. The Kohn-Sham equation is then solved self-consistently: we make an initial guess of ρ, often by using a superposition of atomic densities; compute the exchange-correlation energy by using some approximate form of the functional, and thus compute V_{XC}; solve Equation 2.23 for an initial set of Kohn-Sham orbitals; and find an improved density from Equation 2.22. This process is repeated until the density and exchange-correlation energy converge to within a pre-defined tolerance. The total energy of the system can then be computed from Equation 2.21.

2.4.3 Exchange-Correlation Functionals

Provided we are able to construct the accurate form of the exchange-correlation (XC) functional, we can obtain the exact charge distribution, and therefore exact energy, of a system. The functional can be separated into an exchange (X) functional and a correlation (C) functional, representing the exchange and correlation energies, respectively. These functionals are known exactly only for a homogeneous electron gas, however. Thus the

search for accurate approximations of the exchange-correlation functional is an extremely active field of research.

The simplest approximation, and most fundamental, is the local-density approximation (LDA),

$$E_{\mathrm{XC}}^{\mathrm{LDA}} = \int \rho(\mathbf{r})\varepsilon_{\mathrm{XC}}^{\mathrm{hom}}[\rho(\mathbf{r})]d\mathbf{r} \tag{2.25}$$

where $\varepsilon_{\mathrm{XC}}^{\mathrm{hom}}$ is the exchange-correlation energy per electron in a homogeneous electron gas.[4] Here the exchange-correlation energy depends on the density *only* at the point at which the functional is evaluated. LDA functionals assume a density corresponding to that of a uniform electron gas, i.e. a constant density. This is clearly an approximation as, in molecules, neither the electronic nor positive charge is homogeneous. In order to account for the inhomogeneity in the density, corrections that include the gradient of $\rho(\mathbf{r})$ by way of an enhancement factor, F_{XC} are incorporated to give the generalised gradient approximation (GGA)

$$E_{\mathrm{XC}}^{\mathrm{GGA}} = \int \rho(\mathbf{r})\varepsilon_{\mathrm{XC}}^{\mathrm{hom}}[\rho(\mathbf{r})]F_{\mathrm{XC}}[\rho(\mathbf{r})\nabla\rho(\mathbf{r})]d\mathbf{r} \tag{2.26}$$

A natural progression from the GGA is to have an XC functional which takes the Laplacian of the density, $\nabla^2\rho(\mathbf{r})$, or depends on the orbital kinetic energy density τ to produce a meta-GGA functional.

$$\tau(\mathbf{r}) = \frac{1}{2}\sum_{i=1}^{occ.} |\nabla\phi_i(\mathbf{r})|^2 \tag{2.27}$$

Hybrid, or hyper, -GGA functionals are semi-empirical and mix in a fixed fraction of exact Hartree-Fock (HF) exchange energy with the GGA functional,

$$E_{\mathrm{XC}}^{\mathrm{hybrid}} = \alpha E_{\mathrm{X}}^{\mathrm{HF}} - (1-\alpha)E_{\mathrm{X}}^{\mathrm{GGA}} + E_{\mathrm{XC}}^{\mathrm{GGA}} \tag{2.28}$$

These functionals generally give very good agreement with experiment for a range of molecular properties, though the amount of exact HF exchange energy is often determined by fitting to experimental data to give the desired agreement for specific properties, and as such particular hybrid-GGA functionals may give acceptable results for only some systems.

2.5 Basis Sets

Solving the Schrödinger equation requires the overall wavefunction to be known. For polyelectronic atoms, it is defined as the antisymmetrised product of the one-electron atomic orbitals (AOs). By extension, the overall wavefunction of a polyatomic molecule is the antisymmetrised product of the one-electron molecular orbitals (MOs), each of which in turn is most commonly found by taking a linear combination of AOs (LCAO). The collection of AOs used to find each MO is known as a basis set. In molecular calculations, these are typically composed of one of two forms, Slater-type orbitals (STOs)

$$\chi^{\mathrm{STO}}_{\zeta,n,l,m}(r,\theta,\phi) = NY_{l,m}(\theta,\phi)r^{n-1}e^{-\zeta r} \tag{2.29}$$

or Gaussian-type orbitals (GTOs),

$$\chi^{\mathrm{GTO}}_{\zeta,n,l,m}(r,\theta,\phi) = NY_{l,m}(\theta,\phi)r^{2n-2-l}e^{-\alpha r^2} \tag{2.30}$$

where *N* is a normalisation constant, $Y_{l,m}$ are spherical harmonic functions, *n* is the principal quantum number, ζ and α are constants relating to the decay of the orbitals from the nucleus, and *r* is the electron-nucleus distance.

STOs display a cusp at the nucleus and therefore satisfy Kato's cusp condition.[5] As STOs have an $e^{-\zeta r}$ radial dependence, Coulomb and exchange integrals involving such a dependence cannot by solved analytically and therefore must be found numerically, which is non-trivial. One solution to this problem is to use GTOs, which instead have a Gaussian radial dependence, to approximate an STO. These functions do not have a cusp at the nucleus and display a faster exponential decay at long distances. Taking linear combinations of many GTOs to give a contracted GTO (CGTO) improves the radial description of the AO however and, crucially, the Coulomb and exchange integrals are much easier to solve.

$$\chi(CGTO) = \sum_{i}^{P} c_{i\alpha}\chi_{\alpha}(GTO) \tag{2.31}$$

It should be emphasised that here only the radial part of the wavefunction is discussed, and

that the STOs and GTOs used to model AOs have an *s*, *p*, *d*, *f*, etc. angular form as well.

It is highly important in molecular structure calculations to use a basis set of appropriate and sufficient quality. In order to describe all of the filled AOs, and therefore electrons, in a neutral atom there must be a sufficient number of basis functions. The smallest number of basis functions required is called a minimal basis set, therefore for hydrogen and helium one 1*s* function is their minimal basis set. First row elements require 1*s*, 2*s* and one set of *p*-functions ($2p_x$, $2p_y$, $2p_z$), and elements in the second row need 1*s*, 2*s*, 3*s* and two sets of *p*-functions (2*p* and 3*p*). To improve upon this we double all basis functions to give a Double Zeta (DZ) basis set. Therefore a DZ basis has two *s*-functions for hydrogen and helium (1*s* and 1*s*′), four *s*-functions and two sets of *p*-functions (1*s*, 1*s*′, 2*s*, 2*s*′, 2*p* and 2*p*′) for first row elements, and six *s*-functions and four sets of *p*-functions (1*s*, 1*s*′, 2*s*, 2*s*′, 3*s*, 3*s*′, 2*p*, 2*p*′, 3*p* and 3*p*′) for the second row. The exponents of the *s*/*p*-functions do not equal those of the *s*′/*p*′-functions, resulting in two sets of functions that differ in diffusivity. This allows for a better description of the electron distribution in molecules, where the distribution of valence electrons varies in different directions.

Triple Zeta (TZ) and Quadruple Zeta (QZ) have three and four times as many basis functions as a minimal basis, respectively. Using these basis sets increases computational cost as the quality of the basis set is improved, so once again, the balance must be made between chemical accuracy and computational expense. This doubling or tripling *etc.* of core basis functions is usually not necessary for obtaining a good description of bonding, as valence orbitals are responsible for covalent interactions. Therefore split valence basis sets are often used, where only the valence basis functions are doubled for a DZ basis, termed valence double zeta (VDZ), and the core orbitals are modelled only by a single CGTO function considered to be a sufficient description of the core electrons which are not involved in chemical reactions.

Including functions of higher angular momentum, termed polarisation functions, to those in the minimal basis set also yields a better description of bonding. Adding a single set of polarisation functions, i.e. *p*- and *d*-functions of hydrogen and *p*-block elements respectively, to a DZ basis gives a Double Zeta plus Polarisation (DZP) basis set.

2.6 Relativistic Effects

Elements beyond the third row of the periodic table are considered *heavy* and are subject to significant scalar relativistic effects. The resulting modification of electronic wavefunctions and energies can be divided in two, the first being the direct orbital contraction. This applies primarily to the s and, to a slightly lesser extent, p orbitals. Such effects manifest themselves due to the inner core electrons moving with radial velocities approaching appreciable fractions of the speed of light. As a consequence, the electron mass and radial extensions are modified and the orbital itself contracts. In order to retain orthogonality with the core functions, AOs of the same orbital angular momentum but of higher principal quantum number must also contract.[6]

Concurrently, the d and f orbitals of heavy elements are affected by the second scalar relativistic effect: indirect orbital expansion. The increased shielding from the contracted s and p orbitals of similar radial extension to the d and f functions allows this expansion. The effect is most pronounced for $5d$, $6p$ and $5f$ elements, resulting in significant changes to the valence AOs.

Not to be mistaken as a direct consequence of the AO contraction, relativity has another effect of markedly shortening covalent bond lengths in comparison with those found using non-relativistic methods. A logical explanation for this could, indeed, be that in order for sufficient overlap of the contracted AOs the nuclei should be closer together, however the two observations have been shown to be unrelated. Evidence suggests that these bond length contractions emanate from a reduced kinetic repulsion between the two atoms.[6,7]

Considering the above effects, relativity must be accounted for when studying systems containing heavy elements. This can be achieved using specially modified basis sets and/or by employing a relativistic Hamiltonian. Popular examples of those that include scalar relativistic effects include the Douglas-Kroll-Hess (DKH)[8–11] and the zeroth order regular approximation (ZORA)[12–14] Hamiltonians. The basis sets associated with the ZORA equations have been employed in the present work, in conjunction with the frozen core approximation.[15] Pseudo-potentials (PPs) may also be used to account for relativity. PPs replace the Coulombic potential term of the core electrons with a modified effective core

potential, to provide a simpler calculation of the Schrödinger equation, and are used with a modified set of valence functions to account for the valence electrons. These valence functions have no radial nodes.

In addition to the scalar relativistic effects described above, spin-orbit coupling (SOC) can also modify the electronic wavefunction of heavy elements. These effects alter the symmetry properties of the spin-orbit coupled states, therefore careful consideration of SOC should be included in computational methods, especially in calculations of spectroscopic information. However, the molecules studied in this thesis are all closed-shell, i.e. they contain no unpaired electrons, and as large SOC is not expected in closed-shell systems, SOC effects are not included in our DFT calculations.

2.7 The Quantum Theory of Atoms in Molecules (QTAIM)

The Quantum Theory of Atoms in Molecules, pioneered by Richard F. W. Bader and co-workers, is built around a mathematical treatment of the topology of the molecular electron density, $\rho(\mathbf{r})$.[16] As the name suggests, the theory partitions molecules into their constituent atoms, doing so with mathematical rigour. The method has been used to study a wide range of chemical systems owing to the atomic and bonding properties that can be derived from the observable $\rho(\mathbf{r})$, and the ease with which these can be used to classify interatomic and intermolecular interactions.[17]

2.7.1 The Topology of the Electron Density

Critical points (CPs) of $\rho(\mathbf{r})$, where the first derivative of $\rho(\mathbf{r})$ vanishes, can be categorised by the eigenvalues $\lambda_{1,2,3}$ of the Hessian matrix, i.e. the curvatures, of $\rho(\mathbf{r})$ at the CP. Three negative curvatures correspond to a local maximum, most commonly a nuclear CP (NCP), where the nucleus acts a point charge attractor of the gradient vector field of the electron density, though non-nuclear attractors can also be found. Two atoms are considered to be bonded only if we find a CP between them - a bond CP (BCP), where $\rho(\mathbf{r})$ is a minimum along the axis corresponding to the path of the bond and a maximum in the other two axes.

The term 'bond path' is used to describe the line of locally maximum electron density that connects two NCPs, where ρ_{b} is the point of minimum density along that path. A BCP therefore has two negative curvatures and one positive. In addition to these two CPs, we can also find cage CPs and ring CPs corresponding to extrema with two and three positive curvatures respectively.

The BCP is found on a surface defined by zero flux in $\rho(\mathbf{r})$, i.e it is never crossed by the gradient vectors of $\rho(\mathbf{r})$, and satisfies the equation

$$\nabla\rho(\mathbf{r}) \cdot \mathbf{n}(\mathbf{r}) = 0 \tag{2.32}$$

where $\mathbf{n}(\mathbf{r})$ is the unit vector normal to the surface. This is the interatomic surface and an atom is defined as the region of space that is bound by at least one of these zero-flux surfaces. Integration over the atomic basin using the appropriate operator yields atomic properties such as charge, volume, dipolar polarisation etc.[17]

2.7.2 Characterising the Chemical Bond Using QTAIM

We can categorise the type of interaction between two atoms by examining topological parameters at the BCP. Considering the charge density at this point, ρ_{b}, is the simplest way to do this, where a closed shell interaction (ionic, hydrogen bonding, dispersion etc.) typically has a value of ρ_{b} less than 0.1 au, whereas ρ_{b} for a shared-shell interaction, i.e. a covalent bond, will take values greater than 0.2 au.[17] Here the atomic units correspond to ebohr^{-3}.

The energy density at the BCP is another useful parameter in the description of the nature of a bond. Cremer and Kraka[18] proposed that the total energy density at the BCP be evaluated by

$$H_{\mathrm{b}} = G_{\mathrm{b}} + V_{\mathrm{b}} \tag{2.33}$$

where G_{b} and V_{b} are the gradient kinetic energy and potential energy densities at the bond critical point, respectively. The mechanics of bond formation are such that shared interactions are the result of an excess of potential energy at the BCP, whereas a closed-shell interaction an excess of kinetic energy. H_{b} is therefore < 0 for a shared-shell interaction

and > 0 for closed-shell. The magnitude of H_b is an indicator of the extent of each type of interaction.

Although technically an atomic property, the delocalisation index δ(A, B) gives the magnitude of the exchange of electrons in atomic basin A with those in basin B. This yields a measure of the bond order between A and B if there is no appreciable charge transfer.[19,20]

The Laplacian of the electron density is defined by:

$$\nabla^2\rho(\mathbf{r}) = \nabla \cdot \nabla\rho(\mathbf{r}) = \underbrace{\frac{\partial^2\rho(\mathbf{r})}{\partial x^2}}_{\lambda_1} + \underbrace{\frac{\partial^2\rho(\mathbf{r})}{\partial y^2}}_{\lambda_2} + \underbrace{\frac{\partial^2\rho(\mathbf{r})}{\partial z^2}}_{\lambda_3} \tag{2.34}$$

where λ_1, λ_2 and λ_3 are the curvatures in the three principal axes. The Laplacian at the BCP, $\nabla^2\rho_\mathrm{b}$, is related to the gradient energy densities G_b and V_b by the local virial theorem:

$$\frac{\hbar^2}{4m}\nabla^2\rho_\mathrm{b} = 2G_\mathrm{b} + V_\mathrm{b} \tag{2.35}$$

The value of $\nabla^2\rho_\mathrm{b}$ therefore also allows for characterisation of the type of bonding interaction. When shared interactions are formed, a local contraction of charge along the bond path takes place due to excess potential energy and we observe a large negative $\nabla^2\rho_\mathrm{b}$. Conversely, a closed-shell interaction is the consequence of the local redistribution of charge towards the interacting nuclei as a result of a surplus of kinetic energy, leading to a depletion of charge at the BCP. For these bonding situations $\nabla^2\rho_\mathrm{b}$ is therefore > 0.[21]

2.8 Dispersion Force and Non-Bonding Interactions in DFT

Long-range inter- and intra-molecular interactions play a significant role in the determination of structures and properties of organometallic systems, and as such these interactions must be described as accurately as possible by the chosen DFT method. Dispersion forces are attractive interactions between non-polar molecules or atoms that are not directly bonded to each other, arising from correlated instantaneous dipoles due to fluctuations in charge density.[22] It may be expected that such an interaction be very weak, however Fritz London

showed that they are in fact strong enough to account for the attraction between noble gas atoms.[22,23] The dispersion energy can be approximated by

$$V_{\text{disp}} \simeq \frac{C_6}{r^6}, \qquad C_6 = -\frac{3}{2}\alpha_{\text{A}}\alpha_{\text{B}}\frac{I_{\text{A}}I_{\text{B}}}{I_{\text{A}}+I_{\text{B}}} \tag{2.36}$$

where $\alpha_{\text{A/B}}$ and $\text{I}_{\text{A/B}}$ are the polarisabilities and ionisation energies of atoms A and B, respectively. This attractive interaction decays with $-r^{-6}$, the same r dependence as dipole-induced dipole (Debye) and dipole-dipole (Keesom) forces, with all three of these attractive interactions falling under the umbrella of van der Waals forces. Higher order terms contribute further to the dispersion energy, which may be written as

$$V_{\text{disp}} \simeq \frac{C_6}{r^6} + \frac{C_8}{r^8} + \frac{C_{10}}{r^{10}} + \cdots \tag{2.37}$$

with the higher order terms becoming much more important at shorter distances.

2.8.1 The Performance of Standard DFT

Unfortunately for the computational chemist, standard LDA, GGA and hybrid XC functionals for DFT fail to adequately describe dispersion forces between atoms and molecules. Figure 2.1 illustrates two classic examples of such failures, two Kr atoms on the left, and a π-stacked benzene dimer on the right. B3LYP[24,25] predicts no binding between the two Kr atoms, while PBE[26] finds a very shallow minimum of less than 1 kJmol^{-1} and decays exponentially rather than with $-r^{-6}$, owing to PBE and other semi-local XC functionals relying on density overlaps in finding interactions between atoms. Both PBE and B3LYP predict no binding whatsoever between the two benzene molecules.

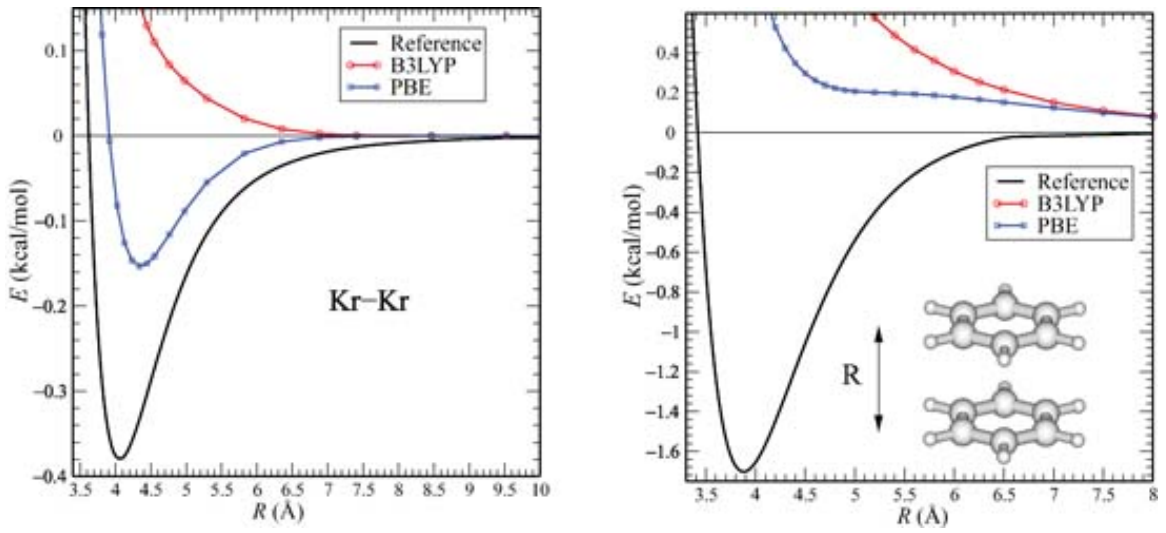

Figure 2.1: Potential energy curves for the interaction between two Kr atoms (left) and two benzene molecules (right). A comparison is made between DFT calculations using PBE and B3LYP XC functionals and the accurate reference CCSD(T) data.[27,28] Image from review by Grimme.[29]

Standard DFT functionals fail to describe dispersion for two reasons; firstly because DFT does not consider instantaneous density fluctuations, for which double excitations, i.e. simultaneous single excitations separated at a distance, are required. For this, post-Hartree-Fock methods such as, at least, Møller-Plesset perturbation theory to the second order (MP2) must be employed. Secondly, the XC energy calculated with DFT is computed from only local or semi-local properties of the electron density, while dispersion forces are exhibited at long distances. Many DFT-based dispersion methods have been developed and are summarised in reviews by Grimme[29] and Michaelides.[30] Here we focus on the methods used to include dispersion forces in the present study - DFT-D3[31] dispersion corrections, and the M06-2X[32] XC functional.

2.8.2 DFT-D Dispersion Correction

A simple approach to ensuring a long range $-r^{-6}$ asymptotic behaviour of the interaction between particles in the gas phase is to add a pair-wise additive energy term which can account for such long range interactions, and is given the general name DFT-D[31,33,34]

$$E_{\mathrm{tot}} = E_{\mathrm{DFT}} + E_{\mathrm{disp}}^{\mathrm{DFT-D}} \tag{2.38}$$

where E_{DFT} is the total DFT energy calculated for a given XC functional. The dispersion interaction energy for DFT-D calculations is given by

$$E_{\mathrm{disp}}^{\mathrm{DFT-D}} = -\sum_{\mathrm{A,B}} \sum_{n=6,8,10,\ldots} s_n C_n^{\mathrm{AB}} / r_{\mathrm{AB}}^n f_{\mathrm{damp}}(r_{\mathrm{AB}}) \tag{2.39}$$

where the C_n^{AB} are the n-th order isotropic dispersion coefficients for pairs of atoms A and B, r_{AB} is their internuclear separation, and f_{damp} is a damping function which corrects the divergence of the $-r^{-6}$ function at short r_{AB}.[33] A global scaling factor s_n is also included in order to adjust the energy correction for the chosen XC functional.

DFT-D1/D2 methods use predetermined, and constant, C_n^{AB} coefficients for pairs of atoms irrespective of their oxidation state or hybridisation. These factors affect the polarisabilities and ionisation energies of the atoms which would lead to C_n^{AB} which vary with atomic environment. The DFT-D3 scheme by Grimme *et al.*[31] facilitates this environment dependence by considering the number of neighbours each atoms has, whereby a more "squeezed" atom will have a smaller C_n^{AB} coefficient. The coefficients are then chosen from a set which have been pre-calculated for a range of pairs of elements in different reference states. Polymerisation pathways display changes in hybridisation states and as such, the DFT-D3 method may be appropriate for these studies.

2.8.3 The Minnesota M06-class of XC Density Functionals

The Minnesota M06 XC functionals are a family of density functionals specifically developed by Donald Truhlar and co-workers to improve the description of systems involved in thermochemistry and kinetics, and where medium to long-range non-covalent interactions are of importance.[32] The suite consists of the meta-hybrid-GGAs M06, M06-2X and M06-HF, and the local M06-L XC functional. They have been fitted to a wide range of datasets including binding energies of dispersion bonded dimers. Figure 2.2 illustrates the improvement of the description of non-bonded interaction between benzene and methane by calculation with the M06 functionals, compared to those obtained using popular standard XC functionals.

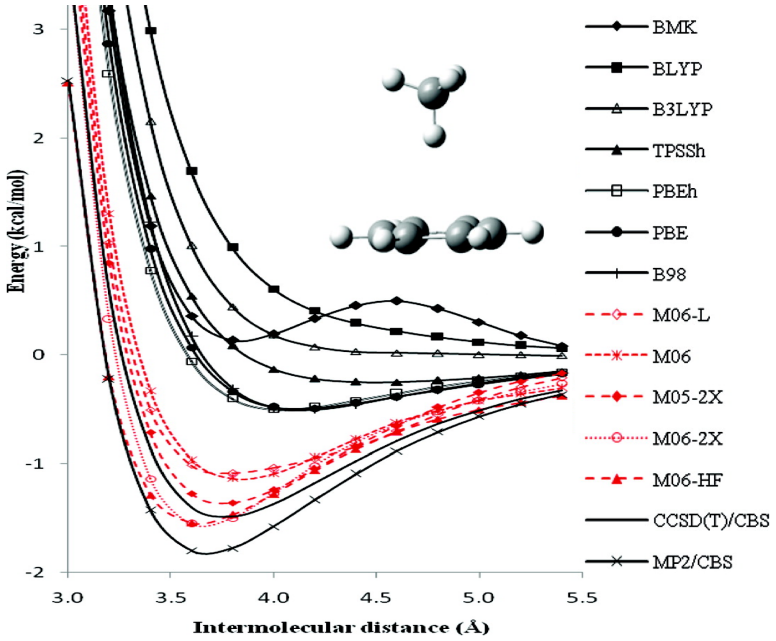

Figure 2.2: Performance of traditional XC functionals (in black) and the M06 suite (plus M05-2X, in red) at reproducing the binding curve of benzene and methane calculated with post-Hartree-Fock methods (bottom two black lines).[35] The interatomic distance is defined to be between the C atom of methane and the centroid of the benzene.

While it is not exactly clear which of the M06 functionals is 'best' in this particular case, Truhlar recommends M06-2X and M06 for studies where main-group thermochemistry, kinetics and non-covalent interactions are all important, and M06-L and M06 for transition metal thermochemistry.[35] The catalytic system that is the subject of Chapters 3 and 4 exhibits intramolecular dispersion interactions between atoms at long-distances, a non-covalent π-interaction between the monomer and the Ti centre, and of course thermochemistry and kinetics, all of which must be adequately described. Although M06 is recommended over M06-2X for use with transition metals, the Ti centre of the catalyst is formally d^0, and hence the use of a functional recommended for open d shells is not required. Since M06-2X performs the best at reproducing main group thermochemistry barrier heights in Truhlar's tests, this functional is chosen for including dispersion and non-bonded interactions in our DFT calculations.

2.9 Inclusion of Solvents in DFT - Polarisable Continuum Model

By default, DFT calculations model systems in the gas-phase. This is of course not the case in many experimental setups - indeed, certainly not always the case for the Ziegler-Natta homo- and co-polymerisations of α-olefins. Methods for including solvent effects in DFT can be divided into two types: those that describe the solvent molecules explicitly and those that treat them implicitly as a continuous medium, though combinations of both methods are also possible.[36–38] Here we focus on the continuum solvation model, specifically the polarisable continuum model (PCM).[39]

The PCM considers the solvent as a uniform polarisable medium with dielectric constant ε. The solute is then placed in a hole in the medium. At this stage there are three contributing terms to the free energy of solvation:

$$\Delta G_{\text{solvation}} = \Delta G_{\text{cavity}} + \Delta G_{\text{disp}} + \Delta G_{\text{elec}} \tag{2.40}$$

where the terms on the right hand side of Equation 2.40 are the destabilising energy required to form the cavity; the dispersion energy between the solute and solvent; and the electrostatic energy due to the charge distribution of the solute polarising the medium, and vice versa. The shape of the cavity in the PCM is formed by interlocking atomic van der Waals radii, named a van der Waals cavity, which are scaled by an empirical factor. The PCM also employs a detailed description of the electrostatic potential and parametrises the cavity and dispersion energy contributions by considering the surface area.[39]

2.10 Codes

The results presented in this thesis were obtained by employing three quantum chemistry codes: Gaussian09 (G09);[40] Amsterdam Density Functional (ADF);[41] and AIMAll.[42] These codes are briefly described below.

2.10.1 Gaussian09

The Gaussian software packages (GaussianXX, with XX denoting the year of each renewed edition's release) are a set of quantum chemistry programs with a wide range of functionality in solving chemical problems. As its namesake suggests, G09 employs GTOs in its descriptions of basis sets, which is one of its major differences compared to the ADF code. G09 can perform a variety of calculations including, but not limited to, ground state molecular structures and energies, transition state energies and structures, NMR shielding, IR and Raman vibrational frequencies, Grimme dispersion corrections, and electrostatic potential surfaces. The majority of the calculations in this thesis which were performed using G09 employed DFT, however some utilised *ab initio* and semi-emperical methods, of which the program has many capabilities. Such capabilities include HF, Møller-Plesset, Coupled Cluster, QCISD, PM6, and many more, as well as molecular mechanics methods. Solvation models are also in-built, of which the PCM is utilised in this thesis. Relativistic effects may be included by using ECPs or the DKH Hamiltonian.

2.10.2 Amsterdam Density Functional

The Amsterdam Density Functional program differs from G09 in that it has been developed with DFT methods as its main focus, and as such is not as comprehensive. More recently, users have been able to utilise semi-empirical methods and molecular dynamics through incorporation of the MOPAC[43] and DFTB,[44] and ReaxFF[45] suites, respectively, which are accessible through GUIs. ADF utilises STOs instead of GTOs in its basis sets for both molecular and periodic calculations, which is enabled by its implementation of a numerical integration scheme for solving integrals. The ZORA Hamiltonian is utilised to incorporate relativity, while the frozen core approximation is used to cut computational expense. Further functionalities and differences between ADF and G09 will be discussed in Section 2.11.1.

Bonding analyses are carried out in Chapter 5 of this thesis, utilising two of ADF's features which are not supported by G09:

Hirshfeld Charge Analysis

The Hirshfeld scheme partitions the spatial volume of a molecule into atomic contributions based on atomic densities.[46] ADF approaches this partitioning scheme by using spherically averaged ground state densities. The sum over all atoms, A, of the ground state atomic densities at each point in space is denoted by the promolecular density, ρ^{pro}.

$$\rho^{\mathrm{pro}}(\mathbf{r}) = \sum_{\mathrm{A}} \rho_{\mathrm{A}}(\mathbf{r}) \tag{2.41}$$

The *actual* molecular density at each point in space, $\rho_{\mathrm{A}}(\mathbf{r})$ is partitioned by weighting factors, w_{A}, according to the promolecular contributions, as follows:

$$w_{\mathrm{A}}(\mathbf{r}) = \frac{\rho_{\mathrm{A}}(\mathbf{r})}{\rho^{\mathrm{pro}}(\mathbf{r})} \tag{2.42}$$

The Hirshfeld charge on atom A, $Q_{\mathrm{A}}^{\mathrm{Hirshfeld}}$, is then defined by:

$$Q_{\mathrm{A}}^{\mathrm{Hirshfeld}} = Z_{\mathrm{A}} - \int w_{\mathrm{A}}(\mathbf{r})\rho^{\mathrm{pro}}(\mathbf{r})dr \tag{2.43}$$

where Z_{A} is atomic number. ADF recommends the use of Hirshfeld charges over charge analyses based on basis functions (e.g. Mulliken).

Ziegler-Rauk Energy Decomposition Analysis

ADF supports an energy decomposition analysis (EDA), developed by Morokuma[47] and by Ziegler and Rauk,[48] that allows for bonding interactions to be interpreted in conceptually simple terms. On splitting a molecule AB into fragments A and B, the overall bond energy between the two fragments, ΔE, is divided into two components, namely the energy of preparation, ΔE_{prep}, and the energy of interaction of the two prepared fragments, ΔE_{int}. The term ΔE_{prep} corresponds to the energy required to distort the fragments from their equilibrium geometric and ground electronic states to their geometries found in the molecular system, and their valence electronic configurations. The total bonding energy can therefore be written

$$\Delta E = \Delta E_{\mathrm{int}} + \Delta E_{\mathrm{prep(geometric)}} + \Delta E_{\mathrm{prep(electronic)}} \tag{2.44}$$

Furthermore, ΔE_{int} can itself be decomposed into three terms that are chemically meaningful: the classic Coulomb interaction ΔE_{elec}; the Pauli exchange repulsion $\Delta E_{\mathrm{Pauli}}$; and the orbital mixing term ΔE_{orb}.

$$\Delta E_{\mathrm{int}} = \Delta E_{\mathrm{elec}} + \Delta E_{\mathrm{Pauli}} + \Delta E_{\mathrm{orb}} \tag{2.45}$$

The term ΔE_{elec} is a consequence of the classical Coulombic interaction of the prepared fragments' frozen charge densities as they approach each other from infinity to their molecular positions, resulting in a total density equivalent to the superposition of the respective fragment densities, $\rho_{\mathrm{A}} + \rho_{\mathrm{B}}$. This contribution to ΔE_{int} is usually stabilising, as a result of dominating nucleus-electron attraction. The product wavefunction, $\Phi_{\mathrm{A}}\Phi_{\mathrm{B}}$, does not obey the Pauli principle however, and must therefore be anti-symmetrised and renormalised to another intermediate state which does. The associated energy change corresponds to $\Delta E_{\mathrm{Pauli}}$, the destabilising interaction between occupied molecular orbitals. Subsequent relaxation from this intermediate state to the converged molecular wavefunction yields ΔE_{orb}; the change in energy associated with orbital mixing which thus provides the covalent contribution to the bond. The decomposition of ΔE_{int} into three meaningful contributions allows for a deeper and more powerful analysis of bonding between two fragments than just by considering the bond energies alone.

2.10.3 AIMAll

AIMAll carries out QTAIM analyses to obtain the topological properties of molecular structures as described in Section 2.7, for which a wavefunction calculated from DFT or *ab initio* must be used as an input. Currently, wavefunctions from calculations using GTOs are supported by AIMAll. As such, for the systems calculated using ADF in Chapter 5 a single point calculation using G09 was required in order for QTAIM analyses to be undertaken.

2.11 Modelling Chemical Reactions with DFT

The reaction mechanisms we draw to describe transformations of molecular species are ultimately depicted by a path following a series of stationary points across a

multi-dimensional potential energy surface (PES). Reactants, intermediates, and products are minima on the PES, whereas transition states (TSs) are saddle points (see Figure 2.3). In order to locate these stationary points, the geometry of molecular structure must be optimised. The methods by which such optimisations are solved are briefly described below. It must be noted that these methods determine the *nearest* stationary point, while a multi-dimensional PES may exhibit many. Figure 2.3 shows a minimum denoted *local*, whereas the minimum that has the lowest energy of all the minima is called the *global* minimum. Care must be taken when choosing a structure from which to start a geometry optimisation, as the optimisation calculation may get "trapped" in a local minimum, yielding inaccurate results, especially when calculating reaction energies.

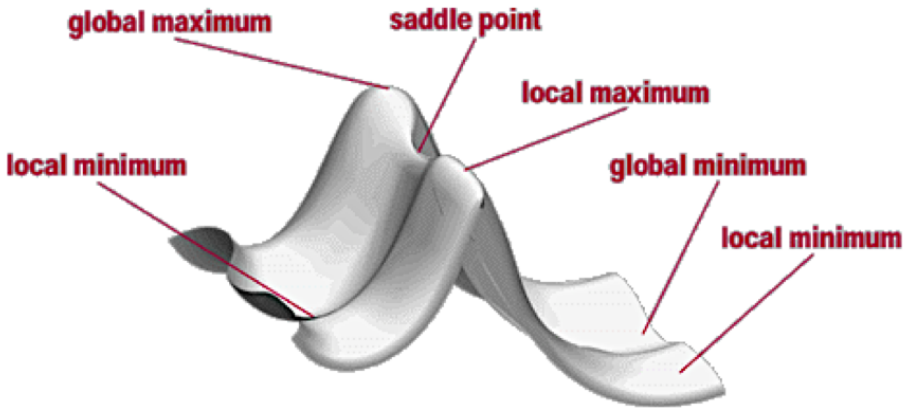

Figure 2.3: A multi-dimensional potential energy surface showing the different types of stationary points.[49]

2.11.1 Geometry Optimisation

The fundamental test to determine whether a geometry is a stationary point is to calculate the SCF energy, followed by the first derivatives of the energy with respect to nuclear displacements. The geometry is characterised as a stationary point only when these first derivatives are zero. If they are non-zero, however, different algorithms may be used to optimise the geometry to meet this criterion. Most algorithms require Cartesian coordinates be converted into internal "redundant" coordinates so that the first derivatives may be calculated with respect to nuclear geometric degrees of freedom. This conversion is carried

out internally by both ADF and G09. It should be noted that the derivatives, depending on computational approach, are calculated with only finite precision, and the gradient can be reduced only to a certain value, i.e. the stationary point cannot be located exactly. Practically, an optimisation is considered converged if the gradient is reduced to below a pre-defined "cut-off" value, or alternatively if a sufficiently small change is observed between two iterations.

The most common methods employed for optimisation of molecular geometries are based on quasi-Newtonian algorithms.[50,51] ADF implements such an algorithm, namely Broyden-Fletcher-Goldfarb-Shanno (BFGS), which uses approximations to the second derivatives of the energy with respect to nuclear displacements (the Hessian matrix), which are iteratively improved at each step, to guide an alteration in geometry.[52–55] An initial Hessian is constructed based on a forcefield.

The default algorithm implemented in G09 was developed by Bernard Schlegel, and is called the Berny algorithm.[56] Together with the Hessian, forces acting on the atoms of the molecule are used to predict structures that may be energetically favourable. Optimisation therefore takes places towards the next local minimum on the PES. The Berny algorithm avoids the costly explicit calculation of the Hessian by constructing an approximate Hessian by applying a valence forcefield and using the energies and first derivatives that are calculated along the optimisation in updating the approximate Hessian. The TS geometries in this thesis were calculated using only G09, where the "CalcFC" keyword was used to explicitly calculate the Hessian at the beginning of the optimisation, followed by its approximation in subsequent iterations.

2.11.2 Vibrational Frequencies

In order to determine whether a stationary point is a minimum energy structure or a TS, a vibrational frequency calculation must be carried out. It is assumed that around a potential well the energy behaves approximately harmonically. By transforming the molecular coordinates into a set of mass-weighted coordinates an eigenvalue problem can be constructed for the second derivative of the energy. The square root of the force constant eigenvalues from the Hessian yields the frequencies, while the eigenvectors give the

vibrational modes. At a true minimum the eigenvalues are positive or zero, while a TS has rigorously one negative eigenvalue in the Hessian. Stationary points with more than one are higher order saddle points. The significance of this is that positive eigenvalues correspond to a vibrational modes which raises the energy of system, whereas negative eigenvalues correspond to modes through which the energy is lowered.

ADF calculates second derivatives by numerical calculation from the first derivatives, together with a full SCF calculation carried out for the displacement in both directions along all three Cartesian axes. ADF can also calculate the vibrational frequencies analytically, however this can only be done for a small subset of XC functionals. Frequency calculations in ADF can therefore be very time consuming. G09 on the other hand, calculates vibrational frequencies by analytical calculation of the Hessian. By default however, the Berny algorithm in G09 evaluates the number of negative eigenvalues of the approximate Hessian at each step of a TS optimisation and if this number is not one, the job is aborted. The "NoEigenTest" keyword is used to suppress this test.

2.11.3 Locating Stationary Points Along a Reaction Path

Much of the work presented in this thesis is related to predicting reaction pathways using DFT. Such predictions require calculation of minima and TSs along reaction profiles. While the starting reactant and final product are often known, the TSs and intermediates along the reaction path must be located. A TS structure may sometimes be found by simply using a good initial guess structure, which may either be from a modification of a similar system, a TS found using another method, or sometimes from chemical intuition. An easy way to check if a guess structure is likely to optimise to the desired TS is to carry out an initial vibrational frequency calculation. If an imaginary mode exists that corresponds to the TS vibration, and it has the lowest imaginary vibrational frequency, it is likely that the optimisation will yield the expected structure. Examples of more rigorous techniques used to locate stationary points along a reaction path are described below.

Synchronous Transit-Guided Quasi-Newton Method

Schlegel and co-workers developed a synchronous transit-guided quasi-Newton (STQN) approach to locate the TS between two known minima.[57,58] This method uses a linear synchronous transit (LST) or quadratic synchronous transit (QST) approach to arrive closer to the quadratic region around the TS, followed by a quasi-Newton or eigenvector-following algorithm to optimise to the TS structure using redundant internal coordinates. A LST is a linear motion approach, which assumes that the atoms of a TS geometry are directly between their positions found in the reactant and products. The QST method instead assumes that the atomic positions of the TS lie on a parabola that connects those in the reactant and product geometries. Such techniques are very effective for simple reactions with a relatively small number of atoms, however as molecular size increases, and the reaction mechanism is more complex than a simple concerted one, they are not reliable. G09 implements the QST approach when using the QST2 and QST3 keywords. The former requires only the geometries of the reactant and product, whereas the latter can be used when an approximate guess TS structure is known. Using these methods in G09 requires that the coordinates of the atoms are input in exactly the same order for all structures.

Linear Transit

A simpler alternative to the synchronous transit methods described above that may be used to locate a TS is scanning a particular coordinate of the PES. If, for example, a reactant structure is known and it is expected that a TS lies somewhere along the torsion of a dihedral angle, a linear transit, or relaxed potential energy scan, of the dihedral angle may be carried out in order to estimate the structure of the TS. This method carries out a series of optimisations at pre-defined points along the PES of a particular variable, and in doing so can produce a potential energy profile such as that shown in Figure 2.4. The structures at the peak/peaks may then be optimised to a TS. This method was often used in locating TSs reported in this thesis.

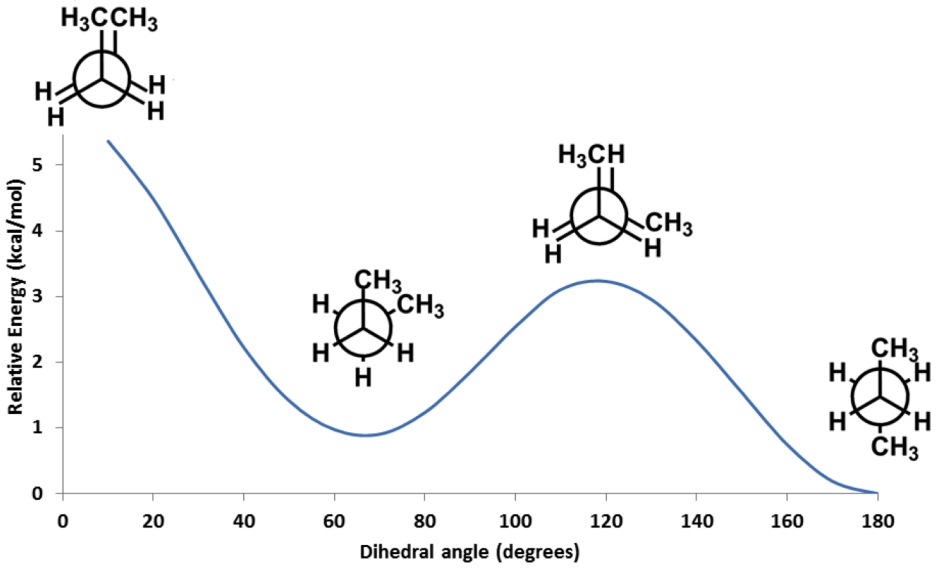

Figure 2.4: A linear transit of the C–C–C–C dihedral angle of n-butane.[59]

Intrinsic Reaction Coordinate

Once a transition state has been located, and confirmed by its negative (or imaginary) vibrational mode, the reactants and products connected by this vibrational mode may be found. A traditional way to do this is to start from the saddle point geometry and move downhill to these associated minima. While different paths taken down the slopes either side of the saddle point may access these minima, the intrinsic reaction coordinate (IRC) is defined as the paths that are followed by a particle taking the steepest descent with infinitely small steps in each direction from the transition state structure to the two minima.[60,61] This method can be used when the system is described by mass-weighted coordinates, as when calculating the normal modes of vibration. The directions in which to start the steepest descents are taken directly from the eigenvector of the imaginary vibrational mode.

The IRC method was used for initial calculations at the beginning of this PhD, however it was found that the calculation would often fail. Instead, minima connected by a TS were located by manually displacing the TS structure in both directions of the imaginary vibrational mode, and optimising these structures to minima.

Chapter 3

Post-Metallocene Catalysed Propylene Homo-polymerisation - A Benchmarking Study

3.1 Introduction

Sixty years have passed since Karl Ziegler's discovery of a titanium-based catalyst for the polymerisation of ethylene[62,63] and Giulio Natta's reports of stereoselective polymerisation of propylene.[64,65] Their combined discoveries caused an explosion of interest in systems containing transition metals as a means to produce poly-α-olefins, and as recognition of their combined efforts in the field of polymers, they were awarded the joint Nobel Prize for Chemistry of 1963. Here we focus on catalysts containing group IV metals, though a plethora of systems containing later transition metals[66–69] and rare-earth elements[70] have been reviewed. The many different types of ligands and co-catalysts and their advantages are not listed exhaustively, as space is limited and our catalyst is pre-defined; the focus is on the polymerisation pathway and related mechanisms.

3.1.1 Ziegler-Natta Catalysis

Ziegler's original catalyst is a heterogeneous $TiCl_4$-$AlClEt_2$ system with edges and dislocations on the surface of the reduced $TiCl_3$ providing active sites for the reaction. The proposed geometric structure of an active site and stereoselective ability of such a system is illustrated in Figure 3.1. A perfectly reproducible surface upon which the reaction

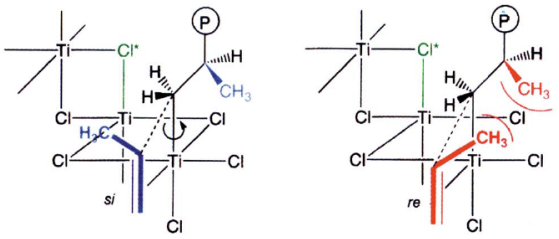

Figure 3.1: A schematic of the $TiCl_3$ coordination site for heterogenous Ziegler-Natta catalysis.[71] The green Cl atom determines the position of the first methyl group of the growing polymer chain, resulting in the stereoselectivity of the catalyst towards insertion of propylene following coordination *via* the *si* face.

takes place cannot be guaranteed, however, and many types of active sites are available, leading to a broad molecular weight of polymers produced in this manner.[72] In lieu of this, much attention turned to the group IV metallocenes, first synthesised by Wilkinson *et al.* in 1953,[73] and the knowledge that $TiCl_2Cp_2$ polymerises ethylene in the presence of $AlClEt_2$ with reasonable activity under similar conditions to heterogenous Ziegler-Natta catalysis.[74–76] The general structure of this pre-catalyst is shown as **3.1** of Figure 3.2, which is known as a bent metallocene complex. Such complexes, of a simple four-coordinate structure with two reactive cis-positioned ligands, allowed for the identification and characterisation of homogeneous polymerisation intermediates, as well as facilitated the justification of mechanistic hypotheses. While polymerisation using this method was slow, Sinn and Kaminsky[77] observed that on addition of water the catalytic system is highly active. The hydrolytic conversion of $AlMe_3$ to methylaluminoxane (MAO), an oligomeric compound with the proposed structure $Me_2Al–[O-AlMe]_n–OAlMe_2$, was suggested as the source of this catalytic activation[78] and now many MAO-based co-catalysts are widely used across the field of olefin polymerisation.

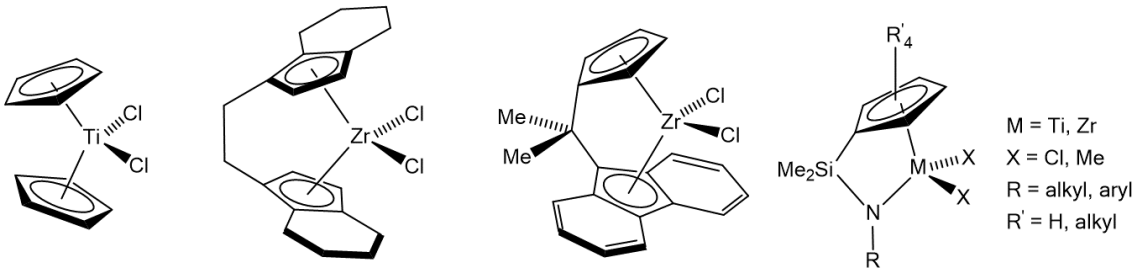

3.1 **3.2** **3.3** **3.4**

Figure 3.2: Metallocene and post-metallocene catalysts capable of olefin polymerisation.

3.1.2 Ansa-metallocenes and Constrained Geometry Catalysts

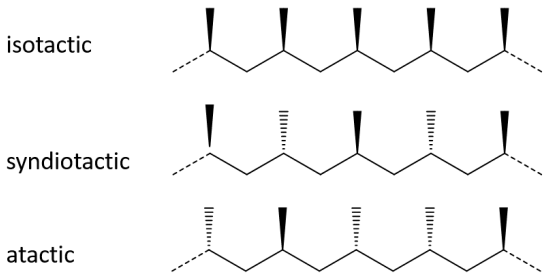

Figure 3.3: Tacticity variation found in polypropylene.

The macromolecular properties of polypropylene are in part governed by its tacticity - the relative orientation of adjacent methyl pendant groups, as shown in Figure 3.3. Careful design of the metallocene catalysts' symmetry was discovered to control the stereochemistry of the resulting polymer.[79] The C_2 symmetric *ansa*-zirconocene catalyst, **3.2** (Figure 3.2), developed by Kaminsky and Britzinger produced highly isotactic polypropylene.[80] The steric environment of the active site is defined by the *ansa*-bridging moiety by preventing rotation of the ligands, resulting in the control of arrangement of the reacting propylene monomer. Catalyst **3.3** is of C_{s} symmetry, and was shown to produce highly syndiotactic polypropylene by Ewen *et al.*.[81] The constrained geometry catalysts (CGCs), **3.4** in Figure 3.2, were then developed to improve upon the low temperature stability and low molecular weight capabilities of *ansa*-metallocenes.[82,83]

3.1.3 Post-metallocenes

New catalyst development become a focus of olefin polymerisation research following the patenting of the systems described above,[79,84] with the isolobal analogy being utilised to replace one or more of the Cp ligands on the metal centre to produce catalysts dubbed "post-metallocenes". Two molecular fragments are considered isolobal when they share similarities in shape, symmetry, and energies of their frontier molecular orbitals. Figure 3.4 compares the single σ-donor and 2 π-donor orbitals of the Cp^- and a κ^1-bound anionic donor, e.g. the imido ligand NR^{2-}. These frontier orbitals may each interact with the metal centre. Many post-metallocene catalysts have been designed which abide by this isolobal

analogy, including numerous half-sandwich complexes with κ^1-bound monoanionic ligands replacing one cyclopentadienide ligand, and are reviewed comprehensively elsewhere.[67,84–86]

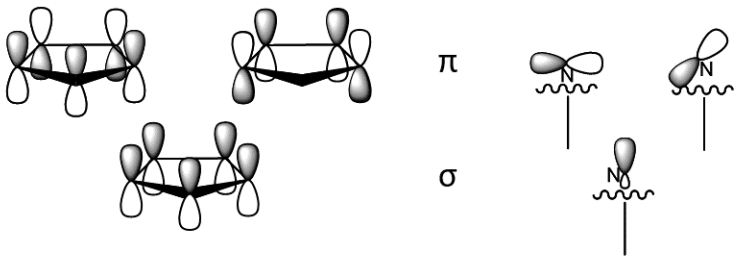

Figure 3.4: Frontier orbitals of cyclopentadienide and imido NR^{2-} ligands.

The κ^1-amidinate ligand binds to a metal centre *via* only the imide nitrogen with a single σ-interaction and the two π-interactions, as the amino nitrogen may mesomerically donate into the π_{CN}, as displayed in Scheme 3.1 below:

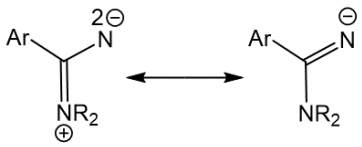

Scheme 3.1: The mesomeric forms of the amidinate ligand.

ARLANXEO Netherlands B.V. recently introduced the κ^1-amidinate (NC(NR_2)Ar, R= alkyl) catalysts, dubbed Keltan ACE$^{\mathrm{TM}}$,[85,87–89] shown in Figure 3.5, and is the subject of the present research. The CpR_5 ligand binds more strongly to the metal centre relative to its Cp analogue, as, being more electron rich, it is a stronger donor. This is advantageous in its resulting increased thermal stability.

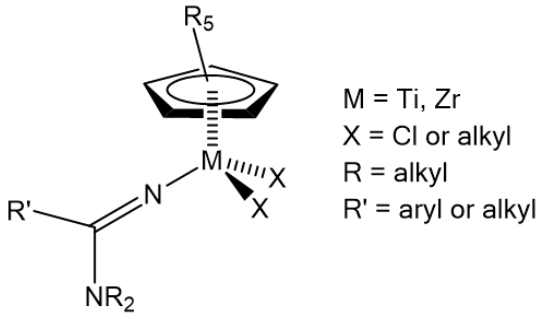

Figure 3.5: Keltan ACE$^{\mathrm{TM}}$ class of catalyst, containing CpR_5 and amidinate supporting ligands.

Before the κ^1-amidinate pre-catalyst can operate in the catalysis of olefins it must first be activated by a co-catalyst by the formation of a cation-anion pair. Various available co-catalysts, as well as the effect of the anion, are discussed in detail in Chapter 4.

3.1.4 Mechanisms for Monomer Coordination and Insertion

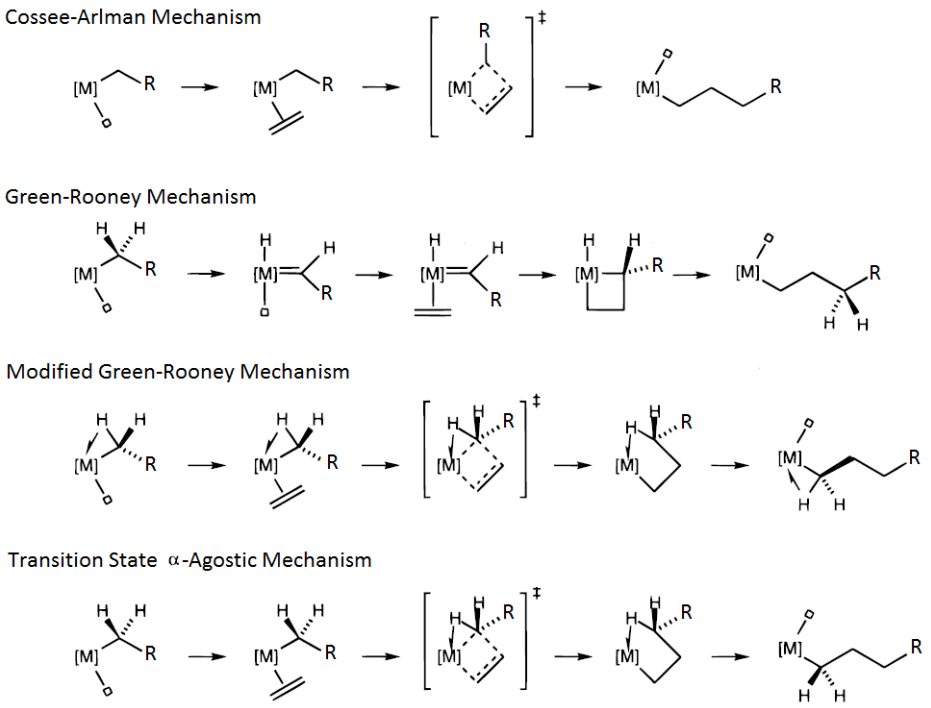

Scheme 3.2: Proposed mechanisms for ethylene enchainment, adapted from a review by Grubbs and Coates.[90] The transition state α-agostic mechanism is also known as the modified Cossee-Arlman mechanism.

Imperative to the development and utilisation of any chemical reaction is the understanding of the mechanisms involved, not least for those used on a large industrial scale. Monomer enchainment has received much attention over the years, for which four general mechanisms have been offered (Scheme 3.2). Shared by all of them is coordination of an olefin monomer succeeded by its insertion into a metal–carbon bond.[91–94] The first to be proposed was the Cossee-Arlman mechanism involving a direct alkyl insertion of the olefin monomer into the growing chain.[95–99] Rooney and Green[100,101] subsequently proposed an oxidative 1,2 hydrogen shift from the alkyl α-carbon to form a metal-alkylidene hydride complex that reacts with the coordinating monomer to give a metallacyclobutane, which then undergoes reductive coupling to give the first insertion

product. This mechanism is not able to describe olefin insertion for d^0 metal systems however, as the oxidative step is not possible. A modification of this mechanism whereby a hydrogen on the α-carbon interacts with the metal centre via an α-agostic interaction, rather than fully binding, was put forward by Green, Rooney and Brookhart.[102–104] An agostic interaction is a 3-centre-2-electron, involving a coordinatively-unsaturated metal with a C–H bond, and is a stabilising interaction in d^0 metal alkyl complexes such as those used in olefin polymerisation.[105] The final mechanism proposed is an amalgam of the modified Green-Rooney and the Cossee-Arlman mechanisms, and sees an α-agostic interaction in only the transition state rather than throughout the enchainment sequence. *Ab initio*[106] and density functional[107] calculations support this α-agostic-assisted transition state mechanism and this model is widely favoured.[90,108]

Turning our attention to the coordination of the olefin monomer, the cationic metal centre must have a coordination site available to which the incoming olefin monomer may bind. This should be carefully considered, particularly for homogenous Ziegler-Natta catalysis where a co-catalyst is required for activation. While little is still known about the structure and coordination strength of MAO, anions such as $[MeBF_{15}]^-$ ($[MeB(C_6F_5)_3]^-$) coordinate fairly strongly and must be displaced before the olefin may approach the metal coordination sphere. Anion-displacement is discussed further in Chapter 4.

3.1.5 Mechanisms for Chain Termination

Chain propagation (CP) is not the only reaction pathway available to the Ziegler-Natta catalytic systems. Chain termination steps involving the transfer of a β-hydride are also possible, two mechanisms for which are illustrated in Scheme 3.3. If the β-hydride is transferred to the metal centre after primary insertion (Scheme 3.3), a unimolecular process termed β-hydride elimination (BHE), a vinylidene-terminated polymer is produced. This process was shown experimentally to occur spontaneously for group IV metallocene alkyl complexes.[109,110] The same α-olefin is produced by the bimolecular β-hydride transfer (BHTM) to an incoming monomer, shown in Scheme 3.3.

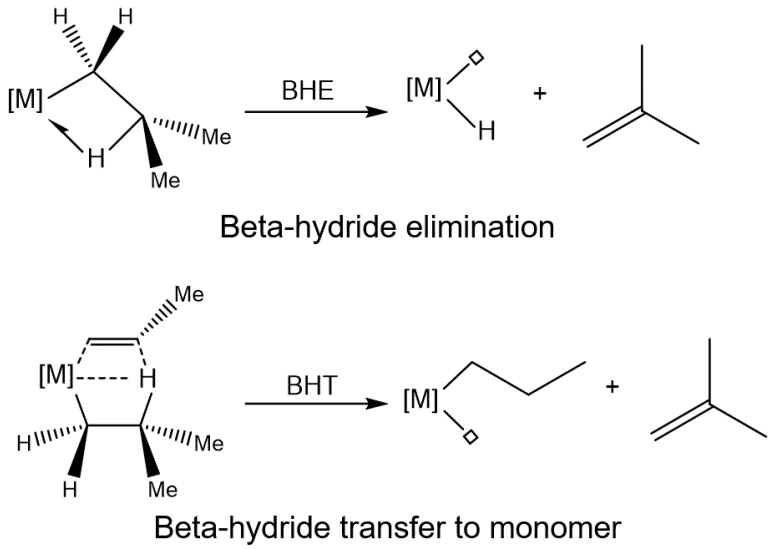

Scheme 3.3: β-hydride transfer mechanisms. Both examples are for the reaction of a $[L_2M–iBu]^+$ system.

The molecular weight of a polymer, here defined as the average degree of polymerisation, $\bar{P}_n$, is proportional to the ratio of the propagation rate r_{P} to the combined rate of termination reactions r_{CT}:

$$\bar{P}_n = \frac{r_{\mathrm{P}}}{\sum r_{\mathrm{CT}}} \tag{3.1}$$

As BHTM and CP are both linearly dependent on the concentration of the monomer, and BHE depends on only the concentration of catalyst, the dependence of the molecular weight on monomer concentration gives an indication as to the preferred termination pathway.

3.1.6 Stereo- and Regiochemistry of α-Olefin Polymerisation

Ethylene is used in the chain propagation mechanistic examples of Scheme 3.2 above as its polymerisation is a relatively simple procedure; there is no stereo- or regiochemistry to consider in the monomer coordination step. The polymerisation of propylene or higher α-olefins becomes a lot more complicated owing to these factors, and the ability of catalysts to control their specifity governs the regio- and stereoregularity of the resulting polymers. In terms of regiochemistry of the olefin coordination, there are two ways in which this can happen, and allow two different types of insertion reactions: 1,2 and 2,1 insertion, as illustrated in Figure 3.6. 1,2, or primary insertion is the name given to the process in which the primary, or unsubstituted, carbon of the α-olefin binds to the metal centre and

the secondary, or most substituted, forms a bond with the growing polymer chain; 2,1, or secondary, insertion is the name given to the opposite process. If one insertion method in favoured over the other, the catalyst is defined as regioselective and will promote the formation of a regioregular polymer. Primary insertion is generally accepted as the preferred insertion method for metallocenes, whereas for some non-metallocene catalytic systems secondary is favoured.[111,112]

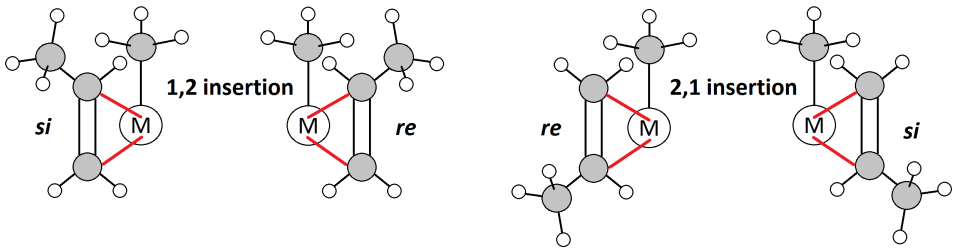

Figure 3.6: An illustration of the different ways in which a propylene monomer may coordinate to the metal centre. Ancillary ligands are not shown for clarity.

As a consequence of the prochirality of α-olefins, there is also stereochemistry to consider in the monomer coordination step. Figure 3.6 illustrates the *re* and *si* coordination possibilities via the two enantiofaces of polypropylene. Specific catalysts may therefore be stereoselective; those which are selective to the same enantioface coordination on each insertion step produce isotactic polymers, while those which allow a switching between *re*- and *si*-face coordination give rise to syndiotactic polymers. If a catalyst has no particularly strong stereoselectivity, an atactic polymer will be produced. It is well known that heterogeneous Ziegler-Natta catalysts such as that shown in Figure 3.1 produce a highly isotactic polymer, owing to the stereoselectivity of the coordination site. This is due to the chlorine atom in green determining the direction of the growing alkyl chain, which in turn preferentially allows the monomer to coordinate with one face (in this case the *si* face). Similarly, in homogeneous catalysis, when the alkyl on the metal is larger than a methyl group, the methyl on the propylene monomer can either lie in (syn) or out (anti) of the plane containing the growing chain. If we once again consider 1,2 insertion of propylene, there is a preference for coordination via the enantioface which puts the methyl substituent of the olefin anti to the first C–C bond of the growing alkyl chain so as to minimise non-bonding interactions.[111] As the direction of the first C–C bond of the growing chain is not necessarily

constant throughout the polymerisation process, the stereospecifity is often governed by the chirality of the catalyst and the structure and symmetry of the ancillary ligands.[71,113]

3.1.7 Theoretical Studies of Propylene Homo-polymerisation

Theoretical calculations have enabled detailed studies of the regio- and stereoselectivities of different Ziegler-Natta catalytic systems with various α-olefin monomers to be undertaken.[114] The ability to model isolated π-coordinated monomers and transition states allows for an easier estimation of reaction barriers relative to the difficulties in experimental methods, and permits a better understanding of the polymerisation process as a whole. Many quantum mechanical (QM) and molecular mechanics (MM), as well as combined QM/MM, calculations of propylene homopolymerisation by Group IV homogenous catalysis can be found in the literature,[115–124] including those found in reference 114; the focus here will be on the most recent theoretical calculations employing density functional theory. These studies follow the modified Cossee-Arlman mechanism as described in Section 3.1.4, and support the four-centre α-agostic transition state model.

The Effect of Solvation on Chain Propagation

In practice, olefin polymerisation via Ziegler-Natta catalysis takes place in solution, gas-phase, or in a slurry, however the majority of DFT studies of propylene polymerisation to date have been calculated in the gas phase. Borrelli *et al.* made a rough estimate of the combined cation-anion interaction and solvation by extrapolating results from Ziegler and co-workers[125] in their calculations of non-chiral biscyclopentadienyl[115] and *ansa*-zirconocene[116] catalysts. They concluded that the solvent effects must be fairly indiscriminate in their considered reactions, as even with such crude approximations they were able to find reasonable agreement with experiment for Gibbs free energy differences between 1,2 and 2,1 insertions. Tomasi and co-workers[121] concluded from their calculations of C_{S} symmetric *ansa*-zirconocenes that counter-anion ([$MeBF_{15}$) and solvent (toluene) effects do not play a major role in stereochemistry of insertion, but that calculations without inclusion of a solvent were incapable of agreeing with experiment. It should be noted again that the effect of the anion will be discussed further in Chapter 4 and is mentioned here

only briefly.

Observations of Regio- and Steroselectivity

The consensus from the literature is for 1,2 insertion preferentially occurring over 2,1, regardless of inclusion of solvent and/or counter-anion in the model. In terms of stereo-selectivity of group IV metallocene-related catalysts, it appears to be very much defined by the ancillary ligand environment. Certainly, a survey of the most recent research indicates that steric effects play a key role in determining whether monomer coordinates *re* or *si* and anti or syn to the growing chain - it also illustrates the sheer complexity of propylene polymerisation, with there being at least different 8 transition states for monomer insertion. Indeed, in order to simplify these theoretical studies, assumptions are often made about which permutations can be ignored from the outset.

In the following results section the effects of methodological set-up on polymerisation reaction pathways is investigated. Before predictions of macromolecular properties of polymers produced with the κ^1-amidinate catalyst may be made, it is imperative that the DFT computational approach reproduces results from experiment. We therefore test different XC functionals, dispersion corrections, and solvation below.

3.2 Computational Details

Density functional calculations were carried out using the G09 Revision D.01[40] program, initially implementing the generalised-gradient approximation to the XC functional of Perdew, Burke and Ernzerhof (PBE).[26,126] Dunning's correlation-consistent polarised valence DZ (cc-pVDZ) basis sets were employed for light elements, and a TZ (cc-pVTZ)[127] used for Ti. The default SCF and geometry convergence criteria were used, along with an ultrafine integration grid.

Starting point geometries for optimisations of the cationic activated catalyst and the transition states involved in the enchainment of one propylene monomer were provided by ARLANXEO Netherlands B.V.. Analytical frequency calculations were performed in order to verify the minima and transition state geometries, and in order to obtain thermodynamic properties. The geometries of the reactants and products connected to the transition states were obtained by manually displacing the transition state geometry a small distance along the imaginary vibrational mode in either direction, and optimising from there. Although intrinsic reaction coordinate (IRC) calculations are theoretically more accurate than this method, it was found that not all such calculations converged, and where they did, the minima closely matched the energies and geometries of those found by the manual displacement method.

Further optimisations using the PBE geometries as starting points were carried out in order to compare different levels of theory and are described in Section 3.3. Where single point (SP) calculations with either the DFT-D3 correction or PCM were carried out, the SCF energy was taken from the SP calculation and used in conjunction with the thermodynamic corrections from the analytical frequency analysis of the gas-phase structures optimised with the appropriate XC functional.

3.3 Results and Discussion

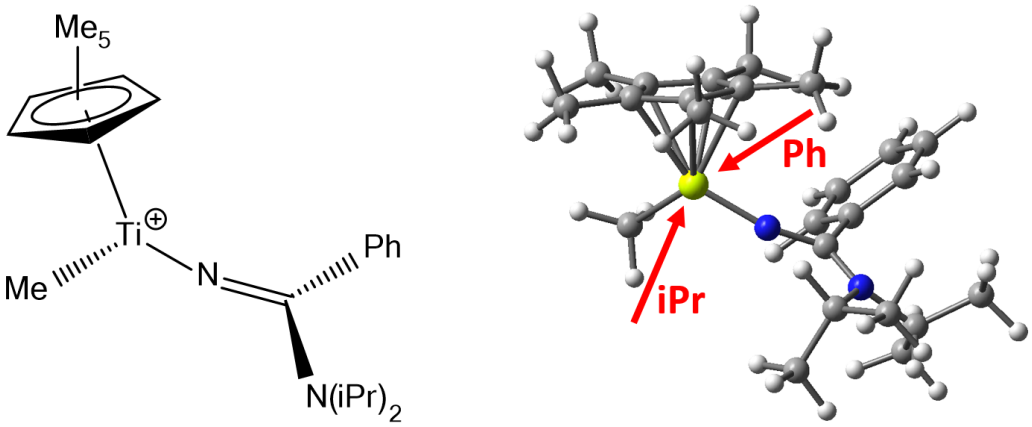

Figure 3.7: Left: schematic showing the structure of the $[MeTiCp^*\{CN(Ph)N(iPr)_2\}]^+$ active catalyst. Right: ball and stick diagram of the active catalyst showing the sides of monomer approach. Ti, C, N, and H atoms are represented by yellow, grey, blue, and white balls, respectively.

The cationic active species employed to study the catalysis of propylene homo-polymerisation is shown in Figure 3.7; this cyclopentadienyl-amidinate titanium catalyst has Cp* and $\{CN(Ph)N(iPr)_2\}$ ancillary ligands. The first polymerisation step begins with this methyl active catalyst shown in Figure 3.7 formed upon activation of the bis-methyl substituted cyclopentadienyl-amidinate titanium pre-catalyst. The propylene monomer may approach the cationic centre from either sides containing the $(iPr)_2$ or Ph components of the $\{CN(Ph)N(iPr)_2\}$ ancillary ligand. These sides of approach are labelled in Figure 3.7 by **iPr** and **Ph**, respectively. The reaction profiles in the following subsections are calculated free of counter-anion. Gibbs free energy barrier to a reaction, $\Delta G^{\ddagger}$, is defined as the total free energy required to overcome the transition state from the lowest energy structure that proceeds it.

3.3.1 The Effect of Changing the XC Functional

The first chain propagation (CP) steps for gas-phase propylene homo-polymerisation from both **Ph** and **iPr** sides of the cationic methyl catalyst as described above were calculated using the PBE XC-functional, the reaction profiles of which are shown in Figure 3.8 (blue

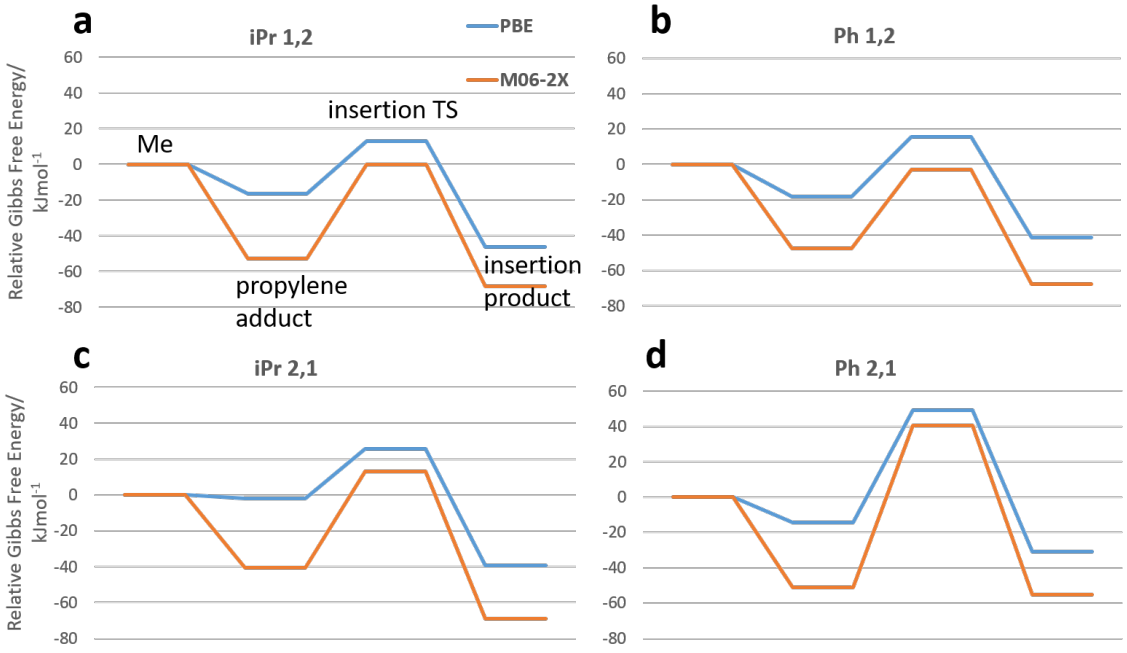

Figure 3.8: Relative Gibbs free energy profiles ($kJmol^{-1}$) for the insertion of propylene into the Ti-Me bond calculated with PBE (blue) and M06-2X (orange) in the gas-phase. The reaction takes place *via* : a) 1,2 insertion from the iPr side; b) 1,2 insertion from the Ph side; c) 2,1 insertion from the iPr side; d) 2,1 insertion from the Ph side. Energies are relative to the active methyl catalyst. Labels are included only for the 1,2 insertion from the iPr side for clarity.

lines). The stationary points along these gas-phase reaction profiles were then re-optimised with M06-2X, in order to test the effect of changing XC functional on profile shape (red lines of Figure 3.8). Note that a detailed analysis of the propagation mechanisms and the stationary points along their reaction profiles is found in Chapter 4, while here a general comparison is made between the results from these two sets of calculations. As previously detailed in Section 1.3.5.3, M06-2X is an meta-hybrid GGA XC-functional developed to model non-covalent interactions and barrier heights better than popular GGA and hybrid functionals. The most notable difference between the results from M06-2X and PBE is the increased stability of between ∼30-40 $kJmol^{-1}$ of the π-complex propylene adducts using M06-2X. This observation can be explained by the better description of the interaction between the C–C π-bond and the Ti centre by the parametrised XC functional, as well as long range intramolecular dispersion interactions, resulting in a lowering of the total energy. While there is also a stabilisation of the TS found using M06-2X compared with using PBE, it is to a lesser extent than the π-complexes, resulting in increased barrier heights for the first CP step *via* all insertion types and sides of propylene approach, as seen in Table 3.1.

Insertion Type	**Side**	$\Delta G^{\ddagger}$**(PBE)**	$\Delta G^{\ddagger}$**(M06-2X)**
1,2 (*re*)	iPr	29.4	52.7
1,2 (*re*)	Ph	33.9	44.7
2,1 (*re*)	iPr	27.5	53.8
2,1 (*re*)	Ph	63.6	91.9

Table 3.1: $\Delta G^{\ddagger}$ (kJmol^{-1}) for the insertion of a propylene monomer into the growing methyl chain calculated using PBE and M06-2X in the gas-phase. Barriers are calculated relative to the monomer adduct preceding each TS.

Not only does the choice of XC functional affect the magnitude of barrier height for these reactions, it also influences the predicted preference of side from which monomer coordination takes place: when employing PBE the barrier to insertion is lower from the side of molecule containing the iPr groups, whereas when M06-2X is used insertion is predicted to occur from the Ph side. Which DFT method provides the "best" description of these systems, however? This question is explored in the next section.

3.3.2 Testing Different DFT Methods

Unfortunately, experimental values of the insertion reaction barriers modelled here are not available for this catalytic system and, as such, a quantitative comparison of results from DFT calculations cannot be made with experiment. We instead compare the reaction barriers of three mechanisms for which an order of rate of reaction may be inferred, namely chain propagation (CP), β-hydride elimination (BHE), and β-hydride transfer to monomer (BHTM). Our sponsors have informed us that this order of rates should follow: $r_{\mathrm{CP}} > r_{\mathrm{BHE}} > r_{\mathrm{BHTM}}$ The first step which must be overcome in the BHE reaction has been computed for this study, and corresponds to β-hydride transfer to Ti (BHTTi).

Table 3.2 lists the different DFT methods employed to compute the structures along the reaction profiles defined above, with the aim to find the best method that describes the system studied. The CP reaction is approximated by the primary insertion of propylene into the cationic isobutyl active catalyst, as this mechanism is expected to be favoured over secondary. The two chain termination reactions, BHTTi and BHTM, are also modelled from the isobutyl catalyst, and the stationary points of these reactions are shown in Figure 3.9.

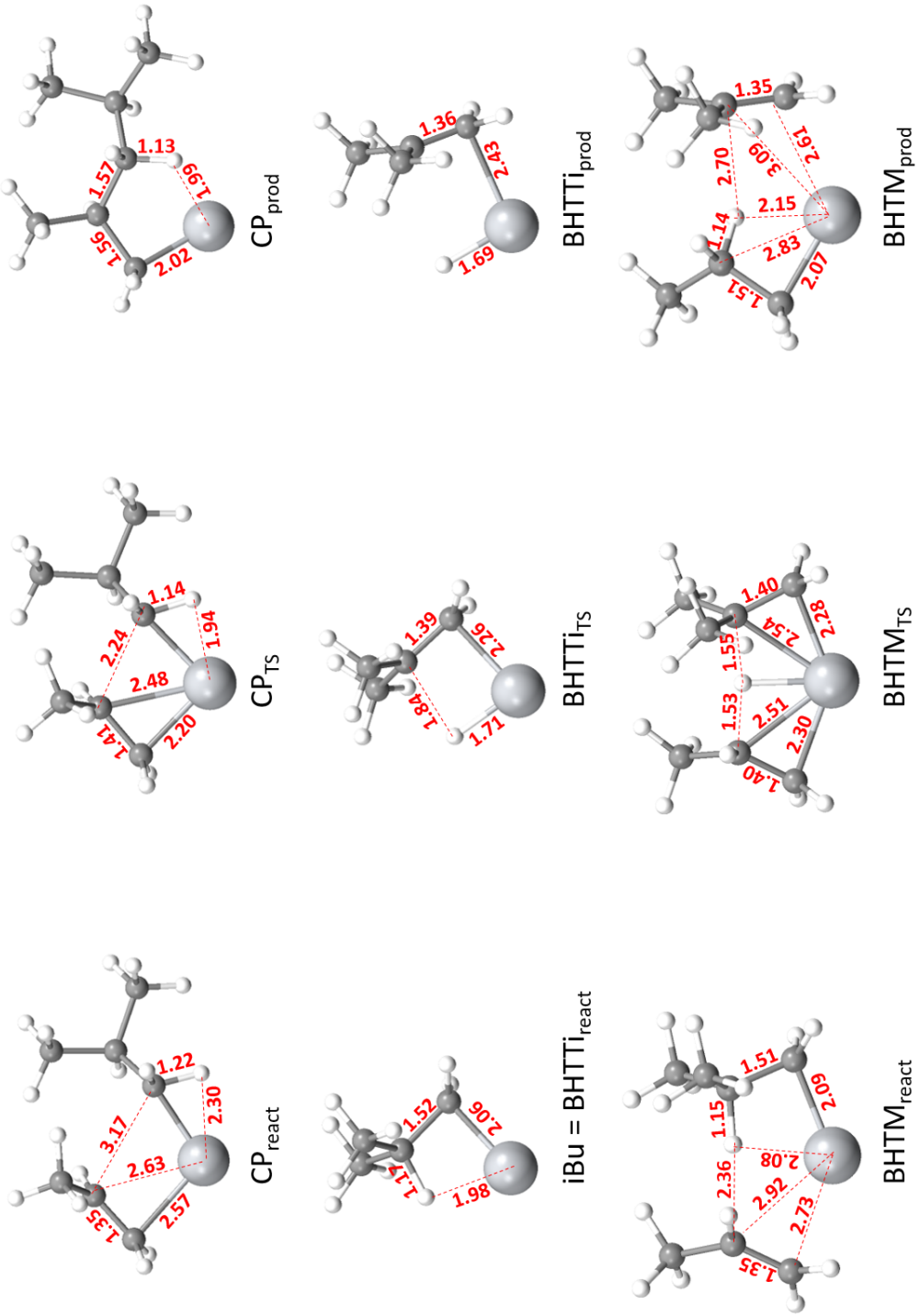

Figure 3.9: Structures of the stationary points along the reaction pathways of CP, BHTTi and BHTM. Ancillary ligands are omitted for clarity. Bond lengths shown are from structures optimised with M06-2X in the gas phase, and are given in Å.

The modelling of dispersion forces in these systems by way of adding a DFT-D3 dispersion correction to the PBE calculations is tested, the advantage of this method over optimising with M06-2X being reduced computational cost. In addition, a PCM of 2,2,4-trimethylpentane is also examined, in order to better mimic experimental conditions. These two modifications to the calculations may be included either in the geometry optimisation step or as a single point calculation (SP) following a gas-phase PBE or M06-2X geometry optimisation, with the SP method being advantageous in terms of reduced computational cost.

XC Functional	DFT-D3	PCM
PBE	-	-
PBE	SP	-
PBE	Opt	-
PBE	SP	SP
PBE	Opt	Opt
PBE	-	SP
PBE	-	Opt
M06-2X	n/a	-
M06-2X	n/a	SP
M06-2X	n/a	Opt

Table 3.2: The different DFT methods tested. Methods in rows 2-10 used the optimised structures from row 1 (PBE, no DFT-D3 correction, gas-phase) as input coordinates.

The rate-constant k of a reaction at a given temperature T may be given by the Eyring equation:

$$k = \frac{k_{\mathrm{B}}T}{h} e^{\frac{-\Delta G^{\ddagger}}{RT}} \tag{3.2}$$

where k_{B} is the Boltzmann constant, h is Planck's constant, $\Delta G^{\ddagger}$ is the Gibbs free energy barrier, or activation energy, and R is the universal gas constant. The reaction barrier heights for the propagation and two chain termination reactions are now compared, where higher barrier heights are approximated to result in lower rate-constants. The barrier heights are thus expected to increase in the reverse order of the rates of reactions defined above, i.e. with CP the lowest, followed by BHE and then BHTM.

Dispersion Corrections in the Gas-Phase

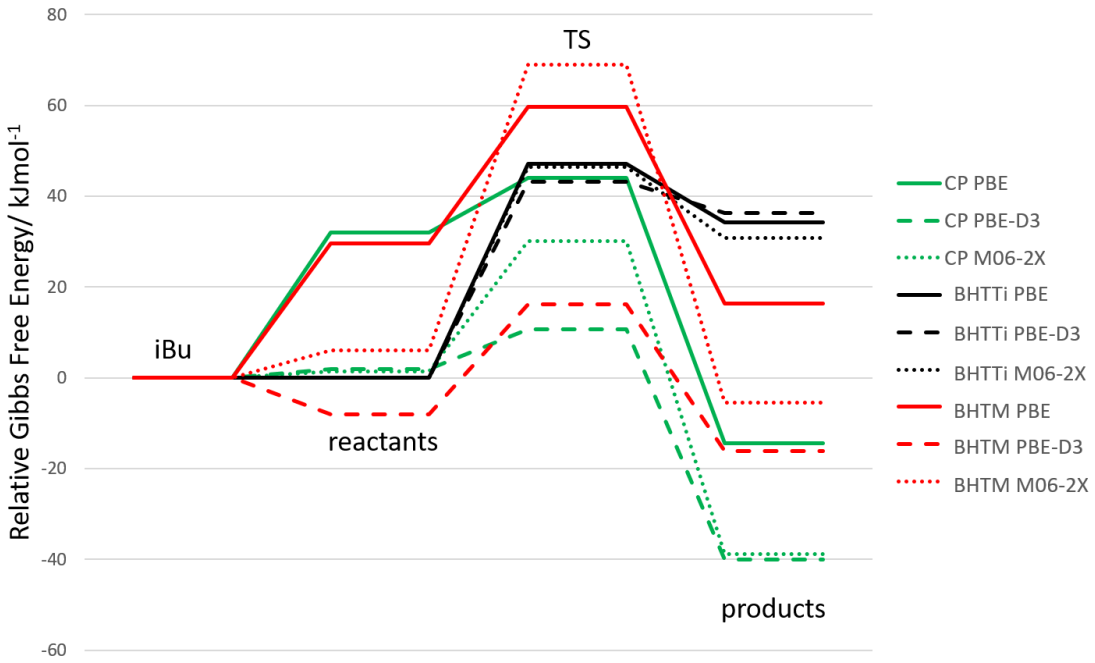

Figure 3.10: Gibbs free energy profiles for the 1,2 insertion of propylene into the Ti-iBu bond from the iPr side (CP), β-hydride transfer to Ti (BHTTi), and β-hydride transfer to monomer (BHTM) calculated with different DFT methods in the gas-phase and at 298 K. Solid lines indicate profiles optimised with PBE; dotted optimised with PBE with a DFT-D3 correction; and dashed with M06-2X.

Figure 3.10 shows the gas-phase reaction profiles for CP and chain termination reactions optimised at room temperature (RT) with and without dispersion corrections. Of note is the difference in profile shape upon changing DFT method for the two bimolecular reactions which involve a monomer, namely CP and BHTM (red and green profiles), indicating that the addition of dispersion corrections results in a change in chemical behaviour of these systems. Inclusion of a dispersion correction lowers the relative free energy of these monomer adducts compared with the "dispersion-free" PBE structures (solid lines). This is also seen for the transition states in these two reactions, excluding transfer to monomer with M06-2X where the TS is higher in relative energy compared to PBE. The DFT-D3 correction appears to reduce the relative free energy of the transfer to monomer TS, so much so that the barrier height for this reaction is reduced to lower than that of BHTTi, resulting in the wrong order of reaction barrier height for this DFT method. Such a large reduction in TS free

energy is not seen for M06-2X, and indeed an increase in TS relative free energy for transfer to monomer is displayed, probably owing to the XC functional's fitting to thermochemical data-sets.

			$\Delta G^{\ddagger}$ (298 K)		
XC Functional	D3	PCM	CP	BHTTi	BHTM
PBE	-	-	43.98	47.15	59.72
PBE	SP	-	11.92	44.23	28.07
PBE	Opt	-	10.73	43.11	24.15
PBE	SP	SP	15.65	44.82	28.43
PBE	Opt	Opt	10.48	47.03	25.59
PBE	-	SP	48.72	47.74	63.32
PBE	-	Opt	43.54	45.07	61.63
M06-2X	-	-	30.17	46.45	68.90
M06-2X	n/a	SP	34.23	47.14	72.16
M06-2X	n/a	Opt	35.09	48.20	71.47

Table 3.3: $\Delta G^{\ddagger}$ (kJmol^{-1}) for CP, BHTTi and BHTM reactions calculated with different DFT methods at 298 K.

For all three methods, the barrier height for BHTTi is fairly constant, as no monomer-Ti interaction needs to be described in the reactant or TS. The relative free energy of the products, which do include a monomer-Ti interaction, are stabilised by about 5kJmol^{-1} if dispersion is included *via* M06-2X, though DFT-D3 does not have this relative energy lowering effect.

Results from Table 3.3 and Figure 3.10 show that, at RT, optimisations with PBE and M06-2X predict the correct order of barrier height for the three reactions studied, while PBE optimisations with the DFT-D3 dispersion correction predict that BHTM should occur more readily than BHTTi. Table 3.3 also shows that, at RT a SP DFT-D3 dispersion correction after a PBE optimisation also predicts the wrong ordering of barrier heights. This DFT-D3 method is therefore not discussed further.

The Effects of a PCM of 2,2,4-trimethylpentane

Experimental research involving our collaborators at ARLANXEO Netherlands B.V. which examined the olefin polymerisation capability of a similar catalytic system[88] used

pentamethylheptane as a solvent. Unfortunately, the PCM implemented in G09 does not have this solvent built-in and the dielectric constant for this particular solvent was not found in the literature or in any available databases. In this instance, from the alkane solvent PCMs available in G09, 2,2,4-trimethylpentane (ϵ=1.9358) was chosen as it contains a similar branching to chain length ratio and the range of alkane solvents available have a narrow range of dielectric constants from 1.8939 (2,4-dimethylpentane) to 2.0402 (n-hexadecane), indicating that a significant change in size of the alkane solvent has only a small effect on the polarising ability.

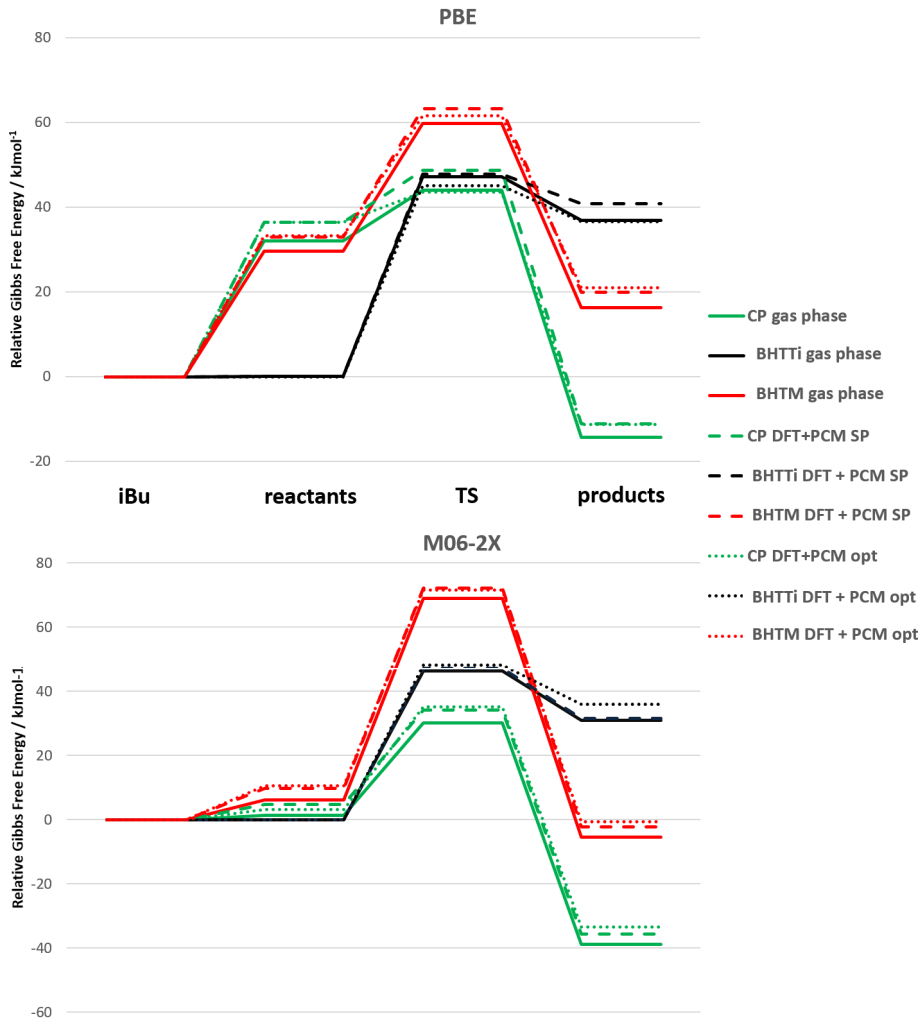

Figure 3.11: A comparison of the Gibbs free energy profiles for CP, BHTTi and BHTM calculated in the gas-phase (solid lines), with a PCM SP after gas-phase optimisation (dashed lines), and optimisation with a PCM (dotted lines), for both PBE and M06-2X XC functionals. The solvent modelled by the PCM is 2,2,4-trimethylpentane.

Figure 3.11 displays a comparison of the CP and chain termination reaction profiles calculated at RT in the gas-phase (solid lines), with a PCM SP (dashed lines) and full optimisation with a PCM (dotted lines) for both PBE and M06-2X. The inclusion of the PCM in either capacity does not affect the relative energies of the structures for either PBE and M06-2X sets of calculations very much, indeed, Table 3.3 shows that the reaction barriers for the three mechanisms vary between only $\sim$1.2-5.8 kJmol^{-1} across all six DFT methods, and inclusion of a solvent model does not affect the ordering in reaction barriers. The smallest of these changes in reaction barriers are for the BHTTi. This result may be expected due to the reaction being unimolecular and not much interference by the solvent cavity is anticipated. The outcome of this test is that absence of a solvent model, as well as either including one as a SP or with full optimisation, give the correct results at RT. For completeness, however, a PCM will be included in calculations moving forward, for which a SP in that PCM following a gas-phase optimisation is expected to produce very similar results to those with an optimisation in the PCM. It is also expected that a PCM will be important in reducing cation-anion interactions, and hence will be necessary in the full ion-pair system.

3.3.3 Temperature Corrections

The surfaces described above are calculated at 298 K, though in order to determine whether the DFT methods tested above predict the correct reaction barrier order at industrially relevant temperatures the surfaces were recalculated with temperature corrections at 363, 373 and 393 K (90, 100 and 120 °C). Values for the temperature corrected reactions barriers for all DFT methods can be found in Appendix A, where is it shown that at higher temperatures PBE with PCM included by both methods discussed above do not predict the expected order of barrier heights. We therefore examine the results of this temperature study just for M06-2X.

Figure 3.12 compares the same reaction profiles calculated employing M06-2X with gas-phase optimisations followed by SPs in the PCM at the four different temperatures. These free energy profiles, and the results in Table 3.4, show that at industrially relevant temperatures the reaction barrier to CP increases to slightly higher than that of BHTTi.

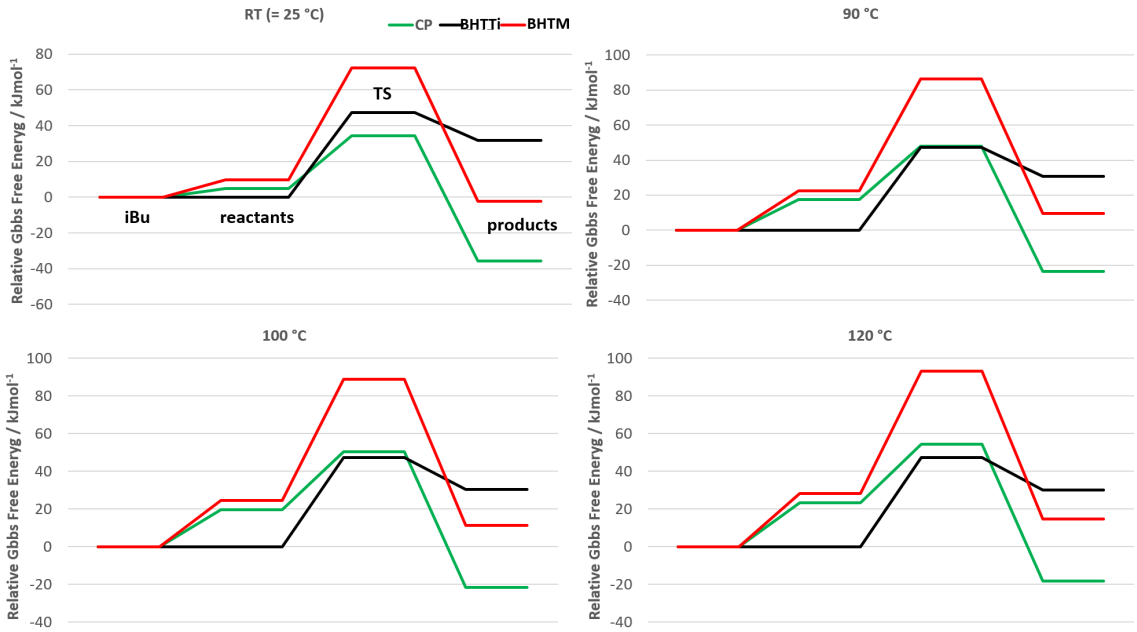

Figure 3.12: Gibbs free energy profiles for CP, BHTTi and BHTM calculated with M06-2X in the gas-phase followed by a PCM SP at 298, 363, 373 and 393 K (25, 90, 100 and 120°C, respectively). Labels along the reactions pathways are only displayed in the RT graph for clarity.

	$\Delta G^{\ddagger}$		
T	CP	BHTTi	BHTM
RT	34.23	47.14	72.16
90	48.05	47.20	86.45
100	50.18	47.21	88.65
120	54.43	47.23	93.02

Table 3.4: $\Delta G^{\ddagger}$ for CP, BHTTi and BHTM calculated with M06-2X in the gas-phase followed by a PCM SP at 298, 363, 373 and 393 K (25, 90, 100 and 120°C, respectively).

The difference in barrier height between CP and BHTTi at elevated temperatures is small however, and the rate constants for these two reactions will therefore have similar values. The rate of reaction r depends on the rate constants by the following relationship,

$$r = k[\mathrm{A}]^n[\mathrm{B}]^m \tag{3.3}$$

where $[\mathrm{A}/\mathrm{B}]$ are the concentrations of reactants A and B, and n and m are the reaction

orders dependent on the reaction mechanism. For BHTTi the rate of reaction depends on only $[\mathrm{catalyst}]$ (i.e. is zeroth order in $[\mathrm{propylene}]$) and may therefore be smaller than that of CP, as the latter is also dependent on $[\mathrm{propylene}]$, which is generally high for polymerisation. It is therefore likely that these reaction barriers at higher temperatures do predict the correct behaviour. Further justification lies in the fact that the barriers to the reverse reaction of BHTTi are very small, whereas CP gives thermodynamically stable products.

3.3.4 Ab initio Benchmarking

Ab initio methods were employed in order for the barrier heights of the three pathways to be compared when calculated using different levels of theory. The structures of the stationary points along the three reaction profiles were stripped down to model systems in order to achieve such results. Figure 3.13 shows the resulting model cation, whereby the Cp* is reduced to Cp, Ph to Me, and iPr to Me.

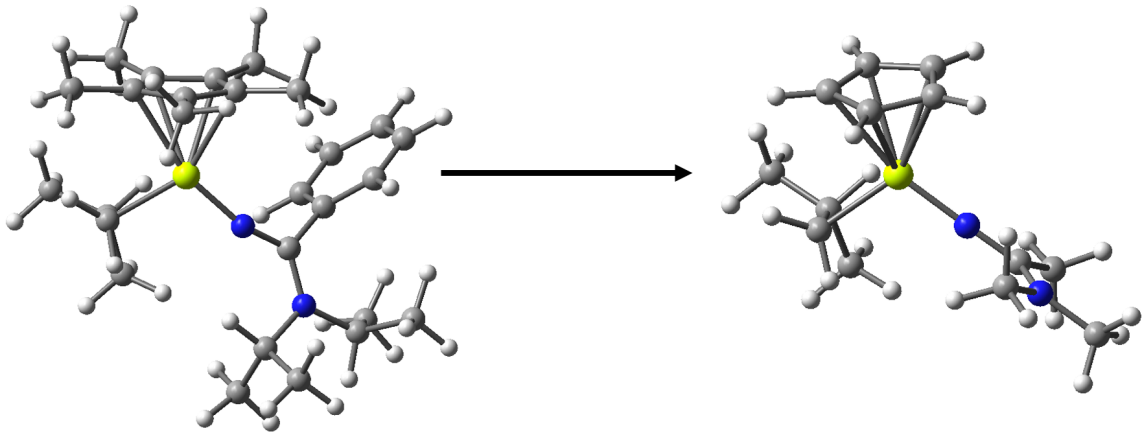

Figure 3.13: Ball and stick diagram showing the real isobutyl catalyst (left) and stripped down model (right).

Using the M06-2X-optimised geometries of the model systems, single point calculations were attempted using HF, MP2, and QCISD with a PCM of 2,2,4-trimethylpentane, cc-pVDZ basis sets for light atoms, and cc-pVTZ for Ti; the thermodynamic corrections from the gas-phase M06-2X vibrational analysis were used in conjunction with the updated electronic energies. Full re-optimisations at the HF level of theory were achievable for CP and BHTTi, however, the BHTM optimisation proceeded towards a Ti–hydride complex with a propylene adduct and isobutylene separated to $\sim$6 Å away. The results from the SP

HF calculations were therefore used to ensure consistency within the results. Unfortunately SPs at a higher level of theory than MP2 (e.g. QCISD) were not feasible owing to SCF convergence failure.

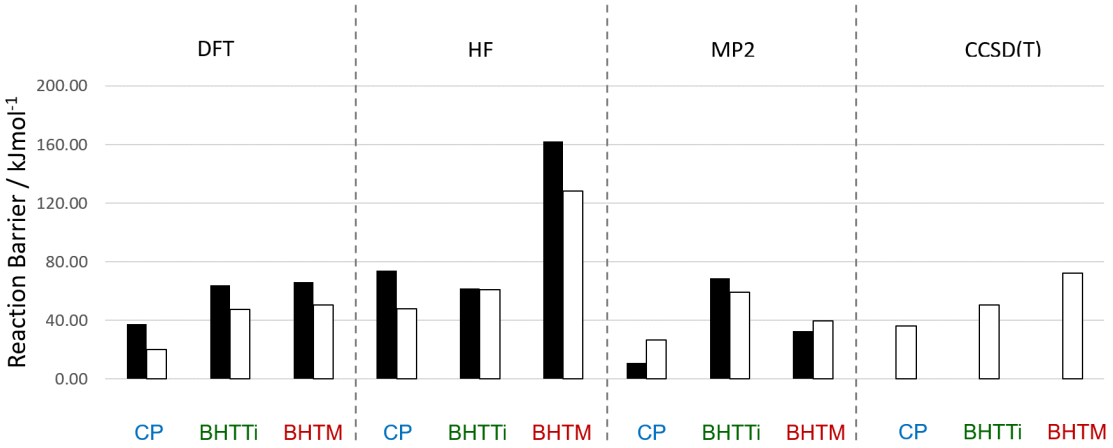

Figure 3.14: Electronic barrier heights for CP, BHTTi and BHTM reactions, calculated with DFT, HF, MP2 and CCSD(T) levels of theory. The black bars correspond to the reaction calculated with the model Ti system shown in Figure 3.13; the white bars correspond to calculations of the reactions with $H_2Si(Cp)_2ZrC_2H_5^+$,[128] where the DFT barriers were calculated using B3LYP; the DFT, HF and MP2 barriers using all electron MIDI basis set of Zr and SVP on light atoms, and CCSD(T) barriers using LANL2DZ on Zr, 6-31G on ligands, and 6-31G(d,p) on reactive groups.

Electronic barrier heights for the model pathways calculated using M06-2X, HF and MP2 levels of theory at 298 K are shown in Figure 3.14 (black bars). Also displayed are the barrier heights for the analogous reactions using $H_2Si(Cp)_2ZrC_2H_5^+$ reported by Talarico *et al.* (white bars), where their DFT results were calculated using B3LYP.[128] At the HF level the barriers to the bimolecular CP and BHTM reactions with the model Ti systems are increased by $\sim$90 kJmol^{-1} and $\sim$150 kJmol^{-1}, respectively, compared to the those calculated with DFT. With the BHTTi barrier relatively unchanged, the order of barrier heights changes to BHTTi $<$ CP $<$ BHTM. The Zr systems from the literature also display increased barriers for the bimolecular reactions at the HF level, but by only $\sim$30 kJmol^{-1} for CP and $\sim$80 kJmol^{-1} for BHTM, resulting in the order of barrier heights to remain CP $<$ BHTTi $<$ BHTM. The large discrepancy between these barrier height increases for the Ti system is likely to be a consequence of the geometry not being optimised at the HF level for the Ti systems, whereas the literature values were verified as stationary points. The fact that the BHTTi barrier is unchanged at the HF for the unoptimised geometries

suggest that the geometry will not differ too much upon optimisation. The bimolecular reaction barriers clearly are affected by the geometries and energies of the reactants and TS containing π-interactions, which are not well represented by HF theory as it does not contain electron correlation required to properly describe this.

At the MP2 level, the barrier heights of the bimolecular reactions with the Ti systems are reduced in comparison to the DFT results and we observe the BHTM reaction predicted over the BHTTi. This change in barrier heights ordering is replicated in the Zr results. MP2 appears to be over-estimating the stabilising effect of the cation-π interactions. The CCSD(T) results from the literature follow the barrier heights order expected for the Ti systems in the present work, and differ by only $\sim$6 kJmol^{-1} with the M06-2X DFT results for the Ti bimolecular results. While it is unfortunate that high level *ab initio* results could not be achieved for our model systems, the agreement of our DFT results with very similar reactions from the literature calculated with CCSD(T) indicates that M06-2X performs well at modelling these kinds of systems. Furthermore, while these benchmarking calculations were being carried out, Ehm *et al.* published extensive XC functional benchmarking against CCSD(T) results for olefin insertion reaction mechanisms and concluded that, for early TM, M06-2X best replicates the thermochemistry for these types systems.[129]

3.3.5 Basis Set Benchmarking

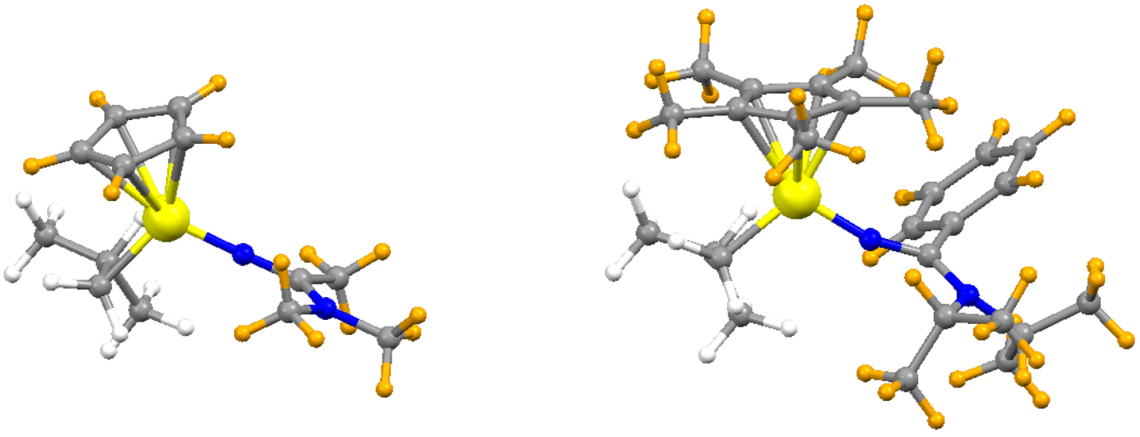

Figure 3.15: Ball and stick diagrams showing the ancillary H atoms in orange of the model (left) and real (right) isobutyl active catalyst. The highlighted atoms are given cc-pVDZ basis sets in entries 1-3 of Table 3.5.

Ehm *et al.* also stated that for geometry optimisation a basis set of at least double zeta quality is sufficient, but that a SP calculation using larger basis sets that include diffuse functions is recommended.[129] SP calculations on the model systems were carried out with increasingly higher quality basis sets going from rows 1 to 4 in Table 3.5. Figure 3.15 shows the H atoms that are considered to be ancillary, i.e. not directly involved in the reaction mechanism, highlighted in orange. In order to reduce computational cost, these atoms are given double zeta basis sets in most cases.

Upon changing the basis set combination from row 1 to 2 the barrier height increases by roughly 4 kJmol^{-1} for the bimolecular CP and BHTM reactions; increasing the quality further has negligible effect on these barriers, i.e. we observe a convergence. The unimolecular BHTTi barrier height appears to be independent of basis set quality, from which we may infer that the description of the monomer adducts is changed when increasing basis set size, and thus the bimolecular reaction barrier heights are only affected. When the same SP calculations were carried out with the real systems, SCF convergence could not be achieved when employing aug-cc-pVTZ basis sets. An increase of between $\sim$2-4 kJmol^{-1} is again seen for CP and BHTM barrier heights when improving the basis set combination from row 5 to 6, with negligible change for BHTTi. We may be able to infer, however, that a convergence of barrier height size beyond the basis set combination of cc-pVTZ on all atoms except ancillary H is expected, and can therefore be confident in employing this basis set combination for further calculations.

	$\Delta G^{\ddagger}$ **(298 K)**			$\Delta G^{\ddagger}$ **(363 K)**			$\Delta G^{\ddagger}$ **(393 K)**		
Basis set combination	**CP**	**BHTTi**	**BHTM**	**CP**	**BHTTi**	**BHTM**	**CP**	**BHTTi**	**BHTM**
Model: Ti=TZ; C/N/H=DZ	42.3	50.3	66.2	48.1	49.9	79.4	53.8	49.7	85.5
Model: TZ; ancillary H=DZ	46.0	50.0	70.0	52.4	49.5	83.3	58.1	49.4	89.4
Model: augTZ; ancillary H=DZ	45.9	50.1	71.0	52.6	49.7	84.2	58.3	49.5	89.6
Model: augTZ	45.9	50.2	70.3	53.2	49.8	83.5	58.9	49.6	90.3
Real: Ti=TZ; C/N/H=DZ	34.2	47.1	72.2	48.0	47.2	86.5	54.4	47.2	93.0
Real: TZ; ancillary H=DZ	38.3	46.8	74.2	52.1	46.9	88.5	58.6	46.9	95.1
Real: augTZ; ancillary H=DZ					*a*				
Real: augTZ					*a*				

Table 3.5: $\Delta G^{\ddagger}$ for CP, BHTTi and BHTM calculated using SP of different basis sets and a PCM of 2,2,4-trimethylpentane in conjunction with thermodynamic corrections at 298, 363 and 393 K, from gas-phase optimisations. Ancillary H are those considered to not be involved in the reaction and are indicated by orange atoms in Figure 3.15. [a] SCF convergence could not be achieved for these SP calculations.

3.3.6 Dissociation of BHTTi products to BHE products

As the temperature of the reaction is elevated to 363 K, BHTTi becomes kinetically favourable over CP by ∼5 kJmol^{-1}, as shown in row 6 of Table 3.5. This might suggest that for our cationic catalytic system polymerisation is unlikely to occur at industrially relevant temperatures. However, the relatively small barrier to the reverse reaction of BHTTi, in comparison with the forward direction (17.2 *vs.* 46.8 kJmol^{-1} at 298 K) indicates that the re-formation of the β-agostic isobutyl active catalyst from the BHTTi product is both kinetically and thermodynamically viable, although this reverse reaction may be inhibited by the dissociation of the BHTTi products to free isobutylene and the catalyst-hydride species for a complete BHE reaction. Lohrenz *at al.* reported electronic and free energy barriers of 111.5 kJmol^{-1} and 69.8kJmol^{-1}, respectively, for the dissociation of the isobutylene monomer from the zirconocene-hydride cation, concluding that chain termination *via* BHE is unlikely.[130]

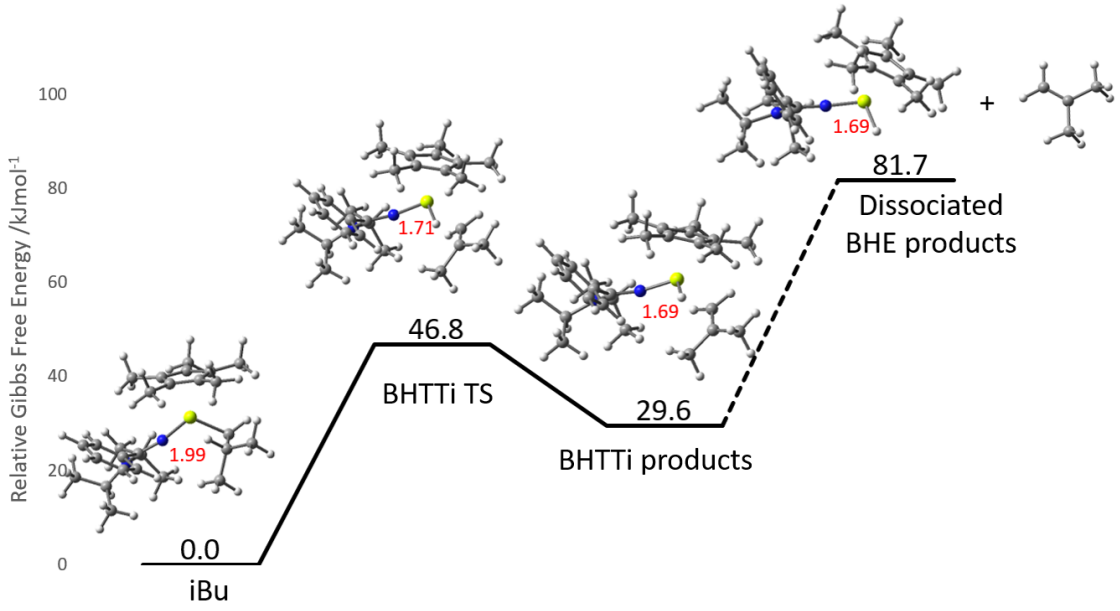

Figure 3.16: Gibbs free energy profile (298 K) showing the BHE reaction pathway ending in dissociation of the BHTTi products. Bond distance indicated in red correspond to the Ti–H$_\alpha$ agostic interaction in **iBu** and Ti–hydride in subsequent structures along the reaction pathway. Stationary points along the reaction profile were located using M06-2X in the gas-phase, followed by a SP with a PCM of 2,2,4-trimethylpentane, cc-pVTZ on all atoms except ancillary H, which had cc-pVDZ basis sets.

The dissociated products of BHE of the isobutyl cation studied in the present work were computed, the structures of which are displayed in Figure 3.16. An electronic barrier of

113.9 kJmol^{-1} is found between the Ti-hydride isobutylene π-complex (BHTTi products) and dissociated species (BHE products) at 298 K, in very good agreement with the literature value above. The Gibbs free energy barrier of 52.1 kJmol^{-1} is lower that the value reported by Lohrenz *et al.*, however these dissociated products lie 81.7 kJmol^{-1} higher in Gibbs free energy than the starting catalyst-isobutyl complex at 298 K, and 68.6 and 62.6 kJmol^{-1} higher at 363 and 393 K, respectively. Table 3.6 shows that at these elevated temperatures the barrier to CP remains lower than the free energy of the dissociated BHE products, indicating that CP *is* kinetically favourable over BHE and polymerisation is predicted.

T/ K	CP	BHTTi	Dissociated BHE products
298	38.4	46.8	81.7
363	52.2	46.8	68.6
393	58.6	46.9	62.6

Table 3.6: $\Delta G^{\ddagger}$ (kJmol^{-1}) for CP, BHTTi, and the Gibbs energy of the dissociated BHE products relative to the isobutyl catalyst starting structure.

3.4 Summary

The barrier heights of the CP and two dominant chain termination reactions, BHTTi and BHTM, calculated using different XC functionals, methods of incorporating dispersion, and solvent effects were compared in order to determine the method which best describes the TiCp*{CN(Ph)N(iPr)$_2$}iBu$^+$ catalytic system. The barrier heights for these reactions are expected to increase in the following order $\Delta G^{\ddagger}_{\mathrm{CP}} < \Delta G^{\ddagger}_{\mathrm{BHE}} < \Delta G^{\ddagger}_{\mathrm{BHTM}}$. Before BHE may occur BHTTi must take place, the barrier of which was calculated for this benchmarking study.

Gas-phase optimisations of the stationary points along these reaction profiles using M06-2X followed by a SP with a PCM of 2,2,4-trimethylpentane best predicts this barrier height ordering, however at temperatures above 373 K the reaction barrier to BHTTi is lower than that to CP.

Ab initio calculations of model systems at both the HF and MP2 levels of theory produced an incorrect ordering of barriers, however, our DFT results agree very well with barrier heights of analogous reactions of $H_2Si(Cp)_2ZrC_2H_5^+$ calculated with CCSD(T), indicating that M06-2X does perform well at describing reactions related to olefin polymerisation. A benchmarking study carried out by Ehm *et al.* confirm this conclusion but also recommend the use of basis sets that include diffuse functions in a SP calculation following optimisation using lower quality basis sets in order to produce accurate thermochemical predictions.

Basis set benchmarking on the model systems show that inclusion of the diffuse functions do not significantly alter the barrier heights of the reactions, and that a convergence is seen beyond using cc-pVTZ basis sets on all atoms except ancillary H atoms, which are given cc-pVDZ basis sets. While SP calculations for the real systems with aug-cc-pVTZ on any of the atoms could not be achieved, an increase in barrier height comparable to that observed for the model systems is seen upon increasing the basis sets from cc-pVDZ to cc-pVTZ on all atoms except ancillary H, and convergence is also

predicted beyond this basis set quality.

The barrier height for BHTTi remains competitive with CP at elevated temperatures upon inclusion of all this methodology. The relative free energy of the separated BHE products is higher than the barrier to CP, however, indicating that the reverse reaction of BHTTi back to the starting isobutyl catalyst followed by CP is kinetically favourable over the full BHE mechanism. This assertion confirms the suitability of the methodology to the systems studied, and all subsequent calculations on the real systems will be carried out as follows:

1. Gas-phase optimisation using M06-2X XC-functional, and employing
    - cc-pVTZ basis set on Ti
    - cc-pVDZ basis sets on light elements
2. SP calculation incorporating a 2,2,4-trimethylpentane solvent *via* a PCM, and employing
    - cc-pVTZ basis sets on all atoms, except . . .
    - cc-pVDZ basis set on auxiliary H atoms, i.e. those not on the monomer or growing alkyl chain.

Chapter 4

Ion-Pair Calculations of Ethylene and Propylene Homopolymerisation

4.1 Introduction

This chapter examines the role of the counter anion in homopolymerisation studies of ethylene and propylene. A review of the literature indicates that there are limited reports of ion-pair calculations for propylene polymerisation. Indeed, an in-depth study of the effects of $[BF_{20}]^-$ on hompolymerisation of propylene has yet to be published. Advancements in modern computing are such that calculations of these magnitude have only recently been affordable.

4.1.1 The Role of Ion-Pairs in Homogeneous Olefin Polymerisation

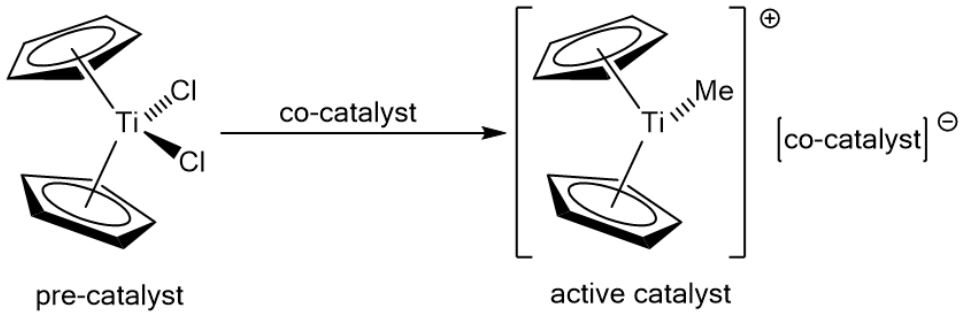

Scheme 4.1: Pre-catalyst activation.

The polymerisation of olefins may occur only if an active site is vacant to allow for monomer coordination. Activation of the pre-catalyst by a co-catalyst must first take place

in order for the active site to become available (see Scheme 4.1). Upon activation a cation-anion pair (henceforth denoted ion-pair) is formed, and it is the interaction between the two counterparts that is fundamental to the activity and stability of the catalytic system. Sinn and Kaminsky's discovery of combining $AlMe_3$ (TMA) and water with $ZrCl_2Cp_2$ as a method to produce polyethylene initiated the explosion of interest in metallocenes, and the activity of this mixture was attributed to the formation of the MAO^- co-anion.[77,78] While MAO-based co-catalysts are popular in Ziegler-Natta catalysis, their drawbacks include poor long-term stability in the solution phase, low solubility in organic solvents required for the catalytic set-up, and the high ratio of Al:M required for reasonable activity (for homogeneous catalysis ratios of $10^3 : 1$ may be needed).[112] The latter problem also leads to large quantities of Al in the resulting polymer, which, depending of the product's use, may be undesirable. In addition, the structure of the oligomeric MAO species is still unknown, and in solution many different aggregation numbers and structures may exist in equilibrium, resulting in uncertainty in characterisation of structures in mechanistic studies.[131–140] Indeed, the computational modelling of MAO-activated olefin polymerisation is non-trivial for this reason. A detailed review of computational studies by Zurek and Ziegler concluded that cage structures consisting of square and hexagonal faces such as that shown in Figure 4.1**a** are more realistic than cyclic, linear, and sheet MAOs, and should be utilised when carrying out olefin polymerisation studies.[141] More recent theoretical studies have indicated how associated TMA oligomers are also important in activating the MAO towards aiding polymerisation, further complicating models of reactions using this co-catalyst.[142,143]

Attention turned to stoichiometric co-catalysts that could easily be characterised, with Marks *et al.* using tris(pentafluorophenyl)borane ("BF_{15}") to activate Group 4 metallocene precatalysts for olefin polymerisation.[144] This strong Lewis acid reacts with a bismethyl pre-catalyst to form a $[\text{catalyst}]^+[MeBF_{15}]^-$ zwitterion-like molecule with a methyl bridge - See Figure 4.1**b**. The coordination of the borane co-anion to the cationic catalyst can be stronger than $[MAO]^-$, however, and has been shown to have significant energies of interaction, which could lead to inhibition of polymerisation.[133,146]

An alternative stoichiometric method is to abstract an R group from the pre-catalyst using the tetrakis(pentafluorophenyl)borate anion ($[BF_{20}]^-$) coupled with the trityl cation

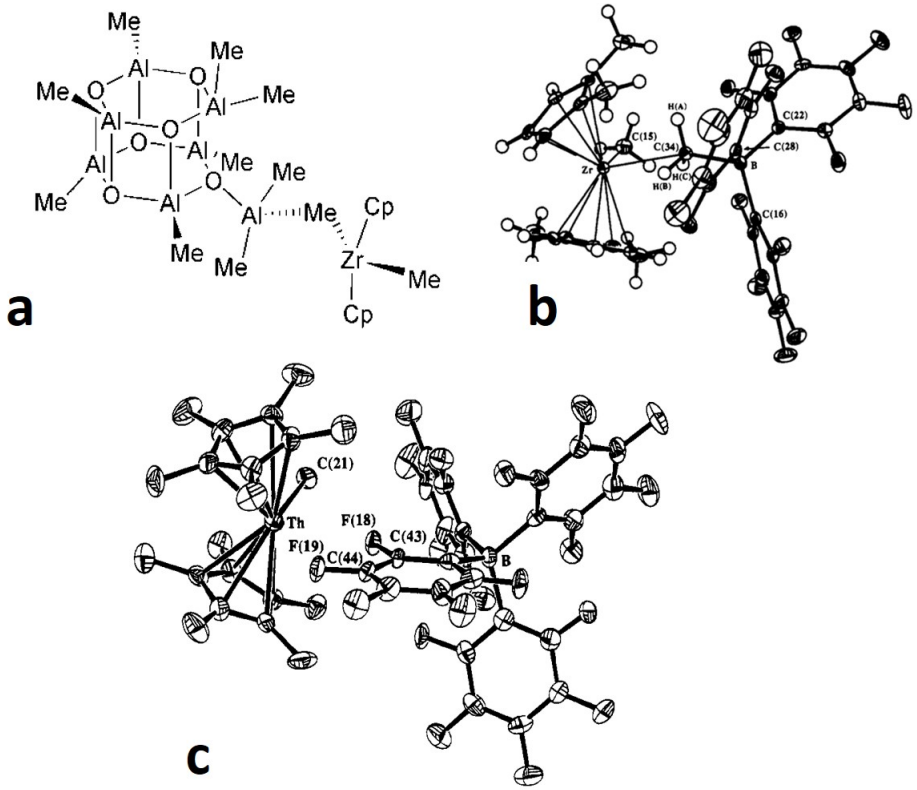

Figure 4.1: Structures of catalytic ion-pairs containing (**a**) $[MAO]^-$-based,[140] (**b**) $[MeBF_{15}]^-$,[144] and (**c**) $[BF_{20}]^-$[145] co-catalysts.

$[Ph_3C]^+$ to give Ph_3CR and a non-coordinating $[BF_{20}]^-$, resulting in an ion-pair such as that shown in Figure 4.1**c**.[147] In some cases the $[BF_{20}]^-$ anion has been shown to be so "non-coordinating" that a solvent molecule preferentially binds to the vacant site.[148–150] Utilising this approach yields very active catalysts for polymerisation,[133] although polymerisation reactions with this ion-pair are more difficult to model than with $[MeBF_{15}]^-$. This is due to the coordination geometry of the two components being hard to define, as compared to the highly directional interaction found in the borane ion-pairs. A number of orientations and/or positions of the cation and anion are reported both experimentally and theoretically for those containing the borate.[151–153] A molecular dynamics study carried out by Correa *et al.* found oscillation between two inner-sphere geometries of the ion-pair $[Me_2Si(Cp)_2ZrMe]^+[BF_{20}]^-$ that differ by the coordination of F atoms to the central Zr cation.[118] Peaks in the distribution functions of Zr-B, Zr-F1 and Zr-F2 distances (see Figure 4.2 for atom labelling) correspond to the two lowest energy orientations where either

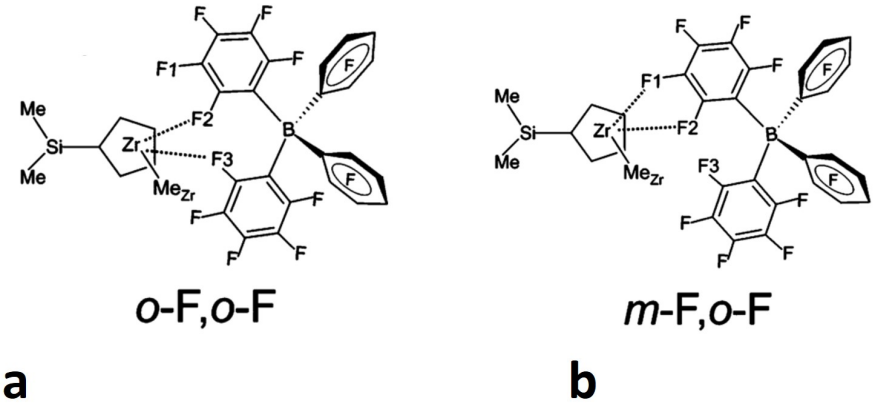

Figure 4.2: Ion-pair geometries of $[Me_2Si(Cp)_2ZrMe]^+[BF_{20}]^-$. Key geometric parameters in **a** are Zr–F1∼4.5Å, Zr–F2∼2.7Å, and Zr–F3∼2.7Å; key geometric parameters in **b** are Zr–F1∼2.7Å, Zr–F2∼2.7Å, and Zr–F3∼4.5Å.[118]

two *ortho*-positioned F atoms of different perfluorophenyl rings have short Zr-F distances (Figure 4.2**a**), and of coordination *via* both *ortho*- and *meta*-F atoms on one ring (Figure 4.2**b**). The free energy of the barrier between these two structures is only 1 kcalmol^{-1}, however, and illustrates just how flat the potential surface for anion coordination may be.

A recent study by Laine *et al*. investigated the lowest energy ion-pair structures of $[Cp_2ZrMe]^+[BF_{20}]^-$, and two bulky *ansa*-zirconocenes (Figure 4.3) and found that the simple zirconocene forms only an inner-sphere ion-pair, whereas the *ansa*- analogues additionally form outer-sphere pairs.[154] The outer-sphere ion-pairs correspond to the anion coordinating without a direct interaction to the metal centre, but instead from behind the ancillary ligands, which is made possible by the stabilisation of the cation by one of the polyaromatic rings of the bridged ligands on *ansa*-metallocenes bending towards the metal centre and forming an interaction between both the five- and six-membered rings and the Zr centre.[155] In the case of the Cp ligands, this cation stabilisation cannot occur, thus only the inner-sphere ion-pair may be found. The inner-sphere ion-pairs were calculated to be between 56-76 kJmol^{-1} more stable than their outer-sphere counter-parts, and their subsequent polymerisation studies begin from these lowest energy inner-sphere pairs.

The $[BF_{20}]^-$ anion forms an ion-pair with the κ^1-amidinate cationic catalyst, and its effect on the polymerisation and chain termination pathways is investigated in Section 4.3 of this Chapter. To the best of our knowledge no previous studies of such anion effects have

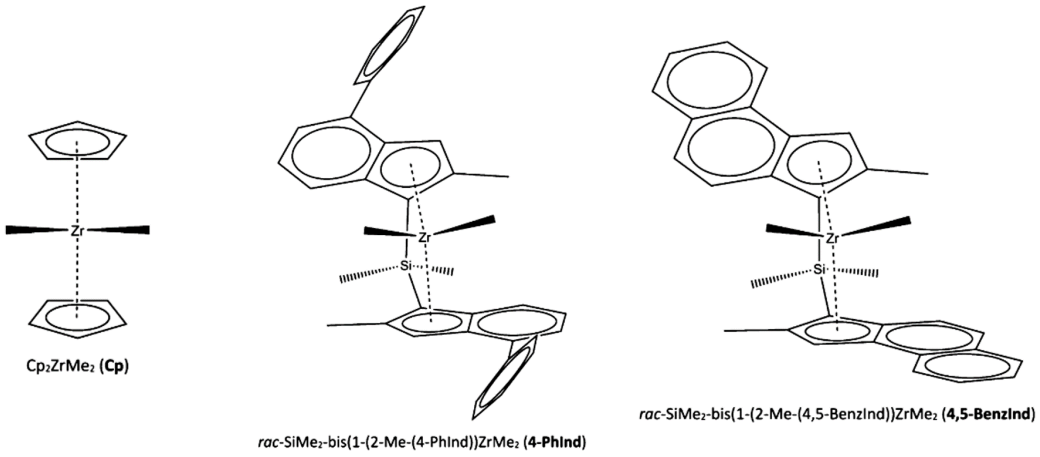

Figure 4.3: The cationic components of the ion-pairs studied by Laine *et al.*.[154]

been reported for the post-metallocene catalysts.

4.1.2 Olefin Complexation

Following activation of the pre-catalyst by the counter-anion, the next step in the polymerisation process is coordination of the olefin to the vacant site on the metal centre. Typically, binding of olefins to transition metal centres is explained in terms of the Dewar-Chatt-Duncanson model, as shown in Figure 4.4. The bonding in this model has two synergistic components: a σ-type forward donation of electron density from the π orbital on the olefin to an empty metal *d* orbital; and a π-type back-donation from a filled metal *d* orbital to the empty olefin π^* orbital. In the case of group IV metallocene-based catalysts however, the d^0 metal centres cannot participate in the back-bonding, and only the forward donation may take place.

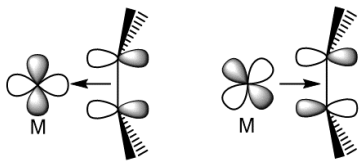

Figure 4.4: Dewar-Chatt-Duncanson model of bonding in metal-olefin complexes.

Electronic olefin binding energies to naked cationic group IV metallocenes and constrained geometry catalysts containing a methyl growing chain have been reported

in the range of ∼30-180 kJmol^{-1}, with large discrepancies between energies calculated with different methods.[114] This coordination is also broadly accepted to be barrierless. Inclusion of electron correlation in the employed theoretical method generally increases the binding energies relative to those which neglect it, an example being the complexation of ethylene to $(SiH_2Cp_2)ZrCH_3$ reported as 80 *vs.* 120 kJmol^{-1} when calculated with HF and QCISD, respectively.[106] The formation of olefin complexes reduces in exergonicity upon increasing the growing polymer chain from methyl to propyl, owing to the required disruption of stabilising agostic interactions.[114] More recent calculations taking thermodynamic corrections into account indicate that while the coordination of a first α-olefin (ethylene, propylene, 1-butene, 1-hexene) to zirconocene and hafnocene is between ∼20-40 kJmol^{-1} exergonic in terms of Gibbs free energy, the second coordination is in fact endergonic, and may involve a barrier to coordination.[124]

Inclusion of the counter-ion in polymerisation studies alters the energetics of olefin complexation somewhat. In order for the olefin monomer to coordinate to the metal centre, the strongly bound inner-sphere ion-pair must be disrupted and the anion displaced to the outer-sphere, as shown in Figure 4.5. The olefin monomer may approach the metal centre from two different directions, labelled *front* and *back*. The *front* approach is also referred to as *cis* approach, as the monomer coordinates *cis* to the anion. The *back* approach is similarly also referred to as *trans* approach. Nifant'ev *et al.* reported Gibbs free energy barriers from *front* ethylene coordination by anion-displacement to β-agostic $[Cp_2ZrEt]^+$ with $[BF_{20}]^-$ and $[MeBF_{15}]^-$ counter-ions of 44 and 91 kJmol^{-1}, respectively. The more nucleophilic $[MeBF_{15}]^-$ anion is harder to displace than $[BF_{20}]^-$. These barriers are greater than the barriers to insertion of the monomer into the Ti–Et bond of ∼10 kJmol^{-1}, indicating that anion displacement is the rate limiting step in this instance. Further discussion of the anion-displacement by incoming monomers may be found in Section 4.1.4.

4.1.3 Agostic Interactions in Olefin Polymerisation

It was shown in Chapter 3 that agostic interactions play an important role in both chain propagation and termination reactions. The term *agostic interaction* was coined by Brookhart and Green in the 1980s and was defined to be describe "the various manifestations

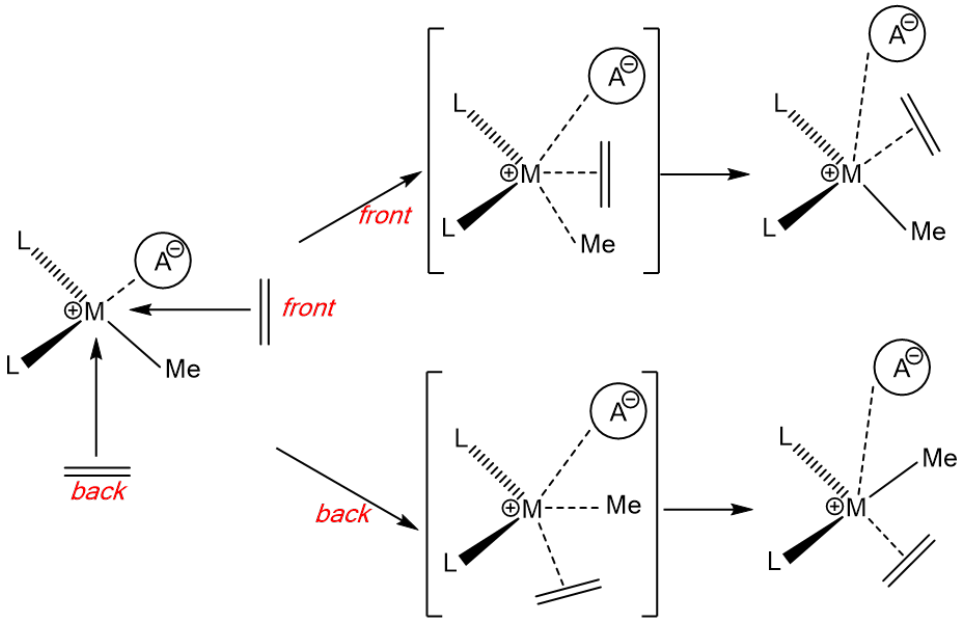

Figure 4.5: Representation of the front and back olefin monomer approaches, and the corresponding anion displacement transition state.

of covalent interactions between carbon-hydrogen groups and transition metal centres in organometallic compounds... in which the hydrogen atom is simultaneously bonded to both a carbon atom and a transition metal atom".[104] It is regularly referred to as a 3-centre–2-electron M–H–C interaction, and the history of its discovery and subsequent explosion of interest is described in two comprehensive reviews by Scherer *et al.*,[105] and Brookhart and co-workers.[108] The exact nature and origin of such interactions are a matter of debate, however an account of this area of discussion is beyond the scope of the present work.[105,108,156–159] Brookhart *et al.* have, however, outlined geometric parameters indicative of agostic interactions and are as follows:

- M—H distance of between 1.8–2.3 Å
- ∠M-H-C angle of between 90–140°

In terms of characterising an agostic bond from an experimental point of view, low $^{1}J_{\mathrm{CH}}$ coupling values of around 50–100 Hz and chemical shifts between -5 and -15 ppm, corresponding to an upfield shift relative to an uncoordinated CH moiety, are expected from ^{1}H NMR spectroscopic studies, in addition to low $\nu_{\mathrm{C-H}}$ vibrational frequencies between 2700–2300 cm^{-1}.[108]

The role of the α-agostic interaction in chain propagation of olefin polymerisation by Ziegler-Natta catalysis was observed in independent studies by Krauledat and Brintzinger, and Piers and Bercaw.[160,161] Both groups observed kinetic isotope effects of $\frac{k_H}{k_D}$ $\sim$1.3 for the polymerisation of an α-olefin catalysed by a $[Cp_2ZrR]^+$ centre, implying the presence of an α-agostic interaction in the TS for insertion. This is in agreement with the modified Cossee-Arlman and modified Green-Rooney mechanisms outlined in Chapter 3, Section 3.1.4. As described there, theoretical studies of olefin polymerisation support the experimental observation of an α-agostic assisted TS.

4.1.4 Ethylene Homopolymerisation

Early theoretical studies of olefin polymerisation catalysed by metallocene-based systems with and without a counter-ion focused on ethylene homopolymerisation, as the mechanism is relatively simple, lacking the stereo- and regio-chemistry involved in propylene polymerisation (see reference 114 and references therein). Experimentally observed barriers to ethylene polymerisation have been reported in the range of 0-$\sim$60 kJmol^{-1}, however it has been suggested that caution should be used in drawing comparisons with experimental data, as "seemingly insignificant changes in the reaction medium perturb the observed polymeric properties".[114] In terms of theoretical barrier heights to ethylene insertion, a mixture of electronic energies and those taking thermodynamic corrections into account have been reported, with the latter falling within the range 5-50 kJmol^{-1}.[107,114,120,124,125,128,133,140,141,143,151,153,162–167]

There is a general consensus that the inclusion of a counter-ion results in endergonic uptake of ethylene. Nifant'ev *et al.* showed that as the nucleophilicity of the anion increases from $[BF_{20}]^-$ to $[MeBF_{15}]^-$ the whole reaction profile for *front* ethylene coordination and insertion is driven to higher free energies, with greater anion-displacement barriers, as shown in Figure 4.6.[151] Transition states for anion-displacement by coordination of an incoming ethylene monomer have been reported for ion-pairs containing MAO based anions,[143] $[MeBF_{15}]^-$,[151,153,162] and $[BF_{20}]^-$,[151,152,154] and range between 7-131 kJmol^{-1}. For models containing the $[BF_{20}]^-$ anion, these barriers fall within 44-131 kJmol^{-1}. Regardless of counter-ion, the *front* direction of approach has a lower barrier to monomer coordination

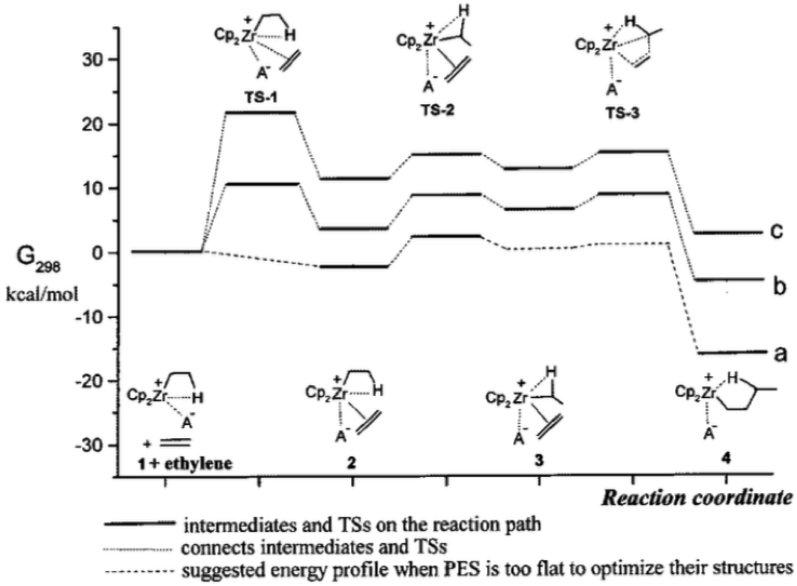

Figure 4.6: Gibbs free energy profiles for the polymerisation of ethylene by $[Cp_2ZrEt]^+$ in the presence of $[MeBF_{15}]^-$ (c), $[BF_{20}]^-$ (b) and no anion (a).[151]

than *back*, rationalised by the *back* approach requiring the growing polymer chain to be pushed towards the site to which the anion is coordinated, causing steric congestion. Laine *et al.* showed that upon increasing the size of the electron-rich *ansa*-ligand the $[BF_{20}]^-$ displacement barriers increase from both directions, justified by the increasing spatial demand of the ligands inhibiting the approach of the monomer.[154]

The effects of solvation on ion-pair interactions have also been studied. Lanza *et al.* concluded that the ion-pair separation energy of a Ti constrained-geometry catalyst with $[BF_{20}]^-$ are reduced on inclusion of a solvent model, and that a greater reduction is observed upon increasing the dielectric constant of the solvent from (gas-phase to) benzene, chlorobenzene, to dichloromethane.[162] An analogous effect was also observed in $[Cp_2ZrR]^+$-$[MAO]^-$ systems calculated in the gas-phase, and with models of n-hexane and toluene.[143] While toluene systematically stabilised the intermediates of the zirconocene and *ansa*-derivatives with $[BF_{20}]^-$, Laine *et al.* found little effect on the relative stabilites of such structures.[154]

Nifant'ev *et al.* showed that for the $[Cp_2ZrEt]^+$-$[MeBF_{15}]^-$ system the coordination of an ethylene monomer can either be such that the C=C bond is orientated in, or deviate

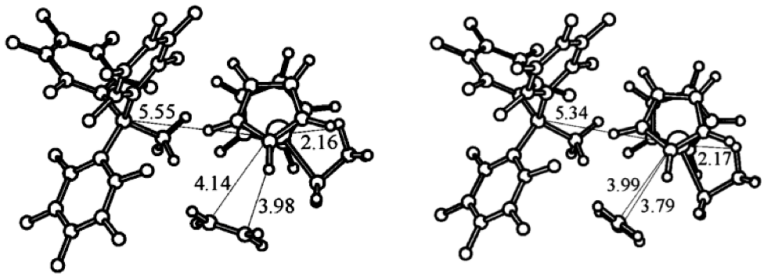

Figure 4.7: The orienatation of the ethylene monomer in their "normal" and "perpendicular" coordinations.[151]

slightly from, the plane in which the 4-centre transition state resides, or perpendicular, or nearly perpendicular, to it.[151] These different ethylene adducts are presented as "normal" and "perpendicular" in the left and right of Figure 4.7, respectively. The perpendicular adduct was shown to be 10 kJmol^{-1} more stable than the normal adduct, and in fact the anion displacement TS to the "perpendicular" adduct is $\sim$30 kJmol^{-1} lower than that of the "normal". The authors' earlier study on the naked cationic zirconocene system, however, reported that the "perpendicular" adduct is $\sim$7 kJmol^{-1} less stable than the "normal" complex.[168] Studies of a set of naked hafnocenes containing different ancillary ligands showed that out of 54 systems, 43 display a preference for the perpendicular adduct, though the relative energies differ by an average of only 2.8 kJmol^{-1}.[166] Rotation of the ethylene in its perpendicular coordination geometry into the plane containing the Ti and α carbon atom of the growing polymer chain is required before insertion may take place, and was estimated to have a barrier of $\sim$15 kJmol^{-1} by Nifant'ev *et al.*.[151]

4.1.5 Propylene Homopolymerisation

As discussed in Chapter 3, four regio- and stereochemical possibilities exist for the coordination of propylene to a methyl catalyst, and are shown in Figure 3.6 of Chapter 3 (page 60). Figure 4.8 shows that different permutations of 1,2 and 2,1 insertions *via* the different *re* and *si* faces of the monomer result in varying tacticities of the polymer produced, and the control of such regio- and stereoregularity by the catalyst has been an area of great interest and reviewed extensively.[111,114,169–171] As described in Section 3.1.2, the high stereoselectivity of the original heterogeneous Ziegler-Natta catalyst has been attributed to

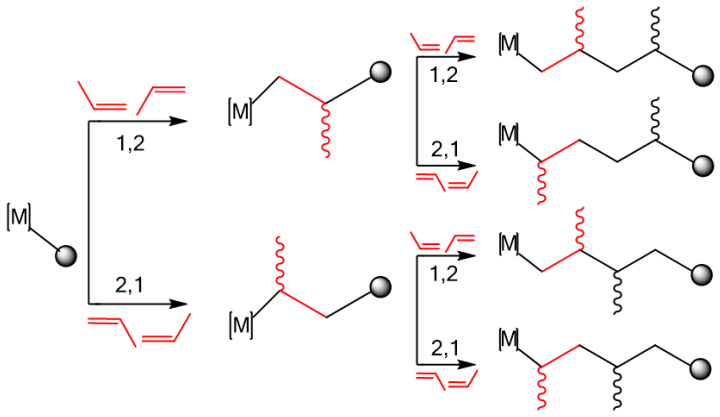

Figure 4.8: Stereo- and regiochemistry of the growing polypropylene chain after two chain propagation steps *via* different insertion mechanisms.

the propylene monomer coordinating *via* the face which minimises the unfavourable steric interactions between the growing polymer chain and the propylene methyl group. This type of stereoselectivity is denoted *chain end control*, while stereoselectivity can also be achieved by chirality at the active site; *enantiomorphic site control*. Excellent examples of catalysts displaying enantiomorphic site control are the C_2- and C_s- symmetric *ansa*-metallocene catalysts, structures **3.2** and **3.3** (Chapter 3, page 55), producing highly isotactic and syndiotactic polypropylenes, respectively. It is generally accepted that metallocene-based catalysts are regiospecific towards 1,2 insertion.[111,112] The mechanisms for propylene polymerisation on inclusion of the $[BF_{20}]^-$ anion may also take place *via front* and *back* directions of approach of the monomer analogous to those for ethylene, but the different regio- and stereoisomers need also be taken into consideration. In addition to the 1,2/2,1 *re*/*si* isomers from both sides of monomer attack, the second insertion reactants and TSs may have the growing propylene chain *syn* or *anti* to the propylene methyl.

From a recent review of the literature it is to the best of our knowledge that only two DFT studies of ion-pair propylene homopolymerisation have been carried out, namely by Laine *et al.*,[154] and Sandhya *et al.*[172] The former article limited the study of the zirconocene, and *ansa*-zirconocenes with $[BF_{20}]^-$ to two consecutive 1,2 insertions, leading to a regioregular isotactic polymer. Structures and relative energies of the stationary points along the reaction pathways were not reported, however, and only the difference in transition state energies of the second propylene insertion relative to an insertion of ethylene, as well as

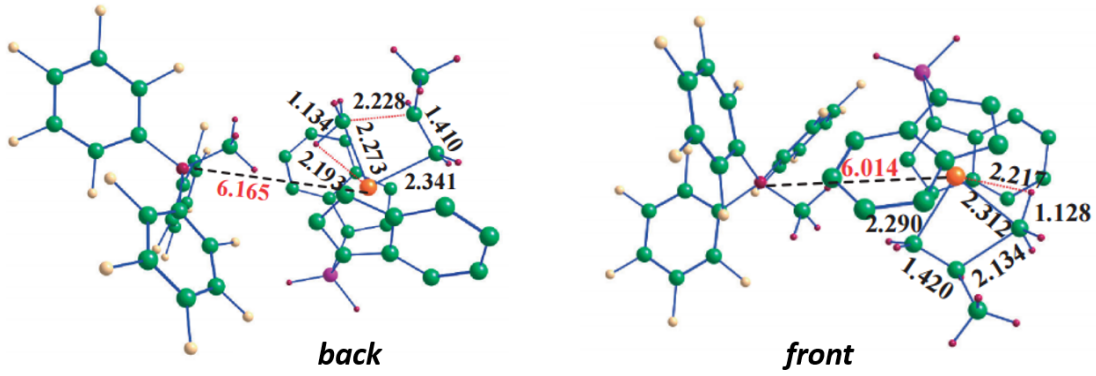

Figure 4.9: Transition states for insertion of propylene *via* the *back* and *front* directions of monomer approach, as reported by Sandhya *et al.* for the the $[SiH_2(Ind)_2ZrMe]^+$-$[MeBF_{15}]^-$ system.[172]

to β-hydride transfer to monomer (BHTM) are given. The more recent study by Sandhya *et al.* examined the effect of $[MeBF_{15}]^-$ on the pathways of propylene polymerisation catalysed by $[SiH_2(Ind)_2ZrMe]^+$. A barrier to anion displacement was not reported, and mechanistic studies instead began from ion-pairs calculated by removing the propylene monomer from the *front* and *back* positions and optimising to give resulting outer-sphere ion-pairs. This method, however, does not provide a direct comparison between the two directions of monomer approach - see Figure 4.9. Indeed, the two ion-pairs from which the mechanistic studies are compared differ in energy by 28 kJmol^{-1}.

Results reported by Sandhya *et al.* show that in the first CP step the 1,2 insertion TSs have lower relative stabilities from both sides of monomer approach, with an 8 and 4 kJmol^{-1} preference for *re* and *si* stereoisomers from the *front* and *back* directions, respectively. Internal barriers to insertion lie within the range 48-86 and 14-75 kJmol^{-1} from the *front* and *back* directions, respectively, with the barriers to *front* 1,2 *re* insertion roughly three times, and those to 1,2/2,1 *si* around 2 times, lower from the *back* than from the *front*. Secondary *re* insertion is the least favoured in both cases. Resting states between the two CP steps were found by optimising structures after removing the second monomer adduct, and TSs connecting the resulting structures to the adducts were not reported. Owing to the large barriers to 2,1 *re* insertion from both sides of approach, this mechanism was omitted from the mechanistic studies of the second CP step. The β-agostic resting states from 1,2 insertion *via* the *front* direction lie over 100 kJmol^{-1} lower in energy than the γ-agostic resting

state from 2,1 insertion, rationalised by the γ-agostic interaction preventing an inner-sphere ion-pair to form. The authors asserted that this indicates the agostic interaction dominates over that between the ion-pair. From both directions the 1,2 insertion barriers are lower than the 2,1. Overall, the authors concluded that the agostic interactions play an important role in ion-pair studies of propylene polymerisation, and are able to prohibit the formation of strong inner-sphere ion-pairs that could hinder CP.

4.2 Computational Details

The computational approach outlined in Section 3.4 (page 81) was also employed in this Chapter. Starting point geometries for optimisations of the cationic activated catalyst and the transition states involved in the enchainment of one propylene monomer *via* the 1,2 *re* and 2,1 *re* mechanisms were provided by ARLANXEO Elastomers B.V.. Analytical frequency calculations were performed in order to verify the minima and transition state geometries, and in order to obtain thermodynamic properties. The geometries of the reactants and products connected to the transition states were obtained by manually displacing the transition state geometry a small distance along the imaginary vibrational mode in either direction, and optimising from there.

The lowest energy structure of the ion-pair $[\text{Cp*}\{\text{CN(Ph)N(iPr)}_2\}\text{TiMe}]^+[\text{BF}_{20}]^-$ was calculated by optimising a set of starting structures with Ti–B bond distances of 15 Å using the semi-empirical method PM6,[173] followed by subsequent optimisation with DFT using the approach described in Section 3.4. The semi-empirical calculations were carried out in order to survey rapidly the potential energy surface and provide starting guess structures for subsequent DFT optimisations. Within the semi-empirical method PM6, only valence electrons are treated explicitly. The PM6 method in a parametrised and modified version of the *neglect of diatomic differential overlap (NDDO) approximation* which ignores differential overlap between diatomic orbitals of different atoms.[174,175]

4.3 Results and Discussion

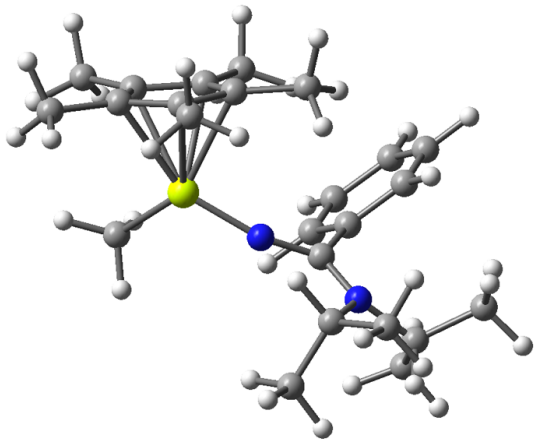

Figure 4.10: Ball and stick model of the cationic active catalyst $[Cp^*\{NC(Ph)N(iPr)_2\}TiMe]^+$.

The following dicussion is related to the ion-pairs and naked analogues of the full catalytic system. The active cationic component of the catalytic system is shown again in Figure 4.10.

4.3.1 The Ion-Pair

As discussed, compared to the clear-cut directionality of cation-anion interaction in catalytic ion-pairs containing the borane co-anion $[MeBF_{15}]^-$, the position and orientation of $[BF_{20}]^-$ is not so easily defined. In order to predict in which configuration the anion and cation are most likely to form an ion-pair, the electrostatic potential (ESP) surface of the two counterparts is considered. The ESP surface can be used to predict regions of chemical activity, and here the most electrophilic and nucleophilic regions of the cation and anion, respectively, are required. If we first examine the $[BF_{20}]^-$ anion (Figure 4.11**a**) the areas of darkest red, those with the most negative ESP and therefore regions to where an electron will be most attracted, lie in the cavities between the fluorinated phenyl rings. The ESP surface for the methyl cation in Figure 4.11**b**, shows that the darkest blue area around the Ti atom is found on the $N(iPr)_2$ side of the molecule. It is here that the electrostatic potential is the most positive, and is where a nucleophile such as the $[BF_{20}]^-$ anion is most likely

to coordinate. It is therefore expected that the $[BF_{20}]^-$ and active cation would slot into each other, forming an ion-pair *via* a Ti–F interaction. In order to verify this hypothesis, a systematic set of geometries was optimised using both semi-empirical method PM6 and our standard DFT optimisation procedure to find the lowest energy ion-pair.

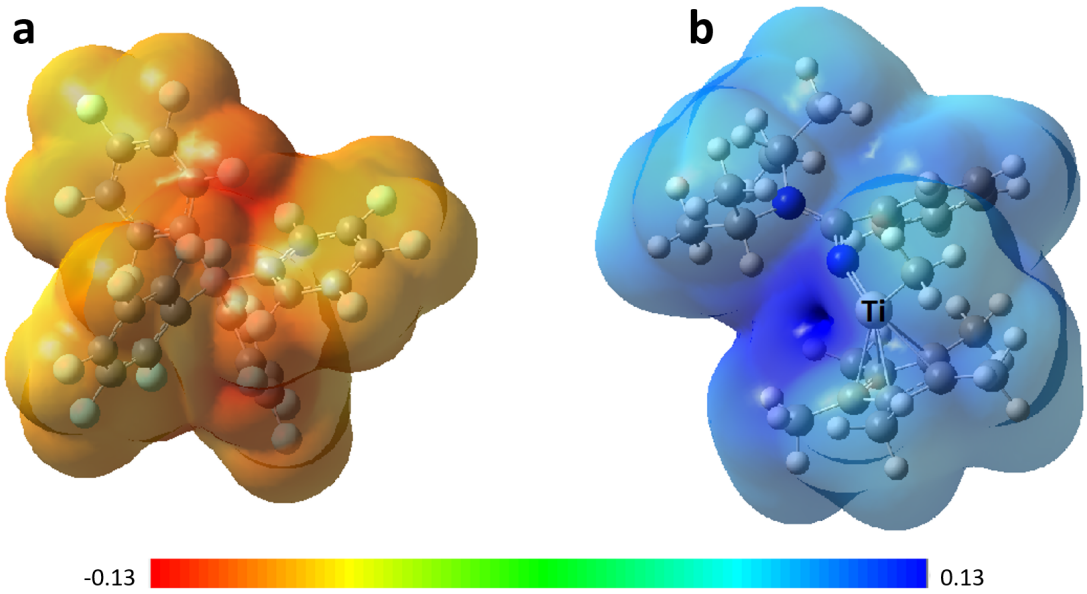

Figure 4.11: Electrostatic potential (ESP) surfaces of $[BF_{20}]^-$ and $[Cp^*\{CN(Ph)N(iPr)_2\}TiMe]^+$ shown at an isovalue of 0.004 atomic units.

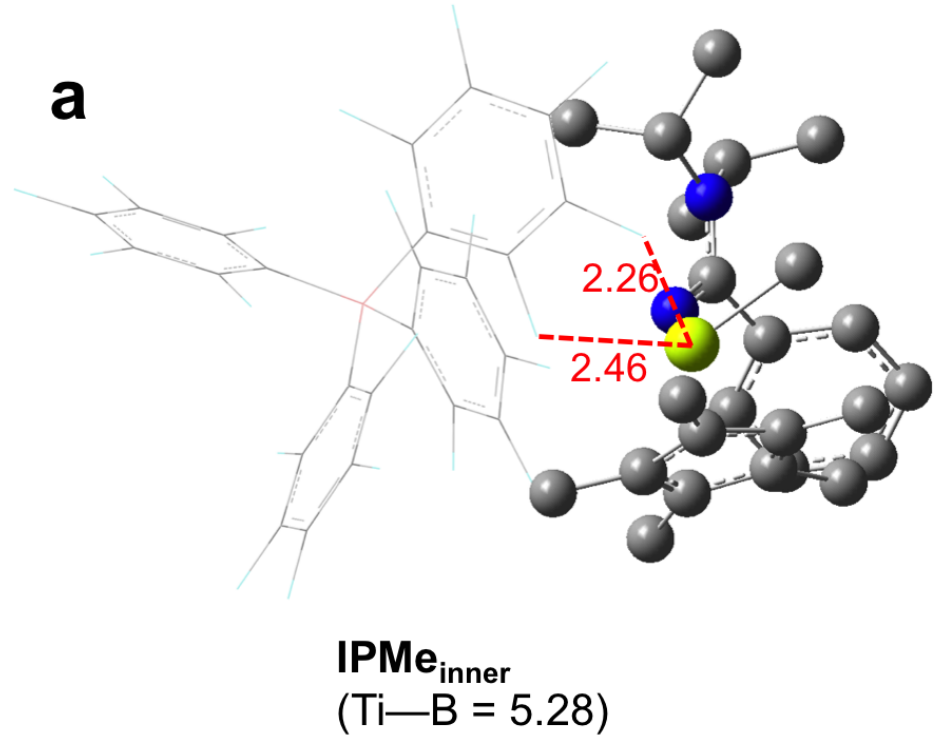

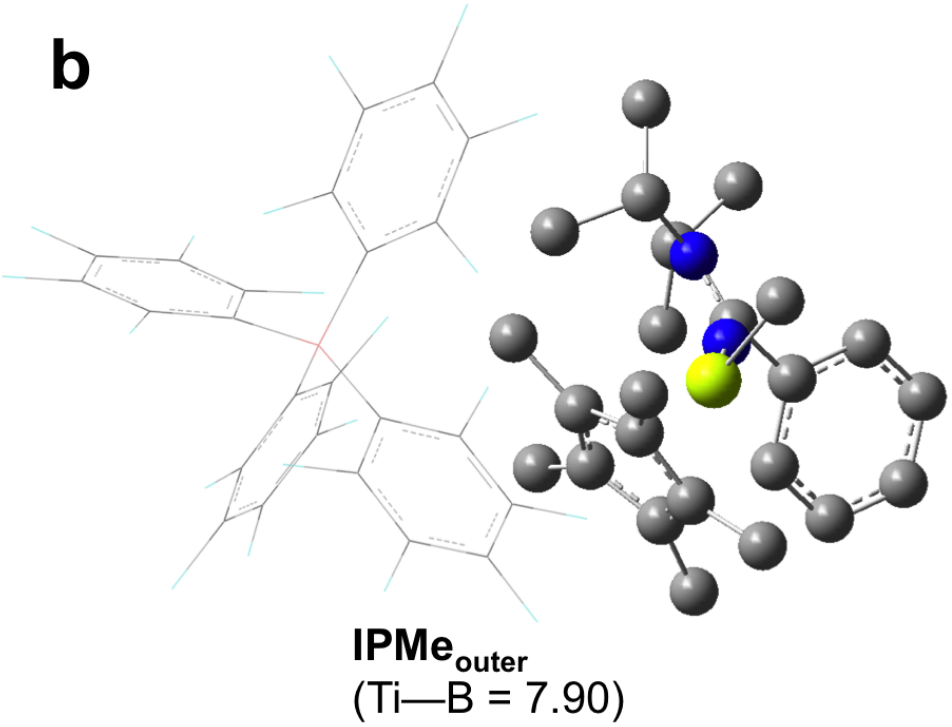

Figure 4.12: The structures of inner- and outer-sphere ion-pairs $[Cp^*\{CN(Ph)N(iPr)_2\}TiMe]^+[BF_{20}]^-$. The cation is rendered as a ball-and-stick model, whereas the anion is displayed as a wire-frame. H atoms are omitted for clarity.

Figure 4.12**a** shows the structure of the lowest energy ion-pair, **IPMe$_{\text{inner}}$** with the shortest Ti–F interactions indicated by red dashed lines. It can be seen that in this ion-pair the anion is located on the N(iPr)$_2$ side of the cation, as predicted by analysis of the ESP surface. Contrary to the ion-pair study of zirconocene^{+}-$[BF_{20}]^{-}$ systems carried out by Laine *et al.*, no favourable π-stacking interaction with the phenyl part of the amidinate ligand is observed.[154] The closest Ti-F distances are 2.26 Å and 2.46 Å for the *m*- and *o*-F atoms, respectively, the shortest of which compares well with the Ti–*m*-F distances reported for two *ansa*-zirconocene complexes with $[BF_{20}]^{-}$ that were studied by Laine, for which distances of 2.27 and 2.28 Å were reported. In the present work, the longer Ti–*o*-F interaction is also involved in the ion-pair coordination along with that of the *meta*, as the $C_{(C_6F_5)}$–F distance for both these positions is elongated to 1.37 Å compared to an average of 1.33 Å for the other $C_{(C_6F_5)}$–F distances. The short Ti–F distances are indicative of an inner-sphere ion-pair, and are not present in the lowest energy outer-sphere ion-pair, **IPMe$_{\text{outer}}$** shown in Figure 4.12**b**. In this ion-pair the anion is also coordinated to the side of the cation containing the N(iPr)$_2$ part of the ancillary ligand, reinforcing the assertion that the ESP surface may be used to predict regions of chemical activity. There are two noticeable differences between the inner- and outer-sphere structures, however: the Ti–B distance of **IPMe$_{\text{outer}}$** is $\sim$2.6 Å longer than that in **IPMe$_{\text{inner}}$**, and the coordination geometry at the Ti centre is substantially altered upon forming an inner-sphere ion-pair. When only an outer-sphere ion-pair is formed, the structure of the cationic Ti centre resembles that of the naked-cation, however, when the F atoms of $[BF_{20}]^{-}$ coordinate to the Ti centre the methyl and Cp* groups are pushed towards the Ph side of the cation.

The ion-pair formation energy, ΔE_{IP}, may be calculated using

$$\Delta E_{\text{IP}} = E_{[\text{LTiMe}]^{+}[\text{BF}_{20}]^{-}} + E_{\text{CPh}_3\text{Me}} - E_{\text{LTiMe}_2} - E_{[\text{CPh}_3]^{+}[\text{BF}_{20}]^{-}} \tag{4.1}$$

where L = Cp*{CN(Ph)N(iPr)$_2$}, and gives $E_{\text{IP}_{\text{inner}}}$ and $E_{\text{IP}_{\text{outer}}}$ of -163.1 and -92.4 kJmol^{-1}, respectively. These energies are very similar to those of forming the inner and outer-sphere $[(4\text{-PhInd})_2\text{ZrMe}_2]^{+}$–$[BF_{20}]^{-}$ ion-pairs, reported as -167.5 and -91.4 kJmol^{-1} by Laine *et al.*, who also employed the M06-2X XC functional.

4.3.2 Ethylene Homopolymerisation

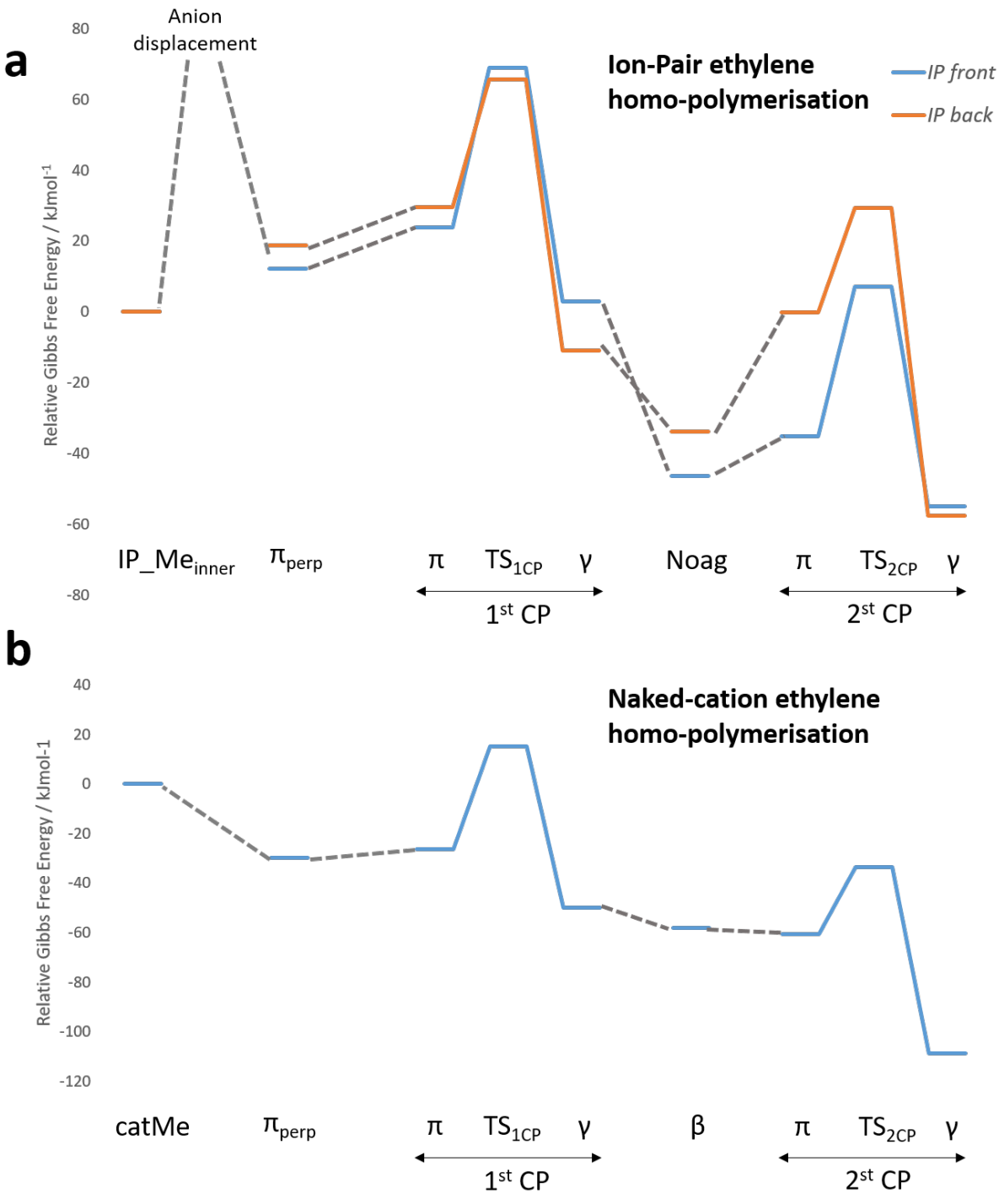

Figure 4.13: Gibbs free energy profiles (298 K) for two chain propagation steps of ethylene homopolymerisation calculated with (**a**) and without (**b**) the $[BF_{20}]^-$ anion.

	Ion-pairs		**Naked-cationic**
	front	*back*	*N(iPr)$_2$*
methyl catalyst	0.0	0.0	0.0
π_{perp}	12.3	18.8	-30.0
π	23.7	29.7	-26.4
TS_{1CP}	69.1	65.7	15.0
γ	2.9	-10.8	-50.0
resting state	-46.3	-33.8	-58.2
π	-35.2	-0.2	-60.6
TS_{2CP}	7.2	29.2	-33.6
γ	-54.9	-57.5	-108.6

Table 4.1: Relative Gibbs free energies (kJmol^{-1}) of the stationary points along the first two chain propagation steps of ethylene homopolymerisation calculated with and without an anion.

The first two chain propagation steps of ethylene homopolymerisation were calculated from the starting methyl ion-pair, **IPMe$_{inner}$** (Figure 4.12**a**), with Gibbs free energy profiles presented in Figure 4.13**a**. This study was carried out for two consecutive *front/front* and *back/back* insertions. Unfortunately, the transition state for anion displacement from neither the *front* nor the *back* directions of monomer approach could not be located - even after great effort (See Appendix B for further information). It may be expected, however, that displacement of the anion from the *front* direction of monomer approach will be favoured over the *back*, as has been reported in previous studies of ethylene polymerisation which take a counter-anion into consideration.[123,151,153,162–164] This observation has been attributed to the assertion that the *back* approach of the monomer requires the methyl of the cation to be pushed towards the coordination site occupied by the anion, causing destabilising steric congestion in the associated TS.[154]

First Chain Propagation Reaction

The ethylene π-adducts are the next stationary points along the reaction profiles for both *front* and *back* monomer approaches that were located after the inner-sphere methyl ion-pair. Perpendicular π-complexes, π_{perp}, were located by rotating those which were located *via* manual displacement along the imaginary modes of the first insertion transition states, TS_{1CP}, and are found to lie higher in energy than the inner-sphere ion-pair

and isolated ethylene from both directions of monomer approach (Table 4.1). These perpendicular systems lie lower in energy than the "normal" adducts, in agreement with the literature described in Section 4.1.4, and it may be assumed that anion displacement by a perpendicular ethylene monomer has a lower barrier than by one in the "normal" orientation. Indeed, Laine *et al.* reported anion displacement TSs with ethylene perpendicular.[154] The geometric data presented in Table 4.2 show that significant anion displacement is required for the coordination of the perpendicular ethylene adduct to the Ti centre (an increase in Ti–B of $\sim$1.8 and $\sim$2.6 Å for *front* and *back* direction, respectively), resulting in outer-sphere ion-pairs. Greater displacement is observed for the *back* approach as the ethylene monomer coordinated in this manner forces the Cp* ligand towards the anion, moving the anion further out of the coordination sphere of the Ti centre, as shown in Figure 4.14. A relatively small barrier of $\sim$15 kJmol^{-1} is expected for the rotation of the ethylene C=C bond to form the "normal" adducts in order for insertion to take place.[151] Both adducts formed from the *front* approach are more stable than those from the *back*, also observed in all three zirconocenes studied by Laine *et al.*.[154]

		front							*back*						
	IP	$\pi_{\mathbf{perp}}$	π	**TS$_{\mathbf{1CP}}$**	γ	π	**TS$_{\mathbf{2CP}}$**	γ	$\pi_{\mathbf{perp}}$	π	**TS$_{\mathbf{1CP}}$**	γ	π	**TS$_{\mathbf{2CP}}$**	γ
Ti–B	5.28	7.11	7.19	6.99	6.74	6.48	6.28	5.95	7.83	7.11	6.94	6.85	6.96	7.01	6.87
Ti–*m*F	2.26	3.72	4.38	3.83	3.45	4.12	4.00	3.77	5.94	4.43	3.95	3.55	4.03	3.92	3.13
Ti–*o*F	2.46	4.28	4.07	4.16	3.89	3.60	3.42	3.10	7.18	4.49	4.15	4.01	4.18	4.22	4.02
Ti–H$_{\alpha/\gamma}$	2.69 [a]	2.7	2.65	2.06	2.10	2.67	2.00	2.04	2.65	2.60	2.06	2.10	2.50	2.00	2.12
C$_{\alpha/\gamma}$–H	1.10 [a]	1.10	1.10	1.13	1.12	1.11	1.14	1.13	1.10	1.11	1.13	1.12	1.11	1.14	1.13
Ti-H-C$_{\alpha/\gamma}$	47 [a]	45.9	48.40	78.30	97.40	48.00	81.70	102.80	48.10	50.60	76.60	93.40	55.50	79.60	102.30

Table 4.2: Key geometric parameters (in Å and °) of the stationary points along the ion-pair Gibbs free energy surfaces of ethylene homopolymerisation *via* the *front* and *back* directions of monomer approach. Labels refer to those shown in Figure 4.13. [a] Average of three methyl H data.

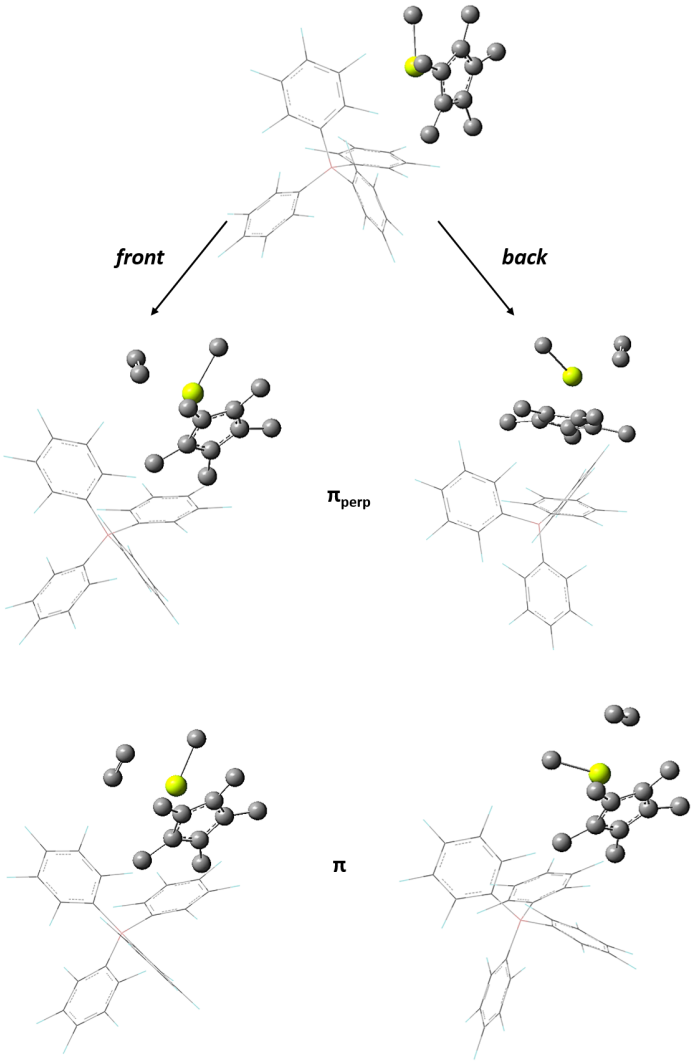

Figure 4.14: The ion-pair structures of the first ethylene π-adducts from the *front* and *back* directions of monomer approach. The cation is rendered as a ball-and-stick model, whereas the anion is displayed as a wire-frame. H atoms and ancillary ligands are omitted for clarity. The ion-pairs are all orientated such that the $N(iPr)_2$ and Ph ligands are aligned on the left and right hand sides, respectively, at the *back* of the Ti atom.

In order to establish the effect of the counter-anion on the free energy profiles of ethylene homopolymerisation, the surfaces were re-calculated anion-free, the results of which are presented in Figure 4.13**b**. The coordination of ethylene from the $N(iPr)_2$ side of the cationic catalyst can be considered analogous to the *front* side approach in the ion-pair model. Of note is the stabilisation of both perpendicular and "normal" π-adducts relative the starting methyl catalyst, as compared to the destabilisation observed in the ion-pair systems. This could be expected due to a polarisation attraction of the electron-rich C–C

π-bonding orbital of ethylene by the cation centre on the Ti atom.

Chain propagation proceeds through **TS_{1CP}**, which is a (close to) planar, four-centre transition state stabilised by an α-agostic interaction for both ion-pair and naked-cation models, the stationary points of which are displayed in Appendix C and D. This observation indicates that the reaction follows the modified Cossee-Arlman mechanism described in Section 3.1.4. Evidence of such agostic interactions may be found in the lengthening of the C_α–H bonds from an isolated C–H bond of ∼1.1 to ∼1.3 Å in all TS studied, as shown in Tables 4.2 and 4.3.

The internal barriers to the first ethylene insertion displayed in Table 4.4 all lie within the range 36.0-45.3 kJmol^{-1}, similar to those calculated by Laine *et al.* of between ∼30-50 kJmol^{-1} for $[BF_{20}]^-$–zirconocene systems and ∼40 kJmol^{-1} for the corresponding naked cation models. In all cases the product of insertion is an n-propyl growing polymer chain stabilised by a γ-agostic interaction.

	Me	$\pi_{\mathbf{perp}}$	π	**TS_{1CP}**	γ	π	**TS_{2CP}**	γ
Ti–$H_{\alpha/\gamma}$	2.62	2.66	2.66	2.04	2.07	2.38	1.98	2.03
$C_{\alpha/\gamma}$–H	1.11	1.10	1.10	1.13	1.13	1.12	1.14	1.13
Ti-H-$C_{\alpha/\gamma}$	48.8	47.1	46.6	78.2	92.2	60.7	81.0	94.9

Table 4.3: Key geometric parameters (in Å and deg) of the stationary points along the naked cationic Gibbs free energy surfaces of ethylene homopolymerisation. Labels refer to those shown in Figure 4.13.

Monomer approach	**Insertion**	$\Delta G^\ddagger$
front	1st	45.3
	2nd	42.4
back	1st	36.0
	2nd	29.4
Naked cationic	1st	41.4
	2nd	27.0

Table 4.4: Gibbs free energy internal barriers (in kJmol^{-1}) for ethylene insertion from the monomer π-adducts.

Isomers of n-propyl Chain End

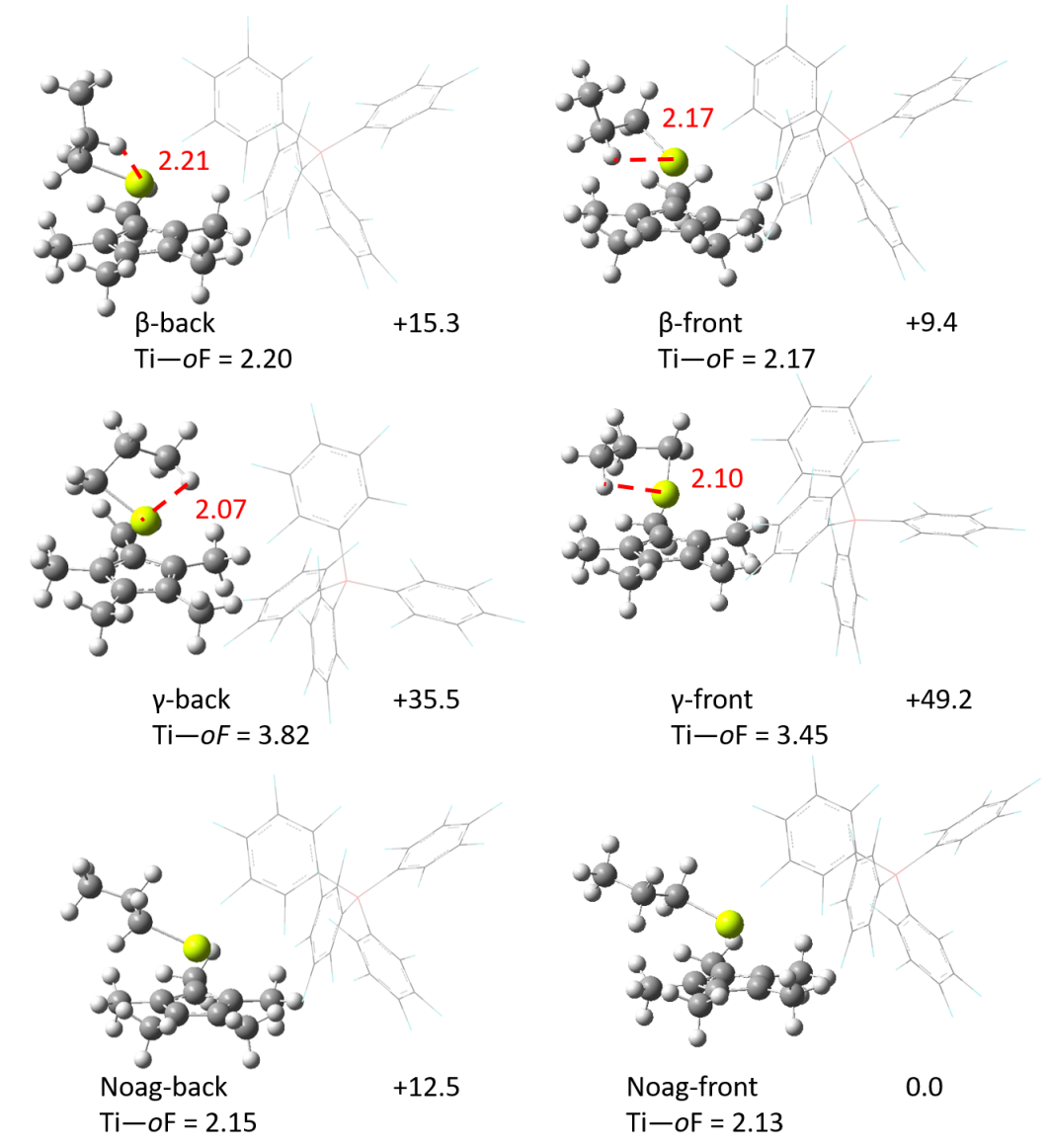

Figure 4.15: Geometries of n-propyl ion-pairs. Distances and relative Gibbs free energies are given in Å and kJmol^{-1}, respectively. γ-**back** and γ-**front** correspond to the reaction products of monomer insertion *via* the *front* and *back* approaches, respectively. The other isomers labelled with "**back**" and "**front**" for clarity and are linked to the γ- isomers with the same suffix by chain rotations. The cation is rendered as a ball-and-stick model, whereas the anion is displayed as a wire-frame. The ancillary ligands are omitted for clarity.

Following the first chain propagation reaction the newly formed Ti-alkyl cation has an n-propyl growing polymer chain stabilised by a γ-agostic interaction. A detailed study of the isomerisation process of n-butyl ziroconocene ion-pairs containing $[BF_{20}]^{-1}$ by Nifant'ev *et al.* showed that for the n-butylene growing chain, isomers containing γ-, β-, and

no-agostic interactions exist.[151] The analogous isomers of the ion-pair n-propyl species are displayed in Figure 4.15, with corresponding energies relative to the lowest energy isomer, "**Noag-front**". It should be noted that here the bold **back** and **front** suffixes relate to structure labels. If we first consider the products of the first CP reaction, γ-**back** and -**front**, we see that γ-**back** is $\sim$14 kJmol^{-1} more stable than that formed by the *front* insertion. This is attributed to the shorter stabilising γ-agostic interaction in γ-**back**, made possible by its formation in the open coordination site away from the Cp* ligand. The agostic interaction located in the vacant site of the coordination sphere is also in competition with the cation-anion interaction in γ-**back**, and owing to this the isomer from the *back* approach has a longer Ti–*o*F distance relative to γ-**front**.

A rotation around the C_α-C_β bonds of the γ-isomers yields ion-pairs containing β-agostic interactions, β-**back** and -**front**. Of these two, the *front* isomer is the more stable in Gibbs energy, owing to shorter agostic *and* Ti–*o*F interactions. The congestion in the vacant site of β-**back** appears to limit the proximities of both the C_β–H bonds and the anion. The agostic interactions of the β- isomers are longer than in the γ- analogues, and it may be expected that this lengthening is accompanied by a destabilisation. By contrast, the rotation of the alkyl chain to allow the C_β–H bond into the Ti coordination sphere allows the anion to move closer to the cationic Ti centre and form inner-sphere ion-pairs.

The most stable n-propyl isomers of both *front* and *back* insertion approach contain no agostic bonds - labelled **Noag-back** and -**front** in Figure 4.15. The rotation of the propyl chain out of the coordination sphere allows a close approach of the anion such that innner-sphere ion-pairs are formed. These are closer-contact ion-pairs than the β-agostomers as the propyl chain is fully directed away from the vacant site. The isomer **Noag-front** containing less sterically hindering H atoms directed towards the anion, *vs.* the $C_\beta H_2$ group in **Noag-back**, results in the most stable n-propyl isomer of the six located.* It is therefore expected that isomerisation of the γ-agostic products of ethylene insertion into resting states containing no agostic interactions will take place.

Transition states between all of the isomers containing the same suffix must exist,

*Isomers containing an α-agostic interaction could not be located, as the structures would consistently relax back into those containing no agostic interactions. In addition, previous theoretical studies on gas phase metal alkyl cations reported the α-agostic cation as $\sim$40 kJmol^{-1} less stable than the β-agostic.[106,107]

however could not be located within the scope of this PhD. Transformations between isomers containing the same (or no) agostic bonds but with different suffixes, e.g. γ-**back** and γ-**front** require a more significant rearrangement. A barrier to isomerisation from a γ-agostic $[Cp_2ZrBu]^+[BF_{20}]^-$ ion pair to a no-agostic isomer was found to be $\sim$30 kJmol^{-1}[1151] and a barrier of similar magnitude is expected for the present systems.

Calculations for the analogous naked cation isomers were carried out, however, in the absence of an anion to stabilise the cationic Ti centre, an isomer free of agostic interaction could not be located as it relaxed into the β-agostomer. In this case, the β-agostomer is the most stable, by $\sim$8 kJmol^{-1} relative to the γ analogue, and can be seen in Appendix D.

Second Chain Propagation Reaction

The second CP step for ion-pair ethylene homopolymerisation is displayed in Figure 4.13**a** (page 100). From the n-propyl isomers containing no agostic bonds (**Noag**-) an ethylene monomer may approach from the *front* or *back* directions. As the **Noag**- isomers are inner-sphere ion-pairs, anion displacement must again take place to allow monomer coordination. If, however, isomerisation from the γ-**front** isomer does not occur, the formation of the π-complex is exergonic relative to this agostomer. The difference in relative energy between the two ion-pair π-complexes is substantial (35 kJmol^{-1}) and the steric congestion caused by the propyl chain being forced towards the bulky anion is the likely explanation for this destabilisation of the *back* π-complex, as compared with the relatively uncongested *front* analogue. The Ti–B and Ti–F distances in the *front* adduct are also shorter than those of the *back* adduct, and the ion-pair interaction is therefore expected to be greater in the *front* analogue, contributing to its increased stability.

The naked cationic ethylene adduct lies very close in energy to both the β-agostomer and the γ-agostic products from the first chain propagation step, with adduct formation being slightly exergonic (-2.4 kJmol^{-1}). It may be expected that a barrier exists between the β-agostic resting state and the second π-adduct, as rotation of the propyl chain is required to cleave the β-agostic bond in order to form an α-agostic interaction in the second ethylene adduct. Interestingly, the ion-pair analogues of these second adducts do not display such

α-agostic stabilising interaction, with Ti–H_α distances of $>$2.3 Å. In the case of the second *back* adduct, the anion is in competition with the C–H bond for proximity to the cationic centre, and in the second *front* adduct the ancillary ligands prevent the C–H bond from bending towards the Ti atom.

The internal barriers to insertion are all lower for the second CP step than the first (Table 4.4), in line with previous studies of olefin homopolymerisation.[114] The most pronounced reduction in barrier heights of $\sim$14 kJmol^{-1} is observed for the the naked cationic model. The C–H and Ti–H distances reported in Table 4.3 are longer and shorter, respectively, in **TS_{2CP}** than in **TS_{1CP}**, indicative of a stronger stabilising α-agostic interaction, and offer a rationalisation of this reduction in barrier height *vs.* the first CP step. The same is true for the ion-pair analogues, as shown in Table 4.2. These products of second monomer insertion have an n-pentyl growing chain, stabilised by a γ-agostic bond.

Summary

Overall, the biggest differences between the ion-pair and naked cationic models lie in the formation of π-adducts, the exergonicity of the insertion reactions, and the geometries of stabilising agostic bonds. Formation of the ethylene adducts requires displacement of the anion in the ion-pairs, reducing the favourable cation-anion interaction and significantly increasing steric congestion at the Ti centre. As the ion-pair separation energy for **IPMe$_{\text{inner}}$** is similar to that of the 4-PhInd *ansa*-zirconocene reported by Laine *et al.*, similar anion displacement barriers of $\sim$70 and 110 kJmol^{-1} for the *front* and *back* directions of monomer approach, respectively, are expected for our post-metallocene system. The anion displacement is therefore expected to be the rate determining step of ethylene homopolymerisation as these values exceed the insertion barriers in the range of 35-45 kJmol^{-1}. In the naked cationic model, however, the formation of π-adducts is expected to be spontaneous, or have only a small barrier to coordination.

Figure 4.13 and Table 4.1 show that the naked cationic model displays greater exergonicity in the chain propagation reactions as compared to that ion-pair model. Indeed, in the case of the first CP step from the *front* direction of the ion-pair system, the n-propyl product lies higher in energy than the starting inner-sphere ion-pair. The difference in exergonicity of the reactions was previously reported by Nifant'ev *et al.*, where they observed a decrease in overall exergonicity upon increasing the nucleophilicity of the counter-anion from $[BF_{20}]^-$ to $[MeBF_{15}]^-$, which also increases the strength of the cation-anion interaction.

The uncongested coordination sphere of the Ti atom in the naked cationic systems, and the lack of competition with the anion for coordination, generally allows for the formation of shorter Ti–H$_{\alpha/\gamma}$ distances and more acute Ti-H-C$_{\alpha/\gamma}$ bond angles relative to the ion-pair analogues. These differences are indicative of stronger agostic interactions and may account for the increased stability of stationary points relative to the starting methyl catalyst as compared to those calculated with the $[BF_{20}]^-$ anion.

4.3.3 Propylene Homopolymerisation

Propylene homopolymerisation studies analogous to those of ethylene were carried out from the inner-sphere ion-pair **IPMe$_{\text{inner}}$**. As described in Section 3.1.6 of Chapter 3,

the prochirality of propylene results in different regio- and stereo-isomers of the CP TS. TSs for anion displacement by an incoming propylene monomer were sought, but could not be located. Perhaps difficulties in locating the TS forced Sandhya *et al.* to compare monomer adduct energies to those from ion-pairs where the adduct had been simply removed.[172]

Propylene Monomer Coordination

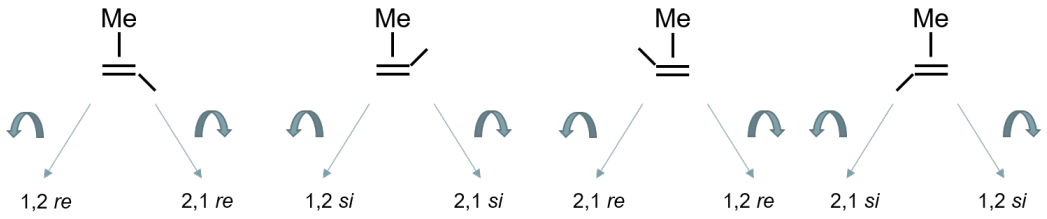

Figure 4.16: Four orientations of "perpendicular" propylene coordination to the Ti-methyl centre, and the rotations yielding "normal" π-complexes required for insertion reaction to take place.

Perpendicular π-complexes, $\pi_{\mathbf{perp}}$, analogous to those found for ethylene, were calculated for propylene. Figure 4.16 illustrates the four orientations in which the propylene monomer may coordinate, and also shows how rotating the monomer clockwise or anti-clockwise from these positions yields π adducts in position ready for insertion. If we examine the relative energies of the adducts we may be able to predict whether some reaction channels could be blocked before the insertion barriers are reached. This is assuming that like ethylene, a TS to anion displacement is favoured with a perpendicular monomer.

Four $\pi_{\mathbf{perp}}$ complexes were located for both directions of monomer approach, the relative stabilities of which are shown in Figure 4.17. From each direction the perpendicular adduct may coordinate *via* either the *re* or *si* face, and have its methyl either pointing towards the Cp* ligand, or the iPr or Ph groups of the amidinate from the *front* and *back* approaches, respectively. The labelling, for example, of *front* $\pi_{\mathbf{perp}}$ coordinated *via* the *si* face with the propylene methyl group pointing towards the Cp* ligand is therefore "*re*-Cp*".

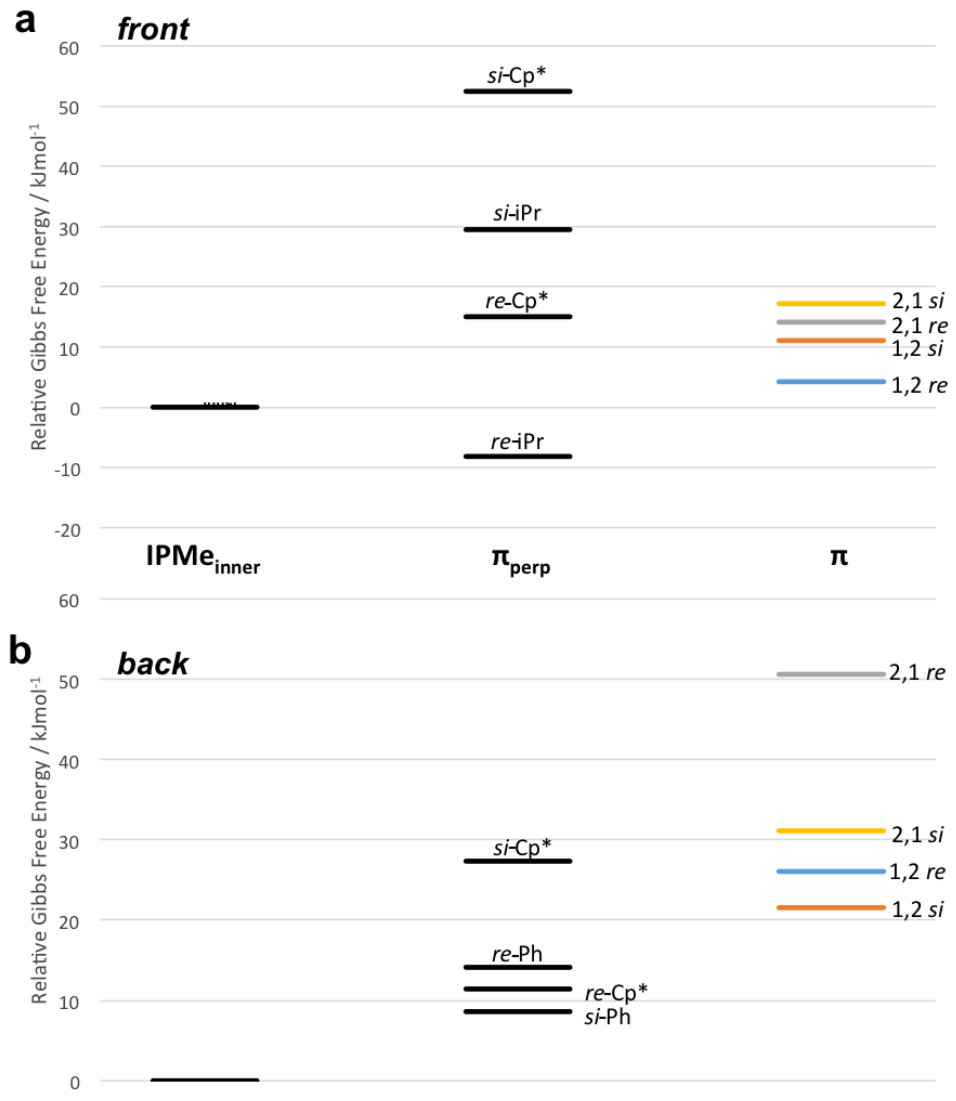

Figure 4.17: Relative Gibbs free energies of coordination of propylene in "perpendicular" and "normal" orientations.

It can be seen that the *front* *re*-iPr coordinated monomer is exergonic relative to the inner-sphere starting ion-pair, while the three other $\pi_{\textbf{perp}}$ are endergonic. If we consider only the Ti–B and Ti–F distances in Table 4.5, we might expect that the *si*-Cp* adduct to be most stable as it displays the closest contact with the anion. In fact, a correlation with an R^2 coefficient of 0.85 is observed between the relative energy of the adducts, and the average Ti–C(C=C) bond distance. This relationship is even stronger for the *back* $\pi_{\textbf{perp}}$, with R^2=0.98. We may therefore infer that the strength, and thus stabilising effect, of the π-adducts is governed by the distance between the two interacting orbitals. This

is intuitive, as greater orbital overlap may take place with closer bond distance. The R^2 value is reduced, however, to 0.68 if both data sets are considered together, indicating that Ti–C(C=C) bond distance alone does not govern the relative stabilities of the perpendicular adducts, and the situation is more complex. Indeed, while Ti–C(C=C) distances of the *back* $\pi_{\mathbf{perp}}$ are in fact shorter than those from the *front*, Ti–B distances are over 1 Å longer. In order to accommodate the propylene adducts in the perpendicular orientation from the *back* approach, the Cp* ligand must swing round towards the anion, displacing the anion from close contact with the Ti centre, and forcing it to "bite" around the Cp* ligand.

		Ti–B	Ti–*o*F	Ti–*m*F	av. Ti–C(C=C)
	IP	5.28	2.26	2.46	
front	*re*-iPr	6.51	3.67	4.25	2.61
	si-iPr	7.14	4.34	3.45	2.65
	re-Cp*	6.67	4.14	4.74	2.64
	si-Cp*	6.38	3.72	2.43	2.76
	1,2 *re*	6.82	4.09	4.34	2.59
	1,2 *si*	6.89	4.18	4.51	2.64
	2,1 *re*	7.24	4.39	4.7	2.66
	2,1 *si*	6.69	3.98	4.46	2.62
back	*re*-Ph	7.91	[a]	[a]	2.59
	si-Ph	7.83	[a]	[a]	2.58
	re-Cp*	7.82	[a]	[a]	2.59
	si-Cp*	7.81	[a]	[a]	2.62
	1,2 *re*	7.22	4.57	4.64	2.65
	1,2 *si*	6.97	4.2	4.00	2.64
	2,1 *re*	7.25	4.63	4.76	2.62
	2,1 *si*	6.97	4.33	4.72	2.57

Table 4.5: Geometric data (in Å) for the perpendicular and "normal" propylene adducts from both *front* and *back* directions of monomer approach. [a]Position of the anion is considerably different to that in the "normal" adduct, such that no direct Ti–F interactions are observed.

Correlations with $R^2 > 0.75$ between geometric parameters and relative stabilities of the "normal" π-adducts are not found, however. In these instances there is an interplay between the stabilising effects of Ti–C(C=C) and ion-pair interactions, and unfavourable steric interactions. The relative energies of the "normal" adducts displayed in Figure 4.17 show that those for primary insertion are more stable than those for secondary, from both *front* and *back* sides, in agreement with the literature consensus. In the configurations for

1,2 insertion the methyl on the propylene monomer is directed away from both the anion and the bulky ancillary ligands. From the *front* side approach the *re* coordinated adducts are slightly favoured over the *si*, for both regio-isomers. In rather pleasing symmetry, we observe the opposite for the *back* side approach, with the *si* coordinated monomers favoured over the *re*. This is expected as, for example, the 1,2 *re* from the front side is approximately mirrored in the 1,2 *si* from the back, i.e. the propylene methyls are pointing away from the sterically congested amidinate region of the catalyst.

Formation of the 2,1 *re* adduct from $\mathbf{IPMe_{inner}}$ is largely endergonic (Figure 4.17). Upon closer inspection this appears to originate in the readjustment of the Cp* ligand to accommodate the propylene in this approximate perpendicular coordination: if the propylene were to lie in plane then its methyl group would be pointing straight at those of the Cp* group (Appendix F, page 175). To prevent this the C=C bond is rotated 51° from the plane in which the transition state resides, and the Cp* group is tilted towards the anion, resulting in a larger ion-pair separation of 7.28 *cf.* 6.97 Å in the 2,1 *si* analogue.

The free energy barriers to rotation of the perpendicular adducts in order to form the adducts in the positions required for CP have not been located, however predictions of preferred directions of rotations may be made. These are based on unfavourable steric interactions with ancillary ligands and the anion, as well as fewer degrees through which to rotate round by in order to form the "normal" adducts. We may therefore be able to establish which "normal" adducts are most likely to form. Figure 4.18 shows the structures of $\pi_{\mathbf{perp}}$, with red arrows indicating where an intuitively obvious preference for rotation in one direction is preferable over the other. From the *front* side of approach, the most stable $\pi_{\mathbf{perp}}$, *re*-iPr, is most likely to form the 1,2 *re* π-adduct, whereas from the *back* side the two lowest energy $\pi_{\mathbf{perp}}$, *si*-Ph and *re*-Cp* are expected to form the 1,2 *si* and *re* adducts, respectively. We therefore infer, in the absence of knowledge of the anion-displacement step, that the coordination of a propylene monomer favours 1,2 insertion from both sides of monomer approach.

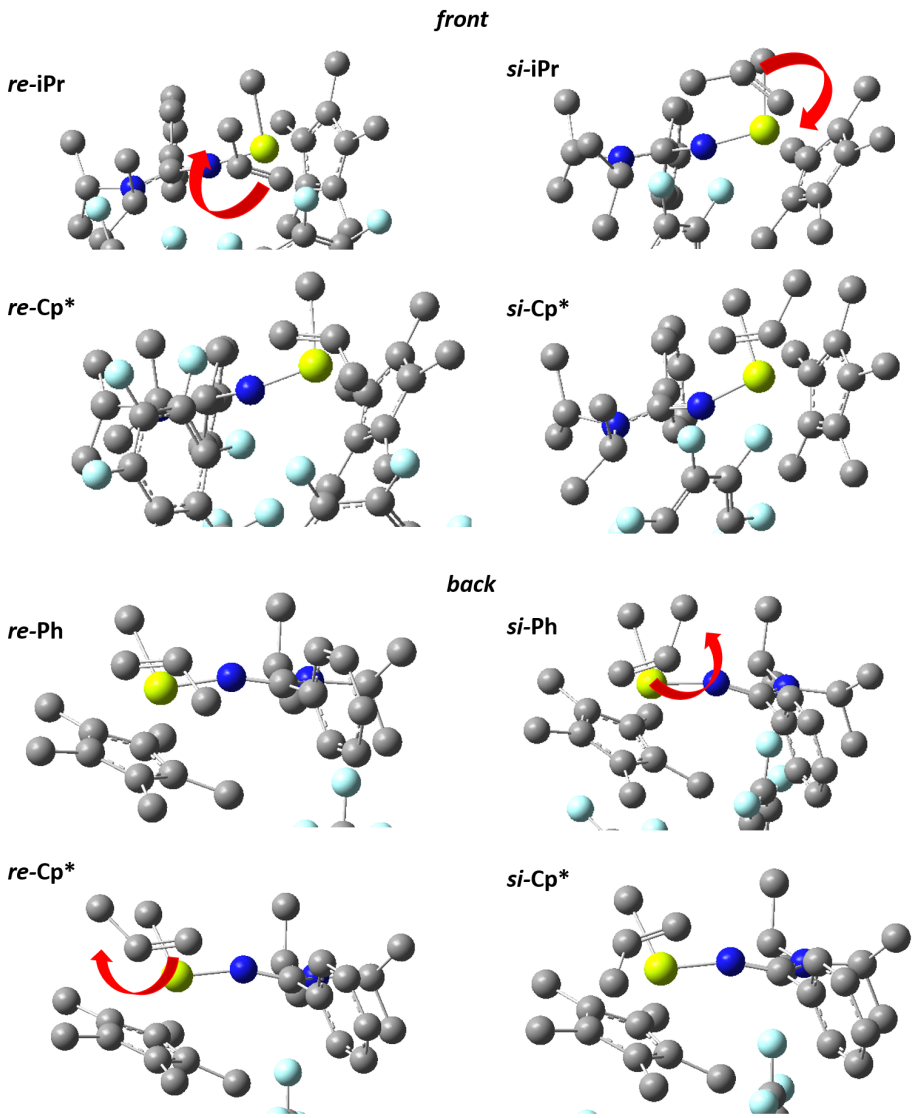

Figure 4.18: Structures of the perpendicular adducts from the *front* and *back* directions of monomer approach. H atoms are omitted for clarity. Red arrows indicated where a lower energy barrier to rotation is expected to exist for coordination in the orientation required for insertion to take place.

Compared to the inner-sphere ion-pair of $[SiH_2(Ind)_2ZrMe]^+[MeBF_{15}]^-$ reported by Sandhya *et al.*, the *front* and *back* propylene π-adducts of this *ansa*-zirconocene lie roughly 70 and 125 kJmol^{-1} higher in energy. These relative energies are far greater than of the adducts presented in this thesis, and indicate that a much larger anion-displacement barrier might need to be overcome for the $[SiH_2(Ind)_2ZrMe]^+[MeBF_{15}]^-$ catalytic pair.

First Chain Propagation Reaction

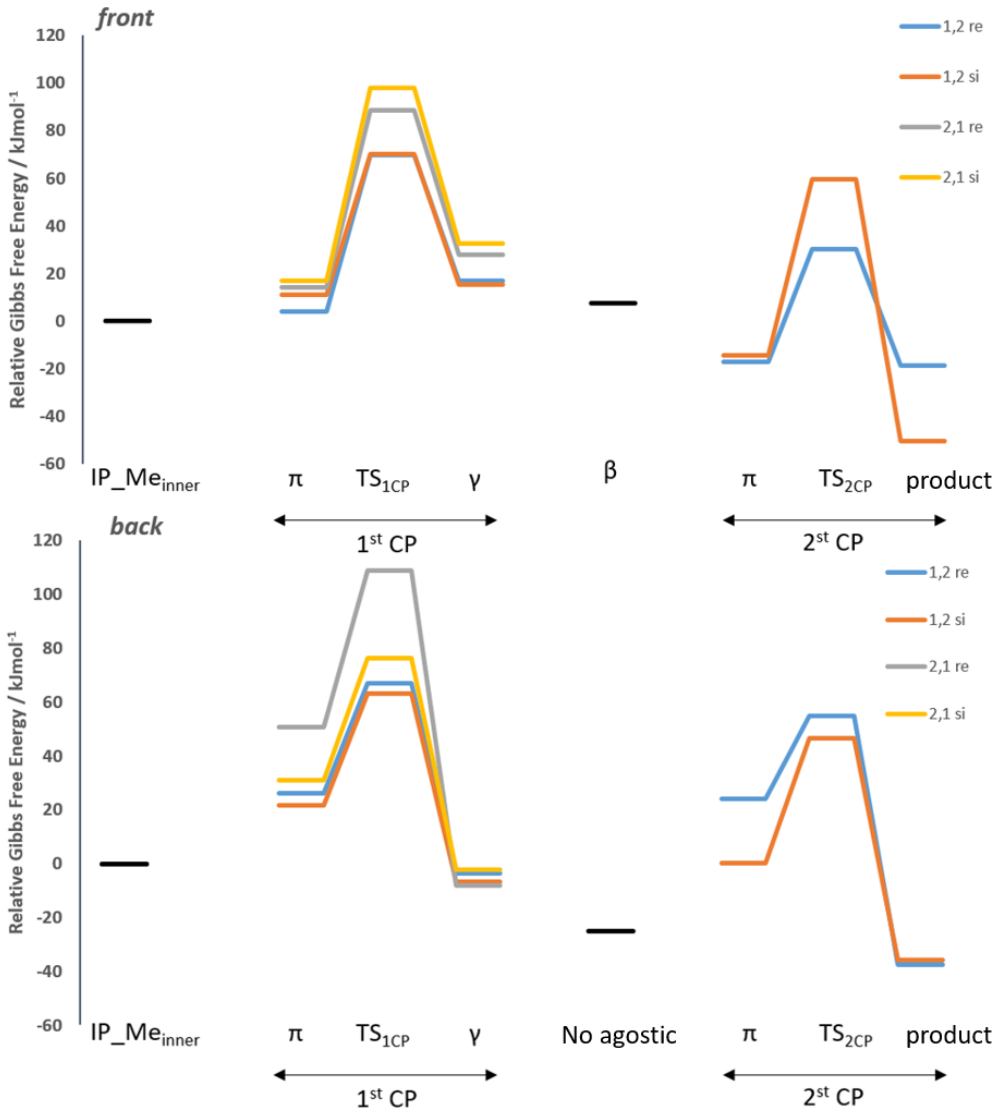

Figure 4.19: Gibbs free energy profiles (298 K) for two chain propagation steps of ion-pair propylene homopolymerisation from the *front* and *back* directions of monomer approach.

The first CP step for propylene homopolymerisation *via* both sides of monomer approach is displayed in Figure 4.19. Geometric data for stationary points, as well as their structures, can be found in Appendices E and F respectively, while Table 4.6 presents their relative Gibbs free energies. As neither anion displacement nor π-adduct rotational TSs are known, we compare the relative free energies of the insertion TSs rather than the internal barriers.

From both sides of monomer approach, 1,2 insertion is favoured over 2,1, in line with the literature consensus, with a slight preference for *re* and *si* stereo isomers. All TS_{1CP} display α-agostic interactions, indicated by Ti–H_α distances $<$2.3 Å, which are not present in the preceding π-adducts (and π_{perp}-adducts). The TS to CP *via* 2,1 *re* insertion from the *back* side is significantly higher in relative energy, and like the π-adduct appears to be due to the unfavourable interaction of the propylene methyl group pointing towards the Cp* group.

Following CP, all products display γ-agostic interactions, with those from the *back* approach being slightly exergonic relative to the starting IP ($\sim$2-8 kJmol^{-1}), and those from the front are being $\sim$15-30 kJmol^{-1} endergonic. A rationale for this may be that the agostic Ti–H interactions in the products from the *back* approach exist in coordination site *cis* to the anion, and this relatively uncongested area allows for the Ti-*o*F distances to be smaller than in the *front* side analogues where the coordination site is occupied by the Ti–C(growing chain) bond. It is therefore expected that the cation-anion interaction is greater for the *back* γ products. It should be noted here that the products formed from 1,2 insertion are isobutyl, whereas those from 2,1 are sec-butyl.

	front				*back*			
	1,2 *re*	1,2 *si*	2,1 *re*	2,1 *si*	1,2 *re*	1,2 *si*	2,1 *re*	2,1 *si*
$IPMe_{inner}$	0	0	0	0	0	0	0	0
π	4.1	11.0	14.1	17.1	26.1	21.6	50.6	31.1
TS_{1CP}	70.0	70.0	88.7	97.9	67.1	63.4	108.8	76.2
γ	16.8	15.3	28.0	32.7	-3.4	-6.7	-8.0	-2.3
resting state	7.4				-25.1			
π	-17.1 (a)	-14.5 (s)			24.2 (s)	0.2 (a)		
TS_{2CP}	30.4 (a)	59.5 (s)			54.8 (s)	46.6 (a)		
product	-18.8	-50.3			-37.3	-35.7		

Table 4.6: Relative Gibbs free energies (kJmol^{-1}) of the stationary points along the first two chain propagation steps of ion-pair propylene homopolymerisation calculated for the *front* and *back* directions of monomer approach.(a) and (s) refer to the propylene methyl anti and syn to the growing polymer chain, respectively.

Second Chain Propagation Reaction

A second CP step was calculated for the 1,2 *re* and *si* mechanisms from both directions of monomer approach. The resting state after the first insertion from the *front* direction is the β-agostic isobutyl ion-pair derived from the 1,2 *re/si* insertion products. Rotation from the *re* product is expected to have a lower energy barrier as a rotation of the alkyl unit by 94°, whereas from the *si* product a more significant rotation of 124° is required. From the *back* direction, however, the competing cation-anion interaction results in the no-agostic isomer being more favourable, *cf.* resting states of the *front/back* ethylene insertion products.

The second π-adducts are exergonic from the *front* direction (Figure 4.19), whereas from the *back* direction they are endergonic relative to the starting IP, the γ products, and the resting states. It is again not clear whether an anion displacement TS is required from the γ products, nor the size of the barriers to form the resting states. In addition, perpendicular adducts may indeed exist for the second insertion step. We therefore compare the relative stabilities of the second CP TSs. From the *front* direction, the TS to 1,2 *re* insertion lies 30 kJmol^{-1} lower in energy than the *si* isomer, indicating that an isotactic polymer is formed kinetically. However, the 1,2 *si* insertion product lies 30 kJmol^{-1} lower in energy than that from *re*, thus a syndiotactic polymer is the thermodynamic product. The reason for its greater exergonicity is due to the fact that an inner-sphere ion-pair is formed instead of a γ-agostomer, which may in fact inhibit polymerisation.

The structures of the growing polymer chains are displayed in Figure 4.20. From the *back* direction the products lie extremely close in energy, with a lower energy TS for *si* insertion. This would suggest that a syndiotactic polymer is produced, however the orientation of the iBu alkyl unit is such that the product from 1,2 *si* insertion is indeed the isotactic product. Without knowledge of the preceding uptake and isomerisation TS, it is difficult to predict the stereoregularity of the polymer produced using the κ^1-amidinate catalyst, however.

The catalyst is said to display chain end control in stereospecifity, as the insertion of the propylene monomer with the methyl pointing away from the growing polymer chain (anti) has lower 2$^{\text{nd}}$ TS relative energies.

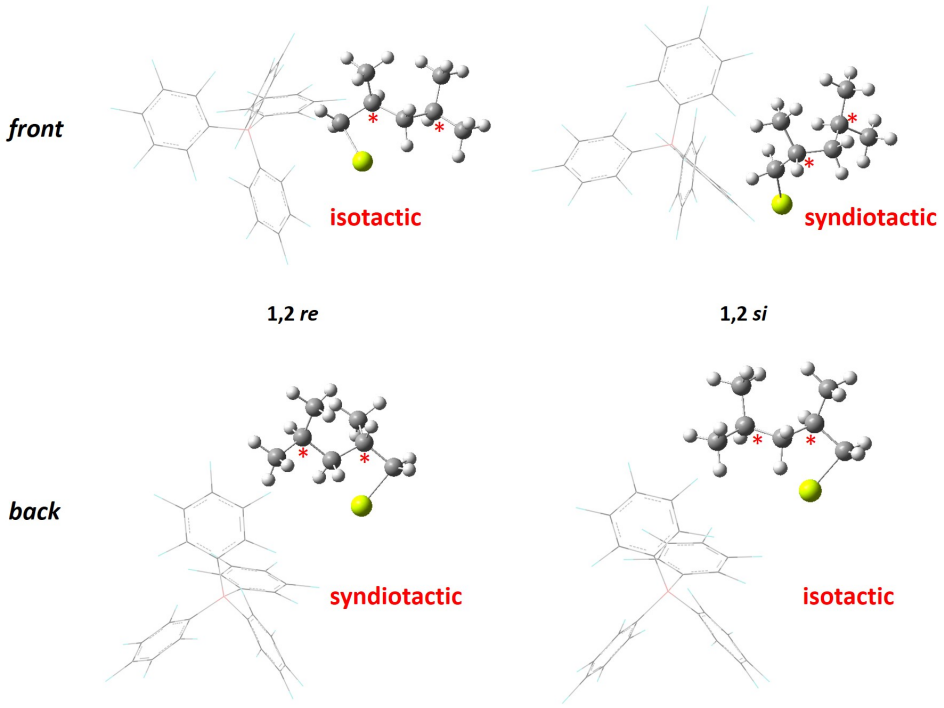

Figure 4.20: Representations of the second propylene insertion products *via* the 1,2 *re/si* mechanisms. Stars indicate chiral centres along the growing polymer chain. The cation is rendered as a ball-and-stick model, whereas the anion is displayed as a wire-frame. The ancillary ligands are omitted for clarity.

Comparison with Naked-Cation Model

In order to study the effect of the anion on propylene homopolymerisation we compare ion-pair surfaces calculated with those calculated using the naked-cation approximation. As with ethylene homopolymerisation, we compare the *front* side approach of monomer coordination with the coordination of propylene to the vacant site *via* the N(iPr)$_2$ side of the catalyst. Figure 4.21 displays such naked-cation surfaces, and values for the relative free energies are presented in Table 4.7. Geometric data and corresponding structures for the naked-cation stationary points may be found in Appendices G and H, respectively. Akin to the naked-cation ethylene homopolymerisation surface, the formation of π-adducts is exergonic for all stereo- and regio-isomers. The same trend in relative stabilities in π as for the *front* direction ion-pair calculations is observed, in that adducts for 1,2 insertion are favoured over 2,1, and coordination *via* the *re* is slightly preferable. The geometric data in Appendix G shows that no agostic interaction is present in these first monomer adducts, in agreement with the ion-pair model.

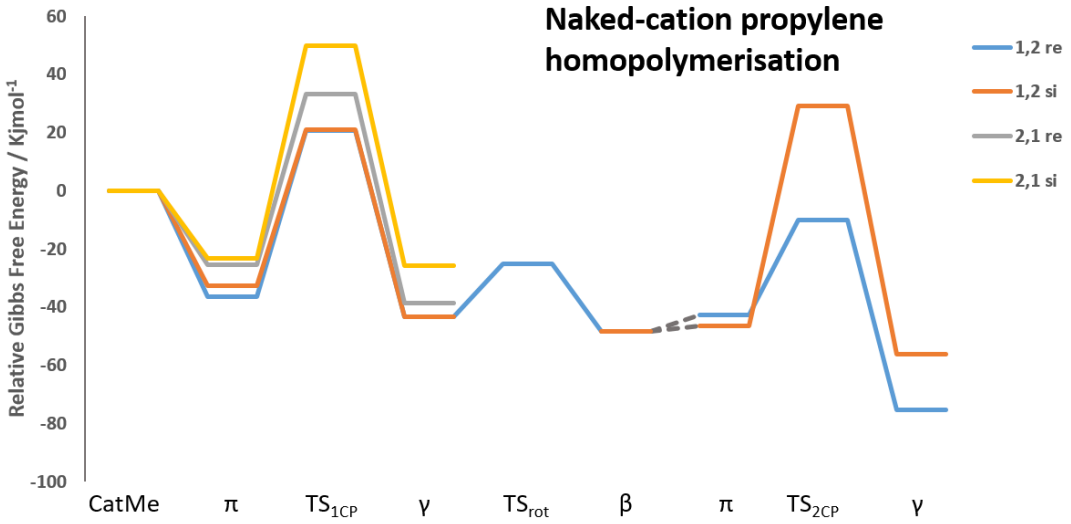

Figure 4.21: Gibbs free energy profiles (298 K) for two chain propagation steps of propylene homopolymerisation calculated with without the $[BF_{20}]^-$ anion.

	1,2 *re*	1,2 *si*	2,1 *re*	2,1 *si*
CatMe	0.0	0.0	0.0	0.0
π	-36.3	-32.7	-25.6	-23.4
TS_{1CP}	20.6	20.9	33.2	50.0
γ	-43.4	-43.3	-38.7	-25.7
TS_{rot}	-25.1			
β	-48.5	-48.5		
π	-42.8	-46.3		
TS_{2CP}	-10.1 (anti)	29.1 (syn)		
γ	-75.5	-56.1		

Table 4.7: Relative Gibbs free energies ($kJmol^{-1}$) of the stationary points along the first two chain propagation steps of propylene homopolymerisation calculated without the $[BF_{20}]^-$ anion.

The relative stabilities (Table 4.7) of the stationary points corresponding to the different stereo- and regio- isomers follow the same ordering as for the ion-pair model, with the exception of the second CP products, where in the naked-cation model both products display γ-agostic interactions in the absence of the counter-anion. The overall exergonicity of the insertion reactions is greater for the cationic model, in agreement with the ethylene study, and the literature. Also echoing the results from the ethylene homopolymerisation study, the

Ti–H and C–H distances are generally shorter and longer, respectively, in the naked-cation model *cf.* the ion-pair.

Internal barriers to first propylene insertion reactions follow the same orders as for the *front* approach IP model, but are ∼10 kJmol^{-1} lower: 1,2 *si* < 1,2 *re* < 2,1 *re* < 2,1 *si*. The rotational TS, **TS$_{rot}$**, between the γ product of 1,2 *re* insertion and the β agostomer was located, and has a relatively small barrier of 18 kJmol^{-1}, yielding a stabilisation of ∼ 5 kJmol^{-1}.

Chain Termination Reactions

Chain termination reactions analogous to those discussed in Chapter 3 were calculated for the β-agostic isobutyl ion-pair. Figure 4.22 shows the reaction profiles for CP modelled by 1,2 *re* insertion into the Ti–C(iBu) bond, BHTTi, and BHTM calculated with thermodynamic corrections at RT and elevated temperatures. As with the surfaces for the naked-cation analogues in Chapter 3 (page 73), the relative energies of the stationary points are shifted upwards upon increasing temperature.

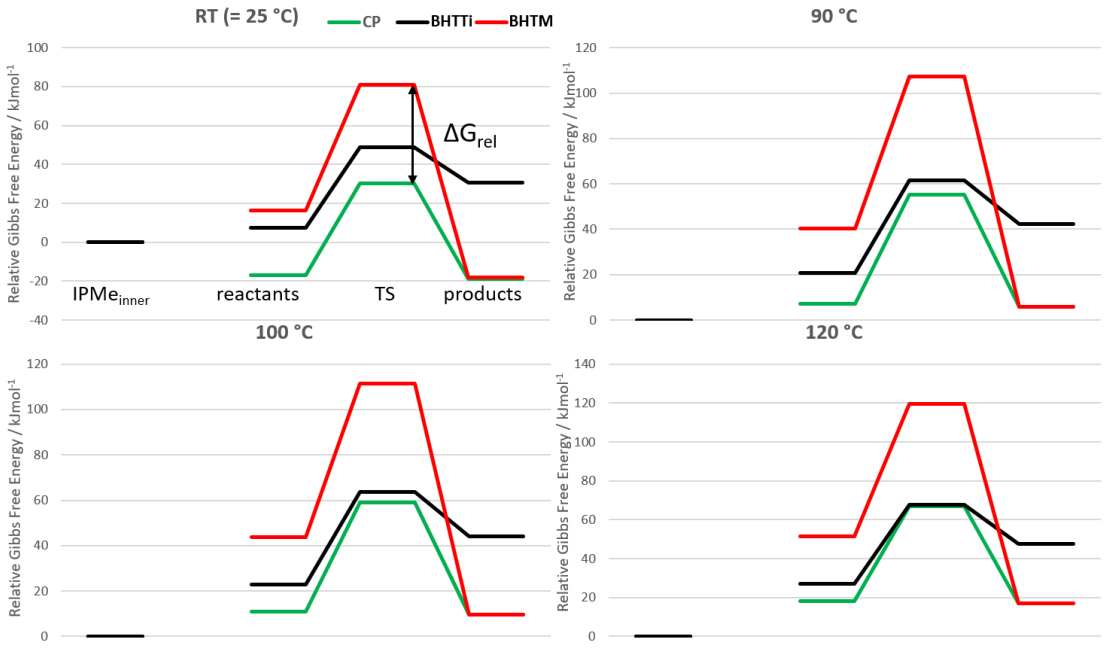

Figure 4.22: Gibbs free energy profiles for CP, BHTTi and BHTM calculated at 298, 363, 373 and 393 K (25, 90, 100 and 120°C, respectively). Labels along the reactions pathways are only displayed in the RT graph for clarity.

For the cationic systems the barriers to CP and CT are expected to be greater than those related to rotations of the iBu chain that may be required for CP to take place, and as such the barriers could be calculated from the same starting point, namely the β-agostic isobutyl catalyst. However, for the ion-pair systems the situation is more complex and a structure from which the free energy barriers should be compared is not immediately clear. In this instance, we instead compare the relative stabilities of the TSs, i.e. their free energies relative to the starting inner-sphere methyl ion-pair. The relative energies are displayed in Table 4.8, along with the difference between the relative energies of the CT TSs, and that of the CP TS ($\Delta G_{\text{rel.}}$), as indicated in Figure 4.22. The same method was also carried out by Laine *et al.* in their study of CP *vs.* BHTM,[154] and allows for a direct comparison to be made.

	T	CP	BHTTi	BHTM
G_{TS}(rel.)	RT	30.4	48.8	80.9
	90	55.3	61.6	107.5
	100	59.2	63.6	111.6
	120	66.8	67.5	119.7
$\Delta G_{\text{rel.}}$	RT		18.4	50.5
	90		6.3	52.2
	100		4.4	52.4
	120		0.7	52.9

Table 4.8: Relative Gibbs free energies (kJmol^{-1}) of the ion-pair transition states (G_{TS}(rel.)) and differences between the relative energies of the CT TSs, and those of the CP TS ($\Delta G_{\text{rel.}}$) calculated at 298, 363, 373 and 393 K (25, 90, 100 and 120°C, respectively). All values are in kJmol^{-1}.

At RT $\Delta G_{\text{rel.}}$ for BHTM relative to CP is 50.5 kJmol^{-1}, in comparison to 10.3, 40.5, and 33.0 kJmol^{-1} for the **Cp**-, **4-PhInd**-, and **4,5-BenzInd**-BF_{20} ion-pairs (See Figure 4.3), respectively, and indicates that the post-metallocene catalyst in the present study is capable of producing a higher molecular weight polymer than the zirconocenes if BHTM was the only termination pathway. BHTTi relative to CP has a $\Delta G_{\text{rel.}}$ of 18.4 kJmol^{-1}, however the BHTTi reaction pathway was not presented in the work by Laine *et al.*. The values of $\Delta G_{\text{rel.}}$ for BHTM relative to CP at elevated temperatures are $\sim$2 kJmol higher, indicating that as T is increased CP becomes slightly more favourable. The BHTTi mechanism for CT, however, becomes increasingly competitive as T is increased and indicates that a lower

temperature is recommended for higher molecular weight polypropylene production.

Summary

On the basis of predicted lowest energy π_{perp} rotations to "normal" π-adducts, and also by comparing relative energies of TS, there is a regio preference for 1,2 insertion. This is *via* opposite stereoisomers from the *front* and *back* directions, as there is enantiomorphic site control to monomer coordination.

Absence of anion displacement barriers prevent a firm statement of the predicted steroeregularity of the polymer produced using the κ^1-amidinate catalyst; however, polymerisation *via* both the *front* and *back* directions predicted the production of an isotactic polymer on the basis of barrier heights, in addition to the fact that the syndiotactic polymer is a stabilised inner-sphere resting state from the *front* direction.

The relative energies of the π-adducts are the key differences between the the ion-pair and naked-cation models, as also observed for ethylene homopolymerisation. Additionally, formation of stable inner-sphere ion-pairs *via* disruption of agostic interactions indicates that resting states are thermodynamically accessible. This is expected to slow the polymerisation process down as more energy is required to displace the close contact anion from the Ti coordination sphere.

Studies of CT mechanisms for the ion-pair show that the TS to propagation is lower than that to BHTTi, even at elevated temperatures. This is in contrast to the naked-cation studies in Chapter 3, and is due to the greater $-T\Delta S$ contribution to the BHTTi TS in the ion-pair. These ion-pair studies show that a higher degree of polymerisation is expected at a lower *T*.

4.4 Concluding Remarks

Ion-pair calculations of ethylene and propylene homopolymerisation were carried out from the *front* and *back* directions of monomer approach, and were compared to the respective naked-cation models. In the case of ethylene polymerisation, the preference for direction of monomer approach does not affect the resulting polymer, only the rate at which polymerisation takes place. Unfortunately, TSs for the expected rate determining anion-displacement step could not be located, however internal barriers to a second ethylene insertion are $\sim$40 and 30 kJmol^{-1} from the *front* and *back* directions of approach, respectively, compared to $\sim$25 kJmol^{-1} for the naked cationic model. The larger barrier from the front approach is attributed to a greater cation-anion interaction in the preceding adduct, illustrated by shorter Ti–B and Ti–F distances, which must be disrupted for insertion to take place. The formation of π-adducts also requires rearrangement of the ion-pair for the active site to become available to the monomer. It is ion-pair interactions such as these that are expected to affect the rate of polymerisation relative to the cationic model. Indeed, thermodynamically stable inner-sphere resting states after *front* insertion of ethylene may inhibit polymerisation by requiring a second anion-displacement TS to be overcome.

The formation of π-adducts is the most significant difference between the ion-pair and naked-cationic models of propylene polymerisation, with anion-cation interactions in resting states requiring distortion in order for monomer coordination to take place. Agostic interactions may prohibit the formation of inner-sphere resting states in both ethylene and propylene homopolymerisation, however. Analysis of agostic interactions, as well as that between the ion-pair, would be an interesting direction in which to take this study further, and could be undertaken using AIMAll. Quantification of the non-covalent interactions may provide insight into the relative stabilities of the TSs for insertion. This, unfortunately, was beyond the scope of the present work, however a brief study by Sandhya *et al.* showed that as well as BCPs for agostic interactions, those for intramolecular interactions between H atoms of the growing polymer chain of those of the Ind ligands were present.[172] Such interactions, although weak (ρ = 0.009-0.010 a.u.) may influence the isotacticity of the polymer.

Chapter 5

Structure and Reactivity of Rare Earth Metal Boryl and Gallyl Compounds

5.1 Introduction

The rare earth metals, despite their name, are relatively abundant in the Earth's crust. Owing to their heavy use in clean technology applications from wind turbines to solar cells, and the geographical locations of their deposits, these elements are safeguarded by the United States Department of Energy under their "Critical Materials Strategy", as it is expected that they will become increasingly exploited in the near future.[176] It is therefore vital that the chemistry of these elements is understood as far as possible, in order to optimise their utilisation and recovery. Coordination chemistry of the rare earth metals is dominated by oxygen and nitrogen based ligand sets, as the high Lewis acidity of the rare earth metals leads them to preferentially form bonds with Lewis base donor compounds. This chapter examines the structure and reactivity of rare earth-containing compounds going beyond these limitations, namely those containing bonds to the group 13 elements, boron and gallium.

5.1.1 Rare Earth Metals

The rare earth metals are a group of 17 elements, including the lanthanides and two group 3 metals, Sc and Y.[177] These two transition metal elements are grouped together with the lanthanides as they are generally found in the same ore deposits, and exhibit similar chemical properties. The rare earth metals are often denoted Ln from herein. The chemistry of these metals is dominated by the $+3$ oxidation state. When electrons are removed from the

neutral metal atom the effective nuclear charge, Z_{eff}, increases, causing stabilisation of the orbitals as the attraction of the electrons to the nucleus becomes stronger. The 4*f* shell with no radial nodes, as well as the 5*d* shell with two radial nodes, are both able to penetrate the inner core electrons to a greater extent than the 6*s* shell displaying five radial nodes. This penetration can be seen in Figure 5.1. The ordering of the stabilisation is therefore 4*f* $>$ 5*d* $>$ 6*s*, resulting in the electrons being first removed from the 6*s* and 5*d* levels, and only when these are empty are subsequent electrons removed from the 4*f*, accounting for the preferred $+3$ oxidation state of the lanthanides. This oxidation state is also the most common for Sc and Y, as their $4/5s$ and $3/4d$ electrons are removed readily.

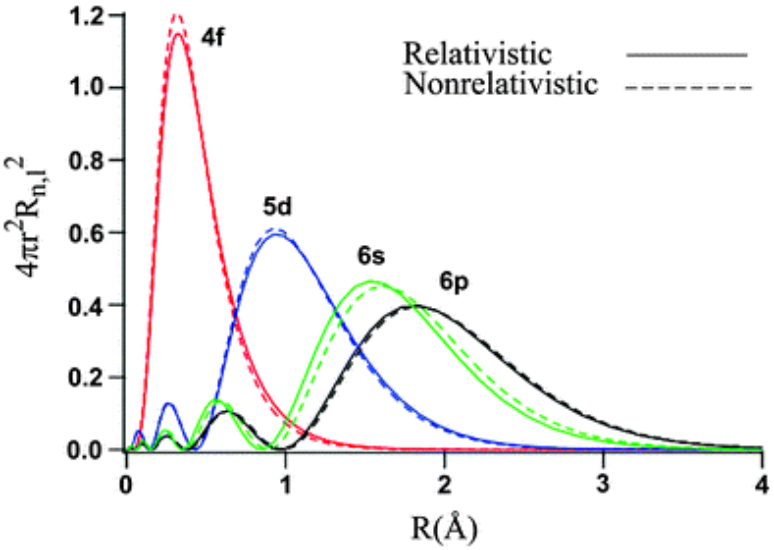

Figure 5.1: Radial distribution functions of the 4*f*, 5*d*, 6*s*, and 6*p* orbitals of Sm^{3+}.[178]

Figure 5.2 shows the decrease in ionic radii of the Ln^{3+} ions as the period is crossed from La to Lu. The trend observed is termed the lanthanide contraction and is attributed to the poor shielding of the other valence electrons by the 4*f* electrons, and Z_{eff} increasing as each additional *f* electron is added. The contraction is responsible for the ordering of ionic radii of Y $>$ Lu $>$ Sc, as displayed in Table 5.1. These Ln^{3+} ions are "hard" owing to their large size and high charge densities, and as such act as Lewis acids with a preference to interact with hard Lewis bases.

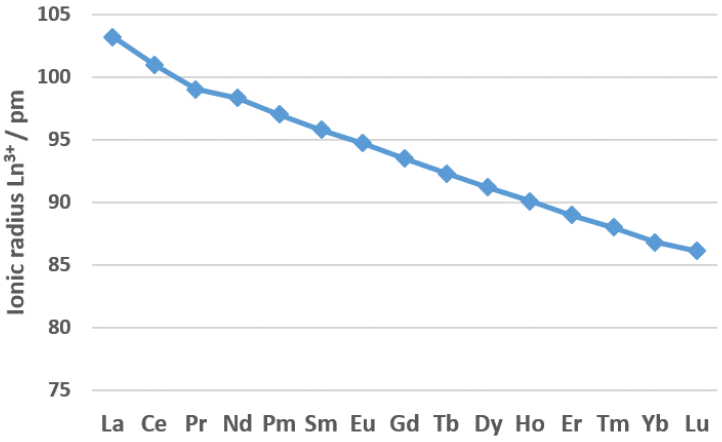

Figure 5.2: Ln^{3+} ionic radii of the lanthanides in pm.[179]

Ln3+	Sc	Y	Lu
Ionic radius /pm	74.5	90.0	86.1

Table 5.1: 3+ ionic radii (pm) of Ln elements.[179]

5.1.2 Group 13

The results discussed in Sections 5.3.1 to 5.3.5 concern the bonding between rare earth metals and two of the lighter elements of group 13, B and Ga. These elements, as well as Al, have been shown experimentally to form stable ions as part of the heterocyclic diazabutadienyl ligand,[180–182] having previously been predicted using DFT by Sundermann *et al.*[183] These compounds are valence isoelectronic analogues of the N-heterocyclic carbene class of ligand, NHC, and the structure of such compounds is shown in Figure 5.3. The left-hand structure is more representative of the boryl-containing ion, where the B–N interaction may be described as a polar covalent bond. For the less electronegative Al, Ga, and In elements, however, the right-hand structure is a better model, as the more electronegative N atoms assume the formal negative charges.[183,184] Here we focus on the structure and bonding behaviour of B and Ga containing analogues denoted boryl and gallyl, respectively.

The group 13 atoms of the boryl and gallyl ligands are sp^2-hybridised, with a lone pair of electrons available for metal-to-ligand σ-bonding occupying one of these hybridised orbitals. (Figure 5.4) While the group 13 atoms in their three-coordinate orientation possess an

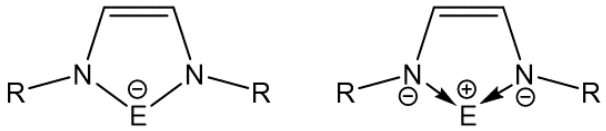

Figure 5.3: Canonical structures of $[E(NRCH)_2]^-$. E denotes a group 13 atom.

"empty" *p*-orbital into which π donation from a transition metal centre may take place, it is generally understood to be a weak interaction.[185] Both the boryl and gallyl ligands have been shown to display *trans* influencing behaviour owing to their electropositivity.[185–187] Zhu *et al.* illustrated that boryl ligands containing N atoms display a greater *trans* influence on the Pt–Cl bond of *trans*-$[PtLCl(PMe_3)_2]$ than those containing O atoms, reflecting the fact that O is more electronegative than N, and boryl ligands containing substituents of greater electronegativity display a weaker *trans* influence.[186]

Figure 5.4: Lone pair on sp^2-hybridised boryl ligand.

The boryl anion, $[B(NDippCH)_2]^-$ (Dipp = 2,6-$(iPr)_2C_6H_3$), was investigated by Yamashita *et al.*, the HOMO of which is shown in the central image of Figure 5.5.[188] A comparison between the left and central images of Figure 5.5 indicates the similarity between the sp^2 lone pair on the boryl anion and that of the phenyl anion. Upon complexation with the Li moiety (right hand image of Figure 5.5) the lone pair character is relatively unaltered, indicating that the B–Li interaction is "polar" in nature. This polar nature was characterised by a small values of ρ and positive Laplacian, 0.029 and 0.084, respectively, for the boryllithium Li–B BCP. This boryllithium complex reacts with various organic electrophiles to form organoboron complexes, validating the nucleophilic nature of the boryl ligand.[182,189]

A decade passed after the isolation of the boryllithium complex described above before a gallyl anion was first characterised by Schmidt *et al*,[180] followed by extensive work in the group of Jones.[187,190–202] Pandey studied the electronic structure of the metal gallyl compounds $[(NHC)M\{B(NPhCH)_2\}]$ (NHC=:C$(NPhCH)_2$, M = Cu, Ag, and Au),

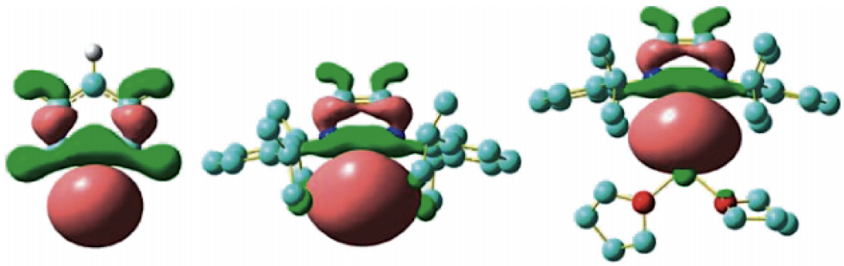

Figure 5.5: HOMO of phenyl anion (left), boryl anion(centre), and boryllithium reported by Yamashita *et al.*[188]

an example of which is shown in Figure 5.6.[203] The M–Ga bonds are shorter than the sums of their respective covalent radii by ∼0.1 Å, with the bond distance increasing from Cu to Au to Ag. It was established that the HOMO-1 displays significant σ-bonding character (Figure 5.6B), with high Ga *s* character (>71%), while the π-backbonding was found to be insignificant. N-Ga-N bond angles were seen to decrease as group 11 is descended, attributed to smaller Ga *s* character of the Ga-N bonds - an analogous structural change is discussed further in Section 5.3.4. An EDA of ionic fragments showed that the interaction energies follow a V-like trend when plotted against M–Ga bond distance, with a minimum at the Ag complex. This was rationalised by relativistic effects which become important for the 5d elements.

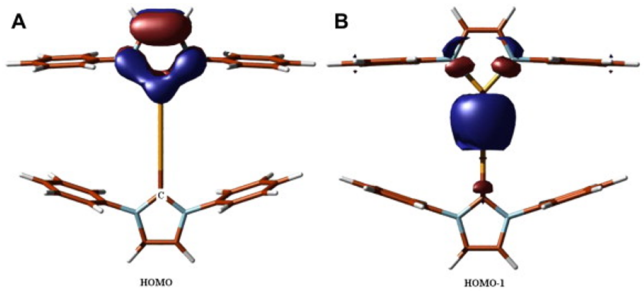

Figure 5.6: HOMO-1 and HOMO of $[(NHC)Ag\{Ga(NPhCH)_2\}]$ (NHC = $:C(NPhCH)_2$).[203]

Protchenko *et al.* reported the difference in reactivity of $[(CHNDipp)_2E]$ anions (E = B, Ga) with half-sandwich titanium imido complex Cp*TiCl(NtBu)py (py = pyridine).[199] While salt-metathesis takes place with the gallyl reagent, the boryl instead attacks the pyridine ligand at the 2 position. The authors attributed this to their differing electronic properties; the boryl moiety is significantly more nucleophilic than its gallium analogue, with a more

negative partial charge at the E atom, and with a more directional lone pair.

5.1.3 Rare Earth Metal Boron and Gallium Bonded Compounds

In addition to the many transition metal-group 13 complexes, rare earth metal boryl and gallyl systems have also been reported. The first Ln-group 13 bond was in fact a Ln-Al bond, in the complexes $Cp^*_2Ln–AlCp^*$, where Ln = Eu and Yb.[204] The interaction is considered largely ionic, with insignificant covalent or charge transfer contributions to the Ln–Al bond. In contrast to the M–Ga bonds described by Pandey, the Eu–Al and Yb–Al bond distances are 0.17 and 0.11 Å longer than the sums on their covalent radii, and a binding energy of 30 $kJmol^{-1}$ indicates the weakness of the interaction.

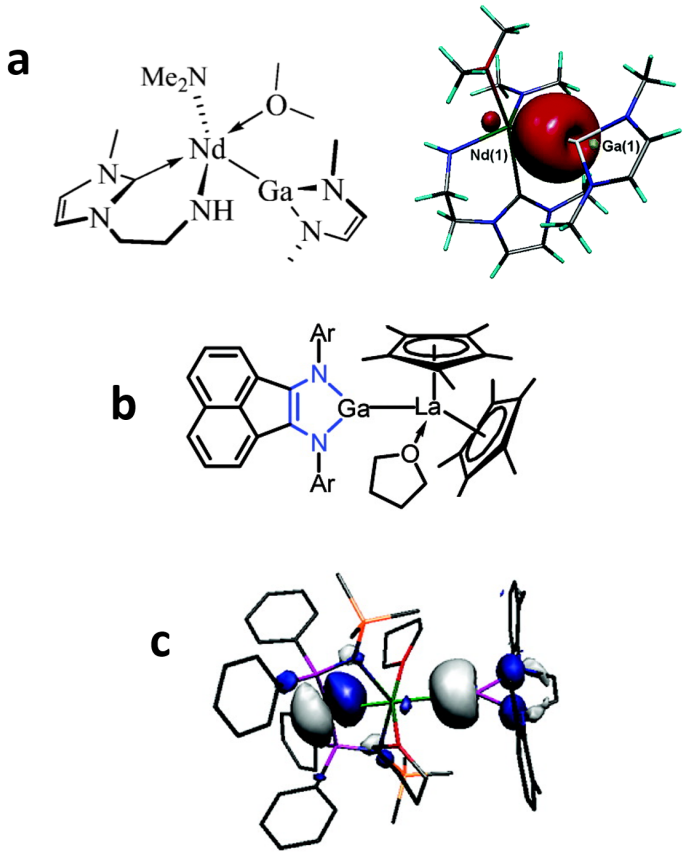

Figure 5.7: **a**) Nd–Ga NBO of $[Nd(L')(N'')(OMe_2)][Ga(NMeCH)_2]$(L = $HNCH_2CH_2\{C(NCHCHNMe)\}$;N'' = NMe_2).[205] **b**) La–Ga compound (dpp-Bian)GaLa$(Cp^*)_2$(THF) (dpp-Bian = 1,2-bis[(2,6-diisopropylphenyl)imino]acenaphthene).[206] **c**) HOMO-2 Y–Ga bonding orbital of $[Y\{Ga(NArCH)_2\}(BIPM)(THF)_2]$ (Ar = 2,6-methylphenyl; BIPM = $\{C(PPh_2NSiMe_3)_2\}^{2-}$).[198]

Arnold *et al.* synthesised the first stable Ln–Ga bond, displaying a Ga$\longrightarrow$Nd interaction of charge transfer and covalent character shown in Figure 5.7**a**.[205] A natural bonding orbital (NBO) analysis of the bond showed contributions of 87 and 13% from the Ga and Nd atoms, respectively. A La–Ga bonded complex, synthesised by Fedushkin *et al.*, also displayed a highly polarised covalent bond, with contributions from Ga and La to two La–Ga bonding orbitals of 80 and 20% (Figure 5.7**b**).[206] The Y–Ga bond of the yttrium carbene-gallyl complex shown in Figure 5.7**c** was also reported as strongly polarised, with only 2% contribution from the Y atom.[198]

As mentioned above, the boryllithium complex of Yamashita *et al.* has been used as a precursor in organoboron chemistry, including the synthesis of the first Ln–B bonds by Saleh *et al.*.[207] Figure 5.8 shows the structures of the Sc and Lu boryl complexes, as well as the Kohn-Sham HOMO of the Y–B complex. On the basis of low values of ρ ($\leq$0.05 a.u.) and small negative value of H at the Ln–B BCP, the interactions were described as predominantly ionic. This was supported by Hirshfeld charge differences between the Ln atom and boryl group of 0.69 and 0.82 for the Sc and Y/Lu complexes. The Sc–B interaction was deemed the least ionic, whereas Y–B the most. The normalised contributions to the σ-bonding HOMO of the Ln–B atoms were also in agreement with this conclusion, with B contributions of 62, 70, and 66% for the Sc–, Y–, and Lu–B interaction, respectively. As there is a greater degree of mixing in the Ln–B σ-bonding orbital than in the Ln–Ga described above, the interactions were described as "largely ionic, albeit with a (highly polarized) covalent contribution". The authors also related the degree of ionicity in the Ln–B bond to the sums of the first three ionisation energies of the Ln atoms, where the lowest sum correlated with the most ionic bond (Y).

5.1.4 Metal-Boryl Reactivity

Metal-boron bonds have been utilised in a range of reactions owing to the relatively high electropositivity of the B atom and the empty *p*-orbitals available when in its sp^2 hybridised, three-coordinate boryl form.[208] Such properties lend themselves well to transformations with small molecules. A multitude of reactions involving the transition metal–boron bond has been reviewed extensively by Irvine, and will not be repeated here; a few key examples

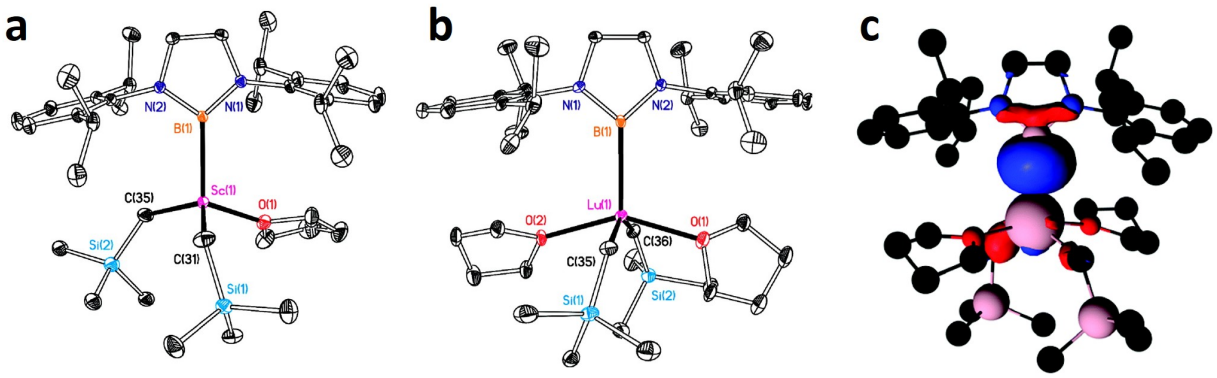

Figure 5.8: **a**) X-ray crystal structure of $Sc\{B(NArCH)_2\}(CH_2SiMe_3)_2(THF)$. **b**) X-ray crystal structure of $Lu\{B(NArCH)_2\}(CH_2SiMe_3)_2(THF)_2$. **c**) HOMO of $Y\{B(NArCH)_2\}(CH_2SiMe_3)_2(THF)_2$ showing Y–B interaction.[207]

are given in this section.[209] Wilkinson's catalyst, $RhCl(PP)_3$), was used in transition metal catalysed hydroboration of alkenes.[210,211] The formation of the Rh–B bond is a key step in the reaction mechanism, followed by insertion of an alkene into the Rh–H bond, and subsequent reductive elimation yielding an alkylborane. Similar mechanisms were also reported for hydroboration utilising Pd–, and Ni–B bonds.[212–214]

Alkyl boronate esters are common synthetic reagents, and have been shown to be the product of the photochemical reaction of alkanes with $CpM(CO)_nB(OR)_2$ (M = Fe, Ru (n = 2), W (n = 3); Cp = Cp, Cp*).[215,216] Such reactions are examples of the functionalisation of unreactive C–H bonds, and are very important for the synthetic chemist. Strikingly, the reaction of pentane with $Cp^*W(CO)_3B(OR)_2$, shown in Scheme 5.1, led to the selective functionalisation of a primary C–H bond, yielding only a linear pentyl boronate ester.

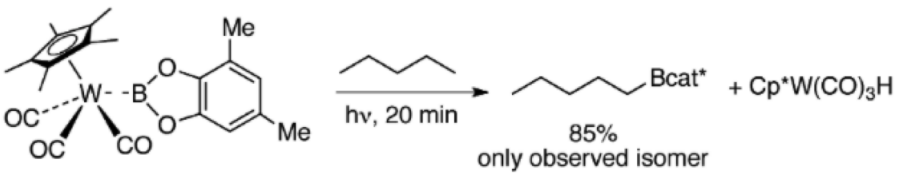

Scheme 5.1: Reaction of $Cp^*W(CO)_3B(OR)_2$ with pentane.[208]

Further important reactions include insertion of small molecules into M–B bonds. The group of Hou has reported the double insertion of CO into the Sc–B bond, shown in Scheme 5.2, producing a ketene species *via* η^2-CO(boryl) and ketene-like intermediates.[217] Subsequent studies utilising the later-discovered Sc-boryl complex,

$[Me_2Si(Cp^*)(NPh)ScB(NDippCH)_2\}(\mu\text{-}Cl)Li(THF)_3]$,[218] were able to isolate the scandium boryl oxycarbene complex shown in Figure 5.9**a**.[218] Hou and co-workers also reported the insertion of the carbodiimide, iPrNCNiPr, into the Sc–B bond as shown in Figure 5.9**b**. The Sc atom is bonded to 6 N atoms in a distorted octahedral geometry and the Sc–N bond distances are ∼0.05 Å longer than in the Sc–B bonded precursor. The insertion of carbodiimides into Ln–E bonds is explored further in Section 5.3.5.

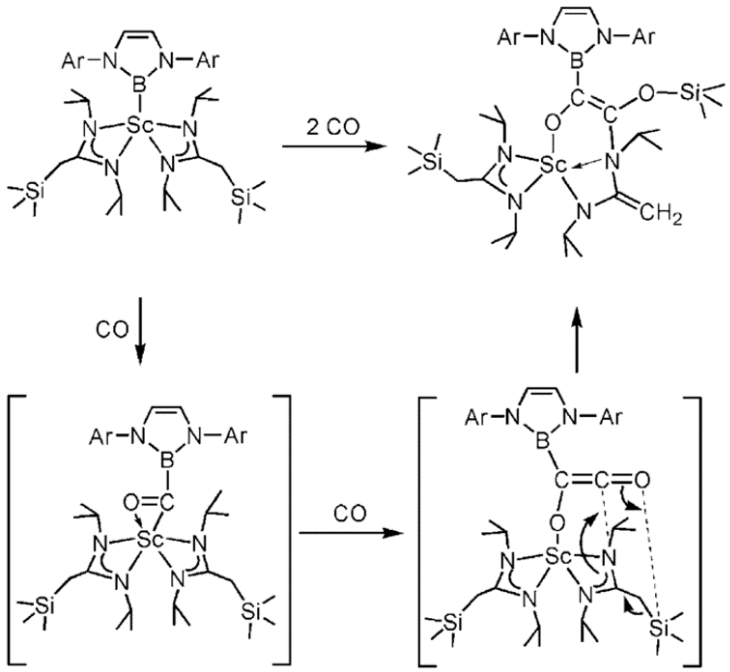

Scheme 5.2: Possible mechanism of formation of ketene species.[217]

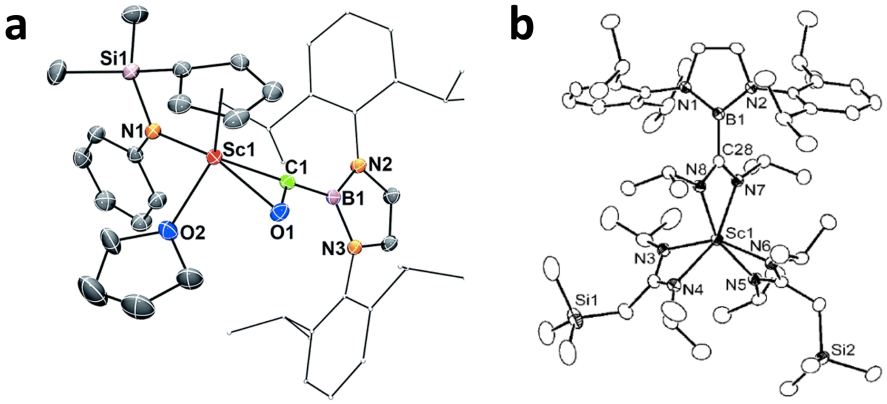

Figure 5.9: **a**) Scandium boryl oxycarbene.[218] **b**) iPrNCNiPr inserted across Sc–B bond.[217]

5.1.5 Metal-Gallyl Reactivity

Compared to the wealth of chemistry involving metal-boryl bonds there are scarcely any examples of the metal-gallyl analogues. Jones *et al.* showed that reactions of alkenes and alkynes with $Pt(dppe)_2\{Ga(NArCH)_2\}_2$ and $Cu\{C(NArCH)_2\}\{Ga(NArCH)_2\}$ resulted in no clean reaction at the M–Ga bond, and a mixture of products were formed.[219, 220]

The following results section examines the geometry and electronic structure of rare earth metal boryl and gallyl complexes in order to understand the differences in reactivity of their respective Ln–E bonds. A mechanistic study of carbodiimide insertion into a Mg–gallyl bond-containing is also presented.

5.2 Computational Details

Scalar relativistic, gradient-corrected DFT calculations were carried out using the Grimme D3 dispersion correction[31] with the PBE functional[26,126] as implemented in Amsterdam Density Functional 2013.01 Rev. C (ADF),[41,221,222] and G09 Rev. D.01[40] quantum chemistry codes. QTAIM analyses were performed using the AIMAll version 14 programme,[42] using formatted G09 checkpoint files as input.

Geometry optimisations were carried out in ADF, using the Zeroth Order Regular Approximation (ZORA) Hamiltonian. Slater Type Orbital basis sets of triple zeta plus double polarization function quality (TZ2P) ZORA basis sets were used for Sc, Y, Lu and Ga, and the double zeta plus polarization (DZP) ZORA basis set for the rest of the atoms. The frozen core approximation was incorporated for all atoms; Sc(2p), Si(2p), Ga(3p), Y(3d), Lu(4d), 1s for all other atoms bar H. The default SCF convergence criteria were used, together with an integration grid of 4.5 and a geometry convergence energy gradient of 0.001 Hartree/Ångstrom. Starting geometries were taken directly from crystal structures of **ScGa** and **LnB** (see overleaf), or a modification thereof, e.g. swapping metal or ligating atoms. Hirshfeld charge,[46] Foster-Boys Localized Orbitals,[223–225] and Ziegler-Rauk bond energy decomposition (EDA)[48,226] analyses were carried out. EDA data for the interacting neutral fragments of the gallyl system without a THF adduct (**LnGa$_{\text{-THF}}$**) could not be obtained owing to difficulties converging the gallyl fragments with Aufbau orbital populations.

Grimme D3 dispersion corrected PBE single point calculations on optimized ADF structures were carried out in G09, to produce formatted checkpoint files for use in AIMALL. A segmented all-electron relativistically contracted basis set, of TZVP quality for Lu,[227] and relativistically recontracted variants of the Karlsruhe def2 TZVP basis sets[228] were used for all other atoms. The Douglas-Kroll-Hess second order Hamiltonian (DKH2) was employed in all G09 calculations.

Mechanistic studies described in Section 5.3.6 were carried out using G09 Rev. D.01, implementing the PBE XC functional. Dunning's correlation-consistent polarised valence DZ (cc-pVDZ) basis sets were employed for all elements. The default SCF and geometry convergence criteria were used, along with an ultrafine integration grid. Structures were

initially optimised without a Grimme D3 dispersion correction and TSs for R, R', R"' = H, R" = Me were found *via* relaxed potential energy scans of relevant coordinates. Minima either side of these TSs were found by manually displacing the structures a small distance along the imaginary vibrational mode in either direction, and optimising from there. TSs for successive larger R, R', R", R"' groups were calculated by first freezing the core atoms of the structures (i.e. those which are not R, R', R", R"') while optimising the positions of the new groups. This was found to yield structures with largest imaginary vibrational mode corresponding to the desired reaction coordinate. Subsequent optimisations of the TSs were carried out with the Grimme D3 dispersion correction, with minima either side calculated as described above. The full systems (R=Me, R',R"' = Dipp, R" = Tol) were optimised with the Grimme D3 dispersion correction, and starting TS structure were built from the D3 optimised structures calculated for (R=Me, R', R", R"' = iPr). A TS between **4c-int** and **Mg-N** could not be located after many relaxed potential energy scan studies.

5.3 Results and Discussion

The following results section refers to compounds that were synthesised and characterised at the University of Oxford by Dr Liban Saleh, Dr Matthew Blake, and Mr Adàn Reyes-Sanchez, under the supervision of Professor Philip Mountford.

5.3.1 Rare-Earth Metal Boryl and Gallyl Compounds

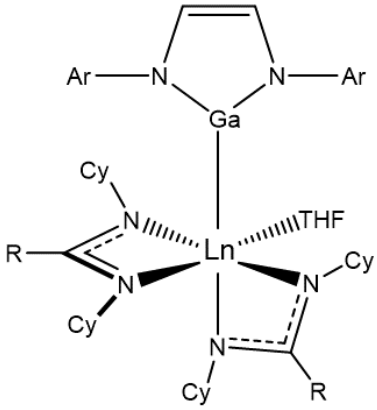

Ln = Sc (**ScGa**), Y (**YGa**), Lu (**LuGa**)
R = CH_2SiMe_3
Ar = Dipp

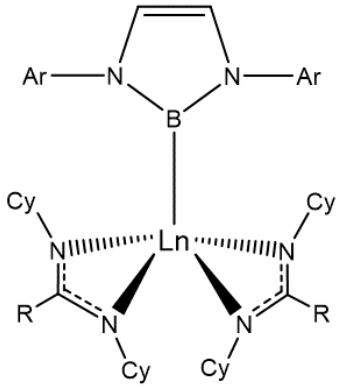

Ln = Sc (**ScB**), Y (**YB**), Lu (**LuB**)
R = CH_2SiMe_3
Ar = Dipp

Figure 5.10: The experimentally isolable **LnGa** and **LnB** (Ln{E(NArCH)$_2$}{Me$_3$SiCH$_2$C(NCy)$_2$}$_2$(THF)$_n$ (Ln = Sc, Y, Lu; E = B, Ga; n = 0, 1)).

Figure 5.10 shows the structures of Ln-gallyls (**ScGa**, **YGa**, **LuGa = LnGa**) and Ln-boryls (**ScB**, **YB**, **LuB** = **LnB**). The Ln-gallyls (**LnGa**) adopt a six-coordinate distorted octahedral geometry, containing one coordinated THF molecule; the Ln-boryls (**LnB**) are of distorted square-based pyramidal (SBP) geometry with the N atoms of the amidinate ligands forming the vertices at the base of the pyramid, and are THF-free. The N atoms of the chelated amidinate ligands of the six-coordinate **LnGa** compounds occupy an axial site and three equatorial sites, arranged such that one N atom is *trans* to the THF, one *trans* to the gallyl moiety, and two *trans* to another N atom.

Parameter	**ScB**	**YB**	**LuB**
Ln–E	2.473	2.638	2.573
	(2.4981(9))	(2.6616(14))	(2.620(5))
∠ N-E-N	99.9	99.8	99.9
	(100.05(7))	(100.43(11))	(101.2(4))
Ln–N (av.)[a]	2.190	2.341	2.298
	(2.1902(7))	(2.3362(11))	(2.2975(4))
Σr_{cov}(Ln,B)	2.54	2.74	2.71

Table 5.2: Key computed geometric parameters of the compounds **LnB**, with X-ray crystallographic parameters displayed in parentheses. Σr_{cov}(Ln,B) is the sum of the covalent radii of the Ln and B atoms. [a]An average of all four Ln–N bonds. Bond distances and angles in Å and °, respectively.

Parameter	**ScGa**	**YGa**	**LuGa**
Ln–E	2.886	3.036	2.974
	(3.0365(3))	-	-
∠ N-E-N	82.8	82.8	83.0
	(83.66(5))	-	-
Ln–N (av. trans to N)	2.201	2.365	2.322
	(2.1896(11))	-	-
Ln–N (trans to Ga)	2.189	2.340	2.296
	(2.1910(11))	-	-
Ln–N (trans to O)	2.153	2.311	2.268
	(2.1554(11))	-	-
Σr_{cov}(Ln,Ga)	2.93	3.13	2.974

Table 5.3: Key geometric parameters of the compounds **LnGa**, with X-ray crystallographic parameters displayed in parentheses. Σr_{cov}(Ln,Ga) is the sum of the covalent radii of the Ln and Ga atoms.**YGa** and **LuGa** could not be experimentally isolated for XRD data to be collected. Bond distances and angles in Å and °, respectively.

Selected structural data from these six compounds are displayed in Tables 5.2 and 5.3, with available crystallographic data shown in parentheses underneath those from the corresponding DFT structure. Both sets of compounds (**LnB** and **LnGa**) exhibit the expected period trend of Sc–E $<$ Y–E $>$ Lu–E bond distances, and all lie within the sum of the covalent radii, Σr_{cov}. The predicted structural data of the boryls **LnB** are in excellent agreement with those from experiment. The DFT Sc–N amidinate bond distances of **ScGa** also compare very well with the experimental data, and a structural *trans* influence effect is observed among all **LnGa**; the Sc–N bonds *trans* to the THF substituent are $\sim$0.05 Å shorter than the Sc–N bonds *trans* to other amidinate N atoms. The gallyl ligand has also been shown to display a significant *trans* influence,[187] however, the Ln–N bonds *trans* to the gallyl are between 0.012-0.026 Å shorter than those *trans* to an amidinate N atom in the DFT structures, indicating that it does not have as strong a *trans* influence as the amidinate N atoms. The data from the experimentally characterised **ScGa** suggest that the *trans* influencing ability of the gallyl and amidinate N atoms are comparable, however.

Experimentally, the Sc–Ga bond of **ScGa** is 0.15 Å longer than that predicted by DFT, although a previous study of Ln-boryl systems showed that alteration of Ln–B bonds by $\pm$0.05 Å from the equilibrium geometry changes the energy of the system by only up to 1 kJmol^{-1}.[207] To establish whether the Sc–Ga bond in **ScGa** also displays this softness, a relaxed potential energy scan of the Sc–Ga bond was carried out, as well as for the Sc–B, Sc–Y, and Lu–B bonds. Unfavourable steric interactions between the Ar and Cy/SiMe3 were found to play a significant role in the overall energy of the systems and therefore the latter organic groups were replaced with Me, in order to give more information about the Ln-E interaction itself. The Ar groups of the gallyl ligand were retained, however, as they are involved in π-conjugation. Figure 5.11 shows a plot of the change in r(Ln–E) of these stripped down versions of **ScGa** and **LnB** *vs.* the associated change in energy. Modification of the bonds by 0.1Å from the equilibrium geometry changes the total energy of the systems by less than 4 kJmol^{-1}, suggesting that the bond distance in **ScGa** is a suitable representation of that found experimentally, and also that caution must be undertaken when analysing these distances.

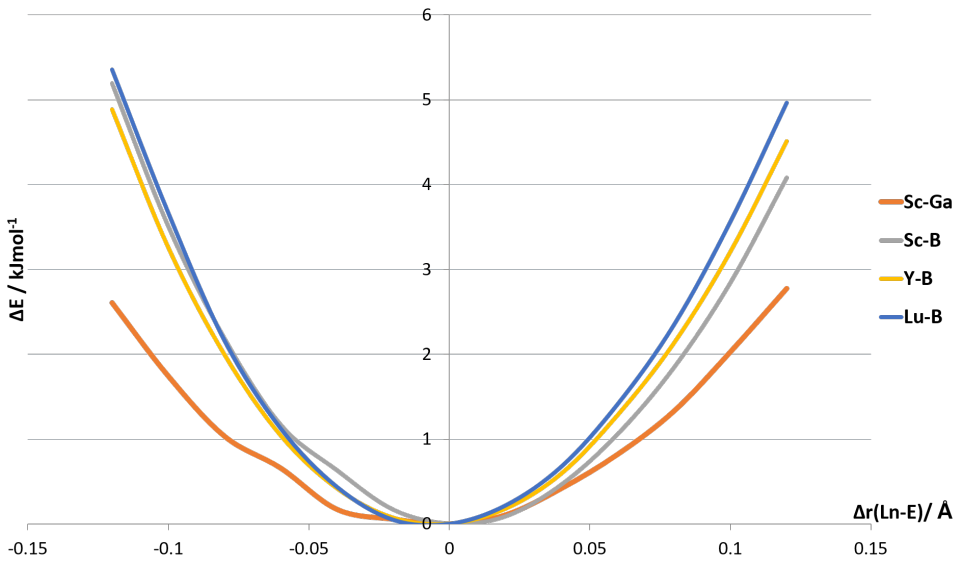

Figure 5.11: Relaxed potential energy scans of the Ln–E bonds of Sc(MeC(NMe)$_2$)$_2${ Ga(NArCH)$_2$}THF and Ln(MeC(NMe)$_2$)$_2${B(NArCH)$_2$}.

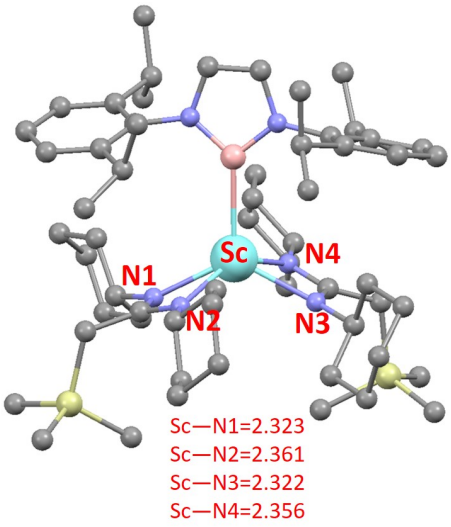

Figure 5.12: The structure of five-coordinate Ln(MeC(NMe)$_2$)$_2${B(NArCH)$_2$} (**ScB**), showing the difference in Ln–N bond distances of the same chelated (bis)amidinate ligands, in Å. H atoms are omitted for clarity.

As described above, the boryl compounds **LnB** adopt an unusual distorted SBP geometries, with noticeable differences in Ln–N bond distances. This distorted structure is displayed in Figure 5.12, showing the geometry of **ScB**. The adoption of such geometries is unlikely to be caused by electronic effects, as the C–N bond distances of the amidinate ligands all lie within 0.004 Å, indicating that the π-electrons are delocalised evenly along the N-C-N backbones. Steric effects are therefore likely to contribute largely to the

geometries in these compounds, forcing the aminidate ligands to twist and distort in order to accommodate the bulky N- and C-bound substituents. The five-coordinate Ln-boryl compounds $Ln(CH_2SiMe_3)_2\{B(NArCH_2)_2(THF)_2\}$ (Ln = Y, Lu) reported by Saleh *et al.* display less distorted SBP geometries, owing to the less bulky CH_2SiMe_3 ligands.[207]

5.3.2 Five- vs. Six-Coordinate Rare Earth Metal Boryl and Gallyl Compounds

Reaction	$\Delta_r H$	$T\Delta_r S$[a]	$\Delta_r G$
ScB + THF → ScB$_{THF}$	-16.0	-42.3	26.3
YB + THF → YB$_{THF}$	-44.6	-56.3	11.7
LuB + THF → LuB$_{THF}$	-31.8	-40.8	9.1
ScGa$_{-THF}$ + THF → ScGa	-87.2	-41.4	-45.8
YGa$_{-THF}$ + THF → YGa	-104.7	-44.9	-59.8
LuGa$_{-THF}$ + THF → LuGa	-103.3	-51.0	-52.3

Table 5.4: Thermodynamic data for the addition of THF to **LnB** and **LnGa$_{-THF}$**. All values are in kJmol^{-1}. [a] T = 298 K.

The rare earth metal gallyls, **LnGa**, exist as six-coordinate compounds with two bis-amidinate ligands and one coordinated THF molecule. To understand why the boryls, **LnB**, exist only as five-coordinate species, hypothetical THF adducts of these compounds, labelled **LnB$_{THF}$**, as well as THF-free version of the gallyls, **LnGa$_{-THF}$**, were also calculated. Reaction enthalpies, entropies, and Gibbs free energies of THF addition are displayed in Table 5.4. All six reactions exhibit favourable $\Delta_r H$ for the formation of a THF adduct, becoming increasingly favourable as the size of the metal covalent radius increases from Sc to Lu to Y. The magnitudes of $T\Delta_r S$ for the boryls, however, are significant enough to result in positive $\Delta_r G$ values, i.e. unfavourable free energies for the addition of THF to **LnB**. This unfavourable addition becomes increasingly so as the covalent radius of the metal decreases. In the case of the gallyls, however, while the $T\Delta_r S$ values are similar to those of the analogous boryls, the $\Delta_r H$ values are 2-5 times larger. This results in favourable $\Delta_r G$ values for the addition of THF to **LnGa$_{-THF}$**, becoming more favourable as the metal covalent radius increases. These results support the experimental observation that the boryls do not form THF adducts, whereas the gallyls indeed do.

Parameter	$\mathbf{ScB_{THF}}$	$\mathbf{YB_{THF}}$	$\mathbf{LuB_{THF}}$
Ln–B	2.589	2.745	2.672
∠ N-B-N	99.1	99.1	99.4
Ln-N (av. trans to N)	2.239	2.386	2.345
Ln-N (trans to B)	2.281	2.434	2.388
Ln-N (trans to O)	2.171	2.335	2.292

Table 5.5: Key geometric parameters for the hypothetical six-coordinate boryls ($\mathbf{LnB_{THF}}$). Bond distances and angles in Å and °, respectively.

The structures of the hypothetical boryls $\mathbf{LnB_{THF}}$ are six-coordinate distorted octahedral structures, resembling those of the gallyls **LnGa**, with selected geometric data displayed in Table 5.5. On increasing the coordination number of the rare earth metal from five to six, a lengthening of the Ln–B bond distances for all three metals in by ∼0.1 is observed. Also of note is a slight decrease of around 1° in the N-B-N angle of $\mathbf{LnB_{THF}}$ relative to **LnB**, which, while being a small change, indicates a slightly more ionic Ln–B interaction for all three rare earth metal-boryl bonds (See Section 5.3.4 for Bent's rule).

The *trans* influencing effect of the N atoms of the amidinate ligands *vs.* that of the THF molecule observed in the gallyls **LnGa** is replicated in the hypothetical six-coordinate boryls $\mathbf{LnB_{THF}}$, where the Ln–N bonds *trans* to the THF are 0.05-0.08 Å shorter than those *trans* to an amidinate N atom. While the structural data of **LnGa** indicate that the gallyl ligand is not quite as *trans* influencing as the N atoms of the amidinate ligands, the Ln–N bonds *trans* to the boryl moiety found in $\mathbf{LnB_{THF}}$ are ∼0.05 Å longer than those *trans* to amidinate N. This observation supports the assertion from the literature that the cyclic gallyl ligand has a weaker *trans* influence than the boryl.[187]

The hypothetical five-coordinate gallyl compounds $\mathbf{LnGa_{\text{-}THF}}$ resemble those of the experimentally isolable boryls **LnB**, exhibiting five-coordinate distorted SBP structures. Key bond lengths and angles $\mathbf{LnGa_{\text{-}THF}}$ are displayed in Table 5.6 and the trends observed in the **LnB** relating to the amidinate ligands are also replicated: the C–N bond distances within the amidiante ligands are similar, again indicating that there is even π-delocalisation across the N–C–N backbones, and that steric effects are responsible for the distortion from SBP geometry. In addition, the Ln–N(amidinate) bond distances are not equal, with one of the bonds on each amidinate ligand ∼0.04 Å longer than the other. This difference in

Parameter	**ScGa$_{\text{-THF}}$**	**YGa$_{\text{-THF}}$**	**LuGa$_{\text{-THF}}$**
Ln–Ga	2.726	2.89	2.825
∠ N-Ga-N	83.9	83.6	83.9
Ln-N (av.)a	2.1585	2.317	2.2735

Table 5.6: Key geometric parameters for the hypothetical five-coordinate gallyls (**LnGa$_{\text{-THF}}$**). Bond distances and angles in Å and °, respectively.

Ln–N(amidinate) bond length is not as large as that observed in the boryls **LnB**, however, and is likely a consequence of the bigger, and less nucleophilic, Ga atom forming longer Ln–Ga interactions, and opening up the coordination sphere around the Ln. With more room around the metal centre, the amidinate ligands of **LnGa$_{\text{-THF}}$** need not distort to such an extent as in the more crowded **LnB**, allowing the Ln–N bonds to arrange in a more equal fashion. The decrease ∼0.15 Å of the Ln–Ga bond distance in **LnGa$_{\text{-THF}}$** upon losing a THF to form a five-coordinate complex is accompanied by a small increase of $\sim 1^{\circ}$ in N-Ga-N angle, indicating a slightly more covalent Ln–Ga interaction for all three rare earth metal-gallyl bonds. The covalency of the Ln–E interactions and the effect on the structure of the boryl/gallyl heterocycles is discussed further in Section 5.3.4.

5.3.3 The Electronic Structure of Ln–E in Five- and Six-Coordinate Rare Earth Metal Boryl and Gallyl Compounds

In order to understand the nature of the Ln–E interaction a series of studies were carried out to examine the electronic structure of the Ln–boryl/gallyl systems.

Ziegler-Rauk Energy Decomposition Analysis

A Ziegler-Rauk energy decomposition analysis (EDA) of the interaction between the charged $[\text{Ln}]^{+}$ and $[\text{boryl/gallyl}]^{-}$ fragments is displayed in Figure 5.13. The boryls **LnB** and **LnB$_{\text{THF}}$** display larger total interaction energies - and indeed of all EDA terms - relative to their gallyl analogues; which may, in part, be a consequence of shorter Ln–E bond distances. The THF-free five-coordinate compounds also display this relative to their six-coordinate analogues. The total interaction energies (blue bars) between the charged fragments are dominated by the electrostatic interactions in all 12 compounds, with the orbital, Pauli, and

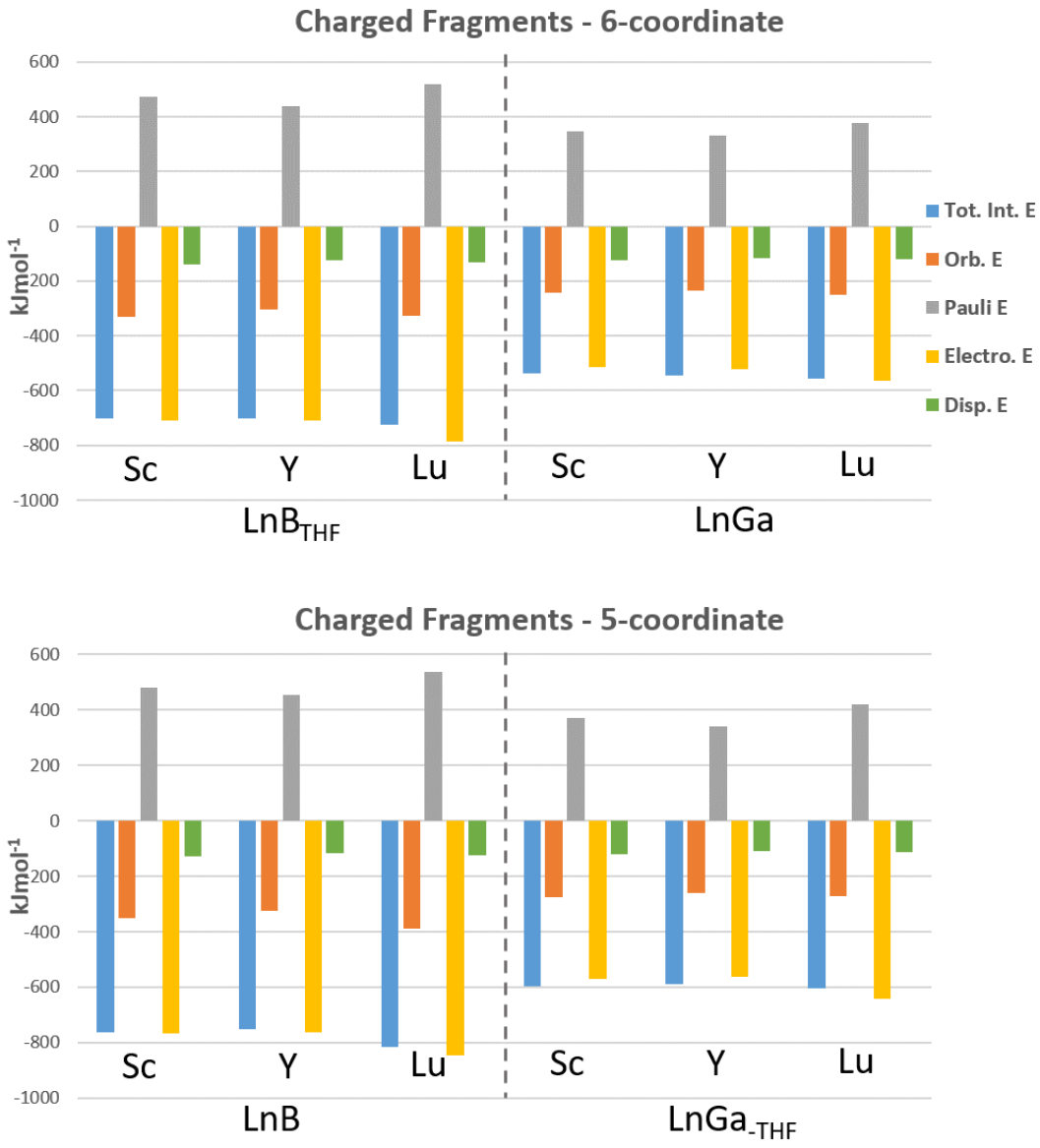

Figure 5.13: Breakdown of the contributions of the total interaction energies between the $[Ln]^+$ and $[boryl/gallyl]^-$ fragments of the six-coordinate **LnB$_{THF}$** and **LnGa** (top), and of the five-coordinate **LnB** and **LnGa$_{-THF}$** systems.

dispersion terms effectively cancelling each other out. It is, of course, expected that the total interaction energy between two charged fragments may be dictated by the magnitude of the electrostatic interaction energy, and an EDA of the interaction of neutral fragments may be more balanced.

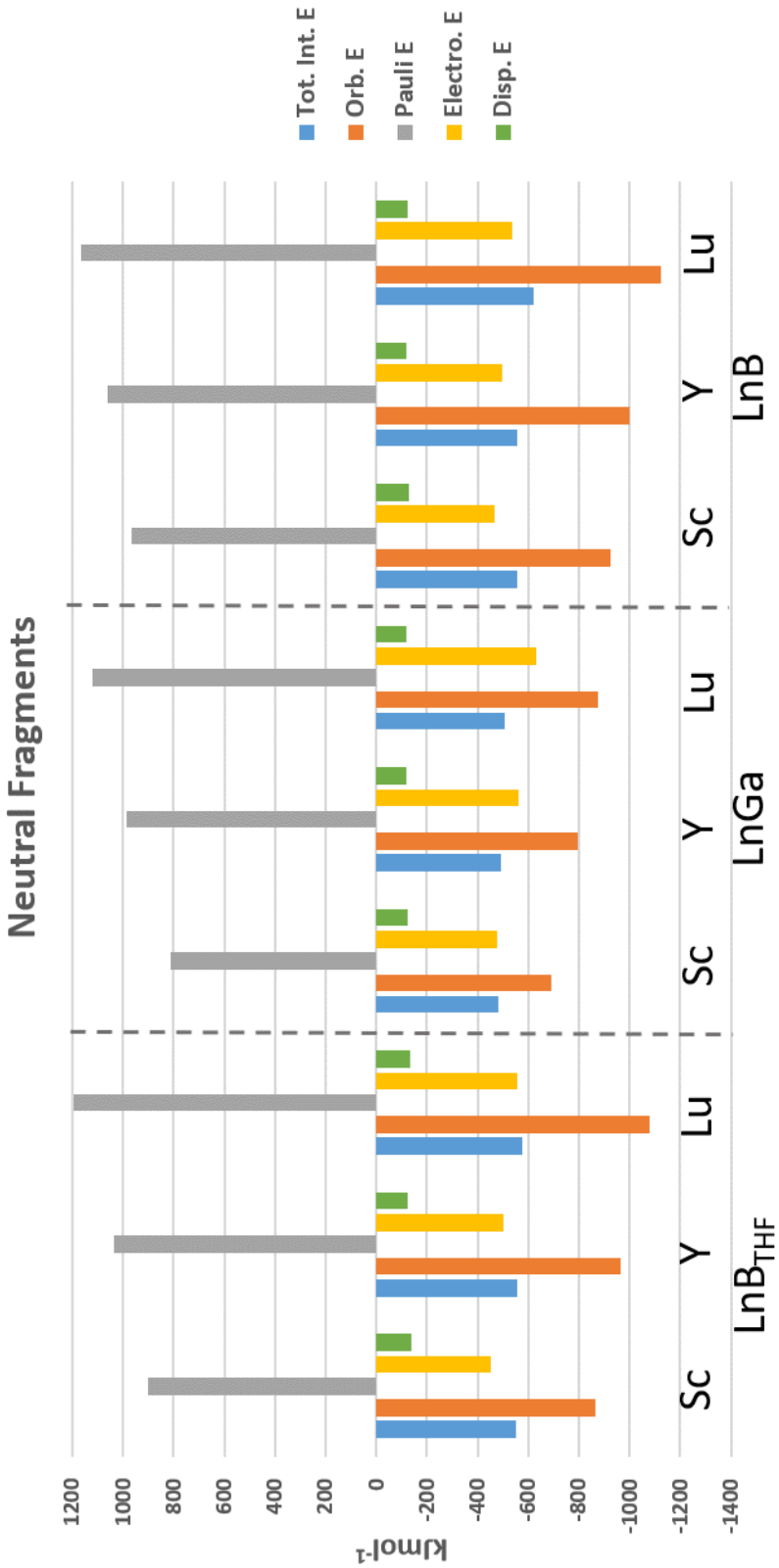

Figure 5.14: A breakdown of the contributions of the total interaction energies between the neutral [Ln]· and [boryl/gallyl]· fragments of the six-coordinate **LnB$_{THF}$** and **LnGa**, and of the five-coordinate **LnB** systems.

Figure 5.14 displays an EDA of the systems partitioned into neutral (radical) fragments. Unfortunately, an EDA could not be achieved for the five-coordinate gallyls **LnGa$_{\text{-THF}}$** owing to non-Aufbau filling of the molecular orbitals in the neutral gallyl fragments in these geometries. The most notable differences between the decompositions of the charged and neutral systems is the large increase in Pauli and orbital interaction terms, expected on going from Ln^+ to Ln, and the decrease in electrostatic and total interactions energies. The orbital and Pauli exclusion terms increase steadily as group 3 is descended from Sc to Y to Lu, as the outer orbitals become less tightly bound to atoms' cores. The strength of the total interaction energies increase from Sc to Lu for both the six-coordinate boryls **LnB$_{\text{THF}}$** and gallyls **LnGa**, as well as the five-coordinate **LnB**; a consequence of increasing orbital interaction terms outweighing that of the unfavourable pre-relaxation terms. This trend is in agreement with the Ln–B bonds of the smaller rare earth metals studies by Saleh *et al.*.[207]

If we compare the total interaction energies between the six-coordinate boryl **LnB$_{\text{THF}}$** and gallyl **LnGa** systems containing the same rare earth metal there is an ~ 200 kJmol^{-1} decrease (less negative) in favourable orbital interaction energy, *vs.* only an ~ 70 kJmol^{-1} decrease is total interaction energy, suggesting less orbital overlap contributing to the total interaction energies in the gallyl systems than the boryls. This may be explained by the fact that as group 13 is descended from B to Ga the atoms go from non-metallic to metallic in character.

In both sets of charged and neutral EDA analyses the dispersion interaction energy term increases (becomes more negative) from Y to Lu to Sc for both the boryls and gallyls, rationalised by a decrease in Ln–E bond distance, which will also be accompanied by a decrease in distance between the non-bonded atoms of the fragments' large ligand frameworks. The values of the dispersion terms are constant between both sets of partitioning schemes as the dispersion energy is a "classical" quantity, in that the electronic structure of the system is not taken into account in its calculation.

	ScGa	**YGa**	**LuGa**	**ScB$_{THF}$**	**YB$_{THF}$**	**LuB$_{THF}$**
r(Ln–E) (Å)	2.886	3.036	2.974	2.589	2.745	2.672
Δq(Ln–E(NArCH)$_2$)	1.27	1.42	1.42	1.23	1.38	1.37
Normalised Ln/E AO contributions to HOLO (%)	19/81	11/89	19/81	26/74	23/77	28/72
ρ_{BCP} Ln–E	0.0329	0.0302	0.0340	0.0482	0.0425	0.0476
$\nabla^2\rho_{\mathrm{BCP}}$ Ln–E	0.0268	0.0307	0.0284	0.0256	0.0340	0.0373
H_{BCP} Ln–E	-0.0059	-0.0047	-0.0073	-0.0100	-0.0085	-0.0118
DI(Ln,E)	0.334	0.326	0.345	0.44	0.411	0.432

Table 5.7: Data relating to the electronic structure of the Ln–E bonds of six-coordinate **LnGa** and **LnB$_{THF}$**. Δq(Ln–E(NArCH)$_2$) is the Hirschfeld charge difference between the Ln atom and the E fragment. QTAIM data are in atomic units.

QTAIM and Hirshfeld Charge Analysis

A QTAIM analysis was carried out to further probe the character of the Ln–E interactions. Values of $\rho_{\mathrm{BCP}}, H_{\mathrm{BCP}}, \nabla^2\rho_{\mathrm{BCP}}$, and DI(Ln,E) are dispalyed in Tables 5.7 and 5.8. These data indicate that the bonding between the Ln–E fragments is predominantly ionic, as evidenced by the small values of $\rho_{\mathrm{BCP}}, H_{\mathrm{BCP}}$, and DI(Ln,E), coupled with the small, positive $\nabla^2\rho_{\mathrm{BCP}}$ values. While the QTAIM data do not unanimously agree on which Ln–B/Ga interaction is the most covalent, there is resounding agreement that the Y–B/Ga interactions are the most ionic in character. The comparison of the QTAIM data between bonds containing B and those containing Ga suggests that the Ln–Ga bonds are the least shared, i.e. most ionic.

The Hirshfeld charge differences Δq(Ln–E(NArCH)$_2$) indicate that the six-coordinate THF adducts display significantly more ionic Ln–E interactions than the five-coordinate analogues, with the Y–E and Lu–E interactions exhibiting the most ionic character within both five- and six-coordinate sub-groups. Further to this, the Ln–Ga bonds are less shared than the Ln–B. The Δq(Ln–E(NArCH)$_2$) data also support these conclusions.

Boys-Foster Localised Orbital Analysis

To further probe the nature of the bonding in these complexes, the canonical Kohn-Sham molecular orbitals were analysed. The Ln–E σ-bonding orbitals located display delocalisation

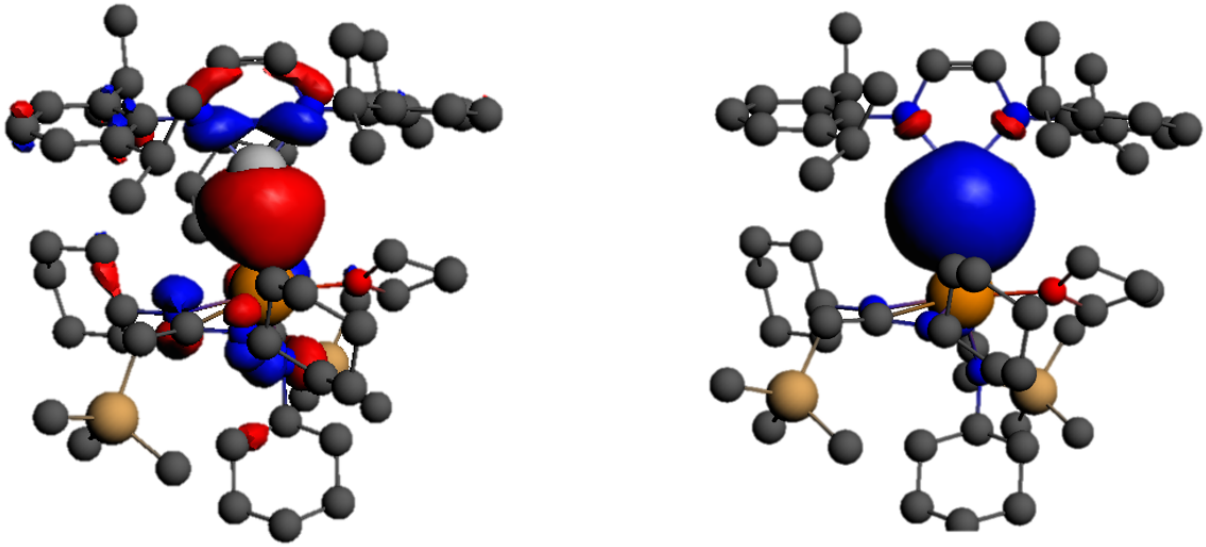

Figure 5.15: Kohn-Sham HOMO (left) and HOLO (right) of **ScGa**.

(see Figure 5.15), and in fact was not able to identity any of the Ln–Ga σ-bonding orbitals of any of the compounds presented. To remedy this, Boys-Foster localised orbitals (LOs) were calculated, which are found by performing unitary transformations of the canonical functions in order to minimize the spatial extent of the resultant orbitals. With this method, the Ln–Ga bonding orbital was identified as the highest occupied localised orbital (HOLO), as shown in Figure 5.15, and is predominantly a σ-bonding orbital. The normalised contributions from the Ln and E atoms to the σ-bonding HOLOs are shown in Tables 5.7 and 5.8. In

	ScGa$_{\text{-THF}}$	**YGa$_{\text{-THF}}$**	**LuGa$_{\text{-THF}}$**	**ScB**	**YB**	**LuB**
r(Ln–E) (Å)	2.726	2.89	2.825	2.473	2.638	2.573
Δq(Ln–E(NArCH)$_2$)	0.73	0.88	0.87	0.70	0.84	0.84
Normalised Ln/E AO contributions to HOLO (%)	22/78	19/81	26/74	28/72	26/74	31/69
ρ_{BCP} Ln–E	0.0438	0.0391	0.0441	0.0582	0.0510	0.0568
$\nabla^2\rho_{\text{BCP}}$ Ln–E	0.0264	0.0293	0.0261	0.0277	0.0332	0.0347
H_{BCP} Ln–E	-0.0104	-0.0087	-0.0122	-0.0143	-0.0125	-0.0164
DI(Ln,E)	0.4631	0.4471	0.4812	0.5164	0.4955	0.5182

Table 5.8: Data relating to the electronic structure of the Ln–E bonds of five-coordinate**LnGa$_{\text{-THF}}$** and **LnB**. Δq(Ln–E(NArCH)$_2$) is the Hirschfeld charge difference between the Ln atom and the E fragment. QTAIM data are in atomic units.

all cases, the E atom is found to be the major contributor, again indicating predominantly ionic bonding interactions. The Sc–E and Lu–E HOLOs showed the largest degree of mixing between the two atoms, while the Y–E HOLO show the lowest degree of mixing.

Overall the Ln–B interaction is found to be less ionic in nature than the Ln–Ga interactions, with slightly smaller Hirshfeld charge differences and a larger degree of Ln–E mixing in the HOLO, as well as the QTAIM metric values indicative of a more shared interaction. In general, increasing the coordination number of the bis(amidinate) Ln–E compounds from five to six leads to a more ionic Ln–E interaction for both boryl and gallyl examples, with significant increases in Hirshfeld charge differences, and lower degrees of mixing in the HOLOs, which may be attributed to the lengthening of the Ln–E bond distance.

5.3.4 Relationship Between Ln–E Ionicity and the Structure of the E Heterocycles

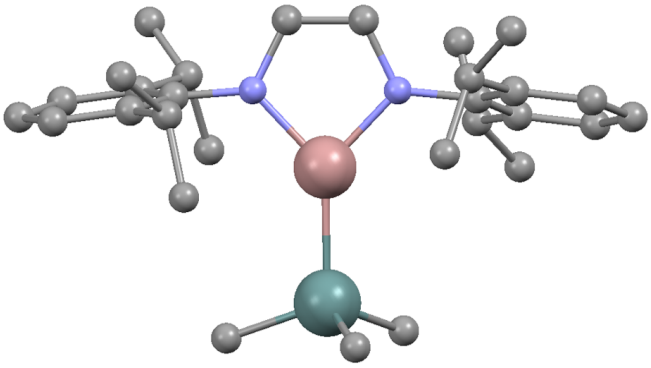

Figure 5.16: The structure of Ge{Ga(NArCH)$_2$}Me$_3$ (**GeGa**). H atoms are omitted for clarity.

The model compound Ge{Ga(NArCH)$_2$}Me$_3$, **GeGa**, (Figure 5.16 and Table 5.9) was studied to allow a comparison with the Ln–E interaction to that of a system expected to demonstrate a less ionic (or more covalent) M-E interaction. Changing the metal from Ln to Ge results in a noticeable widening of N-Ga-N bond angle from a mean of ∼83° in **LnGa** to ∼87°, and may be rationalised by considering Bent's rule. This rule is based on highly electronegative substituents "attracting" *p*-character. As the electronegativity of the atom coordinated to the gallium increases from Sc to Ge the ionic nature of the interaction

	ScGa$_{\text{-THF}}$	**YGa$_{\text{-THF}}$**	**LuGa$_{\text{-THF}}$**	**ScGa**	**YGa**	**LuGa**	**GeGa**
r(M-Ga)(Å)	2.726	2.89	2.825	2.886	3.036	2.974	2.416
Av. r(Ga-N)(Å)	1.935	1.929	1.926	1.979	1.968	1.968	1.881
∠ N-Ga-N (°)	83.9	83.6	83.9	82.8	82.8	82.9	86.7
M/E AO contributions to HOLO (%)	22/78	19/81	26/74	19/81	11/89	19/81	45/55
Ga *s/p* contributions to HOLO (%)	73/27	73/27	74/26	77/23	76/24	77/23	67/33
Av. Ga *s/p* contributions to Ga-N LO (%)	26/74	24/76	25/75	22/78	19/81	21/79	31/69

Table 5.9: Selected geometric and electronic structural parameters of the five- and six-coordinate gallyls, **LnGa$_{\text{-THF}}$** and **LnGa**, respectively. Contributions to the LOs have been normalised.

decreases. Consequently, less 4*s* character on the gallium will be directed towards the newly formed Ge-Ga bond, and is instead directed into the Ga–N bonding orbitals, resulting in the shortening of the Ga–N bonds. While the remaining bonds in the heterocycle are largely unchanged, the N-Ga-N angle becomes more obtuse in **GeGa** as a consequence of this change in Ga–N bond distance. Figure 5.17 shows the effect of change in electronegativity of metals on bond distances and angles in the gallyl heterocycle, with data found in surveying the Cambridge Structural Database.

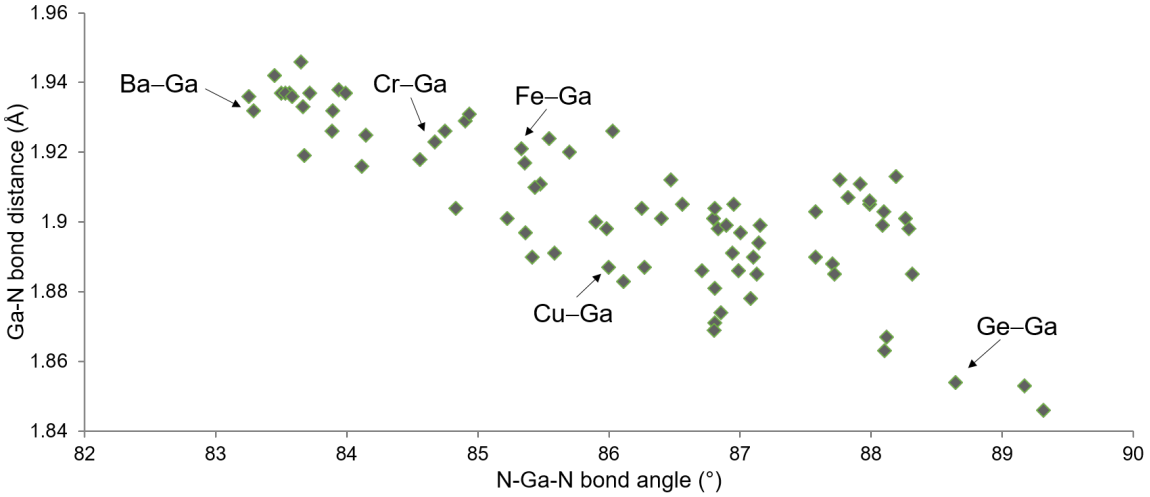

Figure 5.17: N-Ga-N bond angle *vs.* Ga–N bond distance for compounds containing M–Ga(NArCH)$_2$ bonds. Data taken from the Cambridge Structural Database.

The greater extent of mixing in the Ge–Ga HOLO (45/55%) as compared with the Ln–Ga HOLO of, for example, the Sc–Ga bond of **ScGa** (19/81%) supports the predicted change in covalency of the M–E bonding interactions on change of electronegativity of the non-gallium metal. In addition to the Ln-Ga bonding LOs described above, four gallyl-based LOs of Ga–N bonding character were located for each of the five- and six-coordinate gallyl compounds, **LnGa$_{\text{-THF}}$** and **LnGa**, respectively. The *s*- and *p*-orbital contributions from the Ga atoms to the the Ga–N bonds were also calculated, as these contributions will govern the structural features of the heterocycle. Upon increasing the coordination number at the Ln centre, for example from **ScGa$_{\text{-THF}}$** to **ScGa**, the Sc–Ga bond length increases from 2.726 to 2.886 Å, accompanied by an increase in ionicity of the bond, as evidenced by the change in normalised Sc/Ga contributions to the HOLO from 22/78% to 19/81%. The expected reduction in N-Ga-N bond angle and lengthening of Ga–N bond length is also observed. This trend is seen for all Ln-Ga bonds as well as the Ln-B (Table 5.10) upon THF coordination.

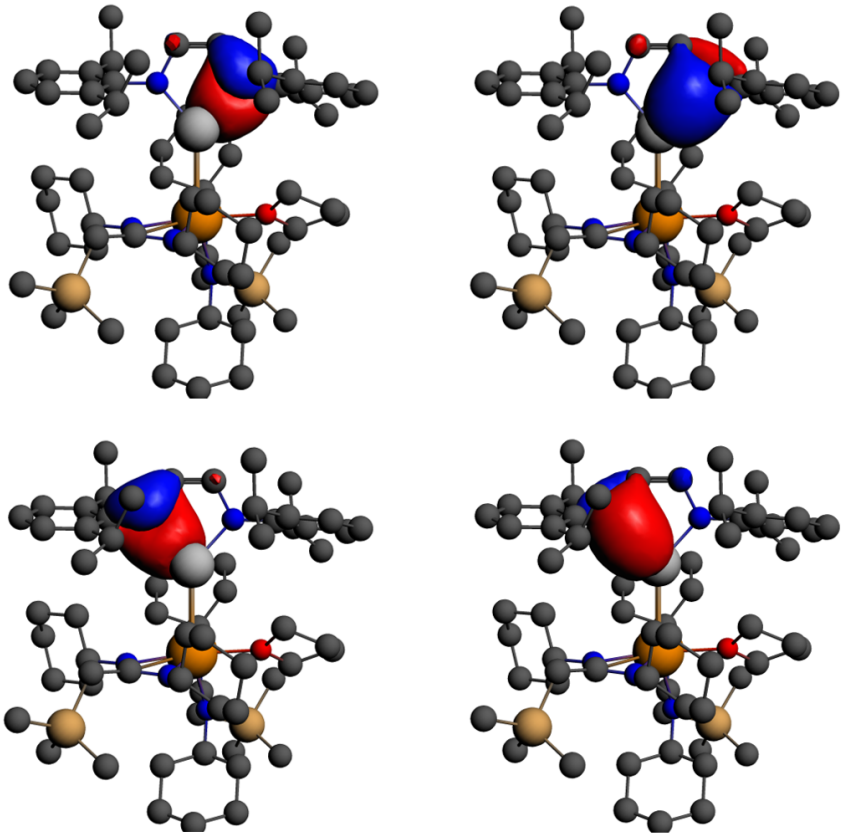

Figure 5.18: Representation of four gallyl-based LOs of **ScGa**. H atoms omitted for clarity.

	ScB	**YB**	**LuB**	**ScB_{THF}**	**YB_{THF}**	**LuB_{THF}**
r(M-B)(Å)	2.473	2.638	2.754	2.589	2.745	2.672
Av. r(B-N)(Å)	1.477	1.471	1.471	1.496	1.487	1.488
∠ N-B-N (°)	99.9	99.8	99.9	99.1	99.1	99.4
M/E AO contributions to HOLO (%)	28/72	26/74	31/69	26/74	23/77	28/72
B *s/p* contributions to HOLO (%)	56/44	57/43	57/43	59/41	59/41	60/40
Av. B *s/p* contributions to B-N LO (%)	28/72	27/73	29/71	27/73	24/76	29/71

Table 5.10: Selected geometric and electronic structural parameters of the five- and six-coordinate boryls, **LnB** and **LnB_{THF}**, respectively. Contributions to the LOs have been normalised.

5.3.5 Carbodiimide Insertion into the Ln–E Bond

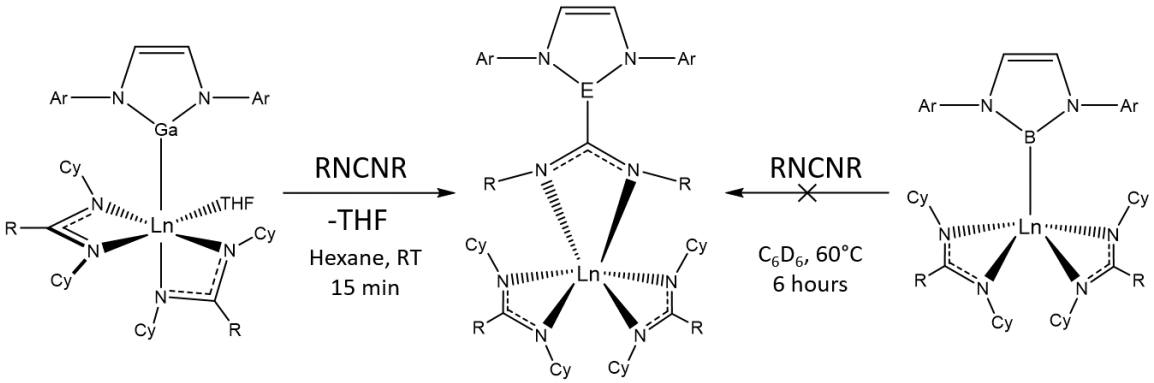

Figure 5.19: Carbodiimide insertion into the Ln–E bond.

It has been experimentally shown that the six-coordinate gallyls, **LnGa**, react with the carbodiimides, RNCNR, to give **LnRGa** (Figure 5.19), resulting in the insertion of the carbodiimide into the Ln–Ga bond. Analogous insertions with the isolable five-coordinate

boryls **LnB** do not occur, however. This difference in reactivity may be attributed to the stronger Ln–B bond relative to the Ln–Ga, as shown by their higher homolytic dissociation energies presented in Table 5.11, as well as the EDA interaction energies between the neutral fragment in Figure 5.14.

	ScB	**YB**	**LuB**	**ScGa**	**YGa**	**LuGa**
BDE	499.5	513.4	536.0	411.0	432.0	442.2

Table 5.11: Homolytic bond dissociation energies (in kJmol^{-1}) of the Ln–E bonds of **LnB** and **LnGa**.

In order to further understand this observation, model carbodiimides **LniPrE** were built and optimised from modified versions of the X-ray structure of **SciPrGa** to assess the thermodynamics of the insertion of iPrNCNiPr into the Ln–E bonds of the experimentally isolable **LnGa** and **LnB**. The results of this test are displayed in Table 5.12 and show somewhat surprising results. The $\Delta_{\mathrm{r}}G$ values for the hypothetical reaction of **LnB** suggest that the formation of insertion products is favourable, and indeed more so than for the observable reactions from **LnGa**. The $\Delta_{\mathrm{r}}H$ values for the reaction involving the gallyl systems **LnGa** are approximately 2.5 times lower than those involving the boryls **LnB**. This relatively low change in reaction enthalpy for the gallyl examples may be attributed to the necessary loss of THF being disfavoured for the gallyl compounds, as discussed in Section 5.3.2. The lack of coordinated THF in the boryls **LnB**, however, results in more negative $T\Delta_{\mathrm{r}}S$ values than for the corresponding reaction of carbodiimide with **LnGa**. While the change in reaction entropy may be more unfavourable for the reactions involving **LnB**, the large and favourable change in reaction enthalpy overcomes the $T\Delta_{\mathrm{r}}S$ term to produce values for $\Delta_{\mathrm{r}}G$ that favour the insertion into the Ln–B bond, and suggests that this reaction would occur more readily than the insertion into the Ln-Ga bond of **LnGa**. Since this is not observed experimentally, the large negative values for $\Delta_{\mathrm{r}}H$ and $\Delta_{\mathrm{r}}G$ in the hypothetical reactions involving **LnB** must have a different origin. It is therefore proposed that, rather than insertion into the Ln–B bond, formation of a B–C bond is the driving force in these reactions.

The B–C BDE is expected to be greater than that of the Ga–C bond, due to a decrease in orbital overlap and energy difference between the respective orbitals as group 13 is

Starting LnE	$\Delta_{\mathrm{r}}H$	$T\Delta_{\mathrm{r}}S$	$\Delta_{\mathrm{r}}G$
ScGa	-137.4	-11.7	-125.8
YGa	-125.6	-13.1	-112.5
LuGa	-131.0	-4.9	-126.0
ScB	-307.2	-52.1	-255.1
YB	-320.1	-60.6	-259.5
LuB	-308.2	-46.2	-262.0
ScB$_{\mathrm{THF}}$	-291.2	-9.9	-281.3
YB$_{\mathrm{THF}}$	-275.5	-4.3	-271.2
LuB$_{\mathrm{THF}}$	-276.4	-5.3	-271.1

Table 5.12: The thermodynamics of insertion of iPrNCNiPr into the Ln–E bonds of **LnGa**, **LnB** and **LnB$_{\mathrm{THF}}$**. All values are given in kJmol^{-1} and are relative to the starting LnE compound plus isolated iPrNCNiPr.

descended. This is supported by experimentally derived BDEs for the E–C(sp^3) bonds X_2B–C and X_2Ga–C of 376 kJmol^{-1} and 245 kJmol^{-1}, respectively.[229] In order to test this hypothesis for E–C(sp^2) bonds and achieve a more relevant comparison, the model systems PhB(NArCH)$_2$ (**PhB**) and PhGa(NArCH)$_2$ (**PhGa**) were calculated, with homolytic BDEs of of 666 and 377 kJmol^{-1}, respectively.

An arguably more appropriate comparison can be made between the reaction energies of **LnGa** and the hypothetical six-coordinate boryls **LnB$_{\mathrm{THF}}$**. Similarly to the five-coordinate boryl systems, $\Delta_{\mathrm{r}}H$ is much larger for **LnB$_{\mathrm{THF}}$** than for **LnGa**, however the process of losing a THF adduct introduces an additional complication, which is not present with **LnB**. The $T\Delta_{\mathrm{r}}S$ values of **LnB$_{\mathrm{THF}}$** are therefore similar to **LnGa**, as both reactions are two reactant-two product processes. The six-coordinate **LnB$_{\mathrm{THF}}$** boryls therefore have smaller $T\Delta_{\mathrm{r}}S$ terms than their five-coordinate analogues, which compensate for the less favourable $\Delta_{\mathrm{r}}H$ values, and results in an overall more favourable $\Delta_{\mathrm{r}}G$. These free energies of reactions for **LnB$_{\mathrm{THF}}$** are significantly larger than for the gallyls **LnGa**, once again owing to the formation of the stronger B–C(sp^2) bonds.

An additional, or alternative, argument can be made about the kinetics of the carbodiimide insertion into the Ln–B bonds. While the insertion products may be of greater thermodynamic stability relative to the reactants for **LnB** and **LnB$_{\mathrm{THF}}$**, the process may have a larger barrier to insertion than for **LnGa**. This may be hypothesised owing to the

shorter (and stronger) Ln–B bonds, hindering the coordination of the carbodiimide to the Ln centre in order for reaction to take place.

5.3.6 Carbodiimide Insertion into the Magnesium Gallyl Bond - A Mechanistic Study

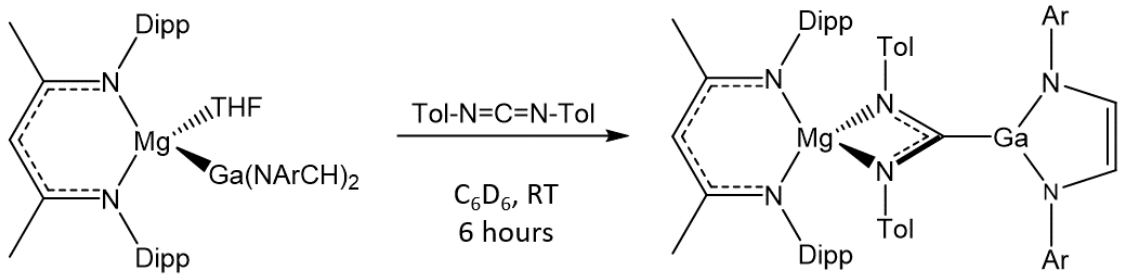

MgGa **MgTolGa**

Figure 5.20: Insertion of a carbodiimide into the Mg-Ga bond of Mg(^{Dipp}NacNac){Ga(NArCH)$_2$} (**MgGa**).

Our collaborators at the University of Oxford have been studying the chemistry of alkaline earth–main group metal bonds. The magnesium gallyl compound **MgGa** shown in Figure 5.20 has been isolated, and it has been shown that the carbodiimide, TolNCNTol, may insert into the Mg–Ga bond to give **MgTolGa**. Owing to the rigidity of the singular NacNac ligand compared to the relatively flexible (bis)amidinate ligands of **LnGa**, and its anticipated greater ease of modelling, the carbodiimide insertion mechanism was investigated for the reaction of **MgGa** above.

For reaction to take place with both the **LnGa** systems and **MgGa**, the THF molecule must be displaced by the carbodiimide in order to form an adduct, a representation of which is shown in Figure 5.21. The adduct was used as a starting point for mechanistic studies of the insertion of the carbodiimide into the Mg–Ga bond, and our approach was to first strip the R, R', and R"' groups down to H atoms, and to remove the Grimme D3 dispersion correction. These steps were taken to simplify the model and method to find starting structures upon which to build. Once a full set of stationary points for this simplified reaction profile was located, the structures of the TS were built up with larger

R groups, and re-optimised. The reactants and products of each TS were then found by manually displacing along the imaginary mode. This approach is more rigorous than simply re-optimising all of the stationary points once built up. While carrying out this study some interesting observations were made, and are discussed below.

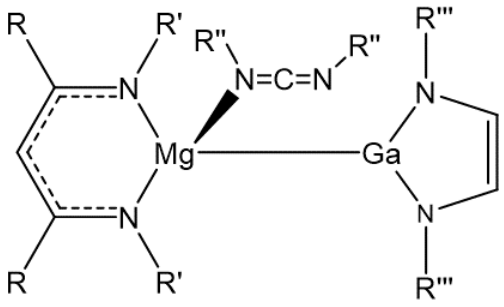

Figure 5.21: Carbodiimide adduct of **MgGa**.

Effect of R Group Size on Complexity of the Reaction Profile

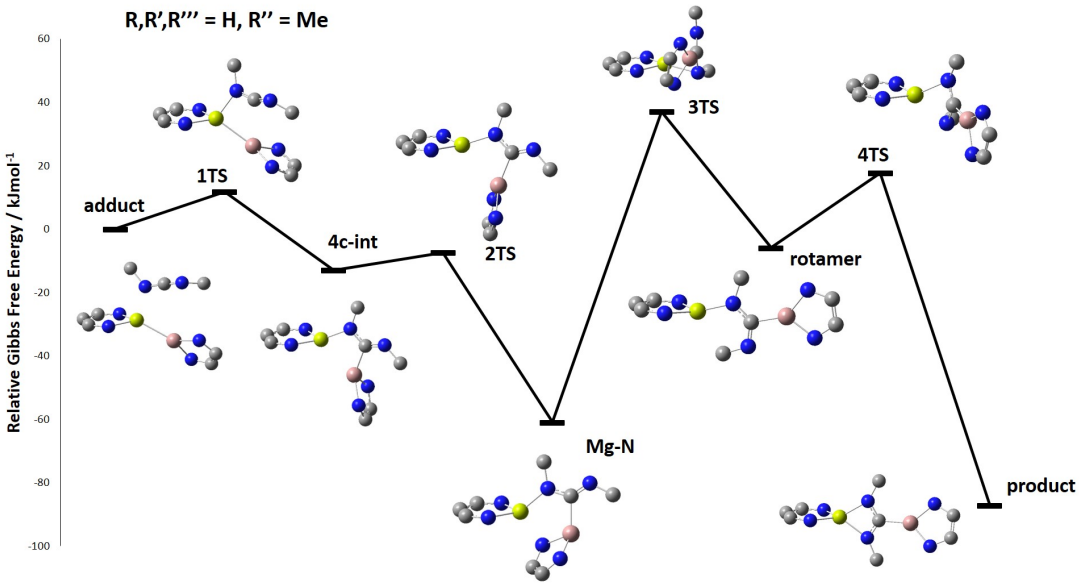

Figure 5.22: Relative Gibbs free energy profile, calculated without dispersion corrections, for the insertion of MeNCNMe into the Mg–Ga bond of Mg(^{H}NacNac){Ga(NHCH)$_2$}.

Figure 5.22 shows the reaction profile for carbodiimide insertion into the Mg–Ga bond, where R,R',R''' = H, R'' = Me. For this simple model the reaction proceeds through a

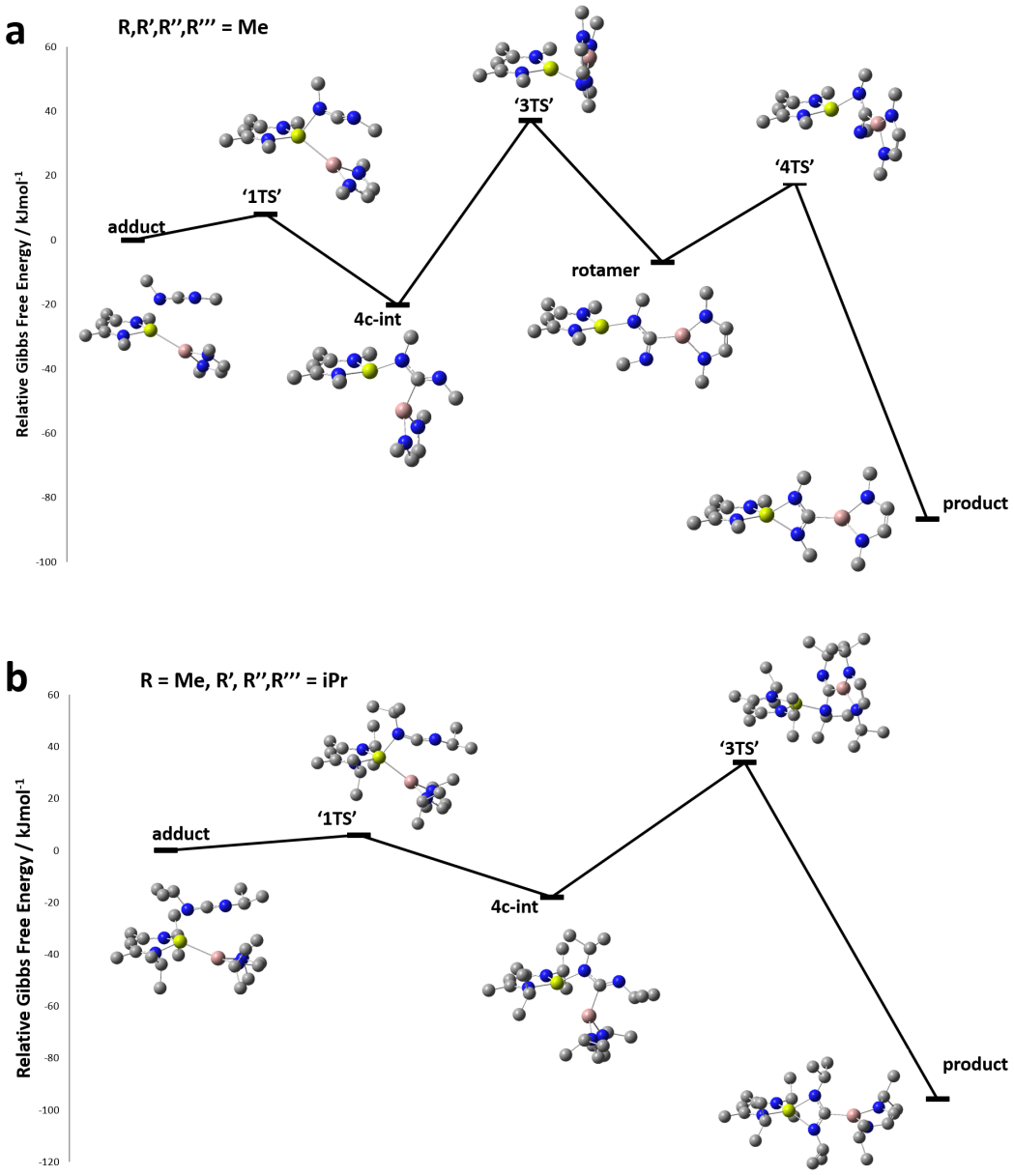

Figure 5.23: Relative Gibbs free energy profiles, calculated without dispersion corrections, for the insertion of R''NCNR'' into the Mg–Ga bond of Mg($^{R'}$NacNac){Ga(NR''$'$CH)$_2$}. The apostrophes around the TS labels indicate that they were located after building up the analogous TS with smaller R groups.

four-centre intermediate (**4c-int**), a local minimum where we observe one N atom of the gallyl moiety tilt towards the Mg atom (**Mg-N**), an intermediate that is a rotamer of the insertion product, and finally through a rotational TS to reach the insertion product. Not counting carbodiimide adduct formation, there are four TS through which the reaction must pass before the insertion product is reached.

If the R groups are increased in size to methyl (Figure 5.23**a**) the **Mg-N** intermediate and **'2TS'** are bypassed and rotation of Mg-N-C-Ga dihedral angle in **'3TS'** yields the **rotamer** intermediate directly, resulting in a three-step reaction. If R size is increased further to iPr, intermediate **rotamer** is also bypassed and the insertion reaction is a simple two-step process. It appears that increasing the steric bulk of the R', R", and R"' groups prevents the formation of intermediates and thereby facilitates the reaction. Furthermore, the rate determining step (**Mg-N/4c-int** $\rightarrow$ **rotamer**) of each insertion reaction decreases from 98.0, to 57.4, to 51.8 kJmol^{-1} upon increasing R', R", and R"' from H, to Me, to iPr, respectively.

Effect of Grimme D3 Dispersion Correction

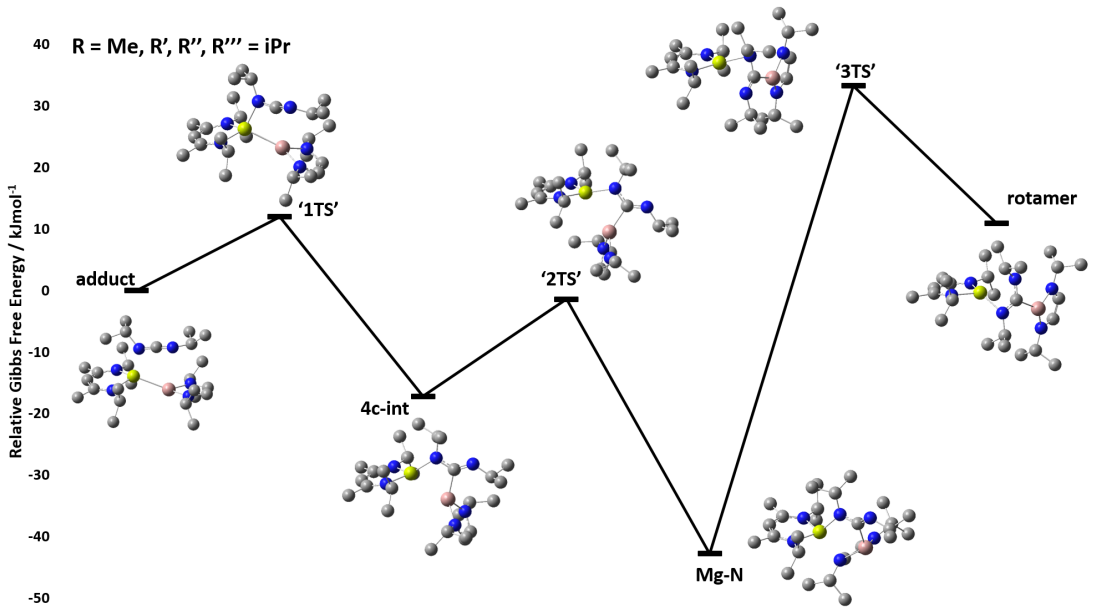

Figure 5.24: Relative Gibbs free energy profiles, optimised with Grimme D3 dispersion corrections, for the insertion of iPrNCNiPr into the Mg–Ga bond of Mg(^{iPr}NacNac){Ga(NiPrCH)$_2$}.

Inclusion of dispersion corrections upon optimisation of the TS along the reaction profiles was found to reintroduce TSs into the insertion process, and often resulted in failure to locate the correct TS. Figure 5.24 shows the incomplete reaction profile for R = Me, R',R",R"' = iPr, calculated with dispersion. We observe that displacement along the reaction coordinate of **'3TS'** yields reactants and products **'Mg-N'** and **rotamer**, respectively, producing a

reaction profile similar to the dispersion-free example in Figure 5.22, where R,R',R'' = H, R'' = Me. This is by contrast to the two step process found without dispersion shown in Figure 5.23**b** above. The profile displayed in Figure 5.24 also shows that **'4TS'** could not be located for R = Me, R',R'',R'' = iPr.

Mechanism for the Full System

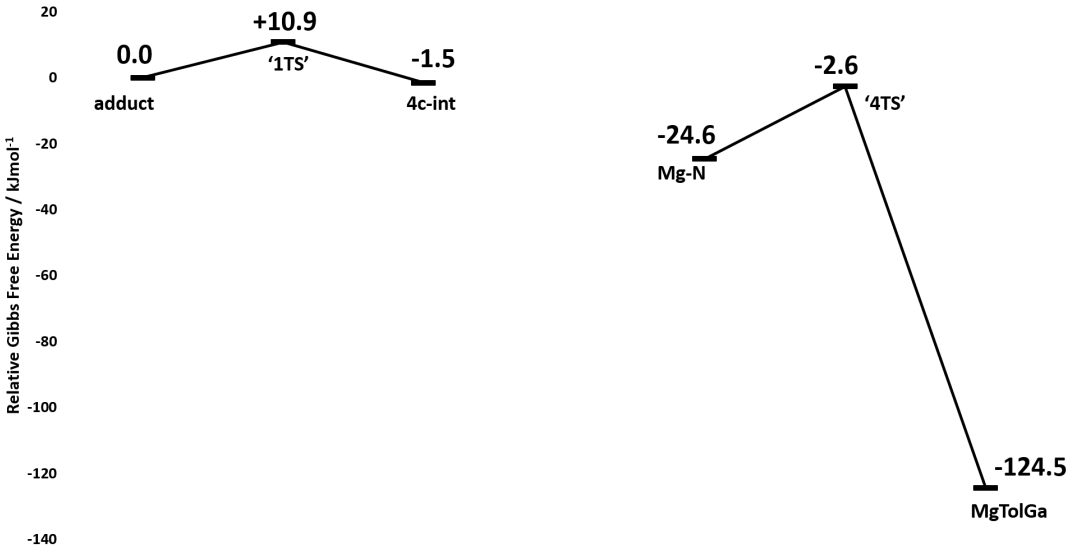

Figure 5.25: Relative Gibbs free energy profile, optimised with Grimme D3 dispersion corrections, for the insertion of TolPrNCNTol into the Mg–Ga bond of Mg(^{Dipp}NacNac){Ga(NDippCH)$_2$}. Structures corresponding to the stationary points are shown in Figure 5.26.

Figure 5.25 shows the reaction profile for the reaction of **MgGa** with TolNCNTol, outlined in Figure 5.20, proceeding from the carbodiimide adduct. The structures of the stationary points that were located are displayed in Figure 5.26. The Mg–Ga distance of the adduct, the structure of which is shown in Figure 5.26, is 2.71 Å, in very good agreement with the experimentally observed distance of 2.75 Å previously reported reported by Bonello *et al.* for the analogous TMEDA adduct.[201] From the carbodiimide adduct a low barrier of 10.0 kJmol^{-1} must be overcome in order to form the intermediate **4c-int**. A TS corresponding to the rotation of the Mg-N-C-N dihedral angle (N, C, and N atoms of carbodiimide) is expected to link **4c-int** with **Mg-N**, which, unfortunately, could not be located after much effort. An upper-limit to this barrier may be given as $\sim$80 kJmol^{-1}, from the vibrational

frequency analysis of the structure of highest SCF energy along a potential energy scan of this angle. It is anticipated that the barrier would be lower than this, as the approximate transition state structure is not fully optimised. The final TS corresponds to the rotation of the N-C-N-C_{Tol} dihedral to allow coordination of the second carbodiimide N atom to the Mg centre, and produces the insertion product, **MgTolGa**. The total Gibbs free energy of reaction from THF adduct to insertion product is -97.8 kJmol^{-1}, indicating that the reaction is thermodynamically spontaneous, and indeed this reaction is observed experimentally at RT.

Compared to the close contact Mg–N(gallyl) distances of 2.2 and 2.3 Å in the **Mg-N** complexes shown in Figures 5.22 and 5.24, respectively, the reactant of **4TS** for the full systems (Figure 5.26) displays a much longer distance of 4.7 Å. In the model systems containing small R groups the close contact of the gallyl N atom to the Mg atom is accompanied by an elongated geminal N–Ga bond by $\sim$0.1 Å, compared to the N–Ga distance of the uncoordinated gallyl N atom. This indicates that an interaction between the N lone pair and Mg centre is present. Such an interaction is expected to stabilise the Mg centre and is likely to account for the large relative stability of the **Mg-N** complexes of the model systems. For the full system, however, the steric bulk of the Dipp ligands inhibits formation of a short Mg–N interaction, and as a result a large energy barrier is not observed for the rotation of the carbodiimide backbone to allow product formation. The close contact **Mg-N** stationary points of the model systems are considered to be artefacts of the oversimplification of the experimental systems.

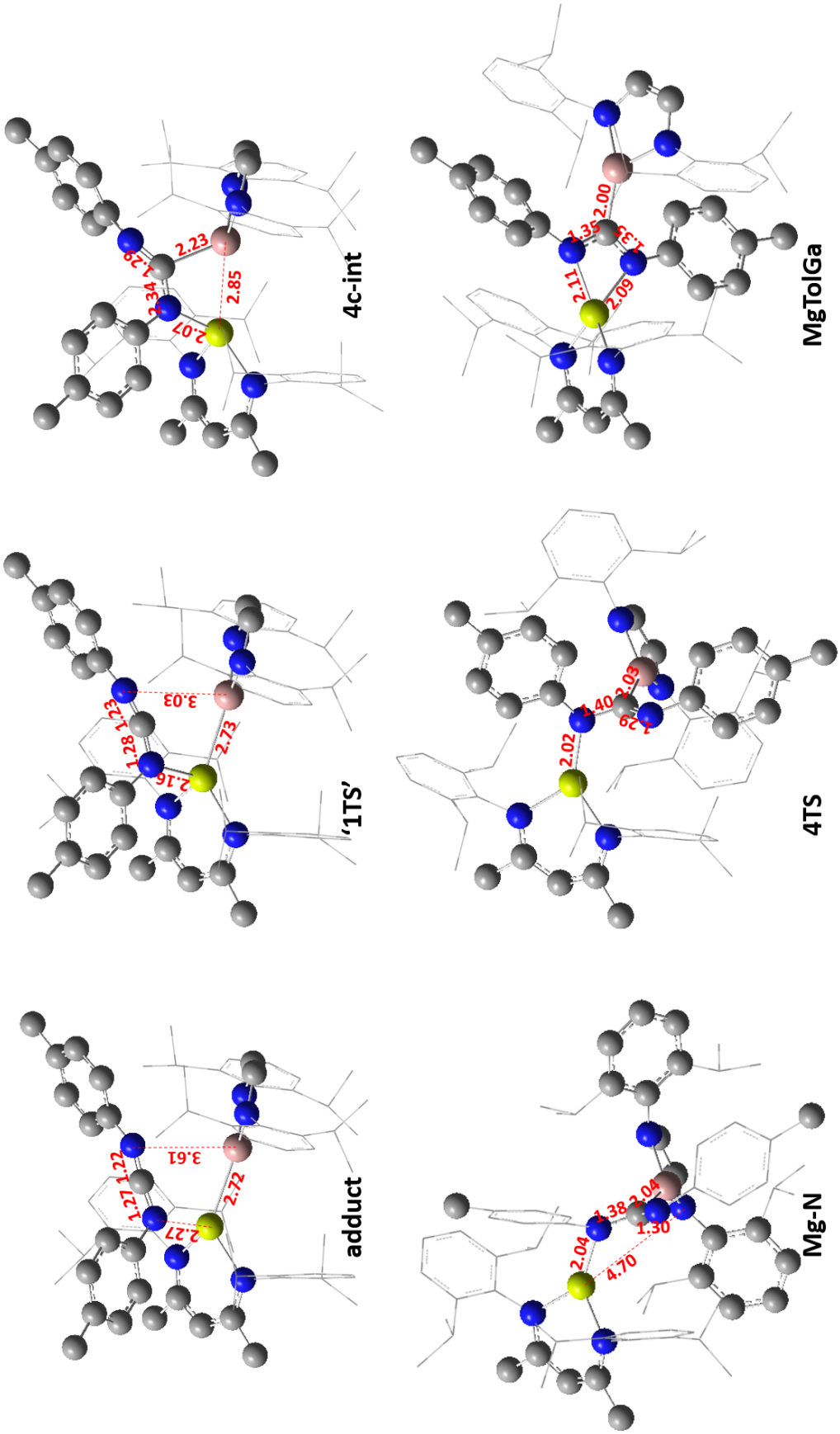

Figure 5.26: Structures of the stationary points along the reaction profile of insertion of TolPrNCNTol into the Mg–Ga bond of Mg(^{Dipp}NacNac){Ga(NDippCH)$_2$} shown in Figure 5.25. H atoms are omitted, and R' and R'' groups are shown are wireframes, for clarity.

5.4 Conclusions

The rare earth metal gallyls, **LnGa**, are experimentally isolated in six-coordinate, distorted octahedral geometries with one coordinated THF molecule, whereas the boryls, **LnB** adopt an unusual five-coordinate square-based pyramidal structure with no THF adduct. In order to understand this difference in geometric preference hypothetical five- and six-coordinated analogues of the gallyls and boryls, **LnGa$_{\text{-THF}}$** and **LnB$_{\text{THF}}$** respectively, were calculated. While the $\Delta_{\mathrm{r}}H$ values for the addition of THF is favourable for all six Ln–Ga/B compounds, those for the gallys, **LnGa$_{\text{-THF}}$**, are 2-5 times larger than for **LnB**. These larger $\Delta_{\mathrm{r}}H$ values outweigh the $T\Delta_{\mathrm{r}}S$ contributions to adduct formation, which are similar for both group 13 sub-groups, resulting in favourable $\Delta_{\mathrm{r}}G$ values for the gallyls, compared to unfavourable $\Delta_{\mathrm{r}}G$ for the boryls. This result supports the experimental structural observations of the differing boryl and gallyl coordination numbers.

The squarebased pyramidal (SBP) geometry of the five-coordinate experimentally isolable boryls, **LnB** and the hypothetical five-coordinate gallyls, **LnGa$_{\text{-THF}}$**, was attributed to the sterics and constrained nature of the amidinate ligand. The longer Ln–E bonds of the five-coordinate gallyls open up the coordination sphere around the Ln centre, resulting in a less distorted SBP geometry than in the boryls. Within the six-coordinate boryl and gallyl compounds, it was shown that the boryl moiety has a stronger *trans*-influencing ability.

Analyses of the Ln–E bonding interactions using EDA, QTAIM, Hirshfeld charge, and Boys-Foster localised orbital approaches illustrated that the Ln–B interactions are less ionic in nature than the Ln–Ga. It was also shown that increasing the coordination number from five to six leads to a more ionic Ln–E interaction. It should be noted that unanimous agreement among the techniques used to give metrics for ionicity of bonding interactions was not reached. A combination of these methods should therefore be used in future analyses of bonding interactions to allow for a balanced analysis.

The insertion of the carbodiimide iPrNCNiPr into the Ln–E bonds was assessed, and indicated that insertion into the Ln–B bond of both five- and (hypothetical) six-coordinate boryls should be more favourable than into the six-coordinate Ln–Ga bonds, on the basis of $\Delta_{\mathrm{r}}G$. This is not observed experimentally however, and a rationale based on the formation

of the energetically preferable B–C(sp^2) *vs.* Ga–C(sp^2) bond was offered to account for this discrepancy with experiment. An alternative argument was given based on barriers to insertion into the Ln–B expected to be larger than those into the Ln–Ga bond owing to the shorter and stronger bonds found in **LnB** compared to **LnGa**. Unfortunately, this hypothesis was not tested, and would make very interesting future work. It should be noted here that these reactivity studies in collaborations with the University of Oxford show the first insertion of unsaturated substrates into Ln–Ga bonds, and indeed the first insertions into an unsupported metal–Ga bond.

The mechanism and kinetics of carbodiimide insertion in the metal–gallium bond of a related species, **MgGa**, was studied, with the problem first reduced to the species involved having minimal ligand size. From this minimal model the dispersion-free insertion mechanism was shown to proceed through four TS, however upon increasing ligand R group size to iPr, the mechanism simplified to one with only two transition states. This was attributed to the larger steric bulk of the ligands prohibiting formation of intermediates. Introduction of dispersion into the methodology reintroduced complexity, however, and resulted in great difficulty in locating TS. Indeed, the mechanism for the full system is missing one TS. A general conclusion that could be drawn from this mechanistic study is that simplification of ligands to facilitate location of TS in unknown mechanisms should be undertaken with caution. The TS for this reaction could be modified to build starting point geometries for the insertion of a carbodiimide into the Ln–E bonds of **LnGa** and **LnB** in order to test the hypothesis given above. Time limitations did not permit such a study, however. The results of the benchmarking study on post-metallocene propylene homopolymerisation mechanisms in Chapter 3 should also be taken into consideration; PBE + D3 dispersion correction did not perform well at describing such mechanisms. The key difference between the two studies is that the carbodiimide insertion does not involve a metal-π-bond interaction, which was the interaction that caused the most discrepancy in energy between the different methods used in Chapter 3. The present study could be extended to test the performance of an M06 XC functional, however, in order to examine the effects of different methods of including dispersion in these systems.

Appendices

Appendix A - Gibbs free energy barriers (kJmol^{-1}) for CP, BHTTi and BHTM calculated using different computational methods at elevated temperatures

	$\Delta G^{\ddagger}$ (363 K)			$\Delta G^{\ddagger}$ (373 K)			$\Delta G^{\ddagger}$ (393 K)		
DFT Method	CP	BHTTi	BHTM	CP	BHTTi	BHTM	CP	BHTTi	BHTM
PBE	58.38	48.23	74.04	60.59	48.39	76.23	65.02	48.72	80.61
PBE-D3 SP	25.30	45.30	32.76	27.52	45.47	34.95	31.95	45.81	39.33
PBE-D3 Opt	24.89	43.77	29.73	27.07	43.87	31.81	31.43	44.08	35.96
PBE-D3 SP +PCM SP	30.05	45.90	36.36	32.27	46.07	38.55	36.70	46.40	42.93
PBE-D3 Opt +PCM Opt	23.73	48.41	36.15	25.76	48.62	38.31	23.73	48.41	36.15
PBE + PCM SP	63.13	48.82	77.63	65.34	48.98	79.83	69.77	49.32	84.21
PBE + PCM Opt	56.96	45.76	75.64	59.02	45.85	77.79	63.15	46.03	82.08
M06-2X	43.99	46.51	83.19	46.11	46.53	85.38	50.36	46.53	89.75
M06-2X + PCM SP	48.05	47.20	86.45	50.18	47.21	88.65	54.43	47.23	93.02
M06-2X + PCM Opt	49.05	48.62	85.64	51.20	48.68	87.81	55.50	48.80	92.14

Appendix B - Methods attempted for locating anion displacement TS by incoming ethylene monomer

1. Bond distances from anion displacement TS *via* perpendicular front approach reported by Laine *et al.*[154] used as a guess starting geometry for optimisation to TS. The sructure began optimising to inner-sphere ion-pair and ethylene removed completely from coordination sphere.

2. Constrained geometry optimisations with fixed Ti–F distances starting from ethylene adduct and bringing anion closer:

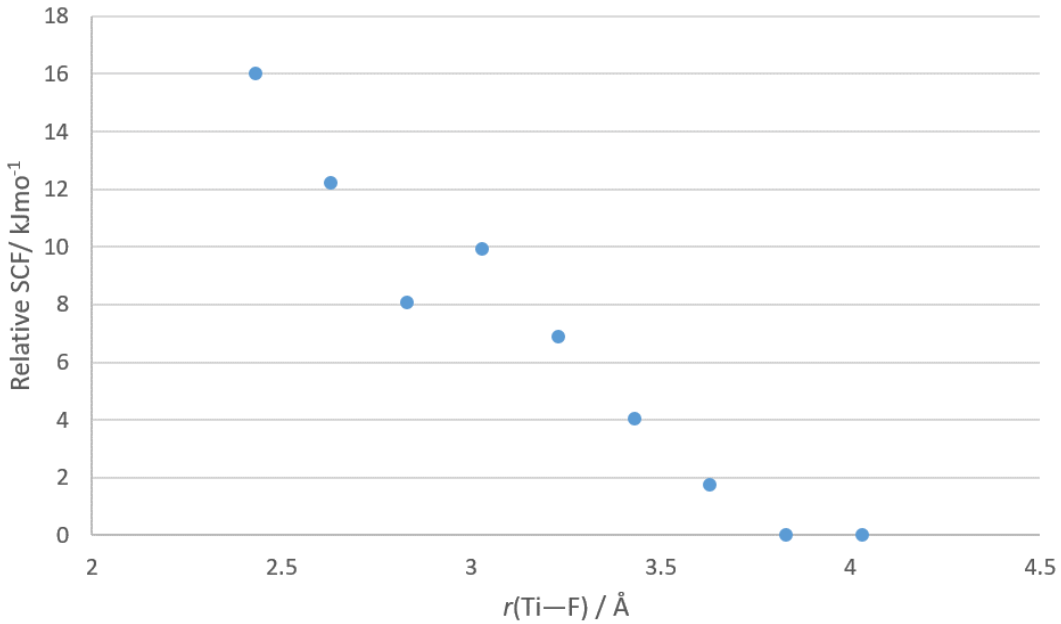

   As observed in the Figure above, the "bump" in energy is only around 2 kJmol^{-1} - extremely flat potential energy surface here. Optimisation to TS was not successful.

3. Constrained geometry optimisations fixing one Ti–C(ethylene) bond length resulted in the other ethylene C atom tilting towards Ti atom. Adding a dummy atom, Bq, at centre of C=C bond caused the C atoms to bend away from Bq towards Ti as the Bq was moved away. Fixing both C atoms introduced a dihedral angle error in optimisation.

4. Back approach displacement TS attempted by series of constrained geometry optimisations with fixed Ti–C(ethylene) distances suggested process is barrierless, however if ethylene removed to 10Å away the SCF energy is reduced by ∼90 kJmol^{-1} (see Figure below). In addition, the geometry of the ion-pair with ethylene at large Ti–C(ethylene) distances does not resemble **IPMe$_{\text{inner}}$** and would therefore not be directly comparable with front direction approach, *c.f.* study by Sandhya *et al.*.[172]

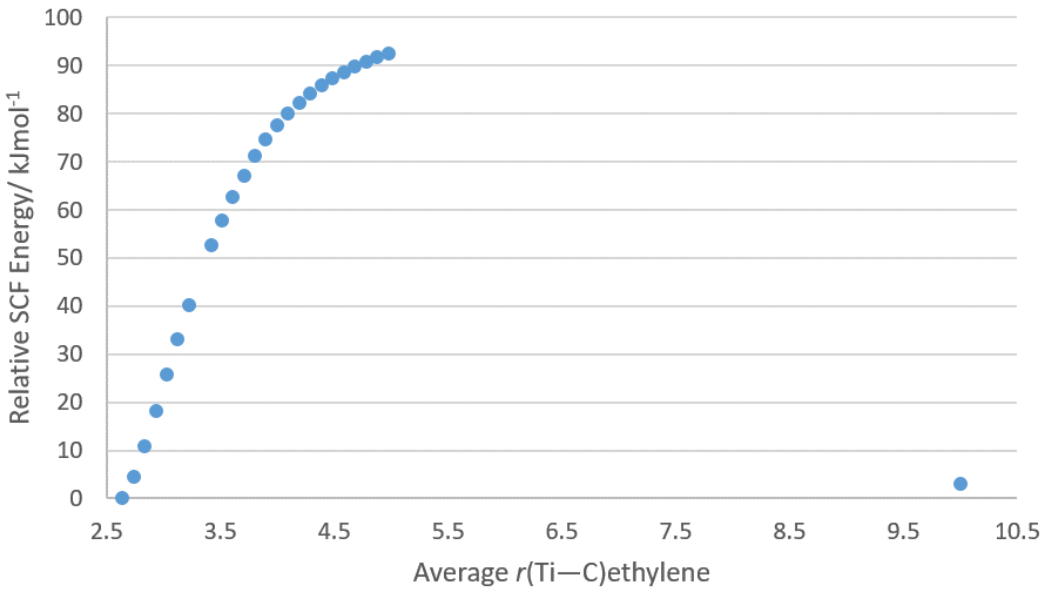
100
90
80
70
60
50
40
30
20
10
0
Relative SCF Energy/ kJmol-1
2.5
3.5
4.5
5.5
6.5
7.5
8.5
9.5
10.5
Average r(Ti—C)ethylene

Appendix C - Ion-pair ethylene homopolymerisation structures

front

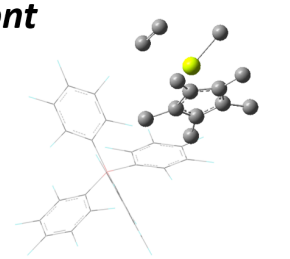

π

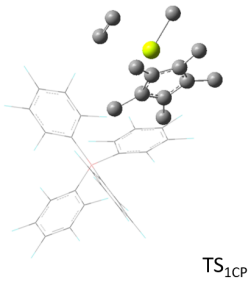

TS_{1CP}

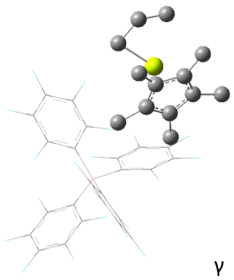

γ

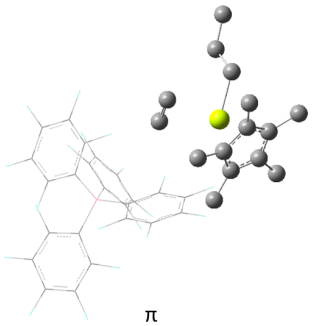

π

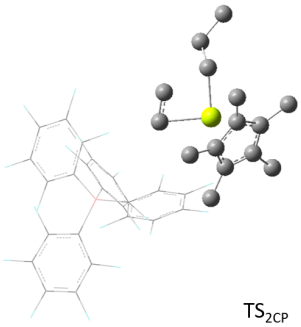

TS_{2CP}

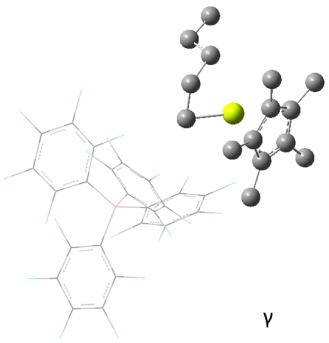

γ

back

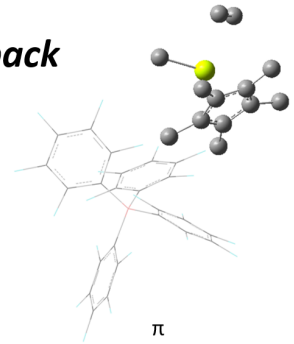

π

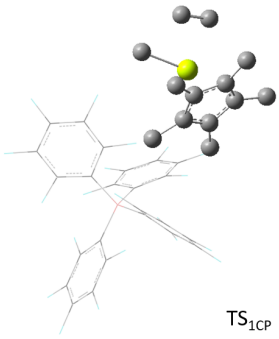

TS_{1CP}

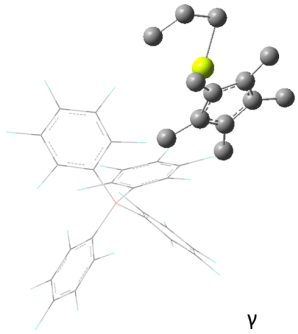

γ

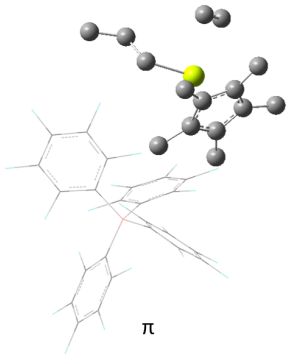

π

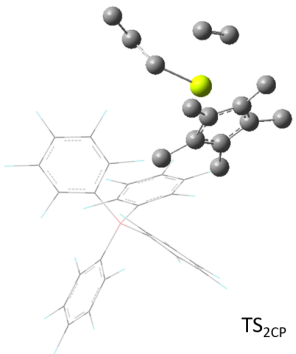

TS_{2CP}

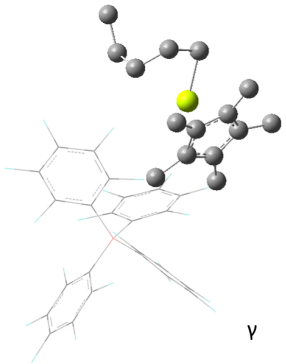

γ

Appendix D - Naked cationic ethylene homopolymerisation structures

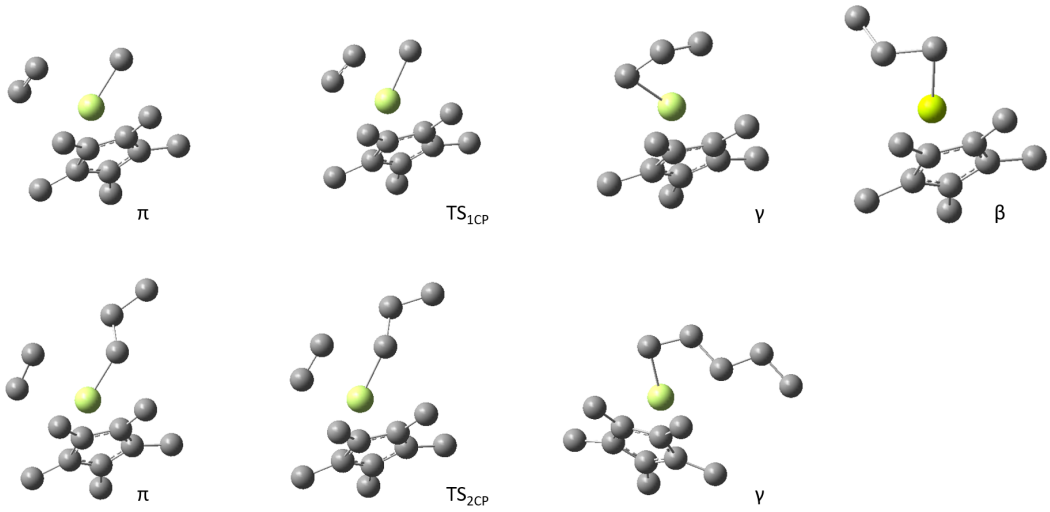

Appendix E - Geometric data of ion-pair propylene homopolymerisation structures

front		Ti–B	Ti–*o*F	Ti–*m*F	Ti–$H_{\alpha/\gamma}$	$C_{\alpha/\gamma}$–H	Ti-H-$C_{\alpha/\gamma}$
$IPMe_{inner}$		5.28	2.26	2.46	2.69	1.101	47
1st π	1,2 *re*	6.82	4.09	4.34	2.65	1.103	48.30
	1,2 *si*	6.89	4.18	4.51	2.66	1.103	47.9
	2,1 *re*	7.24	4.39	4.70	2.70	1.101	46.0
	2,1 *si*	6.69	3.98	4.46	2.70	1.101	45.9
2nd π	1,2 *re*	6.39	3.53	4.08	2.72	1.104	45.5
	1,2 *si*	6.41	3.55	4.14	2.63	1.103	50.4
TS_{1CP}	1,2 *re*	6.65	3.98	4.36	2.05	1.132	79.3
	1,2 *si*	6.74	4.05	4.44	2.03	1.134	80.0
	2,1 *re*	6.81	3.96	4.44	2.04	1.133	79.0
	2,1 *si*	6.48	3.76	4.315	2.07	1.131	78.5
TS_{2CP}	1,2 re	6.42	3.59	4.10	1.96	1.139	83.3
	1,2 *si*	6.24	3.47	4.15	1.99	1.134	83.5
1st γ	1,2 *re*	6.50	3.90	4.44	2.09	1.125	95.6
	1,2 si	6.76	4.09	4.54	2.15	1.122	86.6
	2,1 *re*	6.63	3.74	4.17	2.08	1.126	93.7
	2,1 *si*	6.44	3.56	3.78	2.10	1.124	92.1
2nd γ	1,2 *re*	6.12	3.29	3.92	1.96	1.129	104.3
	1,2 *si*	5.12	2.18	3.03	3.28	1.101	104.4

back		Ti–B	Ti–*o*F	Ti–*m*F	Ti–$H_{\alpha/\gamma}$	$C_{\alpha/\gamma}$–H	Ti-H-$C_{\alpha/\gamma}$
	$IPMe_{inner}$	5.28	2.26	2.46			
1st π	1,2 *re*	7.22	4.57	4.64	2.62	1.104	50.0
	1,2 *si*	6.97	4.2	4.00	2.69	1.100	46.3
	2,1 *re*	7.25	4.63	4.76	2.66	1.102	47.5
	2,1 *si*	6.97	4.33	4.72	2.61	1.103	49.7
2nd π	1,2 *re*	7.03	4.21	3.59	2.14	1.133	70.9
	1,2 *si*	7.83	5.87	5.27	2.31	1.120	64.2
TS_{1CP}	1,2 re	7.04	4.29	4.20	2.07	1.131	76.6
	1,2 *si*	6.93	4.19	4.36	2.07	1.131	76.3
	2,1 *re*	6.97	4.18	3.94	2.05	1.131	77.8
	2,1 *si*	6.94	4.22	4.42	2.06	1.133	76.8
TS_{2CP}	1,2 *re*	7.14	4.33	3.73	1.99	1.142	80.5
	1,2 *si*	7.45	4.46	5.00	1.96	1.139	81.8
1st γ	1,2 *re*	6.96	4.13	3.36	2.17	1.116	88.5
	1,2 *si*	6.86	4.04	3.91	2.08	1.122	96.8
	2,1 *re*	6.91	4.08	3.72	2.09	1.123	94.9
	2,1 *si*	6.87	4.07	4.01	2.08	1.124	95.4
2nd γ	1,2 *re*	6.98	4.15	3.68	2.08	1.125	96.0
	1,2 *si*	7.11	4.39	4.28	2.06	1.132	109.7

Appendix F - Ion-pair propylene homopolymerisation structures

1st CP: 1,2 re

front

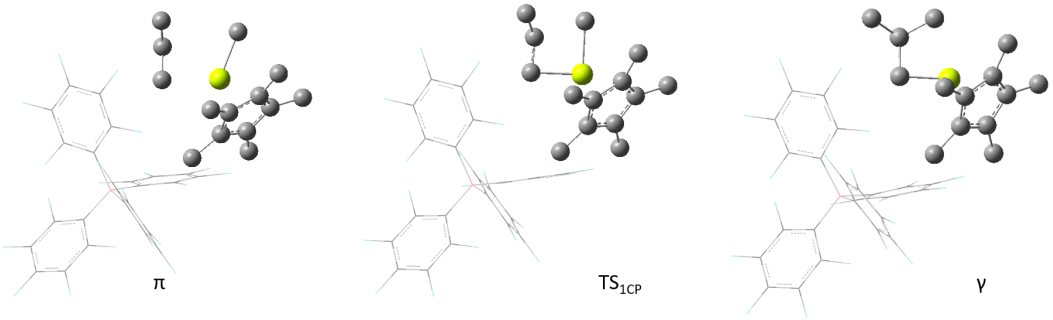

1st CP: 1,2 si

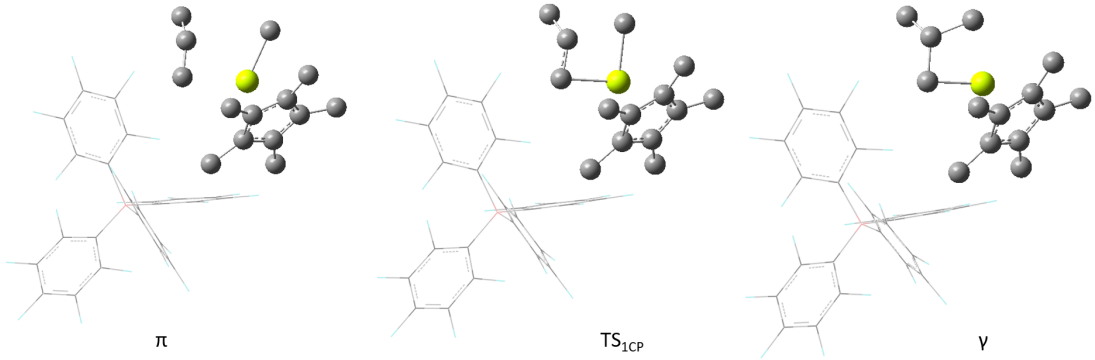

1st CP: 2,1 re

front

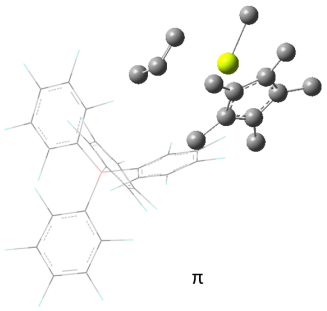

π

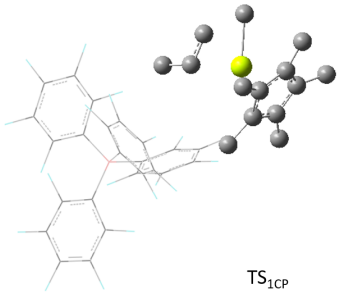

TS_{1CP}

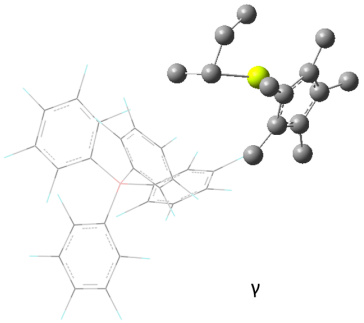

γ

1st CP: 2,1 *si*

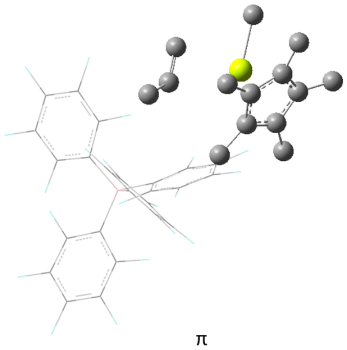

π

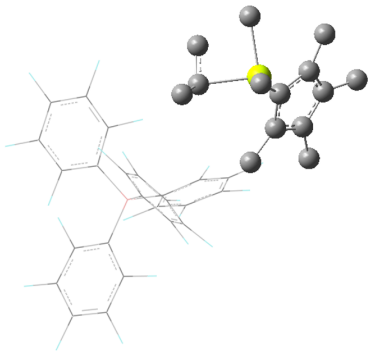

TS_{1CP}

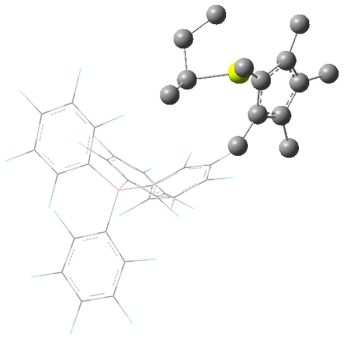

γ

front

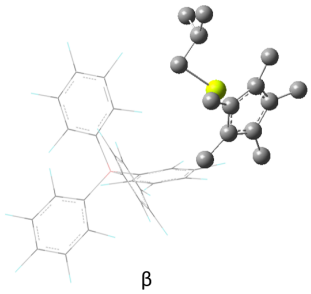

β

2nd CP: 1,2 re

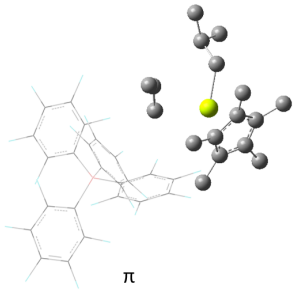

π

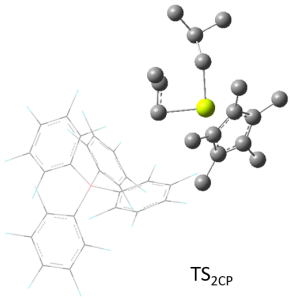

TS_{2CP}

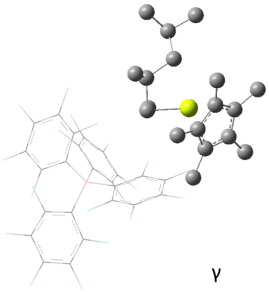

γ

2nd CP: 1,2 si

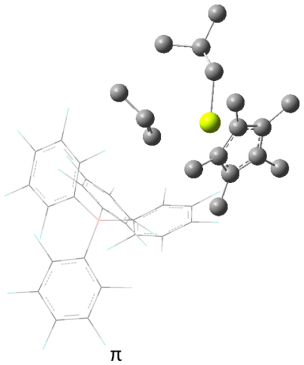

π

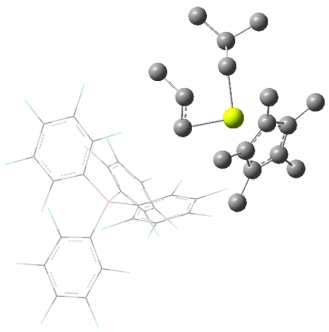

TS_{2CP}

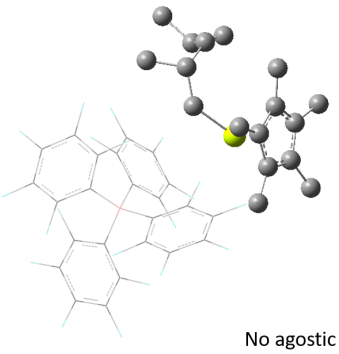

No agostic

1st CP: 1,2 re

back

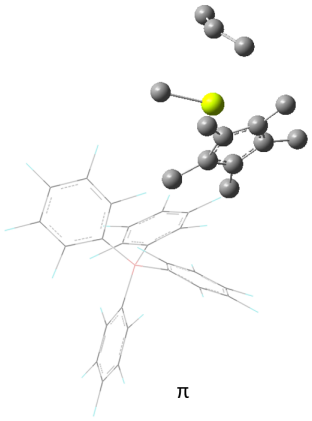

π

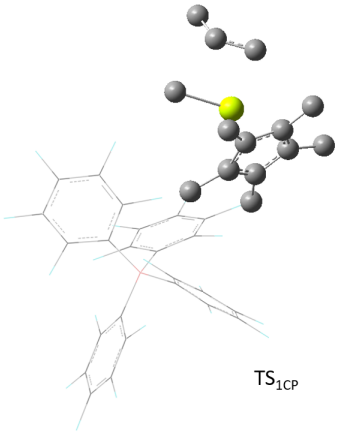

TS_{1CP}

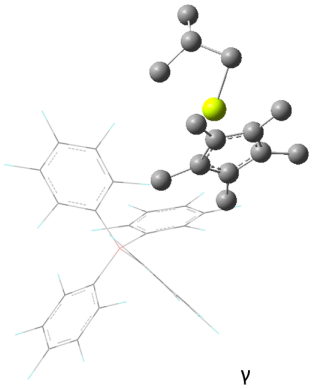

γ

1st CP; 1,2 si

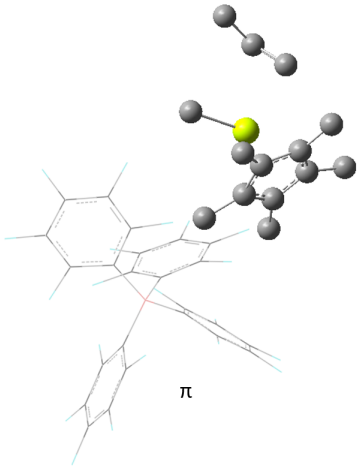

π

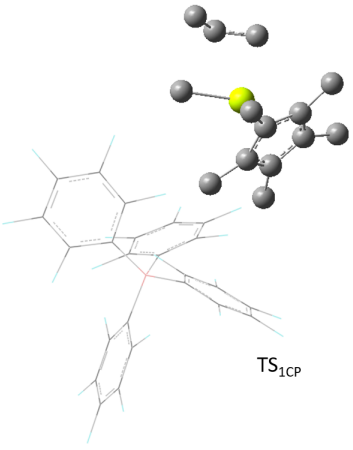

TS_{1CP}

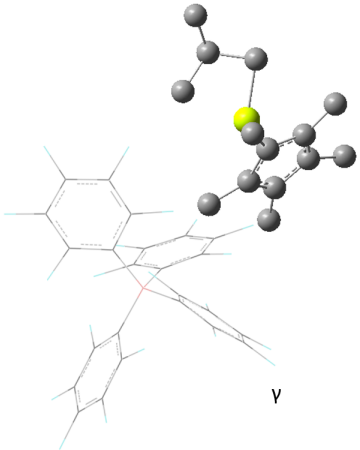

γ

1st CP: 2,1 re

back

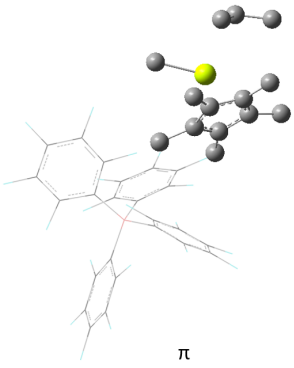

π

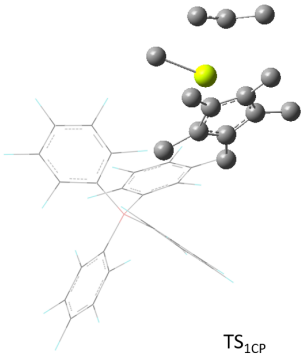

TS_{1CP}

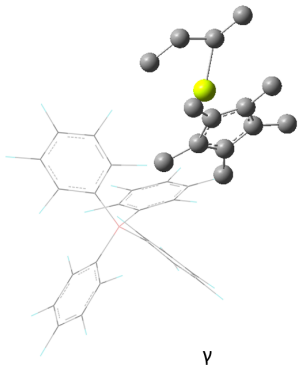

γ

1st CP: 2,1 si

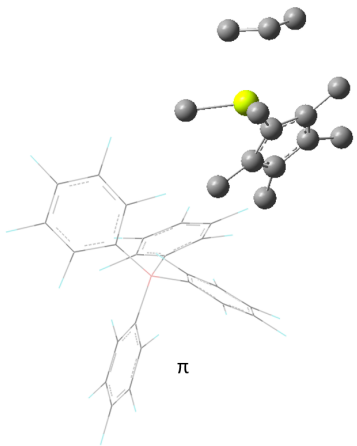

π

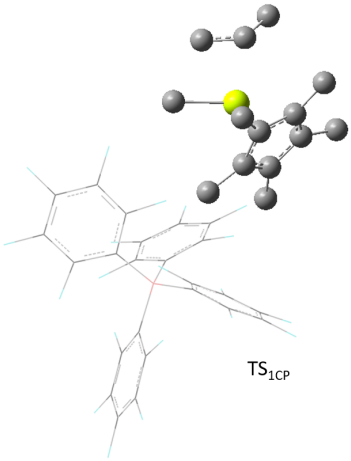

TS_{1CP}

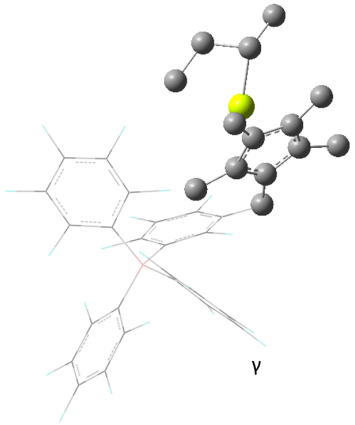

γ

back

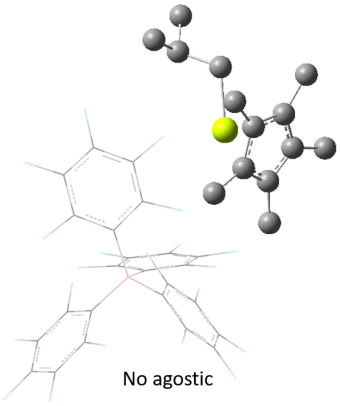

No agostic

2nd CP: 1,2 re

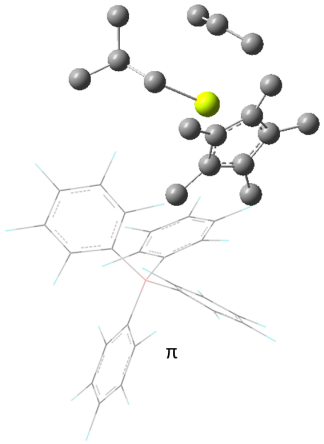

π

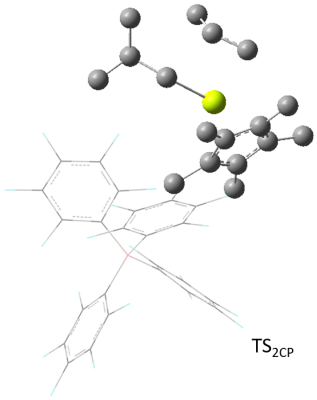

TS_{2CP}

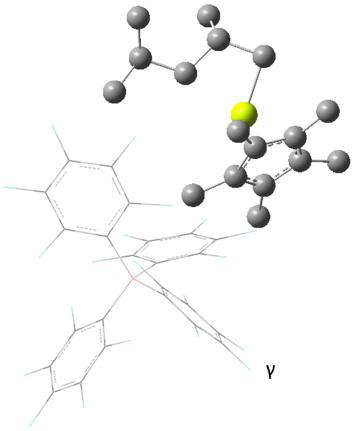

γ

2nd CP: 1,2 si

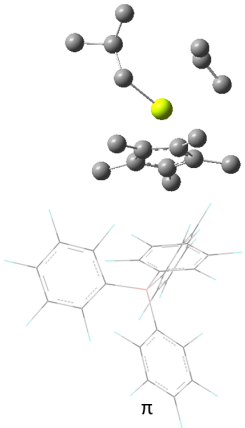

π

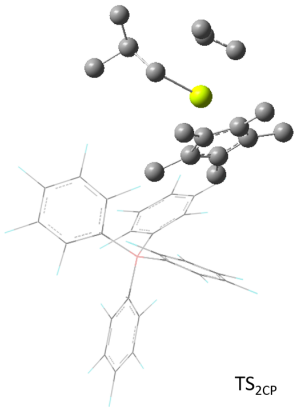

TS_{2CP}

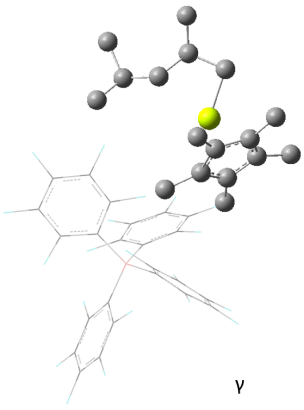

γ

Appendix G - Geometric data of naked cationic propylene homopolymerisation structures

		Ti–$H_{\alpha/\gamma}$	$C_{\alpha/\gamma}$–H	Ti-H-$C_{\alpha/\gamma}$
CatMe		2.62	1.106	48.8
1st π	1,2 *re*	2.65	1.104	47.9
	1,2 *si*	2.65	1.103	47.9
	2,1 *re*	2.67	1.102	46.5
	2,1 *si*	2.70	1.101	45.5
2nd π	1,2 *re*	2.30	1.122	64.6
	1,2 *si*	2.52	1.109	54.7
TS_{1CP}	1,2 *re*	2.04	1.134	78.6
	1,2 *si*	2.04	1.135	78.5
	2,1 *re*	2.04	1.134	78.2
	2,1 *si*	2.06	1.133	77.9
TS_{2CP}	1,2 *re*	1.94	1.144	83.0
	1,2 *si*	1.98	1.137	82.3
1st γ	1,2 *re*	2.08	1.125	93.6
	1,2 *si*	2.12	1.125	87.3
	2,1 *re*	2.07	1.126	93.1
	2,1 *si*	2.09	1.125	90.5
2nd γ	1,2 *re*	1.99	1.133	107.6
	1,2 *si*	2.05	1.134	101.9

Appendix H - Naked-cationic propylene homopolymerisation structures

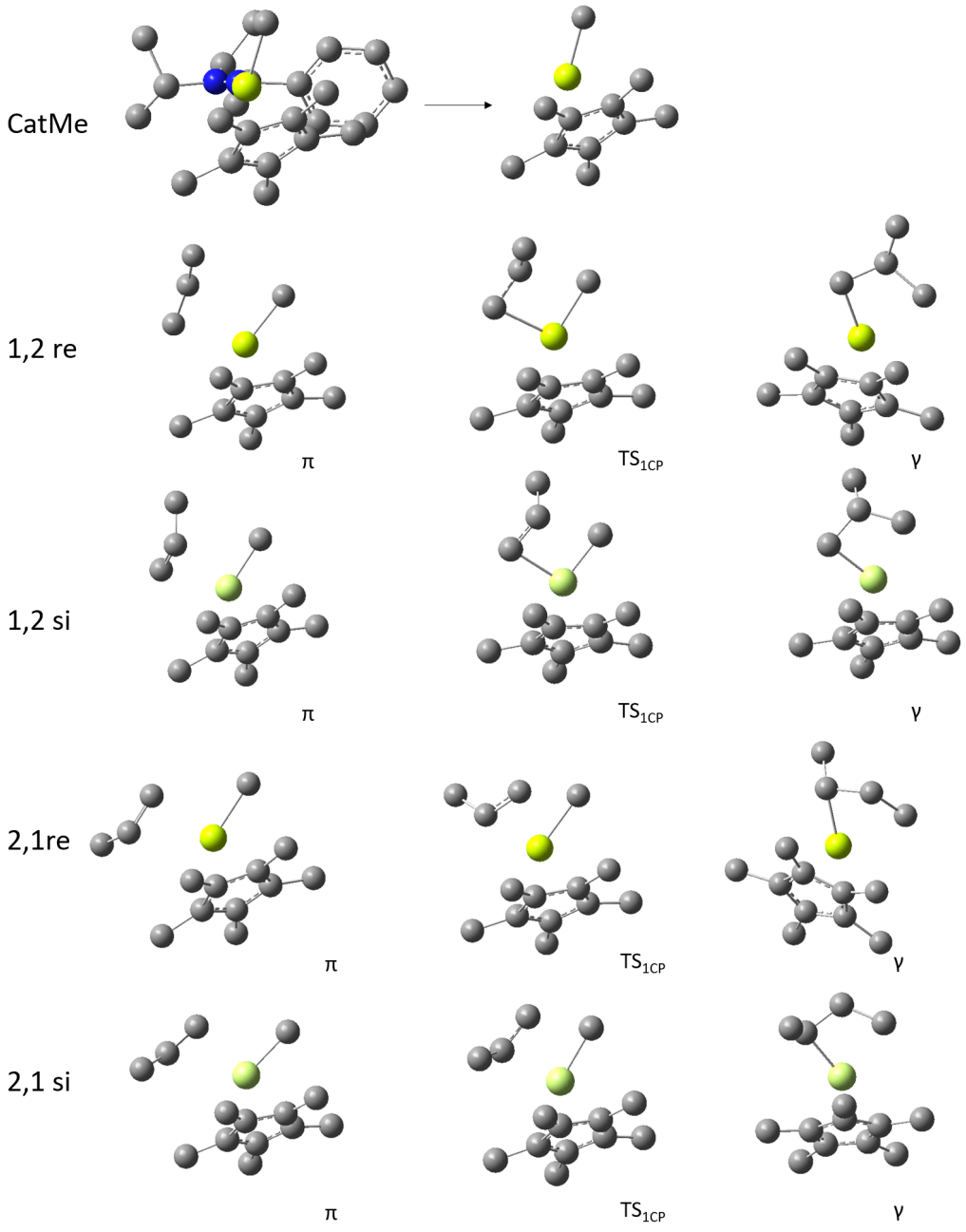

CatiBu

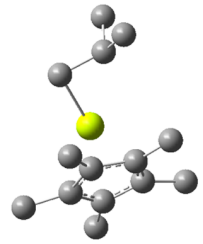

1,2 re

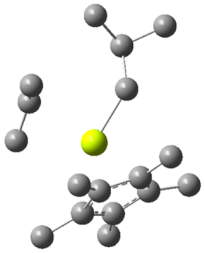

π

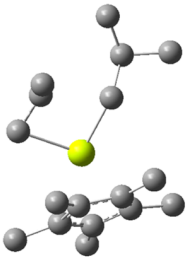

TS_{2CP}

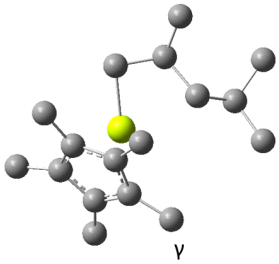

γ

2,1 re

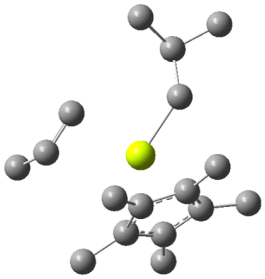

π

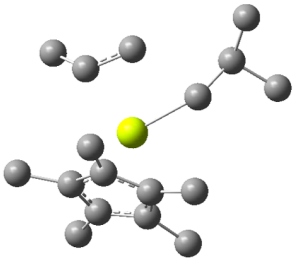

TS_{2CP}

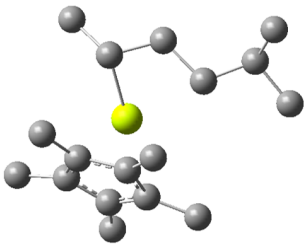

γ

Bibliography

[1] M. Born and R. Oppenheimer. Zur quantentheorie der molekeln. *Annalen der Physik*, 389(20):457–484, 1927.

[2] J. Cizek. On the correlation problem in atomic and molecular systems. Calculation of wavefunction components in Ursell-type expansion using quantum-field theoretical methods. *The Journal of Chemical Physics*, 45(11):4256–4266, 1966.

[3] P. Hohenberg. Inhomogeneous Electron Gas. *Physical Review*, 136(3B):864–871, 1964.

[4] W. Kohn and L. J. Sham. Self-consistent equations including exchange and correlation effects. *Physical Review*, 140(4A):1133–1138, 1965.

[5] T. Kato. On the eigenfunctions of many-particle systems in quantum mechanics. *Communications on Pure and Applied Mathematics*, 10(2):151–177, 1957.

[6] P. Pyykko. Relativistic effects in structural chemistry. *Chemical Reviews*, 88(3):563–594, 1988.

[7] T. Ziegler, J.G. Snijders, and E.J. Baerends. On the origin of relativistic bond contraction. *Chemical Physics Letters*, 75(1):1–4, 1980.

[8] M. Douglas and N. M. Kroll. Quantum electrodynamical corrections to the fine structure of helium. *Annals of Physics*, 82(1):89–155, 1974.

[9] B. Hess. Applicability of the no-pair equation with free-particle projection operators to atomic and molecular structure calculations. *Physical Review A*, 32(2):756–763, 1985.

[10] B. Hess. Relativistic electronic-structure calculations employing a two-component no-pair formalism with external-field projection operators. *Physical Review A*, 33(6):3742–3748, 1986.

[11] G. Jansen and B. Hess. Revision of the Douglas-Kroll transformation. *Physical Review A*, 39(11):6016–6017, 1989.

[12] E. van Lenthe, E. J. Baerends, and J. G. Snijders. Relativistic regular two-component Hamiltonians. *The Journal of Chemical Physics*, 99(6):4597–4610, 1993.

[13] R. van Leeuwen, E. van Lenthe, E. J. Baerends, and J. G. Snijders. Exact solutions of regular approximate relativistic wave equations for hydrogen-like atoms. *The Journal of Chemical Physics*, 101(2):1272–1281, 1994.

[14] E. van Lenthe, A. Ehlers, and E.J. Baerends. Geometry optimizations in the zero order regular approximation for relativistic effects. *The Journal of Chemical Physics*, 110(18):8943–8953, 1999.

[15] E. van Lenthe and E. J. Baerends. Optimized Slater-type basis sets for the elements 1-118. *Journal of Computational Chemistry*, 24(9):1142–1156, 2003.

[16] R. F. W. Bader. *Atoms in Molecules: A Quantum Theory*. Oxford University Press, 1990.

[17] C.F. Matta and R.J. Boyd. *The Quantum Theory of Atoms in Molecules*. Wiley-VCH, Weinheim, 2007.

[18] D. Cremer and E. Kraka. A description of the chemical bond in terms of local properties of the electron density and energy. *Croatica Chemica Acta*, 57(6):1259–1281, 1984.

[19] X. Fradera, M.A. Austen, and R.F.W. Bader. The Lewis model and beyond. *The Journal of Physical Chemistry A*, 103(2):304–314, 1999.

[20] M. A. Austen. *A new procedure for determining bond orders in polar molecules, with applications to phosphorus and nitrogen containing systems*. PhD thesis, McMaster University, 2003.

[21] R. F. W. Bader and H. Essén. The characterization of atomic interactions. *The Journal of Chemical Physics*, 80(5):1943–1960, 1984.

[22] F. London. Zur theorie und systematik der molekularkräfte. *Zeitschrift für Physik*, 63(3-4):245–279, 1930.

[23] R. Eisenschitz and F. London. Über das Verhältnis der van der Waalsschen Kräfte zu den homöpolaren Bindungskräften. *Zeitschrift für Physik*, 60(7-8):491–527, 1930.

[24] A.D. Becke. Density-functional thermochemistry. III. The role of exact exchange. *The Journal of Chemical Physics*, 98(7):5648–5652, 1993.

[25] P. J. Stephens, F. J. Devlin, C. F. Chabalowski, and M. J. Frisch. *Ab Initio* calculation of vibrational absorption and circular dichroism spectra using density functional force fields. *The Journal of Physical Chemistry*, 98(45):11623–11627, 1994.

[26] John P. Perdew, Kieron Burke, and Matthias Ernzerhof. Generalized gradient approximation made simple. *Physical Review Letters*, 77(18):3865–3868, 1996.

[27] P. Slavcek, R. Kalus, P. Paska, I. Odvarkova, P. Hobza, and A. Malijevsky. State-of-the-art correlated *ab initio* potential energy curves for heavy rare gas dimers: Ar_2, Kr_2, and Xe_2. *The Journal of Chemical Physics*, 119(4):2102–2119, 2003.

[28] C.D. Sherrill, T. Takatani, and E.G. Hohenstein. An assessment of theoretical methods for nonbonded interactions: comparison to complete basis set limit coupled-cluster potential energy curves for the benzene dimer, the methane dimer, benzene-methane, and benzene-H_2S. *The journal of physical chemistry. A*, 113(38):10146–10159, 2009.

[29] S. Grimme. Density functional theory with London dispersion corrections. *Wiley Interdisciplinary Reviews: Computational Molecular Science*, 1(2):211–228, 2011.

[30] J. Klimeš and A. Michaelides. Perspective: Advances and challenges in treating van der Waals dispersion forces in density functional theory. *The Journal of chemical physics*, 137(12):120901, 2012.

[31] S. Grimme, J. Antony, S. Ehrlich, and H. Krieg. A consistent and accurate *ab initio* parametrization of density functional dispersion correction (DFT-D) for the 94 elements H-Pu. *The Journal of chemical physics*, 132(15):154104, 2010.

[32] Y. Zhao and D.G. Truhlar. The M06 suite of density functionals for main group thermochemistry, thermochemical kinetics, noncovalent interactions, excited states, and transition elements: two new functionals and systematic testing of four M06-class functionals and 12 other function. *Theoretical Chemistry Accounts*, 120(1-3):215–241, 2007.

[33] S. Grimme. Accurate description of van der Waals complexes by density functional theory including empirical corrections. *Journal of computational chemistry*, 25(12):1463–73, 2004.

[34] P. Jurecka, J. Cerný, P. Hobza, and D.R. Salahub. Density functional theory augmented with an empirical dispersion term. Interaction energies and geometries of 80 noncovalent complexes compared with ab initio quantum mechanics calculations. *Journal of computational chemistry*, 28(2):555–569, 2007.

[35] Y. Zhao and D.G. Truhlar. Density functionals with broad applicability in chemistry. *Accounts of chemical research*, 41(2):157–167, 2008.

[36] H. Ågren and K.V. Mikkelsen. Theory of solvent effects on electronic spectra. *Journal of Molecular Structure: THEOCHEM*, 234:425–467, 1991.

[37] C.J. Cramer and D.G. Truhlar. Implicit solvation models: equilibria, structure, spectra, and dynamics. *Chemical Reviews*, 99(8):2161–2200, 1999.

[38] P.E. Smith and B. M. Pettitt. Modelling solvent in biomolecular systems. *The Journal of Physical Chemistry*, 98(39):9700–9711, 1994.

[39] M. Cossi, V. Barone, R. Cammi, and J. Tomasi. *Ab initio* study of solvated molecules: a new implementation of the polarizable continuum model. *Chemical Physics Letters*, 255(4-6):327–335, 1996.

[40] D. J Frisch, M. J.; Trucks, G. W.; Schlegel, H. B.; Scuseria, G. E.; Robb, M. A.; Cheeseman, J. R.; Scalmani, G.; Barone, V.; Mennucci, B.; Petersson, G. A.; Nakatsuji, H.; Caricato, M.; Li, X.; Hratchian, H. P.; Izmaylov, A. F.; Bloino, J.; Zheng, G.; Sonnenb. Gaussian 09 Revision D.01, 2009.

[41] A.L. Yakovlev E.J. Baerends, T. Ziegler, J. Autschbach, D. Bashford, A. Bérces, F.M. Bickelhaupt, C. Bo, P.M. Boerrigter, L. Cavallo, D.P. Chong, L. Deng, R.M. Dickson,

D.E. Ellis, M. van Faassen, L. Fan, T.H. Fischer, C. Fonseca Guerra, A. Ghysels, A. Giammona, S.J.A. ADF, 2012.

[42] T.A. Keith. AIMAll, 2014.

[43] J.J.P. Stewart. MOPAC2016.

[44] A. Yokovlev, P. Philipsen, S. Borini, R. Ruger, A.F. Oliveira, M. de Reus, M. Ghorbani Asl, D. McCormack, S. Patchkovskii, and T. Heine. ADF DFTB 2016.

[45] A.C.T. van Duin, W.A. Goddard, H. van Schoot, and A.L. Yakolev. ReaxFF 2016, 2016.

[46] F. L. Hirshfeld. Bonded-atom fragments for describing molecular charge densities. *Theoretica Chimica Acta*, 44(2):129–138, 1977.

[47] K. Morokuma. Molecular orbital studies of hydrogen bonds. III. C=O···H–O Hydrogen Bond in $H_2CO\cdots H_2O$ and $H_2CO\cdots 2H_2O$. *The Journal of Chemical Physics*, 55(3):1236–1244, 1971.

[48] Tom Ziegler and Arvi Rauk. On the calculation of bonding energies by the Hartree Fock Slater method. *Theoretica Chimica Acta*, 46(1):1–10, 1977.

[49] http://sf.anu.edu.au/~vvv900/gaussian/ts/.

[50] L. Versluis and T. Ziegler. The determination of molecular structures by density functional theory. The evaluation of analytical energy gradients by numerical integration. *The Journal of Chemical Physics*, 88(1):322–328, 1988.

[51] L. Fan and T. Ziegler. Optimization of molecular structures by self-consistent and nonlocal density-functional theory. *The Journal of Chemical Physics*, 95(10):7401–7408, 1991.

[52] C.G. Broyden. The convergence of a class of double-rank minimization algorithms 2. The new algorithm. *Journal of Institute of Mathematics and its Applications*, 6:222–231, 1970.

[53] R. Fletcher. A new approach to variable metric algorithms. *The Computer Journal*, 13(3):317–322, 1970.

[54] D. Goldfarb. A family of variable-metric methods derived by variational means. *Mathematics of Computation*, 24(109):23–26, 1970.

[55] D. F. Shanno. Conditioning of quasi-Newton methods for function minimization. *Mathematics of Computation*, 24(111):647–656, 1970.

[56] H. B. Schlegel. Optimization of equilibrium geometries and transition structures. *Journal of Computational Chemistry*, 3(2):214–218, 1982.

[57] C. Peng and B.H. Schlegel. Combining synchronous transit and quasi-Newton methods to find transition states. *Israel Journal of Chemistry*, 33(4):449–454, 1993.

[58] C. Peng, P.Y. Ayala, H.B. Schlegel, and M.J. Frisch. Using redundant internal coordinates to optimize equilibrium geometries and transition states. *Journal of Computational Chemistry*, 17(1):49–56, 1996.

[59] http://www.chem.wisc.edu/content/conformations-alkanes.

[60] K. Fukui. The path of chemical reactions - the IRC approach. *Accounts of Chemical Research*, 14(12):363–368, 1981.

[61] L. Deng and T. Ziegler. The determination of intrinsic reaction coordinates by density functional theory. *International Journal of Quantum Chemistry*, 52(4):731–765, 1994.

[62] K. Ziegler, E. Holzkamp, H. Breil, and H. Martin. Das mülheimer normaldruck-polyäthylen-verfahren. *Angewandte Chemie*, 67(19-20):541–547, 1955.

[63] K. Ziegler. Folgen und werdegang einer erfindung Nobel-Vortrag. *Angewandte Chemie*, 76(13):545–553, 1964.

[64] G. Natta. Stereospezifische katalysen und isotaktische Polymere. *Angewandte Chemie*, 68(12):393–403, 1956.

[65] G. Natta. Von der stereospezifischen polymerisation zur asymmetrischen autokatalytischen synthese von makromolekülen Nobel-Vortrag. *Angewandte Chemie*, 76(13):553–566, 1964.

[66] S.D. Ittel, L.K. Johnson, and M. Brookhart. Late-metal catalysts for ethylene homo- and copolymerization. *Chemical Reviews*, 100(4):1169–1204, 2000.

[67] V.C. Gibson and S.K. Spitzmesser. Advances in non-metallocene olefin polymerization catalysis. *Chemical reviews*, 103(1):283–315, 2003.

[68] J. Zhang and G.X. Wang, X.and Jin. Polymerized metallocene catalysts and late transition metal catalysts for ethylene polymerization. *Coordination Chemistry Reviews*, 250(1-2):95–109, 2006.

[69] C. Bianchini, G. Giambastiani, I. G. Rios, G. Mantovani, A. Meli, and A.M. Segarra. Ethylene oligomerization, homopolymerization and copolymerization by iron and cobalt catalysts with 2,6-(bis-organylimino)pyridyl ligands. *Coordination Chemistry Reviews*, 250(11-12):1391–1418, 2006.

[70] M. Nishiura and Z. Hou. Half-sandwich rare earth metal complexes as novel catalysts for olefin polymerization and other chemical transformations. *Bulletin of the Chemical Society of Japan*, 83(6):595–608, 2010.

[71] M. Bochmann. Cationic Group 4 metallocene complexes and their role in polymerisation catalysis: the chemistry of well defined Ziegler catalysts. *Journal of the Chemical Society, Dalton Transactions*, (3):255–270, 1996.

[72] P. Pino and R. Mülhaupt. Stereospecific polymerization of propylene: An outlook 25 years after its discovery. *Angewandte Chemie International Edition in English*, 19(11):857–875, 1980.

[73] G. Wilkinson, P. L. Pauson, J. M. Birmingham, and F. A. Cotton. Bis-cyclopentadienyl derivatives of some transition elements. *Journal of the American Chemical Society*, 75(4):1011–1012, 1953.

[74] D.S. Breslow.

[75] D.S. Breslow and N.R. Newburg. Bis-cyclopentadienyl-titanium dichloridealkylaluminum complexes as catalysts for the polymerization of ethylene. *Journal of the American Chemical Society*, 79(18):5072–5073, 1957.

[76] Giulio Natta, Piero Pino, Giorgio Mazzanti, and Umberto Giannini. A crystallizable organometallic complex containing titanium and aluminum. *Journal of the American Chemical Society*, 79(11):2975–2976, 1957.

[77] A. Andresen, H.G. Cordes, J. Herwig, W. Kaminsky, A. Merck, R. Mottweiler, J. Pein, H. Sinn, and H.J. Vollmer. Halogen-free soluble Ziegler catalysts for the polymerization of ethylene. Control of molecular weight by choice of temperature. *Angewandte Chemie International Edition in English*, 15(10):630–632, 1976.

[78] H. Sinn and W. Kaminsky. Ziegler-Natta Catalysis. *Advances in Organometallic Chemistry*, 18:99–149, 1980.

[79] A.L. McKnight and R.M. Waymouth. Group 4 ansa-cyclopentadienyl-amido catalysts for olefin polymerization. *Chemical Reviews*, 98(7):2587–2598, 1998.

[80] W. Kaminsky, K. Külper, H. H. Brintzinger, and F.R.W.P. Wild. Polymerization of propene and butene with a chiral zirconocene and methylalumoxane as cocatalyst. *Angewandte Chemie International Edition in English*, 24(6):507–508, 1985.

[81] J.A. Ewen, R.L. Jones, A. Razavi, and J.D. Ferrara. Syndiospecific propylene polymerizations with Group IVB metallocenes. *Journal of the American Chemical Society*, 110(18):6255–6256, 1988.

[82] P.J. Sinnema, A.L. van der Veen, L.and Spek, N. Veldman, and J.H. Teuben. Titanium dichloro, bis(carbyl), aryne, and alkylidene complexes stabilized by linked cyclopentadienylamido auxiliary ligands. *Organometallics*, 16(20):4245–4247, 1997.

[83] D.B. Millward, A.P. Cole, and R.M. Waymouth. Catalytic carboalumination of olefins with cyclopentadienylamidotitanium dichloride complexes. *Organometallics*, 19(10):1870–1878, 2000.

[84] G.J.P. Britovsek, V.C. Gibson, and D.F. Wass. The search for new-generation olefin polymerization catalysts: Life beyond metallocenes. *Angewandte Chemie International Edition*, 38(4):428–447, 1999.

[85] K. Nomura and J. Liu. Half-titanocenes for precise olefin polymerisation: effects of ligand substituents and some mechanistic aspects. *Dalton Transactions*, 40(30):7666–7682, 2011.

[86] R.A. Collins, A.F. Russell, and P. Mountford. Group 4 metal complexes for homogeneous olefin polymerisation: A short tutorial review. *Applied Petrochemical Research*, 5(3):153–171, 2015.

[87] K. Nomura, H. Fukuda, W. Apisuk, A.G. Trambitas, B. Kitiyanan, and M. Tamm. Ethylene copolymerization by half-titanocenes containing imidazolin-2-iminato ligandsMAO catalyst systems. *Journal of Molecular Catalysis A: Chemical*, 363:501–511, 2012.

[88] E.G. Ijpeij, B. Coussens, M.A. Zuideveld, G.H.J. van Doremaele, P. Mountford, M. Lutz, and A.L. Spek. Synthesis, solid state and DFT structure and olefin polymerization capability of a unique base-free dimeric methyl titanium dication. *Chemical Communications*, 46(19):3339–3341, 2010.

[89] E.G. Ijpeij, J.H. Windmuller, P.J Arts, H.F. van der Burgt, G. van Doremaele, and M.A. Zuideveld, 2005.

[90] R.H. Grubbs and G. W. Coates. α-Agostic interactions and olefin insertion in metallocene polymerization catalysts. *Accounts of Chemical Research*, 29(2):85–93, 1996.

[91] M. Brookhart, A. F. Volpe, D. M. Lincoln, I. T. Horvath, and J. M. Millar. Detection of an alkyl ethylene complex during ethylene polymerization by a cobalt(III) catalyst. Energetics of the .beta.-migratory insertion reaction. *Journal of the American Chemical Society*, 112(14):5634–5636, 1990.

[92] Z. Wu, R.F. Jordan, and J.L. Petersen. Models for the Elusive $Cp_2Zr(R)(olefin)^+$. Characterization of the d^0 metal olefin complex $Cp_2Zr(OCMe_2CH_2CH_2CH{:}CH_2)^+$. *Journal of the American Chemical Society*, 117(21):5867–5868, 1995.

[93] C.P. Casey, S.L. Hallenbeck, D.W. Pollock, and C.R. Landis. Synthesis and spectroscopic characterization of the d^0 transition metal-alkyl-alkene aomplex $Cp^*_2YCH_2CH_2C(CH_3)_2CH{:}CH_2$. *Journal of the American Chemical Society*, 117(38):9770–9771, 1995.

[94] C.P. Casey, S. L. Hallenbeck, J. M. Wright, and C.R. Landis. Formation and spectroscopiccharacterization of chelated d^0 Yttrium(III)alkylalkene complexes. *Journal of the American Chemical Society*, 119(41):9680–9690, 1997.

[95] D.S. Breslow and N.R. Newburg. Bis-(cyclopentadienyl)-titanium dichloride-alkylaluminum complexes as soluble catalysts for the polymerization of ethylene 1,2. *Journal of the American Chemical Society*, 81(1):81–86, 1959.

[96] P. Cossee. On the reaction mechanism of the ethylene polymerization with heterogeneous Ziegler-Natta catalysts. *Tetrahedron Letters*, 1(38):12–16, 1960.

[97] P. Cossee. The formation of isotactic polypropylene under the influence of Ziegler-Natta catalysts. *Tetrahedron Letters*, 1(38):17–21, 1960.

[98] P. Cossee. Ziegler-Natta catalysis I. Mechanism of polymerization of α-olefins with Ziegler-Natta catalysts. *Journal of Catalysis*, 3(1):80–88, 1964.

[99] E Arlman. Ziegler-Natta catalysis III. Stereospecific polymerization of propene with the catalyst system $TiCl_3$–$AlEt_3$. *Journal of Catalysis*, 3(1):99–104, 1964.

[100] M.L.H. Green. Studies on synthesis, mechanism and reactivity of some organo-molybdenum and -tungsten compounds. *Pure and Applied Chemistry*, 50(1):27–35, 1978.

[101] K.J. Ivin, J.J. Rooney, C.D. Stewart, M.L.H. Green, and R. Mahtab. Mechanism for the stereospecific polymerization of olefins by Ziegler-Natta catalysts. *Journal of the Chemical Society, Chemical Communications*, (14):604–606, 1978.

[102] Z. Dawoodi, M.L.H. Green, V.S.B. Mtetwa, and K. Prout. A titanium-methyl group containing a covalent bridging hydrogen system: X-ray crystal structure of $Ti(Me_2PCH_2CH_2PMe_2)MeCl_3$. *Journal of the Chemical Society, Chemical Communications*, (24):1410–1411, 1982.

[103] D. T. Laverty and J.J. Rooney. Mechanism of initiation of the ring-opening polymerization and addition oligomerization of norbornene using unicomponent metathesis catalysts. *Journal of the Chemical Society, Faraday Transactions 1: Physical Chemistry in Condensed Phases*, 79(4):869–878, 1983.

[104] M. Brookhart and M.L.H. Green. Carbon-hydrogen-transition metal bonds. *Journal of Organometallic Chemistry*, 250(1):395–408, 1983.

[105] W. Scherer and G.S. McGrady. Agostic interactions in d^0 metal alkyl complexes. *Angewandte Chemie (International ed. in English)*, 43(14):1782–806, 2004.

[106] T. Yoshida, N. Koga, and K. Morokuma. *Ab Initio* theoretical study on ethylene polymerization with homogeneous silylene-bridged Group 4 metallocene catalysts. Ethylene insertion and β-elimination. *Organometallics*, 14(2):746–758, 1995.

[107] J.C.W. Lohrenz, T.K. Woo, and T. Ziegler. A density functional study on the origin of the propagation barrier in the homogeneous ethylene polymerization with Kaminsky-type catalysts. *Journal of the American Chemical Society*, 117(51):12793–12800, 1995.

[108] M. Brookhart, M.L.H. Green, and G. Parkin. Agostic interactions in transition metal compounds. *Proceedings of the National Academy of Sciences of the United States of America*, 104(17):6908–6914, 2007.

[109] Y.W. Alelyunas, Z. Guo, R.E. LaPointe, and R.F. Jordan. Structures and reactivity of $(C_5H_4Me)_2Zr(CH_2CH_2R)(CH_3CN)^{n+}$ complexes. Competition between insertion and β-H elimination. *Organometallics*, 12(2):544–553, 1993.

[110] Z. Guo, D.C. Swenson, and R.F. Jordan. Cationic zirconium and hafnium isobutyl complexes as models for intermediates in metallocene-catalyzed propylene polymerizations. Detection of an α-agostic interaction in $(C_5Me_5)_2Hf(CH_2CHMe_2)(PMe_3)^+$. *Organometallics*, 13(4):1424–1432, 1994.

[111] L. Resconi, L. Cavallo, A. Fait, and F. Piemontesi. Selectivity in propene polymerization with metallocene catalysts. *Chemical Reviews*, 100(4):1253–1346, 2000.

[112] L. Resconi, J. C. Chadwick, and L. Cavallo. Comprehensive Organometallic Chemistry III. chapter 9. Elsevier, 2006.

[113] H.H. Brintzinger, D. Fischer, R. Mülhaupt, B. Rieger, and R.M. Waymouth. Stereospecific olefin polymerization with chiral metallocene catalysts. *Angewandte Chemie International Edition in English*, 34(11):1143–1170, 1995.

[114] A. K. Rappé, W. M. Skiff, and C. J. Casewit. Modeling metal-catalyzed olefin polymerization. *Chemical Reviews*, 100(4):1435–1456, 2000.

[115] M. Borrelli, V. Busico, R. Cipullo, S. Ronca, and P.H.M. Budzelaar. Selectivity of metallocene-catalyzed olefin polymerization: A combined experimental and quantum mechanical study. 1. Nonchiral bis(cyclopentadienyl) systems. *Macromolecules*, 35(7):2835–2844, 2002.

[116] M. Borrelli, V. Busico, R. Cipullo, S. Ronca, and P.H.M. Budzelaar. Selectivity of metallocene-catalyzed olefin polymerization: A combined experimental and quantum mechanical Study. The ansa-$Me_2Si(Ind)_2Zr$ and ansa-$Me_2C(Cp)(Flu)Zr$ systems. *Macromolecules*, 36(21):8171–8177, 2003.

[117] G. Guerra, P. Corradini, and L. Cavallo. Molecular modeling of stereo- and regioselectivity of Group 4 heterocenes in the polymerization of propene. *Macromolecules*, 38(9):3973–3976, 2005.

[118] A. Correa and L. Cavallo. Dynamic properties of metallocenium ion pairs in solution by atomistic simulations. *Journal of the American Chemical Society*, 128(33):10952–10959, 2006.

[119] A. Correa, G. Talarico, and L. Cavallo. Regiochemistry of propene insertion with Group 4 polymerization catalysts from a theoretical perspective. *Journal of Organometallic Chemistry*, 692(21):4519–4527, 2007.

[120] A. Motta, I.L. Fragalà, and T.J. Marks. Stereochemical control mechanisms in propylene polymerization mediated by C_1-symmetric CGC titanium catalyst centers. *Journal of the American Chemical Society*, 129(23):7327–38, 2007.

[121] S. Tomasi, A. Razavi, and T. Ziegler. Density functional theory investigation into the stereocontrol of the syndiospecific polymerization of propylene catalyzed by C_s-symmetric zirconocenes. *Organometallics*, 26(8):2024–2036, 2007.

[122] A.and Resconi L. Mercandelli, P.and Sironi and I. Camurati. Comparing propene polymerization with 1-butene polymerization catalyzed by MAO-activated C_2- and C_1-symmetric zirconocenes: An experimental and computational study on the influence of olefin size on stereoselectivity. *Journal of Organometallic Chemistry*, 692(21):4784–4791, 2007.

[123] S. Tomasi and T. Razavi, A.and Ziegler. Stereoregularity, regioselectivity, and dormancy in polymerizations catalyzed by C_1-symmetric fluorenyl-based metallocenes. A theoretical study based on density functional theory. *Organometallics*, 28(8):2609–2618, 2009.

[124] A. Laine, M. Linnolahti, T.A. Pakkanen, J.R. Severn, E. Kokko, and A. Pakkanen. Comparative theoretical study on homopolymerization of α-olefins by bis(cyclopentadienyl) zirconocene and hafnocene: Elemental propagation and termination reactions between monomers and metals. *Organometallics*, 29(7):1541–1550, 2010.

[125] M.S.W. Chan, K. Vanka, C.C. Pye, and T. Ziegler. Density functional study on activation and ion-pair formation in Group IV metallocene and related olefin polymerization catalysts. *Organometallics*, 18(22):4624–4636, 1999.

[126] J.P. Perdew, K. Burke, and M. Ernzerhof. Generalized gradient approximation made simple. *Physical Review Letters*, 78(7):1396–1396, 1997.

[127] T.H. Dunning. Gaussian basis sets for use in correlated molecular calculations. I. The atoms boron through neon and hydrogen. *The Journal of Chemical Physics*, 90(2):1007–1023, 1989.

[128] G. Talarico, A.N.J. Blok, T.K. Woo, and L. Cavallo. Comparison of *ab initio* and DFT methods for studying chain propagation and chain termination processes with Group 4 polymerization catalysts. 1. The ansa-bis(cyclopentadienyl)zirconium catalyst. *Organometallics*, 21(23):4939–4949, 2002.

[129] C. Ehm, P.H.M. Budzelaar, and V. Busico. Calculating accurate barriers for olefin insertion and related reactions. *Journal of Organometallic Chemistry*, 775:39–49, 2015.

[130] J.C.W. Lohrenz, M. Bühl, M. Weber, and W. Thiel. A density functional study on the formation of stereoerrors in the stereoselective propene polymerization with zirconocene catalysts. *Journal of Organometallic Chemistry*, 592(1):11–21, 1999.

[131] L. Resconi, S. Bossi, and L. Abis. Study on the role of methylalumoxane in homogeneous olefin polymerization. *Macromolecules*, 23(20):4489–4491, 1990.

[132] E. Giannetti, G. M. Nicoletti, and R. Mazzocchi. Homogeneous ZieglerNatta catalysis. II. Ethylene polymerization by IVB transition metal complexes/methyl aluminoxane catalyst systems. *Journal of Polymer Science: Polymer Chemistry Edition*, 23(8):2117–2134, 1985.

[133] E.Y.X. Chen and T.J. Marks. Cocatalysts for metal-catalyzed olefin polymerization: Activators, activation processes, and structureactivity relationships. *Chemical Reviews*, 100(4):1391–1434, 2000.

[134] S. S. Reddy and S. Sivaram. Homogeneous metallocene-methylaluminoxane catalyst systems for ethylene polymerization. *Progress in Polymer Science*, 20(2):309–367, 1995.

[135] H. Sinn. Proposals for structure and effect of methylalumoxane based on mass balances and phase separation experiments. *Macromolecular Symposia*, 97(1):27–52, 1995.

[136] M.R. Mason, J.M. Smith, S.G. Bott, and A.R. Barron. Hydrolysis of tri-tert-butylaluminum: the first structural characterization of alkylalumoxanes

$[(R_2Al)_2O]_n$ and $(RAlO)_2$. *Journal of the American Chemical Society*, 115(12):4971–4984, 1993.

[137] D.W. Imhoff, L.S. Simeral, S.A. Sangokoya, and J.H. Peel. Characterization of methylaluminoxanes and determination of trimethylaluminum using proton NMR. *Organometallics*, 17(10):1941–1945, 1998.

[138] T. Sugano, K. Matsubara, T. Fujita, and T. Takahashi. Characterization of alumoxanes by ^{27}Al-NMR spectra. *Journal of Molecular Catalysis*, 82(1):93–101, 1993.

[139] E. Zurek and T. Ziegler. Toward the identification of dormant and active species in MAO (methylaluminoxane)-activated, dimethylzirconocene-catalyzed olefin polymerization. *Organometallics*, 21(1):83–92, 2001.

[140] E. Zurek and T. Ziegler. A theoretical study of the insertion barrier of MAO (methylaluminoxane)-activated, Cp_2ZrMe_2-catalyzed ethylene polymerization: further evidence for the structural assignment of active and dormant species. *Faraday Discussions*, 124:93–109, 2003.

[141] E. Zurek and T. Ziegler. Theoretical studies of the structure and function of MAO (methylaluminoxane). *Progress in Polymer Science*, 29(2):107–148, 2004.

[142] J.T. Hirvi, M. Bochmann, J.R. Severn, and M. Linnolahti. Formation of octameric methylaluminoxanes by hydrolysis of trimethylaluminum and the mechanisms of catalyst activation in single-site α-olefin polymerization catalysis. *ChemPhysChem*, 15(13):2732–2742, 2014.

[143] M.S. Kuklin, J.T. Hirvi, M. Bochmann, and M. Linnolahti. Toward controlling the metallocene/methylaluminoxane-catalyzed olefin polymerization process by a computational approach. *Organometallics*, 34(14):3586–3597.

[144] X. Yang, C.L. Stern, and T.J. Marks. Cation-like homogeneous olefin polymerization catalysts based upon zirconocene alkyls and tris(pentafluorophenyl)borane. *Journal of the American Chemical Society*, 113(9):3623–3625, 1991.

[145] X. Yang, C. Stern, and T.J. Marks. Models for organometallic molecule-support complexes. Very large counterion modulation of cationic actinide alkyl reactivity. *Organometallics*, 10(4):840–842, 1991.

[146] J. Zhou, S.J. Lancaster, D.A. Walker, S. Beck, M. Thornton-Pett, and M. Bochmann. Synthesis, structures, and reactivity of weakly coordinating anions with delocalized borate structure: The assessment of anion effects in metallocene polymerization catalysts. *Journal of the American Chemical Society*, 123(2):223–237, 2001.

[147] J.C.W. Chien, W.M. Tsai, and M.D. Rausch. Isospecific polymerization of propylene catalyzed by rac-ethylenebis(indenyl)methylzirconium cation. *Journal of the American Chemical Society*, 113(22):8570–8571, 1991.

[148] L. Jia, X. Yang, C.L. Stern, and T.J. Marks. Cationic metallocene polymerization catalysts based on tetrakis(pentafluorophenyl)borate and its derivatives. Probing the limits of anion noncoordination via a synthetic, solution dynamic, structural, and catalytic olefin polymerization study. *Organometallics*, 16(5):842–857, 1997.

[149] D.J. Gillis, M.J. Tudoret, and M. C. Baird. Novel arene complexes of titanium(IV), zirconium(IV), and hafnium(IV). *Journal of the American Chemical Society*, 115(6):2543–2545, 1993.

[150] S.J. Lancaster, O.B. Robinson, M. Bochmann, S.J. Coles, and M.B. Hursthouse. Synthesis and reactivity of new nono(cyclopentadienyl)zirconium and -hafnium alkyl complexes. Crystal and molecular structure of $[\{C_5H_3(SiMe_3)_2\}HfMe_2(\eta^6\text{-toluene})][BMe(C_6F_5)_3]$. *Organometallics*, 14(5):2456–2462, 1995.

[151] I.E Nifant'ev, L.Y. Ustynyuk, and D.N. Laikov. DFT Study of ethylene polymerization by zirconoceneboron catalytic systems. Effect of counterion on the kinetics and mechanism of the process. *Organometallics*, 20(25):5375–5393, 2001.

[152] F. Song, S.J. Lancaster, R.D. Cannon, M. Schormann, S.M. Humphrey, C. Zuccaccia, A. Macchioni, and M. Bochmann. Synthesis, ion aggregation, alkyl bonding modes, and dynamics of 14-electron metallocenium ion pairs $[(SBI)MCH_2SiMe_3^+ \cdots X^-]$ (M = Zr, Hf): Inner-sphere ($X = MeB(C_6F_5)_3$) versus outer-sphere ($X = B(C_6F_5)_4$) structures and the implications for "continuous" or "intermittent" alkene polymerization mechanisms . *Organometallics*, 24(6):1315–1328, 2005.

[153] S.Y. Yang and T. Ziegler. Combined CarParrinello QM/MM dynamic study on the propagation and termination steps of ethylene polymerization catalyzed by $[Cp_2ZrR(\mu\text{-Me})B(C_6F_5)_3]$ (R = Me, Pr). *Organometallics*, 25(4):887–900, 2006.

[154] A. Laine, B.B. Coussens, J.T. Hirvi, A. Berthoud, N. Friederichs, J.R. Severn, and M. Linnolahti. Effect of ligand structure on olefin polymerization by a metallocene/borate catalyst: A computational study. *Organometallics*, 34(11):2415–2421, 2015.

[155] M. Linnolahti, T.A. Pakkanen, R. Leino, H.J.G. Luttikhedde, C.E. Wilén, and J.H. Näsman. Conformational preferences of racemic ethylene-bridged bis(indenyl)-type zirconocenes: *Ab initio* HartreeFock study. *European Journal of Inorganic Chemistry*, 2001(8):2033–2040, 2001.

[156] M.P. Mitoraj, A. Michalak, and T. Ziegler. On the nature of the agostic bond between metal centers and β-hydrogen atoms in alkyl complexes. An analysis based on the Extended Transition State Method and the Natural Orbitals for Chemical Valence Scheme (ETS-NOCV). *Organometallics*, 28(13):3727–3733, 2009.

[157] E. Clot and O. Eisenstein. *Agostic interactions from a computational perspective: One name, many interpretations*, pages 1–36. Springer Berlin Heidelberg, Berlin, Heidelberg, 2004.

[158] A. Haaland, W. Scherer, K. Ruud, G.S. McGrady, A.J. Downs, and O. Swang. On the nature and incidence of β-agostic interactions in ethyl derivatives of early transition metal: Ethyltitanium trichloride and related compounds. *Journal of the Americam Chemical Society*, 120(15):3762–3771, 1998.

[159] P.L.A Popelier and G Logothetis. Characterization of an agostic bond on the basis of the electron density. *Journal of Organometallic Chemistry*, 555(1):101–111, 1998.

[160] H. Krauledat and H.H. Brintzinger. Isotope effects associated with α-olefin insertion in zirconocene-based polymerisation catalysts: Evidence for an α-agostic transition state. *Angewandte Chemie International Edition in English*, 29(12):1412–1413, 1990.

[161] W.E. Piers and J.E. Bercaw. α-Agostic assistance in Ziegler-Natta polymerization of olefins. Deuterium isotopic perturbation of stereochemistry indicating coordination of an α-carbon-hydrogen bond in chain propagation. *Journal of the American Chemical Society*, 112(25):9406–9407, 1990.

[162] G. Lanza, I.L. Fragalà, and T.J. Marks. Energetic, structural, and dynamic aspects of ethylene polymerization mediated by homogeneous single-site Constrained Geometry Catalysts in the presence of cocatalyst and solvation: An investigation at the *ab Initio* quantum chemical level. *Organometallics*, 21(25):5594–5612, 2002.

[163] Z. Xu, K. Vanka, T. Firman, A. Michalak, E. Zurek, C. Zhu, and T. Ziegler. Theoretical study of the interactions between cations and anions in Group IV transition-metal catalysts for single-site homogeneous olefin polymerization. *Organometallics*, 21(12):2444–2453, 2002.

[164] Zhitao Xu, Kumar Vanka, and Tom Ziegler. Influence of the counterion $MeB(C_6F_5)_3^-$ and solvent effects on ethylene polymerization catalyzed by $[(CpSiMe_2NR)TiMe]^+$: A combined density functional theory and molecular mechanics study. *Organometallics*, 23(1):104–116, 2004.

[165] K. Ziegler, T.and Vanka and Z. Xu. The influence of the counterion $B(C_6F_5)_3CH_3$ and solvent effects on the propagation and termination steps of ethylene polymerization catalyzed by Cp_2ZrR^+ (R=Me,Pr). A density functional study. *Comptes Rendus Chimie*, 8(9):1552–1565, 2005.

[166] V. A. Karttunen, M. Linnolahti, T. A. Pakkanen, J.R. Severn, E. Kokko, J. Maaranen, and P. Pitkänen. Influence of the ligand structure of hafnocene polymerization catalysts: A theoretical study on ethene insertion and chain propagation. *Organometallics*, 27(14):3390–3398, 2008.

[167] C. N. Rowley and T.K. Woo. Counteranion effects on the zirconocene polymerization catalyst olefin complex from QM/MM molecular dynamics simulations. *Organometallics*, 30(8):2071–2074, 2011.

[168] I. E. Nifant'ev, L. Y. Ustynyuk, and D. N. Laikov. A DFT study of ethylene polymerization by zirconocene catalysts. *Russian Chemical Bulletin*, 49(7):1164–1173, 2000.

[169] P. Corradini, G. Guerra, and L. Cavallo. Do new century catalysts unravel the mechanism of stereocontrol of old ZieglerNatta catalysts? *Accounts of Chemical Research*, 37(4):231–241, 2004.

[170] G.W. Coates. Polymerization catalysis at the millennium: frontiers in stereoselective, metal-catalyzed polymerization. *Journal of the Chemical Society, Dalton Transactions*, (4):467–475, 2002.

[171] K. Angermund, G. Fink, V.R. Jensen, and R. Kleinschmidt. Toward quantitative prediction of stereospecificity of metallocene-based catalysts for α-olefin polymerization. *Chemical Reviews*, 100(4):1457–1470, 2000.

[172] K.S. Sandhya, N. Koga, and M. Nagaoka. Revisiting the stereochemistry of propylene isotactic polymerization reaction mechanism on C_2 symmetric $[SiH_2(Ind)_2ZrCH_3]^+$ and $[SiH_2(Ind)_2ZrCH_3]^+[CH_3\ B(C_6F_5)_3]^-$. *Bulletin of the Chemical Society of Japan*, 89(9):1093–1105, 2016.

[173] J.J.P. Stewart. Optimization of parameters for semiempirical methods V: Modification of NDDO approximations and application to 70 elements. *Journal of Molecular Modeling*, 13(12):1173–1213, 2007.

[174] J.A. Pople, D.P. Santry, and G.A. Segal. Approximate selfconsistent molecular orbital theory. I. Invariant procedures. *The Journal of Chemical Physics*, 43(10):S129–S135, 1965.

[175] J.A. Pople and G.A. Segal. Approximate selfconsistent molecular orbital theory. II. Calculations with complete neglect of differential overlap. *The Journal of Chemical Physics*, 43(10):S136–S151, 1965.

[176] U.S.D. o. Energy. The Department of Energy's Critical Materials Strategy.

[177] N. G. Connelly, Royal Society of Chemistry (Great Britain), and International Union of Pure and Applied Chemistry. *Nomenclature of inorganic chemistry. IUPAC recommendations 2005*. Royal Society of Chemistry, 2005.

[178] G.R. Giesbrecht and J.C. Gordon. Lanthanide alkylidene and imido complexes. *Dalton Transactions*, 0(16):2387–2393, 2004.

[179] R. D. Shannon. Revised effective ionic radii and systematic studies of interatomic distances in halides and chalcogenides. *Acta Crystallographica Section A*, 32(5):751–767, 1976.

[180] E.S Schmidt, A. Jockisch, and H. Schmidbaur. *Journal of the American Chemical Society*, 121.

[181] C. Cui, H.W. Roesky, H.G. Schmidt, M. Noltemeyer, H. Hao, and F. Cimpoesu. Synthesis and structure of a monomeric aluminum(I) compound $[\{HC(CMeNAr)_2\}Al]$ (Ar=2,6i$Pr_2C_6H_3$): A stable aluminum analogue of a carbene. *Angewandte Chemie*, 39(23):4274–4276, 2000.

[182] Y. Segawa, M. Yamashita, and K. Nozaki. Boryllithium: Isolation, characterization, and reactivity as a boryl anion. *Science*, 314(5796):113–115, 2006.

[183] A. Sundermann, M. Reiher, and W.W. Schoeller. Isoelectronic arduengo-type carbene analogues with the Group IIIa elements boron, aluminum, gallium, and indium. *European Journal of Inorganic Chemistry*, 1998(3):305–310, 1998.

[184] W.W. Schoeller, S. Grigoleit, T. Busch, P.v.R. Schleyer, C.H.L. Kennard, R.N. Lamb, and C.L. Raston. On the electronic structure of main group diazadiene complexes, with boron, aluminium, gallium and indium, a density functional evaluation. 88(3):405–409, 2002.

[185] Lin, Z. Reactivities and electronic properties of boryl ligands. *Structure and Bonding*, pages 39–58, 2016.

[186] J. Zhu, Z. Lin, and T.B Marder. Trans influence of boryl ligands and comparison with C, Si, and Sn Ligands. *Inorganic Chemistry*, 44(25):9384–9390, 2005.

[187] S.P. Green, C. Jones, D.P. Mills, and A. Stasch. Group 9 and 11 metal(I) gallyl complexes stabilized by N-heterocyclic carbene coordination: First structural characterization of GaM (M = Cu or Ag) bonds. *Organometallics*, 26(14):3424–3430, 2007.

[188] M. Yamashita, Y. Suzuki, Y. Segawa, and K. Nozaki. Crystal structure of boryllithium with two THF molecules and DFT analysis of its property as a boryl anion. *Chemistry Letters*, 37(7):802–803, 2008.

[189] Y. Segawa, Y. Suzuki, M. Yamashita, and K. Nozaki. Chemistry of boryllithium: Synthesis, structure, and reactivity. *Journal of the American Chemical Society*, 130(47):16069–16079, 2008.

[190] R.J. Baker, C. Jones, M. Kloth, and J.A. Platts. Synthesis and structural characterization of thermally stable Group 13 hydride complexes derived from a gallium(I) carbene analogue. *Angewandte Chemie International Edition*, 42(23):2660–2663, 2003.

[191] R.J. Baker, C. Jones, and J. A. Platts. Analogies between the reactivities of an anionic gallium(I) heterocycle and N-heterocyclic carbenes toward metallocenes. *Journal of the American Chemical Society*, 125(35):10534–10535, 2003.

[192] R.J. Baker, C. Jones, and J.A. Platts. Synthesis, structural and theoretical studies of an irongallium(i) heterocycle complex: Analogies with N-heterocyclic carbene chemistry. *Dalton Trans.*, (19):3673–3674, 2003.

[193] R. Baker and C. Jones. The coordination chemistry and reactivity of group 13 metal(I) heterocycles. *Coordination Chemistry Reviews*, 249(17-18):1857–1869, 2005.

[194] S. Aldridge, R.J. Baker, N.D. Coombs, C. Jones, R. P. Rose, A. Rossin, D.J. Willock, W.P. Leung, and K. Rypdal. Complexes of a gallium heterocycle with transition metal dicyclopentadienyl and cyclopentadienylcarbonyl fragments, and with a dialkylmanganese compound. *Dalton Transactions*, 42(27):3313, 2006.

[195] R.J. Baker, C. Jones, D.M. Murphy, B. Wibbeling, R. Fröhlich, O. Blacque, H. Berke, G.R. Whittell, and L.J. Wright. Evidence for the first oxidative insertion of a transition metal into a digallane(4): synthesis, structural characterisation and EPR studies of $[Cp_2ZrIII\{Ga[N(Ar)C(H)]_2\}_2][Li(THF)_4]$, Ar = $C_6H_3iPr_2$-2,6. *Chemical Communications*, 663(10):1339, 2005.

[196] C. Jones, R.P. Rose, A. Stasch, K R. Senge, B.A. Sturgeon, P.P. Power, B. Wu, P.v.R. Schleyer, H.F. Schaefer, and G.H. Robinson. Synthesis and characterisation of zinc gallyl complexes: First structural elucidations of ZnGa bonds. *Dalton Trans.*, 32(28):2997–2999, 2007.

[197] C. Jones, A. Stasch, and W.D. Woodul. Gallyl lanthanide complexes containing unsupported LnGa (Ln = Sm, Eu, Yb or Tm) bonds. *Chemical Communications*, (1):113–115, 2009.

[198] S.T. Liddle, D.P. Mills, B. M. Gardner, J. McMaster, C. Jones, and W.D. Woodul. A heterobimetallic gallyl complex containing an unsupported GaY bond. *Inorganic Chemistry*, 48(8):3520–3522, 2009.

[199] A.V. Protchenko, L.M.A. Saleh, D. Vidovic, D. Dange, C. Jones, P. Mountford, and S. Aldridge. Contrasting reactivity of anionic boron- and gallium-containing NHC analogues: EC vs. EM bond formation (E = B, Ga). *Chemical Communications*, 46(45):8546, 2010.

[200] C. Jones, D.P. Mills, R.P. Rose, A. Stasch, and W.D. Woodul. Synthesis and further reactivity studies of some transition metal gallyl complexes. *Journal of Organometallic Chemistry*, 695(22):2410–2417, 2010.

[201] O. Bonello, C. Jones, A. Stasch, and W.D. Woodul. Group 2 and 12 metal gallyl complexes containing unsupported GaM covalent bonds (M = Mg, Ca, Sr, Ba, Zn, Cd). *Organometallics*, 29(21):4914–4922, 2010.

[202] D. Dange, S.L. Choong, C. Schenk, A. Stasch, and C. Jones. Synthesis and characterisation of anionic and neutral gallium(i) N-heterocyclic carbene analogues. *Dalton Transactions*, 41(31):9304–9315, 2012.

[203] K.K. Pandey. The nature of MGa in metal(I) gallyl complexes of copper, silver and gold: A theoretical study. *Journal of Organometallic Chemistry*, 701:75–79, 2012.

[204] M.T. Gamer, P.W. Roesky, S.N. Konchenko, P. Nava, and R. Ahlrichs. Al–Eu and Al–Yb Donor-Acceptor Bonds. *Angewandte Chemie International Edition*, 45(27):4447–4451, 2006.

[205] P.L. Arnold, S.T. Liddle, J. McMaster, C. Jones, and D.P. Mills. A LanthanideGallium complex stabilized by the N-heterocyclic carbene group. *Journal of the American Chemical Society*, 129(17):5360–5361, 2007.

[206] I.L. Fedushkin, A.N. Lukoyanov, A.N. Tishkina, M. O. Maslov, S.Y. Ketkov, and M. Hummert. Compounds with direct galliumlanthanum and galliumzinc bonds. *Organometallics*, 30(13):3628–3636, 2011.

[207] L.M.A. Saleh, K.H. Birjkumar, A.V. Protchenko, A.D. Schwarz, S. Aldridge, C. Jones, N. Kaltsoyannis, and P. Mountford. Group 3 and Lanthanide boryl compounds: Syntheses, structures, and bonding analyses of ScB, YB, and LuB σ-coordinated NHC analogues. *Journal of the American Chemical Society*, 133(11):3836–3839, 2011.

[208] J.F. Hartwig. Borylation and silylation of CH bonds: A platform for diverse CH bond functionalizations. *Accounts of Chemical Research*, 45(6):864–873, 2012.

[209] G.J. Irvine, M.J.G. Lesley, T.B. Marder, N.C. Norman, C.R. Rice, E.G. Robins, W.R. Roper, G.R. Whittell, and L.J. Wright. Transition metalboryl compounds: Synthesis, reactivity, and structure. *Chemical Reviews*, 98(8):2685–2722, 1998.

[210] H. Kono, K. Ito, and Y. Nagai. Oxidative addition of 4,4,6-trimethyl-1,3,2-dioxaborinane and benzo[1,3,2]diaxaborole to tris(triphenylphosphine)halogenorhodium. *Chemistry Letters*, 4(10):1095–1096, 1975.

[211] D. Männig and H. Nöth. Catalytic hydroboration with rhodium complexes. *Angewandte Chemie International Edition in English*, 24(10):878–879, 1985.

[212] Y. Satoh, M.and Nomoto, N. Miyaura, and A. Suzuki. New convenient approach to the preparation of (Z)-allylic boronates via catalytic 1,4-hydroboration of 1,3-dienes with catecholborane. *Tetrahedron Letters*, 30(29):3789–3792, 1989.

[213] I.D. Gridnev, N. Miyaura, and A. Suzuki. Regio- and stereospecific preparation of β-(alkylthio)alkenyl-1,3,2-benzodioxaboroles by nickel-catalyzed hydroboration of thioacetylenes with catecholborane. *Organometallics*, 12(2):589–592, 1993.

[214] G. Lesley, G. Nguyen, N.J. Taylor, T B. Marder, A.J. Scott, W. Clegg, and N.C. Norman. Synthesis and characterization of platinum(II)bis(boryl) catalyst precursors for diboration of alkynes and diynes: Molecular structures of cis-[$(PPh_3)_2$Pt(B-4-Butcat)$_2$], cis-[$(PPh_3)_2$Pt(Bcat)$_2$], cis-[(dppe)Pt(Bcat)$_2$], cis-[(dppb)Pt(Bcat)$_2$], (E)-(4-MeOC_6H_4. *Organometallics*, 15(24):5137–5154, 1996.

[215] K. M. Waltz. Selective functionalization of alkanes by transition-metal boryl complexes. *Science*, 277(5323):211–213, 1997.

[216] K.M. Waltz and J.F. Hartwig. Functionalization of alkanes by isolated transition metal boryl complexes. *Journal of the American Chemical Society*, 122(46):11358–11369, 2000.

[217] S. Li, Y. Cheng, J.and Chen, M. Nishiura, and Z. Hou. Rare Earth metal boryl complexes: Synthesis, structure, and insertion of a carbodiimide and carbon monoxide. *Angewandte Chemie International Edition*, 50(28):6360–6363, 2011.

[218] B. Wang, M. Nishiura, J. Cheng, and Z. Hou. Half-sandwich scandium boryl complexes bearing a silylene-linked cyclopentadienyl-amido ligand. *Dalton Transactions*, 43:14215–14218, 2014.

[219] C. Jones, D.P. Mills, R.P. Rose, A. Stasch, L. Grocholl, L. Stahl, R.J. Staples, R. Boomishankar, and A. Steiner. Synthesis and structural characterisation of group

10 metal(ii) gallyl complexes: analogies with platinum diboration catalysts? *Dalton Transactions*, 15(33):4395, 2008.

[220] C. Jones, D.P. Mills, R.P. Rose, A. Stasch, and W.D. Woodul. Synthesis and further reactivity studies of some transition metal gallyl complexes. *Journal of Organometallic Chemistry*, 695(22):2410–2417, 2010.

[221] C. Fonseca Guerra, J. G. Snijders, G. te Velde, and E. J. Baerends. Towards an order-N DFT method. *Theoretical Chemistry Accounts: Theory, Computation, and Modeling (Theoretica Chimica Acta)*, 99:391–403, 1998.

[222] G. te Velde, F. M. Bickelhaupt, E. J. Baerends, C. Fonseca Guerra, S. J. A. van Gisbergen, J. G. Snijders, and T. Ziegler. Chemistry with ADF. *Journal of Computational Chemistry*, 22:931–967, 2001.

[223] C. Edmiston and K. Ruedenberg. Localized atomic and molecular orbitals. *Reviews of Modern Physics*, 35(3):457–464, 1963.

[224] J. M. Foster and S. F. Boys. Canonical configurational interaction procedure. *Reviews of Modern Physics*, 32(2):300–302, 1960.

[225] W. von Niessen. Density localization of atomic and molecular orbitals. I. *The Journal of Chemical Physics*, 56(9):4290, 1972.

[226] T. Ziegler and A. Rauk. A theoretical study of the ethylene-metal bond in complexes between copper^{1+}, silver^{1+}, gold^{1+}, platinum^{0} or platinum^{2+} and ethylene, based on the Hartree-Fock-Slater transition-state method. *Inorganic Chemistry*, 18(6):1558–1565, 1979.

[227] D.A. Pantazis and F. Neese. All-electron scalar relativistic basis sets for the Actinides. *Journal of Chemical Theory and Computation*, 7(3):677–684, 2011.

[228] Personal communication between Nikolas Kaltsoyannis and Dimitrios Pantazis.

[229] S. Aldridge and A.J. Downs, editors. *The Group 13 Metals Aluminium, Gallium, Indium and Thallium: Chemical Patterns and Peculiarities*. John Wiley & Sons, Ltd, 2011.